CHEMIA

STUDIA UNIVERSITATIS BABEȘ-BOLYAI CHEMIA

S T U D I A

UNIVERSITATIS BABEŞ–BOLYAI

CHEMIA

3

CUPRINS – CONTENT – SOMMAIRE – INHALT

In Memoriam Professor Petre T. Frangopol (1933-2020)

In Memoriam Professor Petre T. Frangopol, Ph.D.
Honor Member of the Romanian Academy
1933-2020

It is my great pleasure to see this special issue dedicated to the memory of Professor Ph.D., Petre Frangopol!

Petre Frangopol was a top Romanian scientist, a member of the Romanian Academy, who, during his rich and productive scientific career, was also associated to our university.

I met him in 2005, when I was the personal adviser for research of the minister for education and research, as a partner/consultant in the research/ education reform we started then. He was among the (few) scientists who supported the excellence, as the main framework of the 2005 reform. Then, we together initiated "the Presidential Commission" – around the cabinet of the President of Romania –, which assessed the Romanian education-research system and then proposed a new strategy in education/research, on which the new law of education was built in 2011. After that, we together initiated and created in 2013 the G3A (Analysis/Attitude/Action), a Think Tank continuing the analysis and the monitoring of 2005/2011 reforms and beyond them; the G3A Think Tank produced several influential reports during the years.

In the process, we started to also collaborate scientifically and we even published some works together, relating policy of science and/or scientometrics (e.g., David & Frangopol, 2015, in "Scientometrics": The lost paradise, the original sin, and the Dodo bird: A scientometrics Sapere Aude manifesto as a reply to the Leiden manifesto on scientometrics; DOI:10.1007/s11192-015-1634-2).

In the end, despite the age difference, we became close friends, so his death was not only a professional lost for me and the Romanian academic community, but also a personal one for me!

Thank you, dear colleague and friend, for everything! Your life was inspirational for many of us and you created things, which remains and positively impact many!

Daniel DAVID, Rector of the Babeş-Bolyai University

PETRE T. FRANGOPOL (1933-2020).
ROMANIAN ACADEMIC, SCIENTIST, MENTOR AND FRIEND

GHEORGHE BENGA[a,b,c]

In December 2020, academics and scientists – particularly chemists – received the very sad news that our beloved colleague and friend Petre T. Frangopol passed away. The aim of this obituary is to pay tribute to an outstanding Romanian scientist, a man of great character and an unforgettable friend. Petre T. Frangopol (a.k.a. Petrache for his friends) described in detail the history of his family in a Meeting of the Romanian Academy (October 8, 2018) dedicated to his 85th anniversary. I had the honor to be invited speaker to that event, as we collaborated for several decades. The proceedings of that Meeting were published [1, 2].

Petre T. Frangopol was very proud of the *saga* of his family. His great-grandparents were Greeks from a village in Bulgaria called Mesemvria (Nesebăr of today), where the Greeks (mainly shepherds) formed 100% of the population. After an ethnic cleansing done by the Bulgarians in 1860, all the inhabitants of this village sold their properties and came to the historical region of Romania called Dobruja (Dobrogea), on the Black Sea Coast, namely to Kiustengé (the Turkish name of a village which later would become the city of Constanţa). Petre, born on May 26, 1933, in Constanţa, was the son of Theodor (born in Constanţa) and Ecaterina (born in Varna, Bulgaria). He received a solid education. His father took him to the Greek school, saying: "...you have a Greek name, but you should know that you are Romanian, like your father, who fought for this country in the First World War, which you should love as I myself do" [3]. After graduating from primary school Petrache followed the subsequent grades (1944-1951) at "Mircea the Great," the oldest and most prestigious high school for boys in Constanţa. The majority of professors obtained Ph.D. titles from German or French universities. Many cultural events, including conferences of great scientists and writers, took place throughout the year in the performance hall of the school.

---

a   *Romanian Academy;*
b   *Academy of Medical Sciences of Romania;*
c   *School of Molecular Biosciences, University of Sydney, Australia, gbgbenga@gmail.com*

P. T. Frangopol chose to become a chemist, following the example of some members of his family. He graduated from the Chemical Engineering Department, Polytechnical Institute of Iaşi in 1956 and would receive his Ph.D. (Dr. Eng.) in 1968 at another prestigious university, the Polytechnical Institute of Timişoara, under the supervision of Giorgio Ostrogovich, Department of Organic Chemistry.

P. T. Frangopol recalled [3] Academician Horia Hulubei as most important for his own achievements in life. In 1956 a new Soviet nuclear reactor (cyclotron and betatron) was installed in Bucureşti-Măgurele, Romania thus becoming the 7th country in the world to have a nuclear reactor. A new Institute of Atomic Physics (in Romanian, Institutul de Fizică Atomică, IFA) was founded in Bucureşti-Măgurele, under the aegis of The Romanian Academy. The right person was chosen to organize IFA: Academician Horia Hulubei, who was the first Director (and Founder), of IFA.

Petre T. Frangopol presented in detail the history of IFA [4]. Two problems had to be quickly solved: a) to educate personnel qualified in the field of atomic and nuclear physics (and connected domains: radiochemistry and nuclear technologies); and, b) to set up, at IFA, laboratories specialized in these domains. To solve the problem of education, in 1956-1957 a special one-year program of studies under the aegis of IFA was organized. This program included 80 students selected by competition from among the graduates of different faculties of physics, chemistry and engineering of Romanian Universities or Polytechnics. The students were divided into four groups of 20 each, assigned to: radiochemistry, electronics, biology and medicine. The graduates were then assigned to the different collectives newly formed in 1957, either at IFA or at laboratories in universities, research institutes and in factories.

On the other hand, other new laboratories were set up at IFA. In 1960 Academician Horia Hulubei asked Petre T. Frangopol to found the Laboratory of Labelled Organic Compounds, together with Alexandru T. Balaban. Both of them graduated (1957) the special one-year program of studies in radiochemistry and nuclear technology organized under the aegis of IFA. They were assigned to radiochemistry (and to the cyclotron collective). From 1957 to 1963, Petre T. Frangopol was Staff member, Laboratory of Organic Chemistry (chaired by Academician Costin D. Neniţescu) at Bucureşti Polytechnical Institute, being paid by IFA and having research topics of IFA. Petrache recalled [4] that Horia Hulubei had asked him to take a temporary absence from the laboratory of Professor Neniţescu, to come to IFA and set up a laboratory for the preparation of organic compounds labelled with radioactive iodine (^{131}I) and other (radioactive and stable) isotopes. The technology would be further used by technicians hired specially for the production of these isotopes.

A. T. Balaban was a young lecturer in the Laboratory of Organic Chemistry chaired by Academician Neniţescu (who also supervised Balaban's Ph.D. work). In parallel, Balaban was hired at IFA in 1956. However, Academician Neniţescu asked Alexandru to fulfill all his duties as lecturer (seminars and laboratory work with students). Under these conditions, Petre was forced to set up alone the laboratory.

Such a laboratory had not existed previously in Romania. Petre has not received an adequate space for the laboratory, but a huge empty room – a corridor in the basement, several meters below ground. There, they installed a hood, projected by Petre and made by excellent craftsmen hired by IFA. After 7 months, the group succeeded to prepare, for the first time in Romania, ^{131}I, widely used afterwards for treating diseases of the thyroid.

IFA became a multidisciplinary center of excellence [4]. In the first 6 years after its foundation, over 80 scientific articles have been published by researchers at IFA. Frangopol and Balaban were among the best young researchers of IFA. They performed successful studies aimed to solve important practical problems. An important line of research was the preparation and investigation of stable free radicals for studies of Electron Spin Resonance (ESR), also called Electron Paramagnetic Resonance (EPR), using the ESR spectrometer made by electronics specialists at IFA. It was first necessary to prepare the stable free radical 1,1-diphenyl-2-picrilhydrazyl (DPPH), which is used as standard of the position and intensity of ESR signals. This was the starting point for the development of a domain of basic research at IFA. Other stable free radicals have been prepared, many of them with the essential help of Mioara Frangopol, the distinguished wife of Petre T. Frangopol. Several articles were published in the prestigious journal *Tetrahedron*, mentioned in ref. [4]. Moreover, collaboration of Petre and Mioara Frangopol with other scientists has started. The work on stable free radicals of the group at IFA gained international recognition, being cited in several well known books by foreign researchers [5–7].

As a result of his many scientific accomplishments, P.T. Frangopol obtained financial support for research in Canada (Post Doctoral Fellow, National Research Council, Ottawa, Ontario, 1969-1970), U.S.A. (Post Doctoral Research Associate, with a NASA contract at the George Washington University, Department of Chemistry, Washington, D.C., 1970-1971), and Germany (Dozentenstipendium, Humboldt Foundation, 1972). He was also cited in many articles in leading (mainstream) journals and books published by well known publishers. As a result he was invited to present lectures (as plenary lecturer or key speaker) at many scientific events, Universities, and Institutions around the world: U.S.A. (Gordon Conferences, Argonne National Laboratory, Brookhaven National Laboratory, George Washington University,

Washington DC, Colorado University at Boulder, University of Illinois Urbana etc.), Sweden (Umeå University, Stockholm University), France (Centre d'Etudes Nucleaires de Grenoble et de Saclay), Belgium (Leuven University), Germany (Marburg/Lahn University, German Chemical Societies Annual Meetings), EUCHEM Conferences, Slovakia (Bratislava University), Greece (Athens, Thessaloniki, Patras and Ioannina Universities), former USSR (Novosibirsk Institute of Organic Chemistry, Moscow Institute of Chemical Physics) etc.

Although P.T. Frangopol received many offers to settle abroad, he returned to IFA, since he was leading a laboratory founded and equipped by him at international standards, with technologies of preparation and techniques for measuring the organic compounds labelled with radioactive isotopes developed for the first time in Romania. Unfortunately, his laboratory was completely destroyed by fire during the 1977 earthquake.

In 1976 IFA was reorganized, the Laboratories of physics became institutes, and the name of IFA was changed to "Horia Hulubei" National Institute for Research & Development in Physics and Nuclear Engineering (in Romanian Institutul de Cercetare-Dezvoltare pentru Fizică şi Inginerie Nucleară „Horia Hulubei", abbreviated as IFIN-HH). Petre T. Frangopol had an essential role in organizing a Center of Radiochemical Production, beginning with documentation, project, development of technologies for production of radiopharmaceutical and radioisotopes. Moreover, the results of researches had to have direct economic applications, i.e., to be sold, as no financial support from the budget of Romania was provided before 1989, according to the policy of the communist regime. Thus, the second period of P.T. Frangopol's work at IFA began (1977-1990), when he had again to start everything from scratch: finding the space for the Laboratory for Production of Radioactive Isotopes, procurement and installation of the necessary equipment, in addition to finding the sources for self-financing the production of radioactive isotopes (^{32}P, ^{45}Ca, ^{59}Fe, ^{35}S, ^{192}Ir, ^{99m}Tc) to be used in industry, agriculture, biology and especially in medicine.

P.T. Frangopol extended later his activity, from organic physical-chemistry and radiochemistry, to biophysical chemistry and biophysics. He was the editor of the first annual publication of biophysics in Romania: *Seminars in Biophysics*, a series of 6 annual volumes (1985-1990) published in English by IFA. He developed new projects of applied research having national and international impact, using the equipment built at IFIN: the electron spin resonance (ESR) spectrometer ART-6, the nuclear magnetic resonance (NMR) spectrometer etc. In addition, P.T. Frangopol initiated and managed an extended program of biophysical studies on the interaction of medicines with cell membranes, financed by the Ministry of Chemical Industry. The program (pursued from 1981 till 1991) involved groups of researchers from Bucharest, Cluj-Napoca and Iaşi.

I met Petre T. Frangopol for the first time in 1976, when he came to the Department of Biochemistry, Faculty of Medicine, Institute of Medicine and Pharmacy Cluj-Napoca (today "Iuliu Haţieganu" University of Medicine and Pharmacy, Cluj-Napoca), where I was a young Lecturer. Petre introduced himself and said that he was the leader of a group of researchers from IFA and made a proposal to collaborate with him, since he believed we had mutual research interests in studies using spin labels. He had heard that I had just returned from the U.K., after 12 months of post-doc work in the laboratory of Professor Dennis Chapman, a well-known scientist in the field of biological membranes. My project involved the study of protein-lipid interactions in biological membranes using several techniques, including NMR, spin labelling ESR etc. I published several articles with the British scientists [8, 9] and with Vasile V. Morariu, a former high school coleague (and an excellent Romanian scientist) [10, 11]. I was honoured that such an outstanding scientist as Petre T. Frangopol (11 years older than me, with so many accomplishments) was inviting me to collaborate with him.

After visiting his laboratory in București-Măgurele, I realized that he was really a world-class scientist. In addition, I met his wife, the distinguished Mioara Frangopol, who impressed me deeply, by her competence as a scientist and also by her humane qualities. She was very intelligent. She always found the best ways to perform excellent laboratory work even if the conditions were not as good as in laboratories from abroad. She was always very kind and ready to help as much as she could any person who deserved to be helped. I realized that actually at IFA there was the "Professor Petre T. Frangopol and Dr. Mioara Frangopol group," Mioara being a strong support for Petrache, giving him the best advice in all situations.

A very fruitful collaboration started between the "Frangopol group" in București-Măgurele and the two groups in Cluj-Napoca: V.V. Morariu's group at I.T.I.M. and Benga's group at „Iuliu Haţieganu" University of Medicine and Pharmacy (where I was nominated in 1978 as Chief of the new Discipline of Cell Biology). Our groups have published many papers over several decades [12-15]. In addition, it was for us, the people from Cluj-Napoca, the chance of becoming close friends to Petrache Frangopol. I have learnt a lot of things from him, not only scientific, but also how to write the applications to obtain financial support in Romania, mainly from The *Academy of Medical Sciences* and *The National Council for Higher Education Scientific Research* (in Romanian *Consiliul Naţional al Cercetării Ştiinţifice din Învăţământul Superior*, CNCSIS).

Based on his experience at IFA, Petre T. Frangopol was invited in 1990 as Professor at the University "Alexandru Ioan Cuza" (UAIC) Iaşi, to set up a Section of Biophysics at the Faculty of Physics. He received nothing in terms of spaces and funding of laboratories, since the UAIC leaders claimed that

funding received from the Ministry of Education was provided only for existing sections (not for a new one). Based on his experience from București-Măgurele, P.T. Frangopol obtained annual finances from the Ministry of Research in Romania for his two new laboratories at UAIC: one was the Laboratory of Medical Physics (the first such laboratory in Romania), and the other was the Laboratory of Biophysics (the second such laboratory after that of the București University). In addition, Professor Frangopol obtained funding (over 500,000 USD) by international competition, from the International Atomic Energy Agency, from the European Union programs (Erasmus, Copernicus) etc. Although Professor Frangopol obtained funding, UAIC offered him only a basement space for setting up the laboratories. During his tenure at UAIC, Professor Frangopol edited a series of 6 annual volumes (1992-1997) *Current topics in Biophysics*, published in English by Iaşi University Press. He invited authors from over 35 Universities and Scientific Institutions from 13 countries (U.S.A., Canada, Japan, and Europe) to provide scientific literatures for the bachelor's degree students. He also sent his students abroad, to perform the experimental work for their Ph.D. degree in well equipped laboratories, with which scientific collaboration was established. The results were published in international scientific journals. He supported the further development of the graduates of his Section of Biophysics at well-known universities. Some of them became Professors at: Free University of Berlin, Graz University (Austria), Athens University (Greece), Umeå University, Linköping University (Sweden), University College Dublin (Ireland), University of California at Irvine, Stanford University, Texas A&M University (USA), University of Queensland (Australia) etc.

P.T. Frangopol was Professor of Biophysics and Medical Physics at UAIC from 1991 to 1999. He continued his academic career as Professor of Biophysics and Biophysical Chemistry at the „Babeş-Bolyai" University (Faculty of Chemistry), Cluj-Napoca (1999-2002), the "Vasile Goldiş" Western University Arad (Faculty of Medicine) and the Department of Physics, Polytechnica University Bucureşti (2002-2004). Everywhere, Petre was highly appreciated by the colleagues and students alike, for his competence, as well as for his unique scientific and humane qualities.

From 2012 to 2016, Petre T. Frangopol was the Editor-in-Chief of *Revista de Politica Ştiinţei şi Scientometrie,* a journal of *CNCSIS* and The Ministry of Education and Research (which stopped funding of the journal in 2016). He published a lot of important articles on the problems of the Romanian education and research, i.e., the *Science Policy.* The articles were first published in the weekly supplement *Aldine* of the journal *România Liberă.* Then he compiled the articles assembling 7 volumes entitled „*Mediocrity and Excellence: a radiography of science and education in Romania*", published from 2002 to 2019.

He was also member of the Editorial Board of several important journals from Romania and abroad: *Revue Roumaine de Chimie*, *Journal of Radioanalytical and Nuclear Chemistry*, *Scientometrics*.

P.T. Frangopol had many fields of interest: Chemistry, Radiochemistry, Physical Organic Chemistry, Biophysical Chemistry, Biophysics, Medical Physics, Archaeometry, Oceanography, Science Policy, Management of Science Policy, Scientometrics, and History of Chemistry in Romania.

Over the years, P.T. Frangopol initiated and organized or co-organized many scientific events: multidisciplinary seminars at IFA; four national conferences of the chemical physics program (1986-1989, Iaşi, Cluj-Napoca, Bucureşti, some lectures being published in special issues of *Revue Roumaine de Biochimie*); Seminars on some Romanian original drugs, procain-based drugs, Gerovital H$_3$, and Aslavital, Trofopar and Boicil: analytical methods and effects on cell membranes (1983, 1984); two Romanian Conferences on the Application of Physics Methods in Archaeology, Cluj-Napoca, 1987 and 1989 (with volumes published each time); the 8th workshop "Balcanic Days of Biochemistry and Biophysics", organized for the first time in Romania, Cluj-Napoca, 1990, with Vasile V. Morariu) etc.

Petre T. Frangopol was Scientific Counselor at *CNCSIS*. He contributed to making possible the access of Romanian scientists to Science *Citation Index*, published first by the Institute of Scientific Information of Philadelphia, known as ISI Thomson Reuters. This database is now managed by Clarivate Analytics.

Unsurprisingly, the achievements of P.T. Frangopol were recognized by many prizes and distinctions received throughout his life: the "Constantin Miculescu" Prize of the Romanian Academy (1990, for his work on the biophysics of the interaction of Romanian drugs with cellular membranes), the "Horia Hulubei" Diploma (2006, for his outstanding contribution to the development of IFA), Honorary Professor of The "Iuliu Haţieganu" University of Medicine and Pharmacy Cluj-Napoca (2008), the Great Honor Diploma of the National Comission of Archeometry (1997, awarded by the National Museum of History of Transylvania, Cluj-Napoca), the Diploma of Honor of the National Institute of Marine Research (Constanţa), Diploma of Excellence awarded by the University of Bucharest (2018), Honorary Citizen of Constanţa (2019).

P.T. Frangopol was elected Honorary Member of The Romanian Academy in 2012. I was very pleased to sustain him on the occasion of the Meeting of the Romanian Academy when he was discussed, answering to some querries formulated by venerable members present in the Aula (who were surprized by the many achievements of Petre T. Frangopol). Subsequently, as a Member of the Academy, P.T. Frangopol proved his value, expressing many overtly thoughtful positions on important matters of the Academy's life (including

opinions regarding the candidates for the Academy's leadership). He was nominated by the Section of Chemical Sciences to coordinate the writing of the ample volume on the "History of Romanian Chemistry", published in 2018 by the Romanian Academy Publishing House in the jubilee series on the Romanian Civilization. He did a wonderful job. Unfortunately, Vasile V. Morariu's file has not been discussed by the Section of Biological Sciences of The Romanian Academy while he was alive! Vasile and myself wrote in 2013 a short presentation of the Romanian Biophysics Research School founded by Professor Petre T. Frangopol. The conclusion is really in the title of our article [16].

P.T. Frangopol (Petrache) will be greatly missed by many academics, scientists, former students, friends, and by all who had the pleasure of interacting with him over several decades. I will be grateful to him all my life, considering not only the scientific publications we accomplished, but for many other reasons: the support and competent advice he gave me along the decades, when I had to face a variety of obstacles from various institutions and persons. Petrache came to Cluj-Napoca to participate in all scientific events I organized over almost five decades. He accepted to give the Opening Plenary Lecture at „The Second World Congress on Water Channel Proteins (Aquaporins and Relatives), celebrating the 30th Anniversary of the Discovery of the First Water Channel Protein (Later Called Aquaporin 1)" Cluj-Napoca, Romania, 6-10 May 2015.

Finally, I express again deep regrets for the greatest loss of his life, the death of his beloved Mioara Frangopol, after a long incurable illness.

REFERENCES

1. *Academica*, **2018**, *XXVIII (10-11)*, 34-63
2. P.T. Frangopol; *Mediocrity and Excellence - a radiography of science and education in Romania (in Romanian),* vol. 7, Casa Cărţii de Ştiinţă, Cluj-Napoca, România, **2019**
3. S. Anghel (Coordinator); *Academic Dobrogea (in Romanian)*, Ex Ponto, Constanţa, România, **2019**
4. P.T. Frangopol (Coordinator); *History of Romanian Chemistry (in Romanian)*, Editura Academiei Române, Bucureşti, România, **2018**
5. A.R. Forrester; J.M. Hay; R.H. Thomson; *Organic Chemistry of Stable Free Radicals*, Academic Press, New York, U.S.A., **1968**
6. E.G. Rozantzev; *Free Nitroxyl Radicals*, Plenum Press, New York, U.S.A., **1970**
7. D.C. Nonhebel; J.C. Walton; *Free-radical chemistry-structure and mechanism,* Cambridge Univ. Press, Cambridge, U.K., **1974**
8. Gh. Benga; D. Chapman; *Rev. Roum. Biochim.,* **1976**, *13*, 251-261

9. Gh. Benga; S.J. Strach; *Biochim. Biophys. Acta*, **1975**, *400*, 69-79

10. V.V. Morariu; Gh. Benga; *Biochim. Biophys. Acta,* **1977**, *469*, 301-310

11. Gh. Benga, V.V. Morariu; *Nature*, **1977**, *265*, 636-638

12. V.D. Sholle; E.Sh. Kagan; V.J. Michailov; E.G. Rozantsev; P.T. Frangopol; M. Frangopol; V.I. Pop; Gh. Benga; *Rev. Roum. Biochim.,* **1980**, *17*, 291-298

13. Gh. Benga; V.I. Pop; M. Ionescu; A. Hodârnău; R. Tilinca; P.T. Frangopol; *Biochim. Biophys. Acta,* **1983**,*750*, 194-199

14. Gh. Benga; I.C. Dânşoreanu; M. Frangopol; P.T. Frangopol; *Rev. Chim.*, **2008**, *59*, 1255-1259

15. Gh. Benga; A. Hodârnău; M. Ionescu; V.I. Pop; P.T. Frangopol; V. Strujan; R.P. Holmes; F.A. Kummerow; A comparison of the effects of cholesterol and 25-hydroxy-cholesterol on egg yolk lecithin liposomes: spin label studies, in „*Biomembranes and Cell Function*", F.A. Kummerow, Gh. Benga, R.P. Holmes Eds, Annals of New York Academy of Sciences, **1983**, *414*, pp. 140-152

16. V.V. Morariu; Gh. Benga; *Romanian J. Biophys.*, **2013**, 263-266.

THE NEVER-TIRED APOLLONIAN PETRE T. FRANGOPOL, MY DEAR FRIEND *PETRACHE*

DORU GEORG MARGINEANU[a]

Writing a short tribute *in memoriam* of such a multi-faceted intellectual and real polymath as Petre T. Frangopol is a fairly intimidating endeavor when one wishes to properly evoke a scholar activity that spanned over six decades, covered a spectrum of scientific domains ranging from chemistry to archeology and tackled multiple science- and education-related aspects of the Romanian societal life. Beyond his initial professional activity in organic physical-chemistry and radiochemistry, Dr. Frangopol extended his activity in the decade of eighties to biophysical chemistry and biophysics. He and his team from the Institute of Atomic Physics in Măgurele have contributed, in those years, to several notable studies published in major international journals.

Dr. Frangopol's most significant activity from that distant past was the initiation and management of an extended program of studies on "Biophysics of the interaction of medicines with cell membranes". That program, sponsored by the Ministry of Chemical Industry, was aimed at promoting through research the Romanian medicines. It was pursued from 1981 till 1991 and involved several research teams from Bucharest, Cluj-Napoca and Iaşi. In 1990, some studies from that program received the "Constantin Miculescu" prize of the Romanian Academy. The extended and gratifying collaboration with Petre Frangopol within that program, up to the end of 1988 (when I've moved to Belgium) gave me the chance of becoming a close friend of *Petrache* and of his distinguished wife, Dr. Maria Frangopol (*Mioara*) who was his most faithful coworker, beyond of being his lifelong rock-solid support.

The abrupt political changes of December 1989 entailed a troubled transition period for all the Romanian people, including the academic scientists that suddenly found themselves in a quite uncertain social environment. But, though he approached sixty, my friend *Petrache* was not scared and he took the challenge of further expanding his activity. In 1991 he became a Professor of biophysics and biophysical chemistry in the Faculty of Physics of the "Alexandru Ioan Cuza" University in Iaşi (the town of his student years), where he was instrumental in launching a section of Medical Physics. Then,

[a] Department of Neurosciences, Faculty of Medicine and Pharmacy, University of Mons, 7000 Mons, Belgium, Doru.Margineanu@skynet.be

the never-tired Prof.Dr. P.T.Frangopol successively went to the Biophysics department of the medical school of "Vasile Goldiş" West University in Arad, to the Faculty of Chemistry of the "Babeş-Bolyai" University in Cluj-Napoca, and finally to the Physics department of the "Politehnica" University in Bucharest.

His extended professorial activity did not, however, exhaust the bubbling intellectual energy of that perpetual enthusiastic who was my dear friend *Petrache*. Profoundly attached to the authentic values of Romanian historical heritage in science and deeply preoccupied by country's progress, Petre Frangopol was sensitive to all the drawbacks in the education of new generations and in the politics of science that he deemed put at risk the future of the nation. Testimony of his keen involvement in the fight for a flourishing future of the Romanian society are the numerous articles written by Professor Frangopol in various newspapers and magazines, most notably his extended series of vigorous papers in the weekly supplement *Aldine* of *România liberă*. In 2002, he assembled and structured those articles into a striking volume titled "Mediocrity and Excellence", with the very indicative subtitle "A Radiography of Science and Education in Romania". Then, with an impressive regularity, at about every 3 years Petre Frangopol – an ever vigilant observer of science and education in Romania and never fatigued fighter for the health of these essential domains – issued a new volume in that series, up to the seventh that appeared in 2019. Though that year the author was aged 86, he has kept the same youth of spirit as when we have met, forty years ago.

In the meantime, Professor Frangopol edited a new series of "*Revista de politica ştiinţei şi scientometrie*", to which he was Chief Editor from 2012 to 2016 and virtually acted as factotum, in spite of the extremely painful challenge of the incurable illness of his beloved wife. Also, upon his election in October 2012 as Honor Member of the Romanian Academy, Petre Frangopol brought to the venerable assembly his untired vivacity, as shown by his overt expression of thoughtful positions on main matters of Academy's life, and chiefly by coordinating the ample volume on the "History of Romanian Chemistry", published in 2018 by the Romanian Academy Publishing House in the jubilee series on Romanian Civilization.

Writing a tribute to the memory of Petre T. Frangopol today (the 29th of June), that happens to be his onomastic day, when I used to call him (as for his anniversary, at May 26), I remember that at the beginning of our temporary collaboration and ever-lasting friendship, *Petrache* told me that from his post-doctoral stay in North America he has kept the credo that "*happiness is having something to do, something to hope, someone to love*". No doubt, Professor Frangopol was happy, beyond all inevitable sorrows of every human life, and he radiated around him the joy of struggling for worthy causes. May his apollonian personality remain a source of inspiration!

PETRE FRANGOPOL –
A FIGHTER IN THE PUBLIC ARENA

DOREL BANABIC[a]

I met Professor Frangopol through his articles published in the first part of the 2000s in the Aldine supplement of the newspaper România Libera. Subsequently, we collaborated in various committees and, lately, in organizing symposia on education and research. I had the pleasure to collaborate with Professor Frangopol on the editing of a volume entitled "Romanian education and research. The present state and perspectives" which brings together the works presented in a workshop of the same name organized by the University of Bucharest in 2017.

One of his most well-known public activities is the publication of a series of volumes entitled "Mediocrity and Excellence: a radiography of science and education in Romania." Like clockwork (every three years), from 2002 to 2019 (7 volumes), Professor Petre Frangopol compiled the articles he published in newspapers and specialized journals on the situation in Romanian education and research.

Usually, scientists do not go out in the public forum, for lack of time, because of a sometimes-exaggerated modesty, because they perceive the gesture as useless, out of a self-defense reflex, out of fear, out of comfort, etc. (the list of causes / pretexts is long). Those who do are those capable of self-sacrifice. Those who, although aware of the inequality of forces, go out into the arena and take the bull by the horns. Those who take on the problems of the scientific and academic community and communicate them to the entire society. They represent the part of the scientific community that is eager to change, to progress, to get out of the "transition" and into normalcy, to align with European values (expressively defined by Professor Frangopol in the title of an article, "The second generation of Romanian Youth"). In today's Romania, there are some voices, unfortunately very few, who do the above: they go out to fight with their bare hands, but with candor in their quiver, against an opponent armed "to the teeth" with the practices of manipulation,

[a] *Department of Manufacturing, Faculty of Industrial Engineering, Robotics and Production Management, Technical University of Cluj-Napoca, Memorandumului 28, 400140 Cluj-Napoca, Romania, banabic@tcm.utcluj.ro*

of distortion, indefinite postponement, etc. Usually, these are people who have been waiting for change for a lifetime and for whom "time lost its patience." Their scream, sometimes desperate, a "Munch' scream," is heard from time to time in Romanian society. And it terrifies many, especially those who find themselves in the same state of despair. Does it also terrify those to whom it is addressed? Is their scream "Vox clamantis in deserto"? No. Of course not. I think they are aware that their example will persuade the cowards to join them. Will they be able to tip the balance of truth to their side? Will they mobilize that critical mass needed to bring about the changes so long awaited by the new generation? I think so.

Professor Petre Frangopol was one of those who, consciously taking the risks, went out into the public forum. He did it armed with scientist's toolset: critical spirit, perseverance, lucidity, objectivity, etc. He applied a scientist's critical analysis, in a positive sense, to political decisions and actions, which was not and is not at all convenient to the political factor.

We need such people. We need such "idealists" to "shout" our sorrows; we, who lack the courage to go out in the public arena, can get behind these people. Professor Frangopol was such a man, around whom those with the same ideals gathered. We continue his actions and continue the fight against mediocrity.

PROFESSOR PETRE T. FRANGOPOL – A BRIEF, PERSONAL ACCOUNT ON THE LEGACY HE LEFT IN IAŞI

TUDOR LUCHIAN[a]

More than about a man, this evocation is about some of the ideas, ideals and legacy that will ever define that man. I met Professor Petre T. Frangopol while I was still an undergraduate student, and both our approaches toward one another were short-sentenced, straight, sincere and even blunt. Professor Frangopol was in the incipient phase of developing a new specialization at the Faculty of Physics in Iaşi, and thus in worried need of young, talented, hard-working people able to take on the challenge, while I was in the pursuit of a dream, namely to do research in biophysics. Apparently, we were both in luck those days. As discussions progressed, I still remember vividly the central question Professor Frangopol kept asking me: "...if you would have a lab, what project will you be able to start at once? What's your plan?" Early on our endeavor, I have also heard for the very first time about notions such as curriculum vitae, quality research based on original ideas and not re-vamped projects imported from other labs, the need to respect intellectual qualities of other people despite personal judgements, the need to compare ourselves with the best in our field, to mention very few. Needless to say, I didn't have much of a clue of what biophysics was about, beyond the scarce literature I was able to access and read in the library. As for the infrastructure needed to propel my 'to be' ideas, it was totally absent. Things one gets for granted nowadays in even a modest lab, as a minimal start-up on a research pursuit (e.g., a decent computer, some measuring devices and essential reagents, etc.), were only present … in some leaflets and books found in some corridors of the Faculty.

However, Professor Frangopol was overwhelmingly full of grit, optimism and, above all, he exhibited a contagious, almost obsessive desire to succeed where everyone else told him he would fail, namely to start from practically nothing a world-class new laboratory of biophysics, able to produce good papers from original ideas brewed 'in house'. The hours, days, months and then years passed, and out of many excruciating brainstorming meetings, organized and presided by the tough and fully "focused on the ball" Professor Frangopol,

[a] *Faculty of Physics, 'Al. I. Cuza' University, Iaşi, Romania, luchian@uaic.ro*

research ideas surfaced. Small (from Soros Foundation, Iaşi) followed by large (from International Atomic Energy Agency in Vienna, Austria) grants poured in, students began to attend and later graduate in the Biophysics and Medical Physics specialties from the Faculty of Physics in Iaşi, scientific papers were being produced and people started to take notice of our presence and results. However, one could not state that at all times the institutional appreciation was positively correlated with the results produced, but now this is a matter of history … and I leave to more competent and informed people have the last word on this.

Despite all attempts to bend files of history and saying in brief, main facts that will never loose substance are: *i)* Professor Frangopol brilliantly succeeded in building from virtually nothing to internationally recognized results, two brand new academic and research fields at the Faculty of Physics, later to become the Sections of Biophysics and Medical Physics; *ii)* many students, myself included, were extremely lucky and fortunate in meeting the right person (Professor Frangopol) at the right time, and at the beginning of one of the most brave projects to be implemented in the Faculty of Physics; such bravery eventually contaminated all our spirits, and we all started to undergo some *genotype mutations* **(!)** early in our careers, making us believe that we cannot *afford the luxury* of failing in our pursuit; *iii)* above all, the after-hours education imprinted in our behavior was not only unique at that time and place, but eye- and mind-opening for the subsequent years in our careers: we were to be judged solely by our results and professional performance, and not by whatever objective or subjective motivations or constraints that impeded us from achieving success. In Professor Frangopol words, "only results matter, reasons from not having them interest none". We, the students were quite young then and truly believed that such principles apply generally in any given institution, and we were all equal in front of our achievements or failures. In other words, we were convinced that at the end of the day each of us was to be scaled commensurate with the successes marked, so some sort of moral principles and meritocracy-based karma were to prevail. Well … we were then young, and many lessons were learnt over the following years!

With the essential start-up ideas, financial and moral support brought by Professor Frangopol, the scientific output of the biophysics and medical physics started to grow vigorously over the years, allowing us to steadily implement new research ideas and literally build up from ground other brand-new projects, all around revamped infrastructure and new talented young people. In spite of all said above, it still remains an understatement to assess the pivotal role played by Professor Frangopol not only in bringing such new research venues at the Faculty of Physics in Iaşi, but shaping our characters,

minds and hearts in a (then) new brave world (for us), in which the only realistic way to become visible and possibly accepted among existing peers was to prove ourselves solely through our results.

The writer Amos Oz said thar every person has three names: one given by her/his parents, one given by her/his peers or friends and enemies, and one her/he makes for her(him)self. In my view, the attributes that capture best the third such name Professor Frangopol made for himself, were restless tenacity, patriotism, fighting against all odds and bravery in front of both subjective and objective obstacles. Knowing that no person is gone from among us as long as we keep alive her/his memory, it will remain a personal duty to forever honor and remember Professor's Frangopol influence on my personal career and consolidation of my team and professional dream.

IMPLICATIONS OF WATER CHANNEL PROTEINS (AQUAPORINS AND RELATIVES) IN EPILEPSIES

ILEANA BENGA[a,b]

ABSTRACT. The abundant evidence linking epilepsy with hydroelectrolytical changes in epilepsy reported in the medical literature for over 9 decades is reviewed. Our work on this topic is presented, including the detection by NMR of a decreased water permeability of the red blood cells (RBCs) from children with epilepsy compared with control children. This was interpreted as a generalized membrane defect in epilepsy. The subsequent program of research performed by Gh. Benga's group in Cluj-Napoca led to the discovery of the first water channel protein (WCP) in the RBC membrane, protein later called aquaporin1 (AQP1). A lot of WCPs (AQPs and relatives) have been identified later by various authors, in the body of humans and many other species. The physiological roles of WCPs from the central nervous system (CNS) and their implications in epilepsy and other neurological diseases are reviewed, including the information published in the last months.

Keywords: water channel proteins, aquaporins, epilepsy, paediatric neurology, NMR

INTRODUCTION

Epilepsies are among the most frequent Central Nervous System (CNS) disorders, caracterized by seizures, affecting approximately 1-2% of the world's population [1]. The seizure is the most frequent symptom (after headache) in paediatric neurology [2]. The neurophysiological basis of a seizure is the spontaneous repetitive discharge of a hyperexcitable aggregate of neurons [3, 4].

Abundant evidence linking epilepsy with water metabolism was reported in the medical literature for over 9 decades and was reviewed by many authors [5-7]. Some observations and studies are discussed below. Frisch and Walter [8], Keith et al. [9] and Helmholtz [10] reported a relationship

[a] *Academy of Medical Sciences, 1 Blvd. Ion C. Brătianu, RO-030167, Bucharest, Romania*
[b] *Academy of Romanian Scientists, 3 Ilfov Str., RO-050044, Bucharest, Romania*
   ibenga@yahoo.com

between seizure frequency and water intake in epileptic patients. Moreover, the antiseizure effects of various diuretics were reported by the middle of the 20th century, the topic being reviewed later [11, 12].

McQuarrie [13, 14] in epileptic children and Teglbjaerg [15, 16] in epileptic adults performed the first investigations under carefully controlled conditions. Both groups concluded that fluid restriction reduced seizure frequency, while hyperhydration led to an exacerbation of seizures. McQuarrie et al. [14] studied the balance of water and minerals (sodium, potassium, calcium and phosphorus) in children with epilepsy and found that "a positive water balance was followed by convulsive seizures" and when seizures occured potassium was increased in urine "with a striking increase in the potassium to sodium ratio", while during periods with no seizures sodium was the predominant mineral in urine. The authors concluded: "This apparent 'leakage' of potassium from the cells... may indicate an innate weakness in the retaining membranes, presumably of the cells of the central nervous system. It is possible that abnormal amounts of water and even sodium ions entry at the same time". "The data recorded are tentatively interpreted as favoring the view that an inherent defect in the mechanism for regulating permeability of the brain cell membranes is characteristic of the epileptic state". Schneider [17] observed that in children and adults suffering from *petit mal* epilepsy the exacerbation of *petit mal* events is associated with reduction in urinary volume, and that clinical remission coincides with an increase in water excretion (spontaneous, drug-induced or hormone induced). Reynolds [18], using radioisotopic methods, reported some changes in the whole body distribution of water and sodium in epilepsy, with a magnitude proportional to the frequency of seizures. He concluded that disturbances in body water and sodium are linked in some way to the aetiology of epilepsy. Moreover, comparing two groups of patients, one with idiopathic epilepsy and the other with focal epilepsy, he found "a striking similarity between the two groups of patients for all the biochemical variables" measured, considering that his study supports the concept of an essential unity between the idiopathic and focal epilepsy.

Tower [19] incubated slices of human epileptogenic cortex, which were unable to take up K^+ and extrude excess Na^+ in a similar way as the control cortical samples. He found the same changes in the ability to handle Na^+ and K^+ in cortical slices from cats in which epilepsy had been induced by megimide or methionine-sulfoximine. Tower [19] considered that the characteristic instability of the excitable membrane in epileptogenic neurons is a consequence of an impairment of operation of the Na^+ and K^+ transport system, which is "the final common expression of epileptogenicity".

On the other hand, there were many observations of water intoxication (WI) in non-epileptic individuals. Ferrier [20] described the symptoms of WI: the first include headache, blurred vision, polyuria, vomiting, tremor, followed by

muscle cramps, ataxia, delirium, stupor, coma, and then convulsions can follow. WI caused by polydipsia (compulsive water drinking) was described in schizophrenics, major motor seizures being present in about 80% of cases [21]. There are also experiments in animals. Rowntree [22] reported that WI in mammals produce "extremely severe toxic manifestations" including seizures. Other studies confirmed that ADH and water loading produce seizures in otherwise normal mammals: rats [23-25], rabbits [26].

Wasterlain and Torack [27] described (apparently for the first time) astrocytic swelling and enlarged extracellular space in compact white matter in the absence of any vascular damage or blood brain barrier (BBB) breakdown in brain edema associated with WI. Other reviews regarding the brain volume regulations and brain excitability in response to changes in osmolality have been published [28-31].

RESULTS AND DISCUSSION

Our first studies of hydroelectrolytic changes in child epilepsies

Considering all the above mentioned researches, as well as the local conditions where I was working, I choosed to study hydroelectrolytic changes in child epilepsies as topic for my Ph.D. Thesis [32]. In those years I was Junior Lecturer at Discipline of Child Psychiatry (DCP), Institute of Medicine and Pharmacy (I.M.F.) Cluj-Napoca (to become later "Iuliu Haţieganu" University of Medicine and Pharmacy – U.M.F. – Cluj-Napoca). DCP was functioning together with Discipline of Child Neurology (DCN) in the same Clinic of Child Neuropsychiatry (C.C.N.) Cluj-Napoca, the building belonging to the Cluj Children Hospital. I also worked in the laboratories of Discipline of Medical Biochemistry (DMB) of I.M.F., collaborating with my husband (Gheorghe Benga, Senior Lecturer) and with other distinguished faculty members of DMB. We published some papers regarding the hydroelectrolytic changes in child epilepsies. In one of these [33] we measured the concentrations of Na and K in the red blood cells (RBCs) of 35 children with epilepsy and 25 control children. We found a statistically significant lower concentration of Na and a higher concentration of K in children with epilepsy compared with the control children. We wrote: "These changes observed in case of RBCs of children with epilepsy may indicate the perturbation of mechanisms which maintain the polarization of cell membrane. Tower [19] by measurements on human brain showed that in case of epileptogenìc cortex there is a deficiency of mechanisms which maintain the normal distribution of Na and K across the cell membrane. Our data showed changes of the distribution of Na and K in

RBCs, i.e. at distance from the organ implicated in the generation of convulsive discharges (brain). This makes us to suggest a more general perturbation of the mechanisms which ensure the intra and extracellular concentrations of Na and K in other cells of the body. Our results are in agreement with data of Reynolds [18] who found by radioisotopic methods general changes of distribution of Na and water in the body of patients with epilepsy" [33].

The collaboration with Vasile V. Morariu begins

One day in 1976 my husband told me that he has incidentally met Vasile V. Morariu, his former classmate in the high school (Liceul "Emil Racoviţă" Cluj), who returned from Australia in 1973, where he worked three years as a Ph.D. student (1969-1972) at Canberra National University. Vasile graduated the Faculty of Physics at "Babeş-Bolyai" University (U.B.B.) Cluj-Napoca. After graduation (1966) Vasile Morariu was employed as researcher at the Institute for Stable Isotopes, which soon changed the name to Institute for Isotopic and Molecular Technology (ITIM) Cluj-Napoca (to become in 1999 The National Institute for Research and Development of Isotopic and Molecular Technologies – INCDTIM – Cluj-Napoca). In 1976 Vasile Morariu was researcher at ITIM, leading a group oriented to biophysics, using NMR as the main technique of investigation. My husband has just returned from England, after working 12 months as Post-Doctoral Fellow in the laboratory of Professor Dennis Chapman (a famous scientist in the field of biological membranes), learning NMR, spin labelling ESR and other biophysical techniques to study protein-lipid interactions in biomembranes. Vasile Morariu mentioned to Gh. Benga that he knew a paper of two Australian researchers who used NMR to investigate the water diffusion through the red blood cell (RBC) membrane [34]. Gh. Benga said that we are very interested in such measurements, taking into account the topic of my Ph.D. Thesis [32] and the research we have already performed regarding the hydroelectrolytic changes in children with epilepsies [33].

As described by Professor Petre T. Frangopol [35] in Australia Vasile Morariu has done outstanding NMR work on water adsorbed on silica, elucidating the origin of the "abnormal" water, discovered by some Russian scientists, who considered that it is a special polymerized water. Famous laboratories from the U.S.A. and U.K. have reproduced the experiments of the Russians and many international conferences took place on the subject. It was speculated that under certain conditions the water on Terra could polymerise and the life on our planet could be in danger! Vasile Morariu suggested to his Ph. D. supervisor (Professor R. Mills) to choose the study of "abnormal" water as his Ph.D. work project. His suggestion was accepted and Vasile Morariu

discovered that in fact the polymerization of the "abnormal" water is due to the impurification with silicic acid [36]. Other scientists produced the polymerization with other impurities, so the scientific confrontation (with possible major political and military implications) between the two superpowers (U.S.A. and U.S.S.R.) vanished!

The first results obtained in collaboration with Vasile V. Morariu

Vasile Morariu and Gh. Benga took the decision to start immediately the NMR measurements of water permeability of RBCs in children with epilepsy compared with control children. When my husband informed me about his discussion with Vasile, I told him that Cornelia Morariu, Vasile's wife, is intern in paediatrics, performing a 6 months rotation in the C.C.N. working with me. We met all four in the following days and Vasile explained us the principle of the NMR method of Conlon and Outhred [34] for measuring water permeability of the RBC membrane. The method involves addition of a paramagnetic solution ($MnCl_2$) to the plasma and measurement of the spin-spin relaxation time (T_2) of the RBC water proton. The spin-spin relaxation time of water inside the isolated RBCs is about 140 ms and is much longer than the time required for water to exchange across the membrane (the water exchange time, T_{ae}), which is about 10 ms. If the relaxation time in plasma is made much shorter than the exchange time (by adding the paramagnetic ion Mn^{2+}), the observed relaxation time of the RBC (T_{2b}) is dominated by the exchange process through the membrane. The spin-spin relaxation time is evaluated from a logarithmic plot of the nuclear spin-echo as a function of the time interval 2 ĩ where ĩ is the time interval between the radiofrequency pulses. When the system is characterized by a single relaxation time, the plot is a straight line and the relaxation time is the reciprocal of the slope. For a system characterized by two relaxation times (as for the blood doped with Mn^{2+}) the plot consists of two lines and the relaxation times are calculated from the slopes of these lines. The value of T_{ae} is inversely related to the water permeability (P_d) of RBCs.

We started the work immediately. I selected the patients, helped by Cornelia Morariu, while Vasile Morariu and Gh. Benga performed the laboratory work. All blood samples (obtained by venous puncture, in heparinised tubes) were numbered and transported by Gh. Benga to ITIM, where Vasile Morariu and his co-workers performed the NMR measurements, without knowing which blood samples are from children with epilepsy and which are from control children. Patients were 24 children with epilepsy aged 1-12 years and controls were 24 children aged 2-16 years. The patients included 11 children with

idiopathic *grand mal* (GM), one with idiopathic GM plus *petit mal* (PM) and 12 children with focal epilepsies (7 with focal GM, 3 with minor attacks, 2 with temporal lobe epilepsy). In all children with epilepsy the exchange time of water through the RBC membrane (T_{ae}) was longer than in control subjects. The measurements were made at different temperatures and concentrations of Mn, and two methods were used to measure spin-spin relaxation time: the 90^0 ï 180^0 method and the Carr-Purcell-Meiboom-Gill (CPMG) method (which eliminates errors due to the inhomogeneity of the magnetic field and the molecular diffusion in field gradients) [37]. There were no significant differences in T_{ae} values between idiopathic and focal epilepsies. High values of T_{ae} were found in patients who had seizures every day and in whom the attacks were poorly controlled by anticonvulsant therapy. It was also found that the value of T_{ae} during the seizure was not higher than in the interictal period. This indicated that the low water permeability of RBCs in epilepsy is a permanent alteration (not a transient one). The abnormal water permeability was found in both untreated and treated patients, i. e. was not related to the anticonvulsant therapy. An alteration (decrease) of the permeability to water of RBCs in children with epilepsy was the most likely explanation for our findings. We realized immediately the possible important significance of our findings, as we had already studied extensively the publications regarding the NMR (Vasile Morariu) and epilepsy (myself and my husband). In October 1976 a manuscript was sent to *Nature*, in December 1976 was accepted to be published without changes and in February 1977 it appeared [38]. The idea of a generalised membrane defect in epilepsy was discussed as follows: "Abnormalities in functions of erythrocyte membranes are considered to indicate a generalised membrane defect [39, 40]. Within certain limits a close qualitative and quantitative analogy is possible between the stability of the membrane of the erythrocyte and that of the neuron [41, 42]. Fritz and Swift [43] have shown (by the NMR method we used) that for the frog nerve the exchange rate of the water protons between the intra and extracellular environments is lower for the depolarised nerve than for the polarised nerve. That is, the water permeability of the membrane is smaller in the depolarised state than in the resting state...We suggest that decreased permeability in erythrocytes of epileptics may reflect a membrane defect in all tissues and may be an expression of the individual predisposition in epilepsy; it might be of particular importance in the nervous system. Further studies on erythrocyte membranes in epilepsy may give clues to the understanding of the membrane defect in molecular terms" [38]. The authors were Gheorghe Benga and Vasile V. Morariu, while the contributions of myself and Cornelia Morariu were mentioned as: "We thank Drs. Ileana Benga and Cornelia I. Morariu for helpful discussions and for blood samples".

The results obtained in the following decades regarding the water permeability of membranes and the significance for epilepsies

In the following decades our group continued the research on this line, in agreement with the background and interests of each of us. Vasile Morariu and Gh. Benga evaluated the NMR method of Conlon and Outhred [34] and found that some improvements and standardizations are necessary, including: the calculation of the RBC membrane diffusional permeability to water (P_d) from the water exchange time; the study in detail of the effects of temperature and pH on P_d; the calculation of the activation energy ($E_{a,d}$) of the membrane diffusional permeability to water [44-47].

I continued to publish articles regarding the hydroelectrolytic changes in child epilepsy based on our work [48, 49] and to follow the implications of water channel proteins in epilepsies and other neurological disorders.

Gh. Benga started an extensive program of research aimed to identify the pathway by which the water molecules cross the membrane. Several important aspects had to be studied until the final goal was achieved: NMR measurements of the effects on P_d of various inhibitors, of chemical modification of membrane proteins, measurements on resealed ghosts (prepared by a special procedure: hemolysis to remove hemoglobin and then restoring the membrane integrity), labelling, by a radioactive inhibitor, of the protein involved in water permeability, identification of this protein by polyacrylamide gel electrophoresis etc [50-54]. Obviously, to perform all these procedures there were many requirements: the appropriate laboratories (including those for work with radioactive compounds), the equipment (centrifuges, electrophoresis equipment, NMR spectrometer, a lot of reagents), and people with experience in laboratory work and authorized to work with radioisotopes and funds to purchase all reagents and equipment. In many of these aspects Professor Frangopol played an important role, in his position as Chief of a Center of Radiochemical Production at "Horia Hulubei" National Institute for Research& Development in Physics and Nuclear Engineering (in Romanian Institutul de Cercetare-Dezvoltare pentru Fizică şi Inginerie Nucleară "Horia Hulubei", abbreviated as IFIN-HH). He provided financial support from his grants when we started the collaboration with Vasile Morariu, since the NMR measurements at ITIM required the covering of all expenses (including the salaries of researchers). Professor Frangopol obtained grants from The Academy of Medical Sciences (A.M.S.) and other sources and included Vasile Morariu and his team on the grants. Later Professor Frangopol helped Vasile Morariu and Gh. Benga to get their own grants from A.M.S. Moreover, he played an essential role in the acquisition by Gh. Benga of an NMR spectrometer manufactured at IFIN-HH.

The spectrometer was installed at Cluj-Napoca by the experts from IFIN-HH in a laboratory of the newly founded Discipline of Cell Biology (DCB) which Gh. Benga was appointed to chair. The experts came to Cluj-Napoca and instructed Gh. Benga's team how to use the NMR spectrometer. With another grant from A.M.S. (obtained this time by Gh. Benga) a module of calculations of relaxation times was made by the experts of IFIN-HH, who came again to Cluj-Napoca and installed the module.

After almost a decade of hard work, the water channel protein (WCP) in the human RBC membrane was identified by Gh. Benga's group. The discovery of the first WCP was really achieved in 1985 when the first landmark paper by Benga and coworkers was sent for publication to the prestigious American journal *Biochemistry*, which accepted the publication without changes [53]. The second landmark paper was published by Benga and coworkers in 1986 in a well known European journal [54]. In 1988 the group of Peter Agre in Baltimore purified by chance the protein, calling it CHIP28 (CHannel forming integral membrane protein of 28kDa) having no idea of its function [55]. Gh. Benga presented the novelty of the discovery of his group in reviews published before 1990 [56, 57]. The group of Agre found the water transport property of CHIP28 only in 1992 [58].

The protein identified in Cluj-Napoca was the first water channel discovered. Other WCPs were discovered in 1993: in a plant [59] and in the kidney [60]. The name of aquaporins was proposed for the WCPs [61] and CHIP28 was named aquaporin 1 (AQP1).

In a few years it became obvious that a large family of WCPs exists, with three subfamilies: aquaporins (AQPs), aquaglyceroporins, and S-aquaporins. Moreover, it was discovered that actually the WCP family (with all three subfamilies) belongs to a superfamily of Membrane Intrinsic Proteins (MIPs). The superfamily includes also MIPs with no identified channel activity. MIP is an acronym first used for MIP 26 (Major Intrinsic Protein of 26 kDa) of lens fiber cells in the eye [62]. Later, the number of reviews and of articles on WCPs and their relatives published in various journals continued to increase, since the presence and roles of such proteins in all kinds of species on Terra (from prokaryotes to plants, animals and humans) have been revealed. Lots of reviews have been published in the first decade after the discovery of WCPs [63-70].

Moreover, special issues of prestigious journals [71-74], proceedings of world congresses [75], multi-authored books [76] were dedicated to the newly discovered proteins. Over 300 WCPs were discovered so far and their structures (going down to the molecular level) for a number of them have been elucidated, as described in many reviews [67, 73] and several chapters in ref. [76].

As discussed in ref. [73] a WCP may be defined as a transmembrane protein that has a specific three-dimensional structure with a pore that provides a pathway for water permeation across biological membranes. In order to understand the subsequent description I recommend to access freely the following link: https://iubmb.onlinelibrary.wiley.com/doi/10.1002/iub.156 and look at Fig. 1.

WCPs and MIPs have a relatively small size, most are less than 300 amino acids. Both the NH_2 terminus and COOH terminus are hydrophylic and located in the cytosol. The pore is formed by two regions in the amino acid sequence, called *NPA boxes* (or *motifs*), with three amino acid residues (asparagine-proline-alanine, NPA) and several surrounding amino acids. The NPA boxes have been called the "signature" of WCPs. There are six transmembrane domains (TMD), highly hydrophobic, with α-helix structure and five connective loops. The α-helices are named from the N-end succesively H1, H2, H3, H4, H5 and H6, and the loops are named A, B, C, D, and E. The TMDs and the loops form a *core* (embedded in the lipid bilayer), to which two "legs" (represented by the cytosolic N- and C-ends) are attached. NPA boxes are located in the loops B and E, which are rather hydrophobic in nature and have short (half) helices HB and HE. The six TMDs (tilted at about 30° with respect to the membrane normal) form a right-handed bundle enclosing the *channel* (*pore*) formed by the NPA motifs and the short tetramer helices HB and HE, bended into the six-bundle and connected to the center of the bilayer. This structure is called the *aquaporin fold.* So the channel (pore) is a narrow tunnel in the center of the molecule that has at the extracellular and cytoplasmic faces funnel-shaped openings (atria or vestibules). In the membranes (natural or reconstituted proteoliposomes with purified proteins) WCPs are in the form of *tetramers*, as shown by freeze-fracture electron microscopy (EM). AQP1 tetramers are held together by extensive interactions between helices and loops of the monomers. Each monomer, however, has its own channel, functionally independent.

The nomenclature of WCPs uses the abbreviation AQP followed immediately by the number, (e.g. AQP1, AQP2 etc). Thirteen WCPs have been characterized in humans. Seven are aquaporins (AQP0, AQP1, AQP2, AQP4, AQP5, AQP6 and AQP8), four are aquaglyceroporins (AQP3, AQP7, AQP9 and AQP10), whereas AQP11 and AQP12 are S-aquaporins ("superaquaporins", "subcellular aquaporins" or "unorthodox aquaporins").

1) The AQPs were defined as water specific or water selective channel proteins, "classical", "conventional", "orthodox" etc. 2) The aquaglyceroporins are permeable to water, but also to other small uncharged molecules, in particular glycerol. The "signature" sequence of aquaglyceroporins is aspartic acid residue (D) in the second NPA box. 3) The S-aquaporins have little conserved amino acid

sequences around NPA boxes, being also named "aquaporins with unusual (or deviated) NPA boxes" or "unorthodox aquaporins". The structure and function of AQP11 and AQP12 are currently poorly understood. They have less than 20% homology with other classical AQPs, indicating that they belong to a supergene family of AQPs. Details may be found in ref. [76].

In recent years, it has been found that many cellular functions of aquaporins are regulated by post translational modifications (phosphorylation, ubiquitination, glycosylation, subcellular distribution, degradation, etc.). Insight into the molecular mechanisms, responsible for regulated aquaporin trafficking and synthesis, is fundamental for the development of reliable diagnostic and prognostic biomarkers and therapeutic targets [76].

Gh. Benga had the idea to start (in Cluj-Napoca) a comparative program of studies of water permeability of RBCs in various animals. A review of the first such studies has been published [77]. He also had the idea to extend the investigations to a variety of animal species, including those living in Australia. A collaborative program of research was established with an outstanding Australian scientist, Professor Philip Kuchel (The University of Sydney). The two groups achieved exchange working visits, performing studies of the RBC water permeability of over 30 species and the program is still very active. Kuchel and Benga [78, 79] provided two new explanations for the physiological "raison d'etre" of AQPs in RBC. The first is the "oscillating sieve explanation": the high water permeability of RBC membrane favors the energy driven membrane undulations (or oscillations) of the RBC membrane, a phenomenon also called "flickering" [80, 81]; these movements consume a minimum of energy in simply displacing water. Such membrane undulations perform a valuable role in movement of cells through capillaries. The second is the "water displacement explanation": when ions, such as Cl^- and HCO_3^-, and solutes, such as glucose, are entering into the cells, the water molecules are displaced and exit rapidly the cell, thus obviating a change in cell volume. The molecular volume of these ions and molecules are significantly higher than that of water. In addition, Kuchel and Benga concluded [78, 79]: the parameters characterizing the water permeability of RBC appear to be a species characteristic as there are no changes correlated with the marked alteration in the habitat of the species introduced to Australia (rat, rabbit, sheep, chicken) compared with their European counterpart. The chicken and echidna RBCs have the lowest P_d values ($\sim 2 \times 10^{-3}$ cm s^{-1}) and the highest values of $E_{a,d}$ (over 30 kJ mol^{-1}); this indicates that no functional AQPs are present in chicken and echidna RBCs. Human RBCs have P_d values of $\sim 4 \times 10^{-3}$ cm s^{-1} at 25 ^{0}C and $\sim 7 \times 10^{-3}$ cm s^{-1} at 37 ^{0}C with a value of $E_{a,d} \sim 25$ kJ mol^{-1}. Large and less-active animals (cow, sheep, horse and elephant) have lower values of P_d. In contrast, small and active animals (mouse, rat, guinea pig, rabbit,

small marsupials) have P_d values significantly higher with lower $E_{a,d}$ values (from 15 to 22 kJ mol^{-1}). It appears therefore that AQPs in RBCs ensure the rate of exchange of water across the membrane required in various animals in relation to their physical activity, metabolic rate and the mean rate of circulation of their blood [77-79].

WCPs in the *central nervous system* (CNS) are of great physiological and pathological importance. The CNS is the part of the nervous system consisting primarily of the *brain* and *spinal cord*. The CNS is so named because the brain integrates the received information and coordinates and influences the activity of all parts of the body. The importance of WCPs in the brain is obvious, considering the rigid physical constraint that is imposed to the brain by the bony cranium and that ~80% of the brain is water [31, 82]. The human intracranial volume is ~1400 ml (79) and comprises the brain parenchyma (~1200 ml), intravascular (~100 ml) and cerebrospinal fluid (CSF) (~100 ml) compartments. The brain compartments include the subarachnoidian space and the cerebral ventricles. Most of the brain parenchyma water is intracellular (~1100 ml), while ~100 ml water is distributed in the extracellular space (ECS), also named the brain interstitial space (IBS) [82, 83].

The brain parenchyma is composed of two major cell types: neurons and glial cells. In general, glial cells are smaller than neurons. There are approximately 85 billion glial cells in the human brain, about the same number as neurons. Glial cells make up about half the total volume of the brain and spinal cord. The glia to neuron ratio varies from one part of the brain to another [84, 85].

Glial cells (Gr. *glia* = glue) are divided into two major cell classes: *microglia* and *macroglia. Microglia* (about 10% of glial cells) are small relative to macroglial cells, with changing shapes and oblong nuclei, being mobile within the brain. They subserve immunologic functions in the CNS, protect neurons, being among defense mechanisms against infectious diseases of the CNS. They are normally inactive, but, activated by any pathological change in the CNS (infection, trauma, ischaemia or neurodegeneration) can become macrophages capable of phagocytosis [84].

Macroglia include *astrocytes*, *oligodendrocytes* and *ependymocytes* (or *ependymal cells*). *Tanycytes* in the median eminence of the hypothalamus are a type of ependymal cells that descend from radial glia and line the base of the third ventricle. Tanycytes extend from the hypothalamic median eminence to the hypophyseal portal system providing a pathway whereby hormones may enter or leave CSF [84].

The total number of glial cells in the human brain is distributed into the different types with oligodendrocytes being the most frequent (45–75%), followed by astrocytes (19–40%) and microglia (about 10% or less) [85].

Astrocytes (Gr. *astron* = star) have irregular (star–shaped) cell bodies and are characterized by numerous fine leaflet-like processes, which are in intimate contact with neurons and cover non-synaptic neuronal surfaces in the CNS. In adition, astrocytes have processes called "perivascular feet" which cover 85% of the surface of capillaries in the CNS. These processes form an external glial membrane under the pia mater and an internal membrane under the ventricular ependyma. There are two main subtypes: *fibrous* astrocytes, in the white matter, which have long slender processes and many cytoplasmic filaments, and *protoplasmic astrocytes*, in the grey matter, having shorter, flattened, branched processes with few filaments. They support neurons, structurally and functionally. When damaged they hypertrophy and proliferate to form "a glial scar". Astrocytes are the commonest source of primary malignant tumours in the CNS.

The so called "blood-brain barrier" (BBB) is primarily due to tight junctions between capillary endothelial cells. Astrocytes also contribute to the selective nutritive path between blood vessels and neurons. Astrocytes regulate the external chemical environment of neurons by removing excess potassium ions and recycling neurotransmitters released during synaptic transmission [84, 85].

Verkhratsky et al. [86] observed that since the inception of neurobiology, two centuries ago, our founding fathers of gliology had a clear vision on the active role of glia, i.e. that glia has prominent roles in pathophysiology of the brain. Awkwardly, the twentieth century brought a dominant neurono-centric approach, the starring role has been solely by neurons. This approach has been challenged by the resurgence of neurogliopathology in the past 20 years. The correct approach, however, is to emphasize that it is the interaction between neurons and glia which underlies physiology and pathology of the brain. These major cellular constituents interact, so that perturbing one will affect the other. In epilepsy, astrocytes undergo substantial pathological remodelling, which greatly affects their homeostatic capabilities and is linked to pathophysiology of this disease. In particular, the epileptic astroglial phenotype includes changes (mutations and/or expression levels) in ion channels, receptors and transporters.

The work of our group described above and the idea of a membrane defect affecting water permeability represented in fact a world priority in the field of WCPs, since it showed for the first time the medical implications of alterations of membrane water permeability. Other authors have confirmed the presence of a membrane defect involving WCPs in epilepsy. Some studies are presented below. Ottersen and coworkers [87, 88] compared the variants (SNPs, i. e. single nucleotide polymorphisms) of the genes encoding AQP4 and Kir4.1. in a group of patients with temporal lobe epilepsy and in a group

of controls. The authors found eight single SNPs in Kir4.1. gene associated with temporal lobe epilepsy and considered these findings as a further proof of the implications of astrocytes in the pathophysiology of epilepsy.

Lee et al. [89] studied the expression of AQP4 and other glial molecules (Kir4.1., glial fibrilary acid protein, glutamine synthetase) in the intra-hippocampal kainic acid (KA) model of epileptogenesis and compared the wild-type mice versus AQP4-null (animals lacking AQP4). A marked reduction of AQP4 in both astrocytic fine processes and endfeet were observed following KA status epilepticus in multiple hippocampal layers. In addition, AQP4-null mice had more spontaneous recurrent seizures than wild-type during the first week after KA status epilepticus. These results are interpreted as an indication of dysregulation of water and potassium homeostasis during early epileptogenesis.

Lu et al. [90] examined the seizure susceptibility of AQP4-null mice following traumatic brain injury (TBI). The seizures were induced by injections of pentylenetetrazole and AQP4-null mice were compared with wild-type sham injury controls. AQP4-null mice demonstrated dramatically shortened seizure latency and increased severity grade. Morphometric analysis demonstrated a twofold reduction in astrocytosis with concomitant increase in microgliosis in injured AQP4-null mice.

Altered neuronal activity observed in AQP4 deficiency was reviewed in several publications [31, 82, 91, 92]. In animals lacking AQP4 (AQP4-null animals) the threshold for seizures is reduced while the seizure duration is prolonged. The underlying mechanism may be an impairment of K^+ homeostasis in the absence of AQP4. In addition, in hippocampal atrophy, a feature of mesio-temporal lobe epilepsy, AQP4 expression is increased in samples from atrophic hippocampi from epileptic patients. The accumulated evidence suggests that AQP4 is involved in such diverse functions as regulation of ECS volume following synaptic activation, potassium buffering, CSF circulation, interstitial fluid resorption, waste clearance, neuroinflammation, osmosensation, cell migration and Ca^{2+} signaling [82, 91-93]. The seizure phenotype data in AQP4-null mice raise the possibility that AQP4 modulation may also be effective in epilepsy therapy [94].

Consequently, in the brain, AQP4 stands as a multipurpose aquaporin, quite different from the situation in the kidney where several AQPs act in concert to regulate water transport.

Aquaporins came to the attention of neurologists mainly due to *neuromyelitis optica* (NMO) or *Devic's syndrome*, an autoimmune inflammatory demyelinating condition of the CNS, characterized by optic neuritis and myelitis.The clinical course of NMO is dominated by acute attacks. If untreated, NMO often results in blindness and tetra- or paraparesis. A significant number of

Devic's patients (70-80%) have antibodies against AQP4. The term astrocytopathy was proposed to characterize this disease. Recent reviews are available [95, 96].

The last period of collaboration with Vasile V. Morariu

After finishing the 6 months rotation in the C.C.N, Cornelia Morariu, performed a 6 months rotation in the Section of Neonatology of Cluj County Hospital. Professor Iulian Lupea (Chief of the Section) asked Vasile Morariu to measure the water permeability of RBCs from newborns. It was found that P_d was lower and $E_{a,d}$ was higher than the corresponding values of these parameters in children several years old [97]. On the other hand Gh. Benga and his co-workers found that these parameters are similar in case of RBCs from umbilical cord blood [98]. Then Vasile Morariu and Gh.Benga's group performed a detailed investigation on the age-dependence of the RBC water permeability [99]. It was found that the P_d is the lowest in the newborn, it increases in children, reaching at about 7 years a value that remains rather constant in young and mature subjects. The high permeability to water of the RBC membrane can be correlated at these ages with the ability to undertake a high level of physical activity. In elderly individuals (over 65 years) a further small, but statistically significant, increase in the P_d was observed [100]. In this case the higher RBC water permeability can be correlated with a requirement of the RBC membrane to favour the membrane undulations and the rapid entry or exit of solutes of molecular size greater that water, in conditions when the organism is less physically active, probably has lower metabolic rates and lower mean rates of blood circulation [100].

Recent knowledge about water channel proteins and their implications in epilepsies and other pathological processes in the central nervous system

Important progresses were achieved in the *genetic analyses of WCP genes,* including their localization on chromosomes; e.g. the gene of AQP4 is located in chromosome 18 (18q11.2– q12.1). The sequences of some WCP genes have been analysed (see the link: https://www.omim.org/entry/600308).

New findings were discovered regarding the *choroid plexuses* and the secretion of CSF. Anatomically, choroid plexus tissue is floating in the CSF of the lateral, third, and fourth ventricles. This tissue is well perfused by numerous villi, each having a central capillary with fenestrated endothelium.

Traditionally, the properties of the blood-brain barrier (BBB) were considered to be those of the capillary endothelium in brain. However, in contrast with capillary endothelium elsewhere in the body, the endothelium in brain capillaries is sealed with tight junctions, having a high electrical resistance and a low permeability to polar solutes. Early research unveiled, on the brain side of the BBB, ion channels and transporters capable of providing a net secretion of fluid, driven by $Na^+ - K^+$ ATPase. Accordingly, the BBB was proposed as a secretory endothelium, which produces the brain interstitial fluid (ISF) [101]. Recent research unveiled that the "barrier" function of the BBB is actually the result of highly regulated and complex cellular and molecular transport processes, which allow for the transport of water, solute, larger molecules and even cells [102]. According to the traditional understanding of CSF physiology, the majority of CSF is produced by the choroid plexuses, circulates through ventricles, the cisterns, and the subarachnoid space to be absorbed into the blood by the arachnoid villi. Then it was discovered that AQP1 is present in the *choroid plexuses*, being involved in the secretion of CSF. Novel insights were obtained using molecular and cellular biology tools, as well as neuroimaging. The new information, reviewed by Brinker and coworkers [103], is challenging the old concept regarding the secretion of CSF, indicating that CSF physiology may be much more complex than previously believed, astrocytes, AQPs and other membrane transporters being key elements in brain and CSF homeostasis. The new insights into the physiology of CSF circulation may have important clinical relevance for example for the understanding of hydrocephalus disorders and other brain diseases [104-106].

A very important progress in neurosciences was the discovery of *the glymphatic system* (GS), a novel defined brain-wide perivascular transit network between cerebrospinal fluid (CSF) and interstitial solutes that facilitates the clearance of brain metabolic wastes [105]. By analogy to the lymphatic system found outside the brain, the perivascular space system was named the glymphatic system. In the GS, CSF enters the perivascular space around the arteries to the deeper brain regions, flowing into the brain parenchyma through AQP4 channels in the astrocytic end feet. The interstitial fluid within the brain parenchyma (ISF) exits through the perivascular space around the veins, thereby clearing the waste products. From the perivenous space, the ISF drains into the subarachnoid space and meningeal lymphatics of the parasagittal dura. This is the essential description of the glymphatic system [104].

The glymphatic system was proposed to contribute to lactate concentration changes in the brain, in correlation with sleep–wake cycles and sleep homeostasis. The GS dysfunction is associated with various neurological

disorders, including traumatic brain injury, BBB disruption, hydrocephalus, stroke, brain edema, epilepsy, migraine, immune cell infiltration, neuroinflammation, neuronal apoptosis, Alzheimer's disease. There is evidence for the crucial role of AQP4 in the GS, namely AQP4 facilitates glymphatic fluid transport. AQP4 is also associated with cell movement, the size of the extracellular space and connectivity between neurons.There are many reviews on GS [104-106].

I also mention a very recent review regarding structural, molecular and functional alterations of the BBB during epileptogenesis and epilepsy [107]. It may be accessed freely following the link doi:10.3390/ijms2102051. In addition to seing beautiful figures, one may understand not only the huge progresses in the field of epileptogenesis which took place in recent years, but also the advances in the therapy, the use of modern knowledge to reach finally the stage when new anticonvulsant molecules can be introduced in therapy. Such drugs are necessary all the time, since even today the clinicians are facing the difficult situations to treat patients with drug-resistant epilepsy.

CONCLUSIONS

The hydroelectrolytical disturbances are of utmost importance in epilepsy and this was proven by lots of clinical observations, laboratory investigations, studies of animal and human tissues and cells, including the use of new molecules, out of which new anticonvulsant drugs are discovered and introduced in therapy. The water channel proteins (aquaporins and relatives) play a crucial role in all these aspects.

The discovery of WCPs (aquaporins and relatives) originated from one of the studies of hydroelectrolytical changes in RBCs of children with epilepsy. The start point was the comparative NMR measurements of the RBC water permeability of children with epilepsy and control children performed by us in collaboration with Vasile V. Morariu. In the seminal paper published in 1977 in *Nature* [38], the idea of a generalized membrane defect altering (decreasing) the water permeability of membranes in epilepsy has been clearly stated. The subsequent systematic program of research planned by Gh. Benga led to the identification of the protein responsible for the water permeability of the RBC membrane. The results of the program were reported in two reference papers published in 1986 by the by Gh. Benga's group in well known international journals in the U.S.A [53] and in Europe [54]. The first water channel protein (WCP) in the human RBC membrane was actually identified by Gh. Benga's group in 1985, when the first landmark paper by Benga and coworkers was sent to the prestigious American journal *Biochemistry*,

which accepted the publication without changes [53]. The second landmark paper was published by Benga and coworkers in 1986 in a well known European journal [54].

In 1988 the protein was rediscovered by an American group led by Peter Agre in Baltimore, who purified by chance the protein, calling it CHIP28 (CHannel forming integral membrane protein of 28kDa) having no idea of its function [55]. Only in 1992 the American group discovered the function of that protein as a water channel [58]; however, they have not cited the two papers previously published by Gh. Benga's group [53, 54].In 2003, Peter Agre was awarded the Nobel Prize in Chemistry, which he shared with Roderick MacKinnon for their "discoveries concerning structure and function of channels in cell membranes".

As a final conclusion I am citing what Wolburg and co-workers [108] wrote: "The detection of water-specific membrane channels in red blood cells belong to the fundamentals discoveries in biology of the twentieth century…In 1986 and 1988, the independent groups of Gheorghe Benga and Peter Agre, respectively, discovered the water channel proteins which later were called aquaporins".

Gh. Benga proposed in 2013 the scientific term "aquaporinology" for the new domain of natural sciences which began with the discovery of the first water channel protein, later called aquaporin1 [109, 110]. Additional information may be found in ref. [111] and on the web at gheorghebenga.ro.

DEDICATIONS

This review is dedicated to two outstanding Romanian scientists: Petre T. Frangopol and Vasile V. Morariu. I would like to add my gratefulness for the many years of scientific collaboration and friendship with Professor Petre T. Frangopol and his wife Dr. Mioara Frangopol. Their support was an important stimulus for my own research outlined above.

Professor Petre T. Frangopol fully supported the campaign for the recognition of merits of Gh. Benga's group and of Vasile Morariu from the first moment he met them and until the death of Vasile and of himself.

REFERENCES

1. J. O. McNamara; *Nature*, **1999**, *SUPP399*, A15-A22.
2. I. Benga; *Elementary treatise on pediatric neurology. Vol. I Epilepsy and Non-epileptic Seizures (in Romanian),* Editura Medicală Universitară "Iuliu Haţieganu", Cluj-Napoca, România, **2003.**

3. J. H. Jackson; *Brit. Med. J.*, **1890, 1**, 703-707.
4. C. Ajmone Marsan; *Epilepsia*, **1961, 2**, 22-38.
5. E. H. Reynolds; *J. Neurol. Sci.,* **1970, 11**, 327-358.
6. R. D. Andrew; *J. Neurol. Sci.,* **1991**, *101*, 901-1001.
7. I. Benga; O. Benga; *Mol. Asp. Med.*, **2012**, *33*,590-604.
8. F. Frisch; K. Walter; *Z. Neurol. Psychat.*, **1922**, *79*, 576-588.
9. N. M. Keith; F. H. Smith; M. Whelan; *Arch. Intern. Med.*, **1926**, *37*, 550-558.
10. H. F. Helmholz; *JAMA*, **1927**, *88*, 2028-2032.
11. C. T. Lombroso; D. T. Davidson; M. L. Grossi-Bianchi; *JAMA*, **1956**, *160*, 268-272.
12. E. H. Maa; K. T. Kahle; B. P. Walcott; M. C. Spitz; K. J. Staley, *Epilepsia*, **2011**, *52*, 1555-1569.
13. I. McQuarrie; *Am. J. Dis. Children*, **1929**, *38*,451-467.
14. I. McQuarrie; R. C. Manchester; C. Husted; *Am. J. Dis. Children*, **1932**, *43*,1519-1543.
15. H. P. S. Teglbjaerg; *Acta Psychiatr. Scand.*, **1936**, *S9*, 26-37.
16. H. P. S. Teglbjaerg; *Acta Psychiatr. Scand.*, **1936**, *S9*, 55-84.
17. J. Schneider; *Epilepsia*, **1961**, *2*,358-366.
18. E. H. Reynolds; *J. Neurol. Sci.*, **1970**, *11*, 327-358.
19. D. B. Tower; *Epilepsia,* **1965, 6,** 183-197.
20. I. N. Ferrier; *Br. Med. J.*, **1985**, *291*, 1594-1596.
21. C. J. Jose; J. L. Barton; J. Perez-Cruet, **1979,** *Biol. Psychiatry,* 839-843.
22. L. G. Rowntree; *J. Pharmacol. Exper. Therap.*, **1926,** *29*, 135-139.
23. M. Wender; W. Strzyzewsky; *Eur. Neurol.*, **1968**, *1*, 131-136.
24. G. G. Wasterlain; J. B. *Arch. Neurol.*, **1968**, *19,* 71-78.
25. C. F. Baxter; C. G. Wasterlain; K. L. Hallden; S. F. Pruess;*J. Neurochem.,* **1986**, *47*, 617-624.
26. A. I. Arieff; F. Lach; S. G. Massry; *Medicine,* **1976**, *55*, 121-129.
27. C. G. Wasterlain; R. M. Torack; *Arch. Neurol.*, **1968**, *19,* 79-87.
28. P. A. Schwartzkroin; S. C. Baraban; D. W. Hochman; *Epilepsy Res.*, **1998**, *32*, 275-285.
29. H. Pasantes-Morales; S. Cruz-Ranghel, *Neuroscience*, **2010**,*168*, 871-887.
30. J. G. Verbalis; *Neuroscience*, **2010**,*168*, 872-870.
31. O. Benga; V. J. Huber; *Mol. Asp. Med.*, **2012**, *33*,562-578.
32. I. Benga; *Hydroelectrolytic changes in child epilepsies (in Romanian)*, Ph.D. Thesis, University of Medicine and Pharmacy Cluj-Napoca, **1977.**
33. I. Benga; V. Băltescu; Gh. Benga; *Clujul medical*, **1977**, *50*, 258-260*(in Romanian).*
34. T. Conlon; R. Outhred; *Biochim. Biophys. Acta,* **1972**, *288*, 354-36134.
35. P. T. Frangopol; *Elites of Researchers from Romania. Mathematics-Physics-Chemistry,* Casa Cărţii de Ştiinţă, Cluj-Napoca, România, **2004**, pp. 38-45 *(Vasile V. Morariu, in Romanian).*
36. V. V. Morariu; R. Mills; W. Woolf; *Nature*, **1970**, *227*, 373-374.
37. Th. C. Farrar; F. D. Becker; *Pulse and Fourier Transform NMR*; **1971**, Academic Press, New Academic Press, New York, U.S.A.
38. Gh. Benga, V. V. Morariu; *Nature*, **1977**, *265*, 636-638.

39. M. Hokin-Neaverson; D. A. Spiegel; W. C. Lewis; *Life Sci.*, **1974**, *15*, 1739-1748.
40. H. W. Cho; H. Y. Meltzer; *Biol. Psychiat.*, **1974**, *9*, 109-116.
41. A. K. Sen; R. I. Post; *J. Biol.Chem.*, **1964**, *239*, 345-352.
42. N. Mison-Crighel; C. Pintilie; D. Volanschi; D. Florescu; S. Tudor; *Rev. Roum. Neurol.,* **1973**, *10*, 441-459.
43. O. G. Fritz; T. J. Swift; *Biophys. J.*, **1967**, *7*, 675-687.
44. V. V. Morariu; Gh. Benga; Biochim. *Biophys. Acta,* **1977**, *469*, 301-310.
45. V. V. Morariu; Gh. Benga; Water diffusion through erythrocyte membranes in normal and pathological subjects: nuclear magnetic resonance investigations, in *Membrane Processes: Molecular Biology and Medical Applications,* Gh. Benga, H. Baum, F. A. Kummerow Eds., Springer Verlag, New York, U.S.A. **1984**, pp. 121-139.
46. V. V. Morariu; O. Popescu; Gh. Benga; *Eur. J. Cell Biol.,***1980**, *22*, 479-479.
47. V. V. Morariu; V. I. Pop; O. Popescu; Gh. Benga; *J. Membr. Biol.,* **1981**, *62*, 1-5
48. I. Benga; V. Băltescu; Gh. Benga; *Clujul medical*, **1983**, *56*, 139-141 *(in Romanian).*
49. I. Benga; V. Băltescu; R. Tilinca; O. Pavel; V. Ghiran; D. Muschevici; Gh. Benga; *J. Neurol. Sci.*, **1985**, *67*, 29-34.
50. Gh. Benga; V. I. Pop; M. Ionescu; R. P. Holmes; O. Popescu; *Cell Biol. Int. Rep.,***1982**, *6*, 775-781
51. Gh. Benga; V. I. Pop; O. Popescu; M. Ionescu; V. Mihele; *J. Membr. Biol.,* **1983**, *76*, 129-137.
52. Gh. Benga; O. Popescu; V. I. Pop; *Cell Biol. Int. Rep.,* **1983**, *7*, 807-818.
53. Gh. Benga; O. Popescu; V. I. Pop; R.P. Holmes; *Biochemistry*, **1986**, *25*, 1535-1538.
54. Gh. Benga; O. Popescu; V. Borza; V. I. Pop; A. Mureşan; I. Mocsy; A. Brain; J. Wrigglesworth; *Eur. J. Cell Biol.,* **1986**, *41*, 252-262.
55. B. M. Denker; B. L. Smith; F. P. Kuhajda; P. Agre; *J. Biol. Chem.*, **1988,** 15634-15642.
56. Gh. Benga; *Prog. Biophys. Mol. Biol.*, **1988,** *51*, 193-245.
57. Gh. Benga; Membrane proteins involved in the water permeability of human erythrocytes: binding of *p*-chloromercuribenzene sulphonate to membrane proteins correlated with nuclear magnetic resonance measurements; In Gh. Benga; (Ed.) *Water Transport in Biological Membranes.* CRC Press, Boca Raton, U.S.A., **1989**, Vol. II, Chapter 3, pp. 42-61.
58. G. M. Preston; T. P. Caroll; W. B. Guggino; P. Agre; *Science,* **1992,***256*, 385-387.
59. C. Maurel; J. Reizer; J. L. Schroeder; M.J. Chrispeels; *EMBO J.*, **1993**,*12*, 2241-2247.
60. K. Fushimi; S. Uchida; Y. Hirata; F. Marumo; S. Sasaki; *Nature*, **1993**, *361*, 549-552.
61. P. Agre; S. Sasaki; M. J. Chrispeels; *Am. J. Physiol*, **1993**, *265*, F46.
62. M. B. Gorin; S. B. Yancey; J. Cline; J.-B. Revel; J. Horwitz; *Cell*, **1984**, *39*, 49-59.
63. J. Reizer; A. Reizer; M.H. Saier; *Crit. Rev. Biochem. Mol. Biol.*, **1993**, *28*, 235-237.

64. B. Heymann; A. Engel; *News Physiol. Sci.,* **1999**, *14,187*-193.
65. Gh. Benga; *Cell Biol. Int.*, **2003,** *27,*701-709.
66. R. Zardoya; *Biol. Cell*, **2005,** *97*, 397-414.
67. T. Gonen; T. Walz; *Quart. Rev. Biophys.,* **2006**, *39,*361-396.
68. Gh. Benga; *Cell. Mol. Biol.*, **2005, 52, 10**-19.
69. I. Benga; *Cell. Mol. Biol.*, **2005**, *52*, 46-50.
70. I. Benga; Gh. Benga; *Proc. 9*th *World Multi-Conference on Systemics, Cybernetics and Informatics, Orlando, U.S.A.,* **2005**, pp. 111-115.
71. B. Wu; E. Beitz; *Cell. Mol. Sci.,* **2007**, *64*, 2413-2421**.**
72. Gh. Benga; *Acta Endocrinol (Bucharest),* **2006**, *2*, 323-326.
73. Gh. Benga; *IUBMB Life*, **2009**, *61, 112*-133.
74. Gh. Benga (Ed.); *Water Channel Proteins (Aquaporins and Relatives),* Elsevier Ltd. Oxford, U.K., Special Issue, *Mol. Asp. Med.*, **2012**, *33*, 511-703.
75. Gh. Benga Ed.; *Proceedings of The First Congress on Water Channel Proteins (Aquaporins and Relatives) Celebrating the 25*th *Anniversary of the Discovery of the First Water Channel Protein (Later Called Aquaporin1, Cluj-Napoca, Romania, Second Edition*, Casa Cărţii de Ştiinţă, Cluj-Napoca, Romania.
76. B. Yang (Ed.) *Aquaporins*, Advances in ExperimentalMedicine and Biology, Vol. 969, Springer Science+Business Media B.V., **2017,** Dordrecht, the Netherlands.
77. Gh. Benga; T. Borza; *Comp. Biochem.Physiol.*, **1995**, *112B*, 653-659.
78. P. W. Kuchel; Gh. Benga; *Biosystems*, **2005**, *82*, 189-196.
79. Gh. Benga; *Eur. Biophys. J.*, **2013**, *42*, 33-46.
80. F. Brochard; L. L. Lennon; *J. Phys. (Paris)*, **1975**, *36,* 1035-1047.
81. V. V. Morariu; A. M. Chis; V. Znamirovschi; *Cytobios*, **1996**, *86,* 53-64.
82. M. J. Tait; S. Saadoun; B. A. Bell; M. C. Papadopoulos; *Trends Neurosci.,* **2008**, *31,* 37-43.
83. S. Saadoun; S. Papadopoulos; *Neuroscience,* **2010**,*168,* 1036 – 1046.
84. J. L. Wilkinson; *Neuroanatomy for Medical Students,* Third Edition, Butterworth-Heinemann, **1998**, Oxford, U.K., Woburn, MA, U.S.A.
85. C. S. von Bartheld; J. Bahney; S. Herculano-Houzel; *J. Comp. Neurol.*, **2016**,*524,* 3865-3895.
86. A. Verkhratsky; M.S. Ho; N. Vardjan; R. Zorec; R. Zorec; V. Parpura; doi: 10.1007/978-981-13-9913-8_7.
87. K. Heuser; E. A. Nagelhus; E. Taubøll; U. Indahl; P.R. Berg; S. Lienc; S. Nakken, L. Gjerstada; O.P. Ottersen; *EpilepsyRes.*, **2010**, *88*, 55-64.
88. E.A. Nagelhus; O.P. Ottersen; *Physiol. Rev.*, **2013**, *93*, 1543-1562.
89. D.J. Lee; M.S. Hsu; M.M. Seldin; J.L. Arellano; D.K. Binder; *Exp. Neurol.,* **2012**, *doi: 10.1016/j.expneurol.2012.02.02.002.*
90. D. C. Lu; S. Zador; J. Yao; F. Fazlollahi; G. T. Manley; *J. Neurotrauma*, **2012**, *doi: 10189/neu/2011.2014.*
91. M. Amiry-Moghadam; O. P. Ottersen; *Nature Rev. Neurosci.,* **2003**, *12,* 991-1001.
92. J. Badaut; J.-F. Brunet; L. Regli; *Metab. Brain Dis.*, **2007**, *22*, 251-263.
93. D.K. Binder; K. Oshio; T. Ma; A.S. Verkman; G.T. Manley; *NeuroReport,* **2004**, *15*, 259-262.

94. G. P. Frigeri; B. Nichia; F. Nico; R. Quondamatteo; R. Herken; L. Roncalli; M. Svelto; *FASEB J.,* **2001**, *15*, 90-98.

95. D. W. Wingerchuk; B. G. Weinshenker; *Handb. Clin. Neurol.,* **2014**, *122,* 581-599.

96. T. M. Crout, L. P. Parks; V. Majithia; *Curr. Rheumatol. Rep.*, **2016**, *18*, 54, doi 10.1007's11926-016-0599-3.

97. I. Lupea; C. Morariu; V. V. Morariu; R. Ordeanu; *Pediatria*, **1978**, *27*, 261-263 *(in Romanian).*

98. Gh. Benga; L. Frențescu; S. Țigan; *Clin. Chem. Lab. Med.*, **2001**, *39*, 606-611.

99. V. V. Morariu; C. V. Mihali; L. Frențescu; D. Bechet; Budișan; L., Mândruțiu; Gh. Benga; *Acta Endocrinol (Buc)*, **2014**, *10*, 665-670.

100. A. Țehaniuc; Gh. Benga; *Acta Endocrinol (Buc)*, **2011**, *7*, 299-310.

101. C. E. Weaver; P. N. McMillan ; J. A. Duncan; E. G. Stopa; C. E. Johanson; *Advances in Molecular and Cell Biology*, **2003**, *31*, 269-293.

102. C. E. Johanson; J. A. Duncan; P. M. Klinge; T. Brinker; E. G. Stopa; G. D. Silverberg; *Cerebrospinal Fluid Research*, **2008**, *5*, 10, doi: 10.1186/1743-8454-1.

103. T. Brinker; E. Stopa; J. Morrison; P. M. Klinge; *Fluids and Barriers of the CNS*, **2014**, http://www.fluidbarrierscns.com/content/11/1/10.

104. J. I. Szu; S. Chaturvedi; D. Patel; D. Binder; *Neuroscience*, **2020**,*428,* 140-153.

105. J. J. Iliff; M. Wang; Y. Liao; B. A. Plogg; W.Peng; G. A. Gundersen; H. Benveniste; G. E. Vates; R. Deane; S. A. Goldman; E. A. Nagelhus; M. Nedergaard; *Sci. Transl. Med.*, **2012**, *4*, 147ra111, doi: 10.1126/translmed.3003748.

106. C. Ji; X. Yu; C. Lenahan; S. Tu; A. Shao; *Frontiers in Aging Neuroscience*, **2021**, *340*, 113685, doi : 10.1016/j.expneurol.2021.113685.

107. W. Löscher; A. Friedman; *Int. J. Mol. Sci.*, **2020**, *21,* 591, doi: 10.3390/ijms21020591.

108. H. Wolburg; K. Wolburg-Bucholz; P. Fallier-Becker; S. Noel; A. Mack; *Int. Rev. Cell. Mol. Biol.*, **2011**, *287,* 1- 41.

109. Gh. Benga; *Oltenia for Studies in natural Sciences*, **2013**, *29*, 316-319.

110. Gh. Benga; *Acta Endocrinol (Buc)*, **2014**, *10*, 1-8.

111. F. Marin; *Faculty of Medicine, Cluj Medical School and Hospitals from Cluj (1500-2000), Second Edition*, **2018**, pp. 972-1000, Casa Cărţii de Ştiinţă, Cluj-Napoca, România *(in Romanian).*

FORECASTING AN EMERGENT SYSTEMIC TREND IN NEUROPHARMACOLOGY

DORU GEORG MARGINEANU[a]

ABSTRACT. Neuropharmacology (NP), which evolved along with scientific medicine, got treatments for several common disorders of the nervous system. But, most of the NP drugs are just symptomatic, reducing only the manifestations of brain pathologies. Also, for main neuro-psychiatric pathologies (e.g. the neurodegenerative diseases) there is very poor or no medication, and the output of NP drug discovery declined in the last decades. This review paper argues that those drawbacks derive from the reductionist NP leaning towards single–target selective drugs, at odds with the essential complexity of brain functioning and the multifactorial causality of its pathologies. Most active neuro-drugs (e.g. valproate and levetiracetam) are in fact multi-mechanistic since they have been selected by phenotypic screening *in vivo*, not by single-target binding *in vitro*. A putative solution of the relative NP stagnation seems to come with the emergent systemic approach of network pharmacology. A plausible flowchart of the main stages of a network NP drug discovery endeavor is finally sketched.

Keywords: brain complexity, systems biology, network pharmacology, magic bullet, magic shotgun, multi-mechanistic drug, valproate, levetiracetam, multi-potent drug, poly-therapy

INTRODUCTION

Neuropharmacology (NP) is an important branch of neuroscience and a primary component of pharma industry, devoted to *i)* the study of neurochemical interactions in the central nervous system (CNS), of drug-induced changes in nervous system functioning, and to *ii)* the creation of drugs acting on the nervous system. Its chief importance in both scientific and societal terms derives from the truly foremost role of the brain for us, humans (*H. sapiens sapiens*), more than for any other vertebrate species, and from the high incidence of the neuro- and psycho-pathologies, draining huge

[a] *Department of Neurosciences, Faculty of Medicine and Pharmacy, University of Mons, 7000 Mons, Belgium, Doru.Margineanu@skynet.be*

public costs. CNS diseases are largely recognized as the health challenge of the 21st century, at least 10% of the global population being now affected by a mental health disorder – a proportion set to increase [1].

NP emerged in the 19th century, along with the scientific medicine and got some major achievements even at that distant times. Among the early feats were the gaseous general anesthesia and the local anesthesia with a synthetic cocaine-like compound (the procaine) devoid of abuse potential. Moreover, NP can rightly boast an impressive series of main achievements, got in the 20th century. Among these are the synthesis and introduction in medical practice of a whole panoply of anti-convulsing drugs, of the typical antipsychotics that treat schizophrenia and severe mania, of the most successful class of benzodiazepine compounds (with sedative, hypnotic, anxiolytic and anti-convulsing effects), and of several classes of antidepressant drugs (from the tricyclic imipramine to the selective serotonin reuptake inhibitors) – to quote just a few major examples [2], [3].

In spite of these, one has however to notice that NP is still in its infancy, as most of the NP drugs are merely symptomatic, not curative, they acting on neurological and psychiatric manifestations, not on the underlying causes of the respective pathologies, which remain as yet largely obscure. Also, NP does not meet several bad medical needs, some common neuro-psychiatric pathologies being only poorly treated, if at all. Such are the stroke, the brain and spinal cord trauma, and notoriously the neurodegenerative diseases, chiefly Alzheimer's, whose prevalence rapidly increases in the aging affluent world. Moreover, noteworthy successes of NP often emerged from serendipitous clinical or laboratory observations [4], rather than from attaining purposeful goals of drug discovery programs. Even worse, a decline in output of CNS drug discovery was clearly manifest in the last decades [2], [5] and many of the newly launched medicines were only variations of previous drugs.

This short review, which is an opinion paper, points as a leading cause of the relative lack of efficiency of NP, its unbalanced *reductionist* leaning, at odds with the intrinsic complexity of CNS functioning. A putative solution brought about by a novel *systemic* approach is further sketched.

RESULTS AND DISCUSSION

Basic consequences of the intrinsic complexity of human brain

Ensuring optimal integration in the milieu and monitoring/coordinating all body functions is an exquisite and demanding communicational activity that led the human brain to emerge as a most intricate web of $>2\times10^{10}$ neurons

and >10^{11} glial cells, each neuron acting as a full-fledged computer, connected with some 10^4 other neurons, and functioning on electrochemical and chemical bases. The unanimously recognized complexity of the brain is approached with concepts from mathematics, physics and computer science [6], [7], [8].

Human brain's amazing organizational intricacy goes along with an oddly intense metabolism, draining over 20% of the whole body resting energy consumption [9], though the brain accounts for only 2% of body weight. Its special features render the brain prone to various ailments – physicochemical injury, degeneration, excitability troubles, and intercellular communication alterations – that largely arise from the disruption of milieu's homeostasis needed for suitable neuronal function.

Likewise, brain's sophistication entails the complexity, heterogeneity and, occasionally, the dynamic character of neurological [10] and psychiatric [11] diseases, poorly mastered as yet, making that the etiologies of brain-specific pathologies are but insufficiently understood. This has the corollary that current NP medications are merely symptomatic (not curative). It thus appears fairly obvious that, for achieving to actually cure brain pathologies, the NP should rely on approaches aimed at embracing their intrinsic complexity, transcending the obsessional reductionist search of purportedly highly "selective" drugs, that would strongly interact with just one molecular target, deemed relevant.

The end of last century witnessed the emergence of a far-reaching conceptual move, the ascent of *systems biology* (SB) [12], [13] that rise above the mere analytic (i.e. reductionist) exclusive focus on the molecular components and highlights the complex interactions within the organisms. Therefore, the pathology is seen to reflect alterations of a *network* of interactions that underlie each organismic function and the corresponding *systems* (or *network*) *pharmacology* is aimed at normalizing that network.

This novel view on the diseases contests the benefit of a specific interaction of the drug with a *unique* molecular receptor and its corollary for drug discovery, of aiming to create single-target drugs acting as "*magic bullets*" (an inspired metaphor introduced by Paul Ehrlich in antimicrobial pharmacology). Network pharmacology searches to act on biological networks rather than on a single molecular target, via either multi-drug therapeutics (poly-pharmacology) or multi-targeted single drugs, appearing as a realistic alternative [14], [15]. The neat truth that drugs that interact with several targets are the most active to treat complex pathologies, such as all the common CNS disorders, led to the proposal that the drugs nonselective for a single target but that selectively interact with several targets involved in a given pathology be dubbed – by a rewording of Ehrlich's metaphor – "*magic shotgun*" drugs [16]. Such drugs make effective medications for psychiatric pathologies, and the same was proven valid for epilepsy, too [10], [17], [18]. These points are charted in Table 1.

Table 1. Main focuses of the reductionist (molecule-centric) and the systemic (network-centric) approaches in biology, pathology, and pharmacology, underlying distinct strategies in NP drug discovery.

AREA	**Reductionist** approach	**Systemic** approach
Biology (basic)	Molecular-level components & specific interactions	Emergent functions in the integral living system
Pathology (general)	Altered elementary components	Disturbed network of interactions
Pharmacology (general)	Specific Ligand–Receptor interaction of Drug–Target	Correction of disturbed networks
NP drug discovery *Ideal aim*	Rational drug discovery of clean drugs *Magic bullets*	Multi-potent therapies *Magic shotguns*

Reductionism led to the acclaimed successes of molecular biology, but it fails to account the integrative biological functions that are emergent properties occurring only at organismic level. Likewise, the reductionist goal of single target-selective drugs, contrary to substantiating an efficient drug design, entailed a persistent general decrease in discovery of novel drugs, and this drawback appears particularly marked in NP [19].

The major NP drugs have overt, albeit unwanted, multi-mechanistic nature

The suggestive label "magic shotgun" was coined upon assessing the mechanisms of the drugs for mood disorders and schizophrenia [16], but it is appropriate for virtually all the drugs effective in treating psychiatric and neurological troubles. Hence, along with the anti-psychotic drugs that modulate (at nM − μM concentrations) the function of fairly numerous ligand-gated and voltage-gated ion channels, also the anti-dementia drugs interact with multiple ion channels [20]. The modulation of multiple molecular targets, i.e. the "pharmacological promiscuity" of the major psychiatric drugs is so manifest that strongly suggests that it might impart clinical efficacy.

Most of the current NP drugs, effective for treating neurological and psychiatric troubles interact with multiple targets simply because these drugs have been developed starting from phenotypic observations, largely serendipitous, in integrated *in vivo* systems, rather than by target-oriented rational (!) drug discovery. The mechanistic multiplicity of many important NP drugs that were serendipitously discovered is illustrated in Figure 1 by the case of valproate, emblematical for the diversity of biochemical and cellular effects exerted by a rather simple (MW = 144.2) molecule.
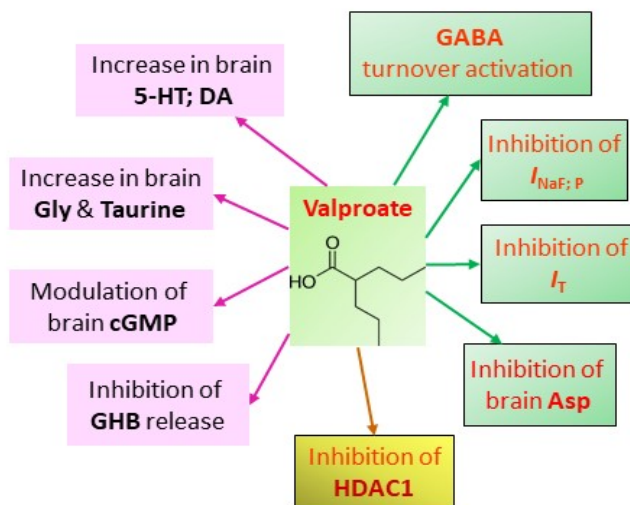
Figure 1. The major NP drug valproate, is largely prescribed as reference anti-seizure medication, to treat bipolar disorder and to prevent migraine. Its multiple molecular effects likely contribute to a wide-spectrum anti-seizure activity [21] (green cases at right), mood-stabilizing and anti-migraine activities [22] (pink cases at left), to a possible anti-cancer activity [23] (yellow case at bottom) and to its toxicity. Acronyms: Asp – aspartic acid, cGMP – cyclic guanosine monophosphate, DA – dopamine, GABA – gamma-aminobutyric acid, GHB – gamma-hydroxybutyric acid, Gly – glycine, HDAC1 – histone deacetylase 1, 5-HT – serotonin, $I_{\text{Na F; P}}$ – sodium currents, fast and lasting, I_T – transient calcium current. Adapted from [21].

The epithet "magic shotgun" undoubtedly fits the antipsychotic drugs for schizophrenia and other severe mental disorders since all of them actually have numerous targets, up to 26 for clozapine and quetiapine [24]. However, this equally holds for many other effective NP drugs. Thus, the fact that all the classical (reference) anti-seizure drugs (ASDs) and the more clinically useful new generation ASDs exert their hypo-excitatory effects upon interacting with multiple ion channels was repeatedly argued and detailed [10], [17], [18].

The multiplicity of effects is manifest even in those cases where a well-defined binding site was revealed for a given drug, by a purposeful investigation subsequent to the phenotypic revealing of that drug. Such is the representative case of the new generation ASD levetiracetam (LEV), illustrated in Figure 2. That figure displays only the cellular effects and the molecular interactions of LEV deemed germane for the anti-seizure activity of that remarkable ASD, not all of its numerous reported effects.
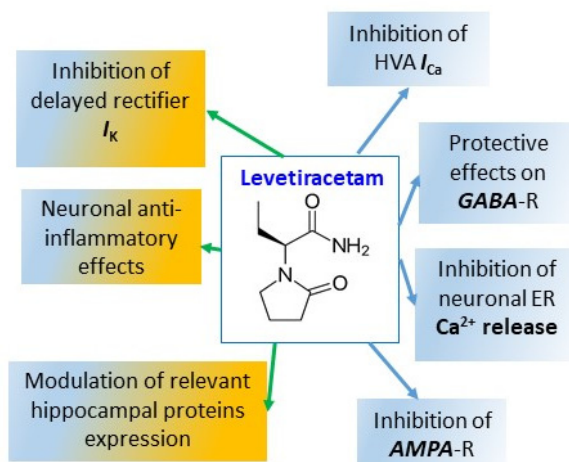
Figure 2. The newer (3rd generation) ASD levetiracetam (LEV) has multiple interactions, generally rather mild and of modulatory type [25] with several types of neuronal ionic channels involved in controlling neuronal excitability: the high-voltage activated (HVA) Ca^{2+} channels [26], the GABA-activated Cl^- channels [27], the AMPA type of glutamate-activated channels [28], and it inhibits the release of Ca^{2+} from neuronal endoplasmic reticulum (ER) [29]. Beside these discernably anti-seizure effects (right side of the figure), LEV also exerts more intricate excitability-modulating effects, such as inhibition of the delayed rectifier K^+ channels [30], modulation of hippocampal protein expression, counteracting inflammatory changes in astroglia etc. (references quoted in [2], from which was adapted this illustration). LEV shows a multi-mechanistic feature shared by all NP drugs revealed by phenotypic screening *in vivo,* even though a specific binding site has been afterwards identified (for LEV, the synaptic vesicle protein SV2A [31]).

The case of LEV (familiar to the present author) is particularly relevant for the subject of the current review. Launched in 2000 in both USA and Europe, LEV became within a few years the most prescribed ASD of newer generation and the first ASD to rise at the status of *blockbuster*. Specialized medical reviews have long concluded that LEV is "a safe, broad-spectrum anticonvulsant drug with highly beneficial pharmacokinetic properties, a favorable long-term retention rate, and a high responder rate" [32]. Also, the continual medical and scientific interest of that drug is clearly attested by a PubMed search of 9 July 2021 with the subject "levetiracetam", that indicated 4,484 publications to date, of which 439 appeared solely in the year 2020, and among which there are 844 review papers.

Chemically, LEV is (S)-α-ethyl-2-oxo-1-pyrrolidine-acetamide, i.e. the (S)-enantiomer of the ethyl analog of piracetam (2-oxo-1-pyrrolidine-acetamide) – the prototype drug of the widely used, though controversial nootropic products [33], purportedly cognitive enhancers. It arose from a chemical synthesis program aimed to generate a better cognitive enhancer, which it did not prove to be, but a general preclinical *in vivo* screening in rodents revealed some less conventional anti-convulsing activity. Professional extension of the early observations in living animals to studies *in vitro*, revealed a correlation of the anticonvulsant effect with a specific binding on a protein present in the brain. That initially mysterious "LEV-binding site" was identified, after nearly a decade, to be the synaptic vesicle protein SV2A [31].

Even before that delayed identification, the correlation between the anticonvulsant activity in a suitable screening test *in vivo* and the affinity towards the LEV-binding site of the different racetam compounds (sharing the pyrrolidone nucleus of piracetam [34]) became a useful tool allowing a target-oriented drug-discovery. It resulted in the selection of a successor of levetiracetam, its 4-*n*-propyl analogue – the *brivaracetam* (BRV) – that has binding affinity and anticonvulsant potency about 10-fold greater than LEV in animal tests [35]. In 2016, BRV became a marketed anticonvulsant drug.

The following Figure 3 shows that the affinity for SV2A of racetam compounds is more manifest when the molecules are bigger, getting a structure that likely fits better the binding site on the receptor. Thus, piracetam has no noticeable SV2A affinity, while LEV (its (S)-α-ethyl derivative) has a significant affinity and BRV (the 4-*n*-propyl derivative of LEV) gets a further increased affinity. That simple plot substantiates two worthy remarks. Firstly, it illustrates in a relevant particular case the general non-specificity of piracetam, a small molecule whose nearly negligible interaction with all chemical components of the organism might probably explain its unusual lack of toxicity [36], but which also obscures its purported effects. However, several other small molecules exert non-specific effects on the brain, being either depressant (e.g. the anesthetic gases) or stimulant (e.g. the methylxanthines). A most prominent example of a small molecule non-specific CNS drug is the ethanol (MW = 46.1) that has multiple effects on the brain functions, not all of them accounted by obvious Ligand–Receptor interactions.

Another remark is the practical utility for drug discovery of identifying a specific binding *in vitro*, provided that the affinity of that binding be tightly correlated with a functional effect *in vivo*. That correlation supports an efficient selection from chemical libraries of candidate molecules to optimize a confirmed therapeutic activity, i.e. to find worthy successors of existing drugs. Obviously, however, those successors will be of basically the same type as the parent drug.
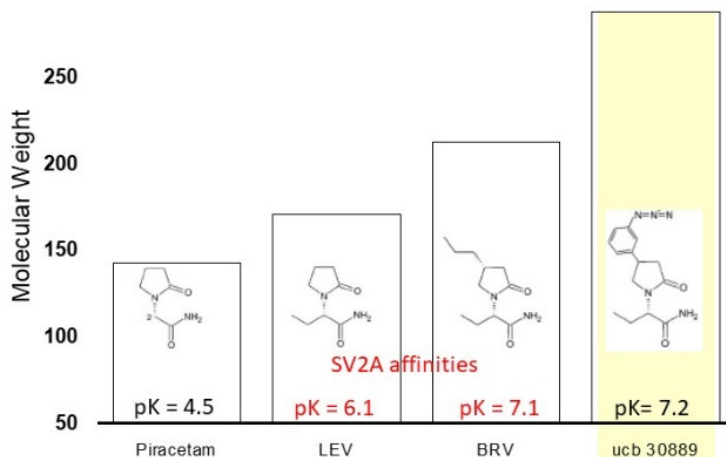
Figure 3. Molecular weight (height of the columns) of four racetam compounds – the nootropic drug piracetam, the ASDs levetiracetam (LEV) and brivaracetam (BRV), and a derivative of LEV (ucb 30889) used as experimental marker – having increasing affinities (the pK values given on each column) for the protein SV2A. Drawing based on crude data from [31], [37], [38].

The account of the anti-convulsive properties of the higher-affinity SV2A ligand BRV [35] was editorially hailed in the *British Journal of Pharmacology* as "a rational drug discovery success story" [39]. However, a truly stern reality concerning *all* the current ASDs, including those recently launched, is that none of them actually cures epilepsy, but only reduce its symptoms. Epilepsy is among the most common chronic neurological pathologies, often life-threating, affecting up to 1% of world population and which was mentioned in writings since more than four thousand years. Its omnipresence in human history entailed considerable focus of NP, making that more than 20 ASD are currently available, a dozen of them licensed in this century. But, in spite of the profusion of ASD options, about 30% of epileptic patients remain drug-refractory [40] and – most disturbingly – the proportion of patients with drug-refractory seizures did not decline since more than half a century [41].

Comprehensibly, drug resistance in epilepsy is the subject of sustained scientific attention [40], [41], [42], [43], but a worrying lack to meet tough medical needs is in no way limited to anti-epileptic pharmacology, it being inherent to virtually all the domains of NP, as briefly outlined in the Introduction. Because a leading cause of NP deficits likely relies on its insufficient matching

of the unequaled intrinsic complexity of human brain, a conceivable solution might be brought by the emerging systemic approach of network pharmacology, as noted in the above section on *Basic consequences of the intrinsic complexity of human brain*.

The idea that, for drugs intended to treat complex pathologies, adjusting the mismatch between multiple receptors is more important than just fixing the anomaly of a single one – so that absolute selectivity is not a suitable ideal in NP – was occasionally expressed prior to the advent of systems pharmacology (for discussion see [21]). But, the preference for single-target selectivity prevailed in NP drug discovery, stirred by the reductionism of molecular biology, prior to the current "postgenomic era". Along with the reductionist mindset, the selectivity dream was also supported by a marketing-driven wish that a medicine should have a forthright image, believed easier to convey to prescribers [18].

Within the integrative SB view, a given CNS pathology reveals a disturbed network of interactions, so that the network NP aims at returning to normal that pathology-disturbed network, via a multi-component therapy or multi-potent drugs. Thus, a first, though not foremost, objective of the systemic approach of NP is a rational poly-therapy, upon identifying combinations of existing neuro-drugs (and adjuvants) with efficacy optimized for each patient. Poly-therapy of CNS pathologies was empirically pursued before the advent of network pharmacology, but the SB approach would bestow on multi-drug therapy a real rationality.

On the other hand, the main objective of network NP should be the design of novel innovative drugs appropriately acting on the ensemble of molecular entities critically involved in each well-defined neuro- / psycho-pathology, to correct the respective disturbed network of molecular interactions. Basically, the application of SB to drug discovery in general involves several types of activities [44]:

- integration of 'omics' data sets and of information available in the literature on responses at cell and organ levels,
- computer modeling of the disease patho-physiology and *in silico* screening,
- experimental approaches to record disease-relevant biological responses by using complex human cell-based assays and occasionally animal models, to capture emergent properties.

Tentatively, the main steps of plausible network NP endeavors can be visualized as in the following Figure 4.
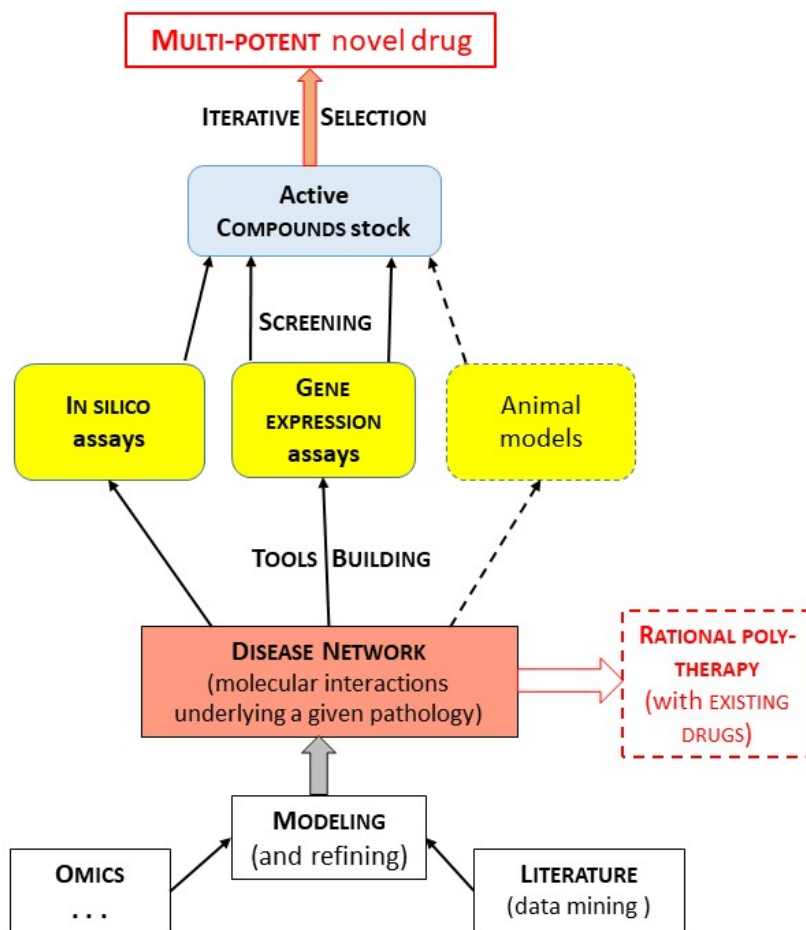
Figure 4. Putative succession of main stages of a network NP drug discovery process aimed at medications for neuro- / psycho- pathologies. Revealing the network of molecular interactions that underlie that pathology in a representative homogeneous group of patients, characterized by the omics (the disease network) sets a rational basis for poly-therapy with possibly existing drugs. It mainly provides the background for creating screening tools to select from chemical libraries active compounds that might finally permit to develop multi-potent drugs. This scheme, adapted from [43], is meant just to illustrate a conceivable endeavor.

Attaining the goal of multi-potent (neuro-) drugs is an arduous task, since optimizing all at once multiple desired activities of a compound, with simultaneous control of unwanted effects, is by far more intricate and cumbersome than the single-target strategy. Yet, significant bioinformatics and chemo-informatics resources are already set in place, computational methods have been put forward, and all advance rapidly.

A wealth of relevant accounts of efforts and achievements advancing the NP along the systemic network pharmacology continuously appear. They refer to quite various aspects, such as: systems level analysis of brain disease-associated proteome alterations [45], network pathophysiology of particular CNS disorders [46], computational approaches for improving NP and innovative drug discovery [47], [48], neuroprotective drugs revealed using artificial intelligence [49], status, opportunities, and challenges of quantitative systems NP [50].

These are but some examples, which, however, illustrate the sustained progress of systemic, network-centric approaches in NP.

CONCLUSIONS

The high scientific and societal importance of NP arises from the unique role of the human brain and the high incidence of the neuro- and psycho-pathologies. NP got some major medical achievements, such as anesthesia and the creation of a large panoply of key drugs to alleviate neurological and psychiatric diseases: many anti-convulsing drugs, the antipsychotics, the benzodiazepine compounds (sedative, hypnotic, anxiolytic, anti-convulsing), and several classes of antidepressant drugs.

But, most of the NP drugs are only symptomatic, relieving the manifestations, not curing the causes of the respective pathologies, which are still vaguely understood. Also, some common neuro-psychiatric pathologies (stroke, CNS trauma and neurodegenerative diseases) are only poorly or not at all treated. Besides, the invention of innovative neuro-drugs clearly declined in the last decades. A chief source of these drawbacks is the mismatch between the unparalleled intrinsic complexity of human brain, making that CNS pathologies are essentially multifactorial, and the unduly reductionist NP orientation towards single-target selective drugs. Combined with a distorted obsession of economic efficacy, the reductionism led NP to rely excessively on the screening *in vitro*, leaving aside the phenotypic screening *in vivo*.

But, the ascent of SB, in the postgenomic era, revealed that pathologies are alterations of the network of interactions that underlie each organismic function, so that a novel network pharmacology aims normalizing networks.

Hence, instead of single-target brain drugs, network NP would overtly search multi-potent drugs. Actually, the best existing neuro-drugs are multi-mechanistic, just because they have been discovered (often serendipitously) by phenotypic screening. The major drug valproate clearly shows manifold actions on various molecular targets in the neurons. Even neuro-drugs for which a specific binding site has been discovered, after their development via *in vivo* tests, are nevertheless multi-mechanistic. Such is the case of the major new generation ASD levetiracetam.

The purposeful invention of multi-potent drugs has to integrate omics and literature data on responses at cell and organ levels, computer modeling of the disease pathophysiology, *in silico* screening, and the record of disease-relevant biological responses in human cell-based assays. The task is highly demanding, but some tools are already in place and they progress rapidly.

DEDICATION

This paper is devoted to the memory of my faithful friend of long date Prof. Dr. Petre T. Frangopol, Honor Member of the Romanian Academy.

REFERENCES

1. A. G. Phillips; P. Hongaard-Andersen; R. A. Moscicki; B. Sahakian; R. Quirion; K. R. R. Krishnan; T. Race; *Int. J. Neuropsychopharmacol.*, **2015**, *19*, 1–16
2. D. G. Margineanu; *BioSystems*, **2016**, *141*, 1–9
3. E. Shorter; *Curr. Opin. Psychiatry*, **2008**, *21*, 593–597
4. T. A. Ban; *Dialogues Clin. Neurosci.*, **2006**, *8*, 335–344
5. B. H. Yokley; M. Hartman; B. S. Slusher; *ACS Chem. Neurosci.*, **2017**, *8*, 429–431
6. W. Singer; *EMBO Rep.*, **2007**, *8*, S16–S19
7. Q. Mu; Y. Chen; J. Wang; *Genomics Proteomics Bioinformatics*, **2019**, *17*, 344–366
8. J. L. Ji; M. Spronk; K. Kulkarni; G. Repovš; A. Anticevic; M. W. Cole; *Neuroimage*, **2019**, *185*, 35–57
9. S. B. Laughlin; T. J. Sejnowski; *Science*, **2003**, *301*, 1870–1874
10. D. G. Margineanu; *Epilepsy Res.*, **2012**, *98*, 104–115
11. T. Takahashi; *Prog. Neuropsychopharmacol. Biol. Psychiatry*, **2013**, *45*, 257–265
12. H. Kitano; *Science*, **2002**, *295*, 1662–1664
13. U. Sauer; M. Heinemann; N. Zamboni; *Science*, **2007**, *316*, 550−551
14. C. T. Keith; A. A. Borisy; B. R. Stockwel; *Nature Rev. Drug Discov.*, **2005**, *4*, 71–78
15. A. L. Hopkins; *Nature Chem. Biol.*, **2008**, *4*, 682–690

16. B. L Roth; D. J. Sheffler; W. K., Kroeze; *Nature Rev. Drug Discov.,* **2004**, *3*, 353–359
17. M. T. Bianchi; J. Pathmanathan; S. S. Cash; *Med. Hypotheses*, **2009**, *72*, 297–305
18. D. G. Margineanu; *Epilepsy Behav*., **2014**, *38*, 131–142
19. J. Arrowsmith; *Nature Rev. Drug Discov*., **2011**, *10*, 1
20. M. T. Bianchi; *Med. Hypotheses*, **2010**, *74*, 297–300
21. D. G. Margineanu; Systems (network) pharmacology for brain functionality restoration. In *Homeostatic Control of Brain Function*; D. Boison, S. Masino Eds.; Oxford University Press, New York, USA, **2015**; pp. 231–247
22. C.-T. Chiu; Z. Wang; J. G. Hunsberger; D.-M. Chuang; *Pharmacol. Rev*., **2013**, *65*, 105–142
23. S. Chateauvieux; F. Morceau; M. Dicato; M. Diederich; *J. Biomed. Biotech.*, **2010**, article ID 479364, doi:10.1155/2010/479364
24. J. Sun; H. Xu; Z. Zhao; *Chem. Biodiv.*, **2012**, *9*, 900–910
25. D. G. Margineanu; H. Klitgaard; Levetiracetam mechanisms of action. In *Antiepileptic Drugs*, 5th ed.; R. H. Levy, R. H. Mattson, B. S. Meldrum, E. Perucca Eds.; Lippincott Williams & Wilkins, Philadelphia, USA, **2002**; pp. 419–427
26. I. Niespodziany; H. Klitgaard; D.G. Margineanu; *Neurosci. Lett.,* **2001,** *306*, 5–8
27. P. Poulain P.; D. G. Margineanu; *Neuropharmacol.*, **2002**, *42*, 346–352
28. I. Carunchio; M. Pieri; M. Ciotti; F. Albo; C. Zona; *Epilepsia*, **2007**, *48*, 654–662
29. M. Ängehagen; D. G. Margineanu; E. Ben-Menachem; L. Ronnback; E. Hansson. H. Klitgaard; *NeuroReport*, **2003**, *14*, 471–475
30. M. Madeja; D. G. Margineanu; A. Gorji; E. Siep; P. Boerrigter; H. Klitgaard; E.-J. Speckmann; *Neuropharmacol*., **2003**, *45*, 661–671
31. B. A. Lynch; N. Lambeng; K. Nocka; P. Kensel-Hammes; S. M. Bajjalieh; A. Matagne; B. Fuks; *Proc. Nat. Acad. Sci. USA*, **2004**, *101*, 9861–9866
32. T. De Smedt; R. Raedt; K. Vonck; P. Boon; *CNS Drug Reviews*, **2007**, *13*, 57–78
33. D. G. Margineanu; *Rev. Quest. Sci*, **2011**, *182*, 33–52
34. B. M. Kenda; A. C. Matagne; P.E. Talaga; P. M. Pasau; E. Differding; B. I. Lallemand; A. M. Frycia; F. G. Moureau ; H. V. Klitgaard; M. R. Gillard; B. Fuks; P. Michel; *J. Med. Chem.*, **2004**, *47*, 530–549
35. A. C. Matagne; D. G. Margineanu; B. Kenda; P. Michel; H. Klitgaard; *Br. J. Pharmacol.*, **2008**, *154*, 1662–1671
36. B. Winblad; *CNS Drug Reviews*, **2005**, *11*, 169–182
37. M. Gillard; B. Fuks; P. Michel; P. Vertongen; R. Massingham; P. Chatelain; *Eur. J. Pharmacol.*, **2003**, *478*, 1–9
38. P. von Rosenstiel; *Neurotherapeutics*, **2007**, *4*, 84–8
39. M. A. Rogawski; *Br. J. Pharmacol*., **2008**,*154*, 1555–1557
40. A. Golyala; P. Kwan; *Seizure*, **2017**, *44*,147–156
41. D. G. Margineanu; H. Klitgaard; *Expert Opin. Drug Discov.*, **2009**, *4*, 23–32
42. W. Löscher; H. Potschka; S. M. Sisodiya; A. Vezzani; *Pharmacol. Rev.*, **2020**, *72*, 606–638
43. D. G. Margineanu; *Med. Res. Arch.*, **2021**, *9*, in press

44. E. C. Butcher; E. L. Berg; E. Kunkel; *Nature Biotechnol.*, **2004**, *22*, 1253–1259
45. M. Keck; G. Androsova; F. Gualtieri; A. Walker; E.-L. von Rüden; V. Russmann; C. A. Deeg; S. M. Hauck; R. Krause; H. Potschka; *Neurobiol. Dis.*, **2017**, *105*, 164–178
46. A. B. Elgoyhen; B. Langguth; S. Vanneste; D. DeRidder; *Front. Systems Neurosci.,* **2012**, *6*, doi: 10.3389/fnsys.2012.00001
47. K. Shameer; A. Nayarisseri; F. X. R. Duran; H. González-Díaz; *Curr. Neuropharmacol.,* **2017***, 15,* 1058–1061
48. A. Talevi; *Expert Opin. Drug Discov.*, **2016**, *11*, 1001–1016
49. D. Romeo-Guitart; J. Forés; M. Herrando-Grabulosa; R. Valls; T. Leiva-Rodríguez; E. Galea; F. González-Pérez; X. Navarro; V. Petegnief; A. Bosch; M. Coma; J. M. Mas; C. Casas; *Sci. Rep.* **2018**, *8,*1879 doi:10.1038/s41598-018-19767-3
50. H. Geerts; J. Wikswo; P. H. van der Graaf; J. P.F. Bai; C. Gaiteri; D. Bennett; S. E. Swalley; E. Schuck; R. Kaddurah-Daouk; K. Tsaioun; M. Pelleymounter; *CPT Pharmacometrics Syst. Pharmacol.*, **2020**, *9*, 5–20

MAGNETIC AND TRANSPORT PROPERTIES
OF DOUBLE PEROVSKITES

EMIL BURZO[a]

ABSTRACT. The magnetic and transport properties of polycrystalline Sr_2FeMoO_6 perovskites are strongly dependent on their microstructure. A cluster glass type behavior was shown at the grain boundaries. The increase of the sintering time from 4 to 8 hrs in $Sr_2FeMo_{1-x}W_xO_6$ and $Ca_{1.5}La_{0.5}FeMo_{1-x}W_xO_6$ series improves the crystallographic order. As a result there is an increase of both the saturation magnetizations and of spin polarizations.

Keywords: perovskites, magnetic behavior, transport properties

INTRODUCTION

The $A_2BB'O_6$ (A = Sr, Ca; B=Fe and B'=Mo) double perovskites are receiving attention due to their possible spin electronics applications and magnetoresistance based devices [1, 2]. The technical uses are facilitated by their Curie points located above ambient temperature.

The aristotype cubic ordered double perovskites A_2FeMoO_6 can be described by cubic sharing FeO_6 and MoO_6 octahedra, which alternate in three directions. The A site cations occupy the cavities formed by corner sharing octahedral network. Due to small Ca^{2+} cation radius, the FeO_6 and MoO_6 octahedra are considerably tilted in anti-phase order in the basal plane and along the crystallographic **c**-axis, the crystal structure of Ca_2FeMoO_6 decreasing, to monoclinic, space group $P2_1/n$ [3]. The crystal structure of Sr_2FeMoO_6, due to the same reasons, is tetragonal, space group I4/mmm [4].

The ideal magnetic structure of A_2FeMoO_6 can be described by an antiparallel arrangement of Fe^{3+} and Mo^{5+} magnetic moments, respectively [1]. The lower magnetization than the value of 4 μ_B/f.u., predicted by the above magnetic structure, is a general characteristic of these perovskites. This is the result of some competitive effects: (a) the presence of antisites, where the Mo atoms are located at the Fe position and vice versa; (2) the iron ions

[a] *Babeş-Bolyai University, Faculty of Physics, 1 Kogalniceanu str., RO-400028, Cluj-Napoca, Romania, emil.burzo@ubbcluj.ro*

having mixed valence states. In highly ordered Sr_2FeMoO_6, both Fe^{3+}-Mo^{5+} and Fe^{2+}-Mo^{6+} states are evidenced [5, 6]; (3) antiphase domains [7]; (4) nonuniform distribution of constituting elements inside and at the grain interface [8]; (5) oxidation at the grain boundaries; (6) decomposition of Sr_2FeMoO_6 sample with formation of $SrMoO_4$ [9], (7) changes with time of the Fe^{2+}/Fe^{3+} ratio [10] and (8) the Mo^{5+} moment smaller than 1 μ_B/ion.

The A_2FeMoO_6 double perovskites have half metallic behaviour under the assumption of a perfectly ordered crystal structure. In this case the down-spin conduction band crossing the Fermi level, E_F, is dominated by the Fe3d-Mo4d t_{2g} states, while the up-spin band, below E_F, is mostly due to the Fe3d e_g states [1]. Commonly, deviations from perfectly ordered crystallographic and magnetic structures are present, strongly influencing the transport properties.

Previously, we analysed the magnetic and transport properties of $Sr_2FeMo_{1-x}M_xO_6$ with M = W, Ta [11, 12], $Ca_{1.5}La_{0.5}FeMo_{1-x}W_xO_6$ [13] and $A_2Fe_{1-x}Ni_xMoO_6$ with A = Ca [14, 15] and Sr [16]. Some of these perovskites have Curie temperatures above the ambient one and thus possible technical uses. The physical properties were shown to be influenced both by composition and the sintering process. As an ongoing work on double perovskites, the effects of thermal treatment and sample compositions on the magnetic and transport properties of Sr- and Ca-based double perovskites are investigated.

RESULTS AND DATA ANALYSIS

The Sr_2FeMoO_6 perovskites were sintered at 1300 ºC under argon flow with 1.7 % (sample S-3) and 0.8 % (sample S-5) hydrogen, at T = 1300 ºC. The determined AS content by XRD was 3 % for sample S-3 and 5 % for the perovskite S-5. The XPS studies indicate the presence of 70 % Fe^{3+} - Mo^{5+} and 30 % Fe^{2+}-Mo^{6+} states.

The microstructure of sample S-3 consists from grains having 0.2-0.3 μm diameter and also regions in which the grain coalesced in bands, while the perovskite S-5 is constituted from grains having 2-3 μm dimensions. The iron content in sample S-3 was little smaller, while in perovskite S-5 higher than the ideal value (25 %). The molybdenum content decreased little from the center of the grain towards their boundaries. Around the grain boundaries the iron content was by 0.7 % (S-3) and 1.5% (S-5) higher than that inside the grains.

The analysis of the ^{57}Fe Mössbauer spectra, for the two Sr_2FeMoO_6 perovskites showed: (1) the AS content was 3.9 % in sample S-3 and 6.5 % in perovskite S-5, in rather good agreement with the values obtained from XRD method; (2) an iron-fraction of 5.8 % in S-3 and 6.2 % in S-5

perovskites, respectively are located in the antiphase domain boundaries (APB). The above differences in the microstructures of the two Sr_2FeMoO_6 perovskites are reflected in their magnetic and transport properties.

The temperature dependence of magnetization for sample S-3 is given in Fig.1.The saturation magnetization at 4.2 K, M_s=3.4 μ_B/f.u., is by 0.6 μ_B smaller than that estimated assuming a ferrimagnetic ordering and the already determined antisite fractions and iron valence states. The molybdenum moment was assumed to be $\cong$ 0.4 μ_B/atom, as determined by neutron diffraction study [17]. These data suggest the presence of antiphase domains and possible cluster glass type ordering at the grain boundaries. The saturation magnetization of sample S-5 is by $\cong$ 0.1 μ_B smaller than that of S-3 one, correlated with a larger fraction of antisites and APB. The saturation magnetization of sample S-3 decreased by 0.15 μ_B/f.u. by keeping in air around 9 months.
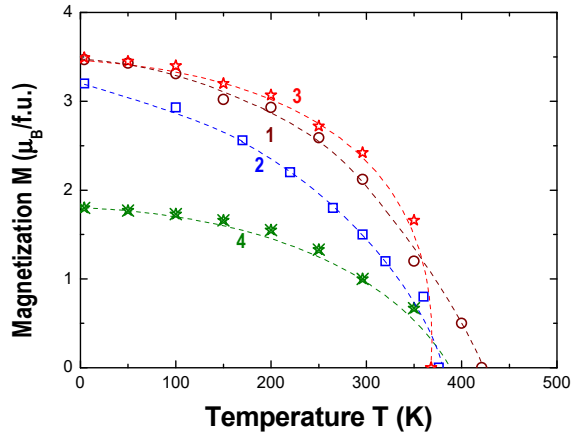
Figure 1. Thermal variations of magnetizations in 1-Sr_2FeMoO_6 (S3), 2-$Sr_2FeMo_{0.7}W_{0.3}O_6$, 3-$Ca_{1.5}La_{0.5}FeMoO_6$ and 4-Ca_2FeMoO_6 double perovskites

The magnetization isotherms, M(H), at T=4.2 K, do not follow the classical approach to saturation law, suggesting the presence of an additional small magnetic contribution superposed on that due to ferrimagnetic-type ordering. The better agreement with experimental data was obtained when the M(H) curves were analyzed assuming a field dependence, typical for a cluster glass system with weak anisotropy [18] – Fig.2.

$$m(H) = M(H)/M_s = (1 - aH^{-1/2}) \qquad (1)$$

By fitting the magnetization isotherms at T=4.2K, with the relation (1), values a = 0.15$T^{1/2}$ for sample S-3 and 0.18 $T^{1/2}$ for the perovskite S-5, respectively were obtained. The above results show the presence of cluster glass type behavior at the grain boundaries, which is superposed on the main magnetic contribution resulting from the antiparallel alignment of B(Fe) and B'(Mo) magnetizations.
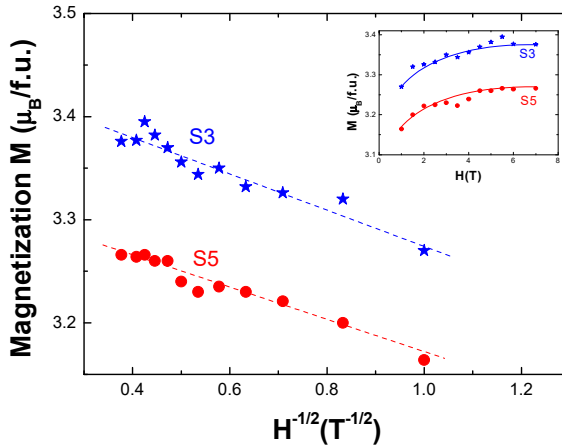
Figure 2. The magnetization isotherms, at T = 4.2 K, for two Sr_2FeMoO_6 perovskites (inset) and the dependences of the magnetizations, at T = 4.2 K on $H^{-1/2}$. The fitted curves are shown by dashed lines.

The previous studies on Sr_2FeMoO_6 perovskites showed both semiconducting and metallic behavior, depending on the preparation method [19, 20]. Differences between resistivities of the two Sr_2FeMoO_6 samples correlated with their microstructures, are also present, as seen in Fig.3. The perovskite S-3 has a resistivity by two orders of magnitude lower than that of the S-5 sample. The higher resistivity of sample S-5 can be attributed mainly to differences in the compositions inside the grains and at their interfaces. The iron content at the grain boundary is by $\cong$ 1.5 % higher, and consequently the cluster glass contribution to the magnetizations, as suggested from the analysis of magnetizations isotherms. The number of antisites in sample S-5 is twice than that in perovskite S-3. The lower hydrogen content in the mixture with argon, used during sintering, can lead to possible oxidation of the grain boundaries, affecting also the transport properties of sample S-5.

Figure 3. The temperature dependences of the resitivities for 1-Sr_2FeMoO_6 (S-3),
2 – Sr_2FeMoO_6 (S-5), 3-$Sr_2FeMo_{0.7}W_{0.3}O_6$-8hrs, 4-$Ca_{1.5}La_{0.5}FeMoO_6$ and
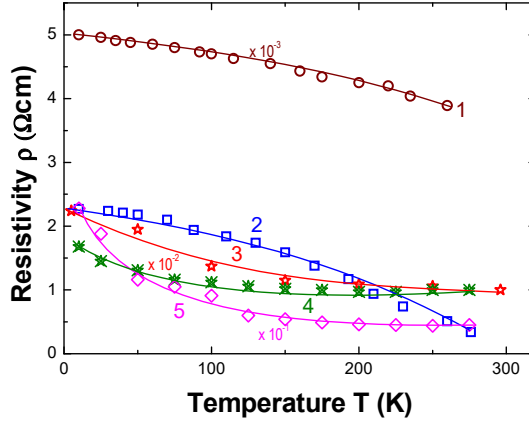5-$Ca_{1.5}La_{0.5}FeMo_{0.7}W_{0.3}O_6$

The magnetoresistances (MR) of the perovskites are determined by two contributions: (1) the spin disorder inside the grains, proportional to the external field, $MR_d = -bH$; (2) the intergrain magnetic tunneling magnetoresistance (ITMR) which depends of the structure and magnetic state at the grain boundaries. The contribution of magnetic state at the grain boundaries to the ITMR, MR_i, in polycrystalline perovskites, can be analysed for systems where the applied field is smaller than the exchange field [21, 22]. By using the mean field approximation, the exchange interactions parameters inside and between the B and B' magnetic sublattices in Sr_2FeMoO_6, were determined ($J_{BB'} = -17$, $J_{BB} = 98$) and on this basis, the exchange field. The exchange field acting on B sublattice, of 200 T, is by $\cong$ 30 times higher than the field used in present measurements. Consequently, the model [21, 22] can be used also in analysing the transport properties of A_2FeMoO_6-based series.

Starting from a network of tunnel junctions, whose electrodes are double perovskite grains, separated by an insulating layer and assuming elastic tunneling across a single barrier, averaged over random grain orientations, the MR_i contribution to magnetoresistance can be described by [22]:

$$MR_i = \Delta\rho(\Delta H,T)/\rho(H,T) = -P^2m(H)^2[1+P^2m(H)^2]^{-1} \qquad (2)$$

By P is denoted the spin polarization and m(H) is the reduced magnetization at the grain boundaries, given by the relation (1). As seen from Fig. 4, the low field magnetoresistance of polycrystalline perovskites is determined by spin polarized tunneling between the grains and the high field contribution is related mainly to the intragrain contribution.
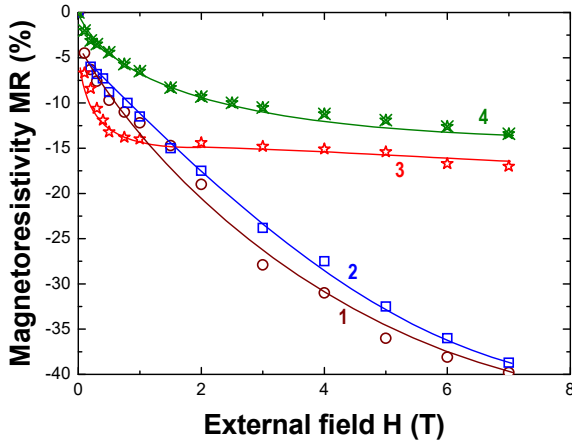
Figure 4. The field dependences of the magnetoresistances, at T = 10 K for 1-Sr_2FeMoO_6 (S-3), 2-$Sr_2FeMo_{0.7}W_{0.3}O_6$, 3- Ca_2FeMoO_6 and 4-$Ca_{1.5}La_{0.5}FeMoO_6$

By fitting the experimentally determined magnetoresistances with the relation $MR = MR_d + MR_i$, the temperature dependences of the spin polarizations, P, were determined in both Sr_2FeMoO_6 samples as well as in others pseudo-quaternary perovskites – Fig. 5. The spin polarization of sample S-3 is of 58 %, at T = 10 K, and decreases nearly linearly with temperature. The extrapolated temperatures where P= 0, are close to the Curie points. The spin polarization of perovskite S-5, at T = 10 K is nearly half as compared with that evidenced in sample S -3.
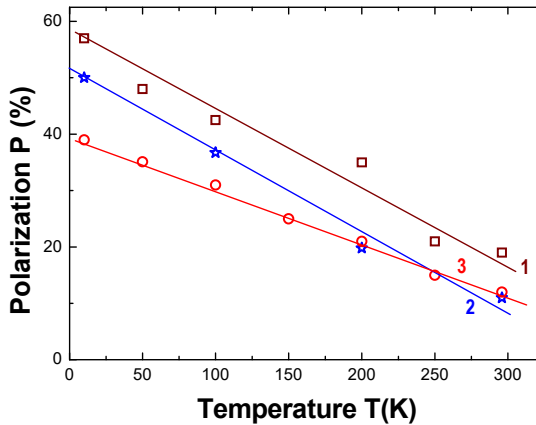
Figure 5. Thermal variations of spin polarizations in 1-Sr_2FeMoO_6 (S-3), 2-$Sr_2FeMo_{0.7}W_{0.3}O_6$, 3- Ca_2FeMoO_6 perovskites.

The comparative analysis of the physical properties of Sr_2FeMoO_6 perovskites sintered in different conditions show: (1) the microstructure of the perovskites, the homogeneity of the grain and at the grain boundary are significantly influenced by the sintering conditions; (2) the magnetic properties are mainly determined by the iron valence states and the antisite content; (3) the transport properties are influenced by the energy of the barriers at the grain boundaries, respectively.

The effect of substitutions of Mo by W [11, 23-25], of Fe by Ni and of Ca_2 by $Ca_{1.5}La_{0.5}$ [13-16] on the physical properties of double perovskites were also analysed. The composition dependences of the Curie temperatures for $A_2Fe_{1-x}Ni_xMoO_6$ with A = Sr and Ca, $Sr_2FeMo_{1-x}W_xO_6$ and $Ca_{1.5}La_{0.5}FeMo_{1-x}W_xO_6$ double perovskites are shown in Fig. 6. Although the Curie points of $Sr_2FeMo_{1-x}W_xO_6$ decrease, as molybdenum is replaced by tungsten, these remain located above the room temperature. The presence of W improve the crystallographic ordering. The increase of sintering time at 1300 °C, from 4 to 8 hrs, leads to a better homogeneity of the grains and diminishes the number of antisites [11]. The cluster glass contribution to the magnetization also decreases. The presence of tungsten, influence only little the magnetoresistance. Even if 30 % of Mo is replaced by W, only a small reduction of spin polarization, as compared to that of the end series member can be shown – Figs. 4 and 5.
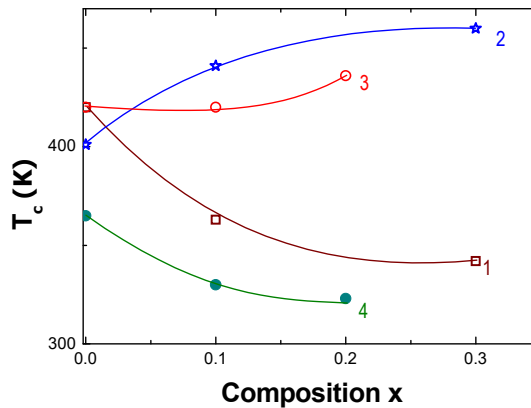
Figure 6. The composition dependences of the Curie temperatures in 1-$Sr_2FeMo_{1-x}W_xO_6$, 2-$Ca_{1.5}La_{0.5}FeMo_{1-x}W_xO_6$, 3-$Sr_2Fe_{1-x}Ni_xMoO_6$ and 4-$Ca_2Fe_{1-x}Ni_xMoO$ double perovskites.

The partial substitutions of Mo by W in $Ca_{1.5}La_{0.5}FeMo_{1-x}W_xO_6$ series, increase also the crystallographic ordering. As a result, higher Curie temperatures and saturation magnetizations, as compared to end series

perovskite, are shown [13]. There are little changes in the magnetoresistances of the W substituted samples. The spin polarization at T = 10 K, increase from 40 % for x=0 up to 53 % when 30 % Mo is replaced by W.

The iron valence states in $Ca_{1.5}La_{0.5}FeMoO_6$ are dependent on pressure. As the pressure increases, the resistivities decrease followed by an abrupt drop at $p \cong 2$ GPa [26-28], correlated with changes in iron valence states [26]. This suggests that the transport properties of the perovskites can be tuned by pressure.

The Curie temperatures of $A_2Fe_{1-x}Ni_xMoO_6$ double perovskites increase as iron is substituted by nickel when A = Sr and decrease if A = Ca. The above trend can be analysed in correlation with exchange interactions between B and B' sites magnetizations, resulting from the composition dependence of the antisite content [16].

We note that in $La_{1-x}Pb_xMnO_3$ perovskite, a spin polarization of $\cong 90$ % was obtained for a composition x = 0.4 [29, 30]. Unfortunately, the Curie temperatures of the series are rather low and consequently cannot be used in spintronic applications, working at room temperature.

CONCLUSIONS

The physical properties of A_2FeMoO_6 double perovskites with A = Sr, Ca, as well as of series obtained by substitutions at A, Fe and Mo sites are strongly dependent on the sintering process (temperature, time, atmosphere). The partial substitution of Mo by W improve the crystallographic ordering. Their magnetic and transport properties are influenced by aging or by keeping in air.

EXPERIMENTAL SECTION

The double perovskites were prepared by solid state reaction. The amounts of $SrCO_3$, $CaCO_3$, Fe_2O_3, La_2O_3, WO_3 and NiO powders, corresponding to the requested sample compositions, were mixed and calcinated in argon atmosphere at T = 900 °C. The calcinated powders were pelletized and sintered at temperatures 1200–1300 °C, between 4 and 8 hrs, in a stream of argon flow atmosphere having 0.8 % up to 1.7 % hydrogen.

The XRD spectra showed the presence of only one phase. The spectra were analysed by Rietveld method by using a TOPAS program [31]. In this way, the lattice parameters and antisite (AS) content were determined. The $Sr_2FeMo_{1-x}W_xO_6$ and $Ca_{1.5}La_{0.5}FeMo_{1-x}W_xO_6$ series with x≤0.3, crystallize in

a tetragonal and monoclinic structure types, respectively. The $A_2Fe_{1-x}Ni_xMoO_6$ with A = Sr, Ca perovskites form solid solutions up to x = 0.2.

Scanning electron microscopy (SEM) and energy disperse spectroscopy (EDS) measurements were made with a JEOL-type equipment. The compositions, grain dimensions and the distribution of constituting elements along the grains were analysed.

Magnetic measurements have been performed by extraction method, in the temperature range 4.2 K to Curie points, in fields up to 7 T. The ^{57}Fe Mössbauer studies have been made, at T = 77 K, on Sr_2FeMoO_6 perovskites synthesized in different conditions.

The resistivity and magnetoresistance were investigated in the 10 K ≤ T ≤ 300 K temperature range and fields up to 7 T, by using the four terminal method.

ACKNOWLEDGMENTS

REFERENCES

1. K. I. Kobayashi; T. Kimura; H. Sawada; K. Terakura; Y. Tokura; *Nature*, **1998**, 395, 677
2. D. Rubi; I. Nogues; J. S. Munoz; J. Fountcuberta; *Mat. Sci. Eng. 2006, B126, 279*
3. R. P. Borges; R. M. Thomas; C. Cullinan; J. M. D. Coey; B. Suryanarayanan, L. Ben-Dor; I. Pinsard-Gaudart; A. Recolevschi; *J. Phys.: Condens. Matter*, **1999,** 11, 1445
4. E. Burzo; Perovskites, *Landolt-Börnstein Handbook, Springer Verlag,* **1996**, vol. 27F1ß
5. K. Kuepper et all; *Phys. Stat. Solidi (a),* **2004**, 201, 3252
6. M. Raekers et all; *J. Opt. Adv. Mater,* **2006**, 8, 455
7. J. M. Greneche; M. Venkatesan; R. Suryanarayanan; J. M. D. Coey; *Phys. Rev.* **2001,** B63, 174403
8. D. Yang; T. Yang; Q. Sun; Y. Chen; G. L. Lapronti; J. Alloys. Comp. 728, 337 (2017)
9. J. Navarro; C. Frontera; D. Rubi; N. Mestres; J. Frontcuberta; *Mater. Res. Bull.,* **2003**, 38, 1477
10. K. Kuepper; M. Raekers; C. Taubitz; H. Hesse; M. Neumann; A. T. Young, C. Piamonteze; F. Bondino; K. C. Prince; *J. Appl. Phys.,* **2008**, 104, 036103
11. E. Burzo; I. Balasz; M. Valeanu; I. G. Pop; *J. Alloys Comp.,* **2011**, 509, 105
12. E. Burzo; I. Balasz; S. Constantnescu; I. G. Deac; *J. Magn. Magn. Mater.,* **2007**, 316, e741

13. E. Burzo; I. Balasz; M. Valeanu; D. P. Kozlenko; A. V. Rutkauscas; B. N. Savenko; *J. Alloys Comp.*, **2015**, 621, 71
14. E. Burzo; I. Balasz, *Rom.J. Phys.*, **2017**, 62, 601;
15. E. Burzo; I. Balasz; *AIP Conf. Proc.*, **2016**, 1722, 080003
16. E. Burzo; G. Souca; *J. Mater. Sci.: Mater. Electron.* **2021**, 32, 2200
17. D. Sanchez; J. A. Alonso; M. Garcia-Hernandez; M. J. Martinez-Lope; J. L. Martinez; A. Mellergard; *Phys. Rev.,* **2000**, B65, 104426
18. J. Tejada; B. Martinez; A. Labarta; E. M. Chudnovsky; *Phys. Rev.* , **1991**, B44, 7698
19. Y. Tomioka; T. Okuda; Y. Okamoto; R. Kumai; K. I. Kobayashi; Y. Tokura; *Phys. Rev.* , **2000**, B61, 422
20. G. Suchaneck; N. Kalanda; E. Artiukh; M. Yarmolich; N. A. Sobolev; *J. Alloys Comp.* **2021**, 860, 158526
21. D. Niebieskikwiat; F. Prado; A. Caniero; R. D. Sanchez; *Phys. Rev.,* 2004, B70, 132412
22. D. Serrate; J. M. De Teresa; R. A. Algarabel; M. R. Ibarra; J. Galibert; *Phys. Rev.*, **2005**, B71, 104409
23. S. Ray; A. Kumar; S. Magundar; E. V. Sampathkumaran; D. D. Sarosa; *J. Phys. : Condens Matter,* 13607 (2001)
24. K. I. Kobayashi; T. Okuda; Y. Tomioka; T. Kimura; Y. Tokura; *J. Magn. Magn. Mater.*, **2000**, 218, 17
25. M. Karppinen; H. Yamauchi; Y. Yasukawa; J. Linden; F. S. Chan; R. S. Liu; J. M. Chen; *Chem Mater.,* **2003**, 15, 4118
26. E. Burzo; D. P. Kozlenko; N. T. Dang; S. E. Kichanov; N. O. Golosova; *J. Alloys Comp.*, **2016**, 664, 363
27. P. Zhao; R. C. Yu; F. Y. Li; Z.H. Liu; M. Z. Jin; C. Q. Jin; *J. Appl. Phys.,* **2002**, 92, 1942
28. D. Morrocchelli; P. Postorino; D. D. Castro; E. Arcangeletti; P. Dore; M. C. Guidi; S. Ray; D. D. Sarma; *Phys. Rev.*, **2007**, B76, 172405
29. E. Burzo; I. Balasz; M. Isobe; Y. Ueda, *J. Alloys Comp.***, 2012**, 535, 129
30. E. Burzo; I. Balasz; I. G. Deac; M. Neumann; *Physica,* **2008**, *B*403, 1601
31. *DIFRAC plus TOPAS General profile and structure analysis software for powder diffraction data*, **2001**, Bruker AXS Gmb, Karlsruhe

BIOCOMPATIBILITY OF TITANIUM IMPLANTS COATED WITH BIOCOMPOSITE IN A RAT MODEL OF FEMORAL FRACTURE

**DANIEL OLTEAN-DAN[a], PETRE T. FRANGOPOL[&],
REKA BALINT[b, *], GHEORGHE TOMOAIA[a,c],
AURORA MOCANU[b], MARIA TOMOAIA-COTISEL[b,c]**

ABSTRACT. The biocompatibility of uncoated titanium, Ti, nails and coated with an innovative biocomposite is assessed in a rat model of femoral fracture. The biocomposite is based on multi-substituted hydroxyapatite, ms-HAP containing Mg, Zn and Si, and is used as a coating material deposited on Ti implants, due to the excellent biocompatibility and osteoconductive property of ms-HAP. Specific focus has been given to biocomposite coating made of ms-HAP functionalized with collagen (ms-HAP/COL, core/shell nanoparticles) NPs embedded into poly lactic acid, PLA, matrix and finally covered by COL layer. This coating on Ti implants is noted as ms-HAP/COL@PLA/COL and named HAPc, and is characterized by SEM images and EDX spectra. Twenty-four Wistar albino rats with left femoral fracture, were used and divided in two equal groups, namely the control group, CG, with uncoated Ti implants and HAPc rat group with Ti implants coated with HAPc biocomposite through layer-by-layer, LBL, dip coating technique. After two- and eight-weeks post-surgery, they were evaluated by bone markers serum concentration, micro-CT and histological study. The alkaline phosphatase (ALP) and osteocalcin (OCN) expression, in the HAPc group showed higher values with an osteoblastic activity more intense and a more advanced callus stage. The micro-CT results showed that biocomposite coating significantly increased the bone volume/ tissue volume (BV/TV). The most advanced stage of bone remodelling with osseointegration of the Ti implants was observed in HAPc group, where the new formed trabecular bone is almost completely replaced by compact bone.

[a] *Iuliu Hatieganu University of Medicine and Pharmacy, Department of Orthopedics and Traumatology, 47 Gen. Traian Mosoiu Str., RO-400132, Cluj-Napoca, Romania*
[b] *Babeş-Bolyai University, Faculty of Chemistry and Chemical Engineering, Research Center of Physical Chemistry, 11 Arany Janos Str., RO-400028, Cluj-Napoca, Romania*
[c] *Academy of Romanian Scientists, 3 Ilfov Str., RO-050044, Bucharest, Romania*
[&] *Deceased on December 11, 2020*
[*] *Corresponding author: Reka.Balint@ubbcluj.ro*

DANIEL OLTEAN-DAN, PETRE T. FRANGOPOL, REKA BALINT, GHEORGHE TOMOAIA, AURORA MOCANU, MARIA TOMOAIA-COTISEL

This study provides a novel strategy for the treatment of bone fracture with a superior osseointegration of biocomposite coated Ti implants and potential orthopaedic applications.

Keywords: biocompatibility, titanium implants, biocomposite coating, multi-substituted hydroxyapatite, PLA, collagen

INTRODUCTION

The development of novel orthopaedic and dental implants has been focused for many years to produce an optimal osseointegration between the implanted material and the living bone, without interposition of non-bone tissue [1]. To accomplish this major objective an optimal bone-implant interface needs to be designed and created through modification of the implant surface topography and chemical composition. The concept of direct contact between the bone and the implant was described as direct structural and functional connection between the living bone and the surface of a load-carrying implant [1-5] to prevent the fibrous tissue attachment.

An ideal implant material needs to have a biocompatible chemical composition similar to that of bone to avoid adverse bone tissue reaction, and to minimise bone resorption around the implant. Therefore, a newly developed implant needs to obey the requirements of biocompatibility and safety, and it must undergo rigorous testing *in vivo*. Results obtained *in vitro* studies might be difficult to extrapolate to the *in vivo* situation. For this purpose, the use of animal model is a crucial step in orthopaedic implants testing prior to clinical use in humans or in animals.

To achieve osseointegration various metals, ceramics and polymers were used. Major metal used was titanium, Ti, and its alloys being recognized as biocompatible material to promote osseointegration [4,6,7].

The host bone response to a Ti implant is influenced by its topography, roughness and porosity. It was observed that Ti surface morphology influences osteoblast and osteoclast attachment and metabolism [8]. However, the immune system is still considering Ti implants as foreign bodies and fibrosis around the implants can occur. In this case the osteoblasts are constrained to create bone ingrowth at the surface of the implant and osseointegration is restricted. This situation leads to loosening and failure of the implant [9,10]. The limitation of fibrous tissue production around the Ti implant can be reached by bioactive coating of the Ti surface with hydroxyapatite which can lead to benefits in terms of cell adhesion, differentiation, and bone matrix formation [9].

The hydroxyapatite can be substituted to create a composite more chemically closer to the normal bone tissue. Cationic substitution of the calcium ions within the hydroxyapatite, HAP, lattice can be performed with Mg^{2+}, Zn^{2+}, or Ag^+ [10,11]. Ionic substitution modifies the physico-chemical parameters of the hydroxyapatite, such as crystal morphology, degree of crystallinity, solubility and thermal stability, leading to various biological responses. Partial substitution, even in small quantities, leads to increased solubility and thermal stability of the hydroxyapatite lattice [11] and facilitates bone regenerative capacity, by promoting the cellular response. Silicon, magnesium and zinc increased bioactivity and implant integration and stimulated bone formation by facilitating the adhesion, proliferation and differentiation of osteoblasts [12]. Zinc substituted HAP and strontium substituted HAP were used in orthopaedic cement and it has been histologically shown that these materials were surrounded by bone tissue compared to poly methyl methacrylate, PMMA, which is encapsulated in fibrous tissue [13,14]. Collagen jointly with HAP have shown superior bioactivity and biocompatibility with better integration, reduced local reactions and earlier remodeling around the Ti rods, but they are rather fragile structures that can cause bone lysis [15].

The aim of the current study was to evaluate the biocompatibility and osseointegration of uncoated Ti nails [16-18] and coated Ti implants with biomimetic composite, in a rat model of femoral fracture. We selected this animal model [16] because most fractures occur in elderly patients with advanced osteoporosis of femur. Thus, we want to evaluate whether we can bring improvements in the osseointegration of Ti implants in the case of this population category at risk.

RESULTS AND DISCUSSION

Surface morphology of HAPc biocomposite coated Ti implants

FE-SEM image of grit-blasted and acid etched standard (control) Ti implant (Fig. 1A) and EDX spectrum of Ti implant shown in Fig. 1B, before and after coating by ms-HAP/COL@PLA/COL (Figs. 1C,D), which is made through LBL dip coating method on the surface of Ti implant.

As shown in Fig. 1C, the surface of the HAPc, ms-HAP/COL@PLA/COL, biocomposite is rather porous with the COL fibers on its surface. The surface of coated Ti implants was also characterized by EDX spectrum (Fig. 1D), which gives the surface chemical composition of coating on Ti implant corresponding practically to ms-HAP (i.e., HAP-1.5%Mg-0.2%Zn-0.2%Si) composition.

DANIEL OLTEAN-DAN, PETRE T. FRANGOPOL, REKA BALINT, GHEORGHE TOMOAIA, AURORA MOCANU, MARIA TOMOAIA-COTISEL

In the EDX spectrum, all constitutive elements: Ca, P, O, Mg, Zn and Si of ms-HAP are practically given. This finding indicates a homogeneous distribution of ms-HAP within HAPc biocomposite which contains also collagen and PLA.

In EDX spectrum, Au can be seen, which was used for enhancing FE-SEM imaging. The topography of outermost COL layer was visualized by AFM images showing the nanofibers of collagen on the surface of HAPc coating on Ti implants (not shown).
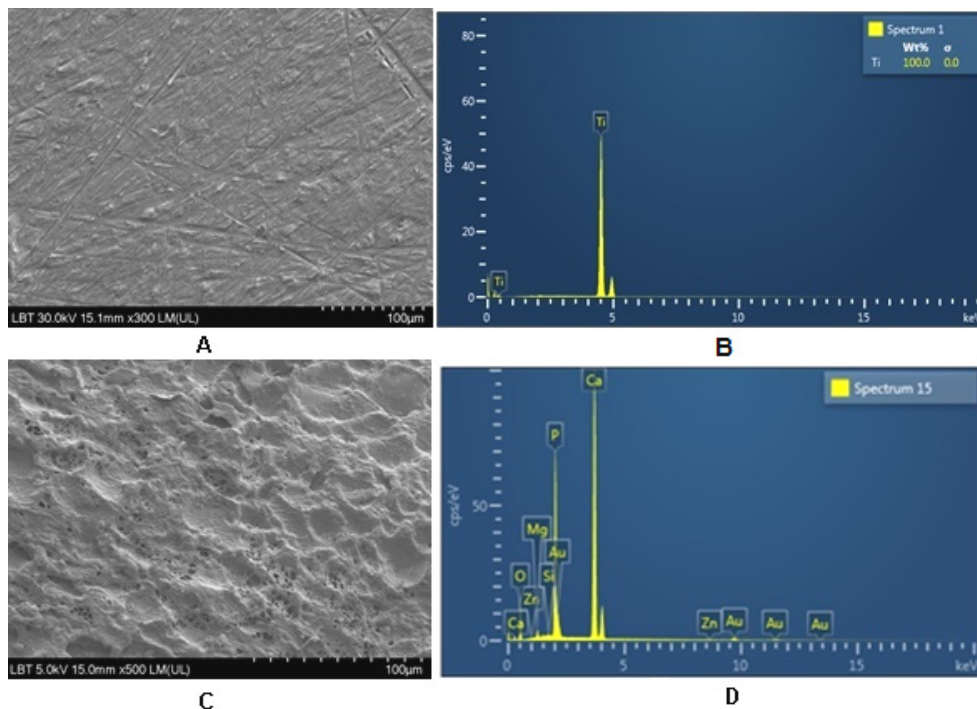
Figure 1. A) FE-SEM image on the surface microstructure of uncoated Ti rod (20 mm x diameter 1 mm) and its EDX spectrum in Fig. 1B, showing the highest purity of Ti rod, and after its coating with HAPc biocomposite, SEM image (Fig. 1C) and EDX spectrum (Fig. 1D), indicating a porous HAPc structure, multi doped with essential elements.

Bone markers: alkaline phosphatase and osteocalcin results

An increase in alkaline phosphatase (ALP) concentration (Fig. 2A) was observed in both groups at 2 weeks compared to initial values ($p < 0.0001$). The most significant increase was in the HAPc group (173%), compared to CG (152%), $p < 0.001$. At 8 weeks, ALP values decrease ($p < 0.0001$), with approximately equal or even lower bone serum concentrations, compared to the initial values (0 weeks).

The osteocalcin (OCN) values (Fig. 2B) increased substantially in both groups, compared to initial values, with the highest increase of 230% in the HAPc group. Furthermore, values in the control group, CG, at two weeks were significantly lower compared to the HAPc group ($p<0.0001$). Afterwards, at eight weeks, OCN expression decreased significantly, remaining with 31%-36% higher than the initial value ($p <0.05$).
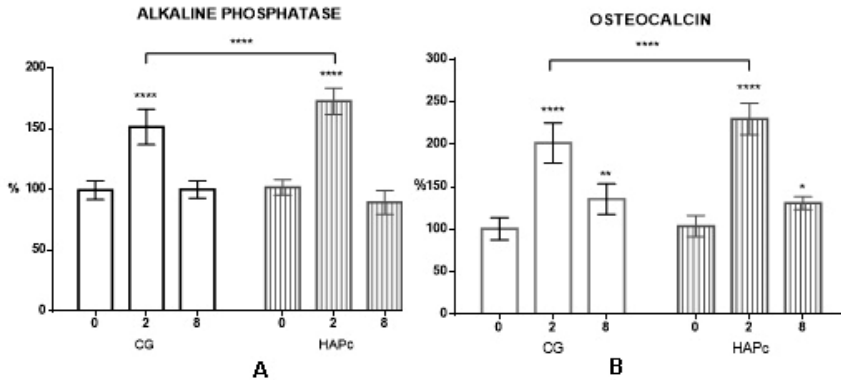
Figure 2. Bone markers, alkaline phosphatase (A) and osteocalcin (B), serum concentration at zero time (initially), two- and eight-weeks post-surgery; *statistically significant $p<0.05$; **statistically significant $p<0.01$; ***statistically significant $p<0.001$; ****statistically significant $p<0.0001$.

Table 1. Bone markers, alkaline phosphatase (ALP) and osteocalcin (OCN), serum concentration at initial (0 weeks), two- and eight-weeks post-operatively; *statistically significant $p<0.05$; **statistically significant $p<0.01$; ***statistically significant $p<0.001$; ****statistically significant $p<0.0001$.

Rat group		CG	HAPc
ALP (%)	0 weeks	100 ± 13	102 ±6
	2 weeks	152 ±14****	173 ± 10****
	8 weeks	100 ± 7	89 ± 8
OCN (%)	0 weeks	100 ± 15	104 ± 13
	2 weeks	202 ± 24****	230 ± 18****
	8 weeks	136 ± 18**	131 ± 8*

Micro-CT results

Table 2. Implant osseointegration assessed by micro-CT; bone volume per total tissue volume (BV/TV) and the mean trabecular number (Tb.N); $^{*}p < 0.05$: HAPc group vs CG.

Rat group	CG	HAPc
BV/TV(%)	25.5±4.3	38.8±5.4*
Tb.N (1/mm)	154±18	180±18*

DANIEL OLTEAN-DAN, PETRE T. FRANGOPOL, REKA BALINT, GHEORGHE TOMOAIA,
AURORA MOCANU, MARIA TOMOAIA-COTISEL

At eight weeks after implantation, the development of newly formed bone and the degree of osseointegration were evaluated by the formation of trabecular and cortical bone at the fracture site (Figs. 3A,B).

An *in vivo* evaluation of biocompatibility of the two different surfaces of uncoated Ti and coated HAPcTi implants is required for the understanding of the role of surface features and chemical composition of coatings on Ti implant surface in the osseointegration of implants and living host bone.

Histological results

The biocompatibility of uncoated and coated Ti implants and their osseointegration at the fracture level were assessed by using optical microscopy, on hematoxylin and eosin (H&E) stained tissue samples from each of the two studied animal groups, at eight-weeks postoperatively.
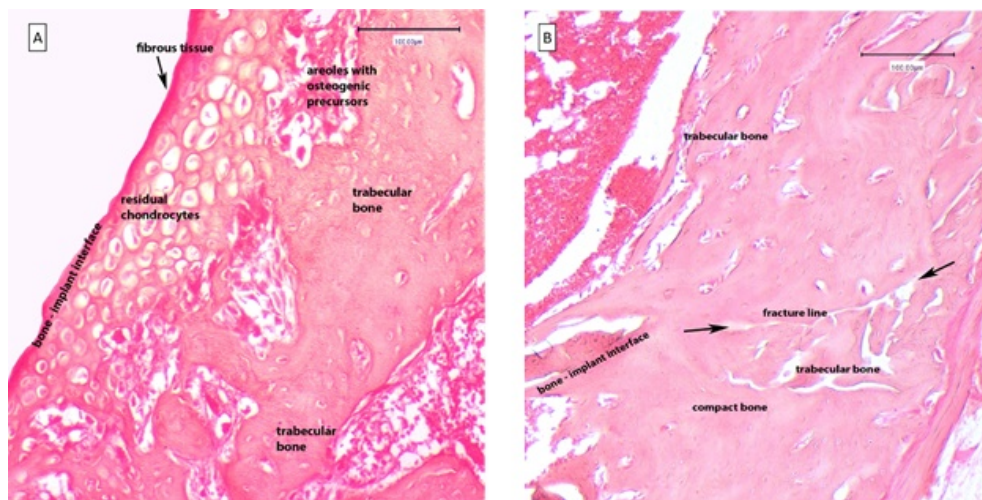
Figure 3. Optical microscopy images of H&E stained slides of tissue samples at bone-implant interface near the fracture site, at eight weeks after implantation. (A): control group revealed fibrous tissue in the proximity of Ti intramedullary implant and residual cartilaginous tissue, indicating a transition from cartilaginous precursors to incipient bone trabeculae formation. (B): HAPc group displayed around HAPcTi implants, the bone trabeculae well defined, compact bone with lamellar disposition of bone matrix, and osteocytes around Havers canals, with osteoblasts lining their surface, and clear delimitation of areole between the trabeculae, with areas of compact lamellar bone deposition.

Results Analysis

Fig. 1A shows the FE-SEM image of the uncoated Ti implant, which was grit-blasted and acid etched treated, having the highest purity (Fig. 1B). Fig. 1C displays the FE-SEM image and the surface structure of Ti implant coated with HAPc composite. The morphology of the composite coating, ms-HAP/COL@PLA/COL, illustrates that the surface of HAPc composite is porous, and NPs of ms-HAP/COL are well dispersed in PLA matrix. The EDX spectrum (Fig. 1D) unveils the presence of ms-HAP as HAP-1.5%Mg-0.2%Zn-0.2%Si homogeneously distributed within HAPc composite.

The alkaline phosphatase (Fig. 2A) and osteocalcin (Fig. 2B) play a vital role in bone mineralization being valuable biochemical markers in assessing newly bone formation. Osteoblasts, the bone-forming cells, express ALP on their surface, while ALP isoforms can be derived from bone or non-specific tissue. Osteocalcin is the most abundant non-collagenous bone protein [19].

In this work, an experimental investigation on an animal (rat) model was achieved using diaphyseal femoral fracture. To stabilize the fracture site, titanium intramedullary nails uncoated or coated with HAPc composite were introduced in a retrograde method. Afterwards, the rats were divided into two distinct groups of twelve rats each; namely group CG: the control group where uncoated titanium nails were implanted; HAPc group: where titanium nails coated with ms-HAP/COL@PLA/COL composite were implanted. Ionic substitution within the HAP lattice, specifically 1.5%Mg, 0.2%Zn and 0.2%Si, causes changes in its surface structure and, in terms of its electrical charge, increases the solubility and capacity of substituted HAP to participate in the natural process of bone remodeling, in substantial agreement with related materials [20].

The HAP/COL composites have been used in rabbits to demonstrate their ability to fulfil osteochondral defects, showing the formation of active bone tissue [21-23]. The HAP/COL composite was also used to cover the titanium nails placed subperiosteally at the level of the skull, which were completely surrounded by bone tissue, while more than 50% of the titanium rods coated with simple HAP were encapsulated in fibrous tissue [24]. In addition, collagen coating on titanium enhances the connection between titanium and newly formed bone and can be used in cases that require better osseointegration [25].

The use of titanium coated with calcined hydroxyapatite-collagen ensures both the mechanical stability and the rigidity of the fixation method, maintaining long-term osteoconductive properties [26]. In addition, substituted HAP continuously releases its ions, with specific effects in bone biochemistry and mineral homeostasis [27].

DANIEL OLTEAN-DAN, PETRE T. FRANGOPOL, REKA BALINT, GHEORGHE TOMOAIA,
AURORA MOCANU, MARIA TOMOAIA-COTISEL

Also, the use of titanium coated with type I collagen/chondroitin sulphate showed a better integration at the bone-implant interface in case of osteoporosis [28].

Poly lactic acid is a bioresorbable polyesters [29], but its clinical use is limited due to low hydrophilicity and difficulty in controlling the rate of hydrolysis [30]. Therefore, the use of HAP and PLA composites can reduce the rate of PLA degradation and strengthen the biomaterials [31]. Experimental studies [32-35] on bone tissue models have shown that these composites have an active role in bone formation, by facilitating ossification without producing inflammation [34].

Titanium surfaces coated with silicon [36], zinc [37] and magnesium [38] substituted hydroxyapatite enhance the bioactivity and promote osteogenic differentiation of preosteoblasts *in vitro*, which has a real potential to enhance implants osseointegration.

The ALP evolution in the HAPc group shows a faster growth compared to the control group until two weeks, after which the ALP activity decreases [39].

Our results revealed a significant increase of alkaline phosphatase in animals treated with HAPc coated titanium nails in the bone consolidation process with a 73% increase significantly over the initial values. Moreover, *in vitro* studies, used to examine the osteoblastic differentiation of cells cultured on days 7, 14 and 21, showed the maximum ALP activities at 14 days of culture and decreased thereafter in all groups and samples. This is a typical dynamic of the ALP activity, characteristic of early osteoblastic differentiation [40]. ALP increases the local concentration of phosphate ions and the deposition of calcium salts. Moreover, osteoblasts actively secreted bone matrix and released large amounts of alkaline phosphatase. This activity is correlated with the formation of new bone [41].

Hydroxyapatite and especially multi-substituted hydroxyapatite create a microclimate favourable to cellular recruitment, and due to its osteoconductive capacity, stimulates the activity of osteoblasts and facilitates bone strengthening, demonstrated by a higher activity of ALP. Subsequently, after 2nd to 8th week, ALP activity reverted to approximately the initial values. The ALP values at eight weeks were significantly lower than initial values (at 0 weeks) in groups where titanium intramedullary nails coated with multi-substituted hydroxyapatite were used. The marked decrease in ALP activity indicates an increase in fracture focal stability and a more advance stage of bone consolidation, which is more evident in these groups.

Osteocalcin has been shown to be a more specific marker in changes in bone metabolism than alkaline phosphatase, being a late marker of bone formation [42]. Alkaline phosphatase, although less specific, is an effective marker in increased bone turnover in fracture healing, but its elevated levels are maintained for a lower period of time than osteocalcin. According ALP activity at 2 weeks, the OCN values increased significantly

in both groups compared to initial values with the highest increase in the HAPc group. Furthermore, values in the control group at two weeks were significantly lower compared to the HAPc group. At eight weeks, OCN expression decreased significantly in all groups compared to values at two weeks, with 31%-36% higher than initial values with statistical differences for all groups ($p<0.05$).

Normally, levels of OCN changes are evident in the final stages of osteogenic differentiation, when this protein is secreted by osteoblasts. Osteocalcin activates both osteoblasts and osteoclasts during early bone formation and causes an earlier onset of bone remodelling process. This has been demonstrated *in vitro* and *in vivo* studies on Wistar albino rats in which cylindrical nanocrystalline hydroxyapatite/collagen implants have been implanted in the tibia by accelerating bone formation and regeneration [43].

Consequently, in terms of the dynamics of ALP activity and OCN expression, in the groups treated with multi-substituted hydroxyapatite-collagen-PLA coated titanium intramedullary nails, the values are higher, with osteoblastic activity more intense and bigger callus. Considering that alkaline phosphatase is an early bone formation marker, at eight weeks its activity diminished, when the fracture is stabilized by the newly formed trabecular bone. On the other hand, OCN as a late bone formation marker, its values remained higher even after eight weeks.

Micro-CT assessments and histological evaluations were employed to investigate the osseointegration and bone formation around the implants and the host bone around them. Bone volume relative to total tissue volume (BV/TV) and trabecular number (Table 2) provide the changes, regarding the bone neo-formation between the intramedullary nail and the host bone around it [44].

Furthermore, hematoxylin and eosin stains showed the changes in the activity of cells and tissues and in the degree of mineralization at the bone-implants interface. Regarding the quantitative results of implant osseointegration assessed by micro-CT, coating composed of ms-HAP/COL@PLA/COL composite produced anabolic effect on bone around the implant, with significantly increased of BV/TV and Tb.N compared to control group. In the case of ovariectomized rats, good results have been demonstrated regarding osteointegration, in the case of strontium hydroxyapatite coatings [45].

H&E colored slides analysis, at eight weeks post fracture, revealed bone remodeling processes at fracture site and displayed major differences between the investigated groups. In control group (Fig. 3A), there was an intense eosinophilic band representing fibrous tissue at bone-implant interface, which indicates a lower osseointegration capacity of titanium nails in this group, while HAPc group implants (Fig. 3B) revealed a better osseointegration.

DANIEL OLTEAN-DAN, PETRE T. FRANGOPOL, REKA BALINT, GHEORGHE TOMOAIA,
AURORA MOCANU, MARIA TOMOAIA-COTISEL

The novelty of our study is the use of a new biomimetic composite, consisting of multi-substituted hydroxyapatite with silicon, magnesium and zinc, NPs covered with collagen and jointly incorporated in a poly lactic matrix in a unilateral femoral fracture rat model. We also evaluated the effect of those coatings at different time points (0 weeks, 2 weeks and 8 weeks post-surgery) during the bone consolidation and osseointegration process. In all the cases, we used biocomposite coatings and we didn't encounter any case with inflammation signs.

Our results showed that more bone was formed during the first two weeks in the fracture focal point, especially in the rats treated with HAPc coating. Regarding the bone implant contact in the metaphyseal region, the coating based on multi-substituted hydroxyapatite showed better results compared to the control group at 8 weeks postoperatively. Micro-CT and histological changes revealed that HAPc coating of the conventional titanium nails enhances bone healing and osseointegration of the intramedullary implants, as well. In clinical situation, these findings can play an important role by diminishing the risk of cut-outs of the implant and also in the prevention of the implant loosening.

The HAPc coating, comprising Mg-Zn-Si-HAP and COL in PLA matrix, is enriched in Mg and is self-assembled on Ti implants. This HAPc coating can induce *in vivo* early formation of a bone-to-implant interface in good agreement with recent studies on related materials [46-52], including the bone sites with osteoporosis, making this surface treatment of the highest osteogenic potential, due to the release of Mg, Zn, and Si *in vivo*.

CONCLUSIONS

Titanium intramedullary nails coated with multi-substituted hydroxyapatite and collagen in a poly lactic acid matrix enhance bone healing and also increase implant osseointegration by improving the bone microstructure around the implant. In the case of clinical applications, these implants may decrease the risk of implant loosening.

EXPERIMENTAL SECTION

Materials, sample preparation and characterization

Rods of Ti (99.6% purity) were purchased from Goodfellow Cambridge Limited, Huntingdon, England. The Ti implants were prepared, as follows: the surface of Ti rods (20 mm x diameter 1 mm) was firstly improved by grit-blasting with P500, and cleaned by ultrasonication process using a ultrasonic processor Sonics Vibra-Cell, model VCX 750 (Sonics & Material Inc., Newtown,

CT, USA) in deionized water at room temperature for 2 hrs. Subsequently, the Ti rods were chemically activated by acid etching with 50 wt % phosphoric acid solution, for 10 min, and sterilized through ethylene oxide procedure leading to standard Ti implants, noted Ti implants, of controlled surface roughness. Then, Ti implants were further coated by HAPc composite, deposited on Ti rods through layer-by-layer, LBL, method resulting HAPc Ti coated implants. The HAPc composite comprises multi-substituted hydroxyapatite, ms-HAP: HAP-1.5%Mg-0.2%Zn-0.2%Si, nanoparticles (NPs) covered by collagen, COL, namely ms-HAP/6%COL (core/shell NPs), incorporated into poly lactic acid, PLA, matrix (ms-HAP/COL@PLA) and finally covered by COL layer (ms-HAP/COL@PLA/COL), which was deposited on Ti surface through self-assemblies (LBL) method.

Characterization of HAPc composite coatings on Ti implants was carried out by field emission scanning electron microscope (FE-SEM), Hitachi SU-8230, to explore the structure of composite surface. FE-SEM was equipped with Oxford energy-dispersive X-ray spectrometer for elemental analysis (energy-dispersive X-ray, EDX, spectra). Therefore, FE-SEM and EDX were used for surface morphology and elemental analysis of coated Ti implants.

Study protocol

The research was carried out in accordance with the principles of the Basel Declaration and recommendation of ARRIVE guidelines. The animal research protocol was approved by Veterinary Sanitary Committee of Cluj County, Romania (Approval No. 85/19.07.2017) and Ethics Committee of "Iuliu Hatieganu" University of Medicine and Pharmacy, Cluj-Napoca.

In the present study, Wistar albino rats (N=24) were used, and divided in two equal groups (N=12/group): CG control group, with uncoated Ti implants and HAPc group with Ti implants coated with HAPc coating, noted HAPcTi implants.

Surgical procedures

The rats were two months old, weighing 218 ± 11 g. They were anesthetized with an intramuscular cocktail of 2% xylazine and 10% ketamine. The surgeries were performed by a team of two orthopedic surgeons. After the establishment of the surgical asepsis through a lateral approach of the thigh, a transverse fracture of the femoral diaphysis was performed.

By a longitudinal incision at the knee level, uncoated Ti implants (CG, N=12) and coated with HAPc: ms-HAP/COL@PLA/COL (HAPc group, N=12) were introduced in the left femur. At the end, the subcutaneous plane and the tegument were sutured. Postoperatively, the animals were kept in cages, in a controlled environment with a day/night cycle of 12h, without food restrictions, at a temperature of 22°C.

DANIEL OLTEAN-DAN, PETRE T. FRANGOPOL, REKA BALINT, GHEORGHE TOMOAIA,
AURORA MOCANU, MARIA TOMOAIA-COTISEL

Animal euthanasia was performed by overdose of anesthetic at 2 weeks (N = 12, N = 6/group) and at 8 weeks (N=12, N = 6/group), and the left femoral bone was carefully taken, by push-out method, not to destroy bone callus and placed in 10% formaldehyde.

Alkaline phosphatase and osteocalcin

Bone formation markers, osteocalcin (OCN) and alkaline phosphatase (ALP), were evaluated using the non-specific ELISA kit ER1205, Rat OC / BGP (Osteocalcin), commercially available (Wuhan Fine Biological Technology Co) and OSR6504 reagent (alkaline phosphatase), for use on the AU 680 system (Beckman Coulter, USA). Around 0.6 mL of blood was harvested from each rat, at the beginning of the experiment (N=24), at two weeks (N=24) and at 8 weeks (N=12).

Micro-CT

Multilevel threshold was applied to discriminate the bone and calcified cartilage, dense cortical bone and un-mineralized tissue. At the time of sacrifice, the left femoral bone with implants (N=12/group) were scanned using Bruker micro-CT system SkyScan 1172 (Kontich, Belgium). The volume of interest (VOI) was established at 2 mm below the growth plate, with a height of 1 mm and a ring of 1.5 mm diameter around the implant. Afterwards, the bone volume percent (BV/TV) and the mean trabecular number (Tb.N) were assessed within the volume of interest.

Histological assessment

The biocompatibility of uncoated and coated Ti implants and their osseointegration at the fracture level was assessed by using optical microscopy, on hematoxylin and eosin (H&E) stained tissue samples from each of the two studied animal groups, at two- and eight-weeks postoperatively. After harvesting, the rat femurs were fixed in 4% paraformaldehyde solution for the first 24 hrs. Then, 5% nitric acid solution, continuously shacked and changed daily for 10 days, was used in order to get the decalcification of bone samples. Samples were then dehydrated in increasing degrees of alcohol (50%, 75%, 100%), cleared in xylene (for alcohol removal) and embedded in paraffin. Afterwards, the cross sections of 5µm thickness attached on glass slide were deparaffinised, rehydrated and then stained with H&E. The slides were photographed by using a Leica DMD 120 microscope. At two weeks after implantation, the *inflammatory response* was not identified. At eight weeks postoperative, the formation of newly formed bone and the degree of osseointegration were assessed by the formation of trabecular and cortical bone at fracture site [17,18].

Statistical analysis

For statistical analysis GraphPad Prism 6 for Windows was used. Values of bone markers concentration were converted to percentages and were defined as the mean value ± standard deviation (SD). Statistical significance was identified using one-way ANOVA test followed by Tukey post-hoc test.

ACKNOWLEDGMENTS

REFERENCES

1. A. F. Mavrogenis; R. Dimitriou; J. Parvizi; G. C. Babis; *J. Musculoskelet. Neuronal Interact.,* **2009**, *9(2)*, 61-71.
2. P. I. Branemark; *Scand. J. Clin. Lab. Invest*., **1959**, *11*(Suppl. 38), 1-82.
3. P. I. Branemark; *J. Prosthet. Dent*., **1983**, *50(3)*, 399-410.
4. B. M. Isaacson; S. Jeyapalina; *Orthop. Res. Rev*., **2014**, *6*, 55-65.
5. R. D. Bloebaum; K. N. Bachus; N. G. Momberger; A. A. Hofmann; *J. Biomed. Mater. Res.,* **1994**, *28(5),* 537–544.
6. R. Depprich; H. Zipprich; M. Ommerborn; C. Naujoks; H. P. Wiesmann; S. Kiattavorncharoen; H. C. Lauer; U. Meyer; N. R. Kubler; J. Handschel; *Head Face Med*., **2008**, *4*, 30. DOI: 10.1186/1746-160X-4-30.
7. P. Thomsen; C. Larsson; L. E. Ericson; L. Sennerby; J. Lausmaa; B. Kasemo; *J. Mater. Sci. Mater. Med*., **1997**, *8*(*11*), 653–665.
8. A. B. Novaes Jr; S. L. Scombatti de Souza; R. R. Martins de Barros; K. K. Y. Pereira; G. Iezzi; A. Piattelli; *Braz. Dent. J*., **2010**, *21*(*6*), 471–481.
9. W. Wang; C. K. Poh; Titanium Alloys in Orthopaedics. In *Titanium Alloys - Advances in Properties Control*, J. Sieniawski, W. Ziaja Eds.; Intech Open; London, UK, **2013**, chapter 1, pp. 1-20.
10. A. Mocanu; G. Furtos; S. Rapuntean; O. Horovitz; C. Flore; C. Garbo; A. Danisteanu; G. Rapuntean; C. Prejmerean; M. Tomoaia-Cotisel; *Appl. Surf. Sci*., **2014**, *298*, 225-235.
11. F. Goga; E. Forizs; A. Avram; A. Rotaru; A. Lucian; I. Petean; A. Mocanu; M. Tomoaia-Cotisel; *Rev. Chim. (Bucharest)*, **2017**, *68*(6), 1193-1200.
12. J. T. B. Ratnayake; M. Mucalo; G. J. Dias; *J. Biomed. Mater. Res. B Appl. Biomater*., **2017**, *105(5)*, 1285–1299.
13. D. Shepherd; S. M. Best; *Biomed. Mater*., **2013**, *8(2)*, 025003. DOI: 10.1088/1748-6041/8/2/025003

14. N. Kourkoumelis; *Ann. Transl. Med.*, **2016**, *4*(Suppl. 1), S10. doi: 10.21037/atm.2016.10.03

15. H. C. Wu; T. W. Wang; J. S. Sun; Y. H. Lee; M. H. Shen; Z. R. Tsai; C. Y. Chen; H. C. Hsu; *Materials (Basel)*, **2016**, *9(3)*, 198. DOI: 10.3390/ma9030198

16. D. Oltean-Dan; G. B. Dogaru; M. Tomoaia-Cotisel; D. Apostu; A. Mester; H. R. Benea; M. G. Paiusan; E. M. Jianu; A. Mocanu; R. Balint; C. O. Popa; C. Berce; G. I. Bodizs; A. M. Toader; Gh. Tomoaia; *Int. J. Nanomed.*, **2019**, *14*, 5799-5816.

17. R. Marsell; T. A. Einhorn; *Injury*, **2011**, *42*(*6*), 551-555.

18. A. Schindeler; M. M. McDonald; P. Bokko; D. G. Little; *Semin. Cell. Dev. Biol.*, **2008**, *19*(5), 459-466.

19. Y. T. Tsao; Y. J. Huang; H. H. Wu; Y. A. Liu; Y. S. Liu; O. K. Lee; *Int. J. Mol. Sci.*, **2017**, *18*(*1*), 159. DOI: 10.3390/ijms18010159.

20. D. M. Ibrahim; A. A. Mostafa; S. I. Korowash; *Chem. Cent. J.*, **2011**, *5*(*1*), 74. doi: 10.1186/1752-153X-5-74

21. F. G. Lyons; J. P. Gleeson; S. Partap; K. Coghlan; F. J. O'Brien; *Clin. Orthop. Relat. Res.*, **2014**, *472*(*4*), 1318-1328.

22. F. Yu; M. Li; Z. Yuan; F. Rao; X. Fang; B. Jiang; Y. Wen; P. Zhang; *Int. J. Nanomed.*, **2018**, *13*, 7845-7858.

23. A. Tsuchiya; S. Sotome; Y. Asou; M. Kikuchi; Y. Koyama; T. Ogawa; J. Tanaka; K. Shinomiya; *J. Med. Dent. Sci.*, **2008**, *55*(*1*), 91-99.

24. M. Uezono; K. Takakuda; M. Kikuchi; S. Suzuki; K. Moriyama; *J. Biomed. Mater. Res. B Appl. Biomater.*, **2013**, *101B*(*6*), 1031-1038.

25. A. Murakami; T. Arimoto; D. Suzuki; M. Iwai-Yoshida; F. Otsuka; Y. Shibata; T. Igarashi; R. Kamijo; T. Miyazaki; *Nanomedicine*, **2012**, *8*(*3*), 374-382.

26. G. G. Walmsley; A. McArdle; R. Tevlin; A. Momeni; D. Atashroo; M. S. Hu; A. H. Feroze; V. W. Wong; P. H. Lorenz; M. T. Longaker; D. C. Wan; *Nanomedicine,* **2015**, *11*(*5*), 1253–1263.

27. D. Govindaraj; M. Rajan; M. A. Munusamy; A. A. Alarfaj; K. K. Sadasivuni; S. S. Kumar; *Nanomedicine*, **2017**, *13*(*8*), 2661-2669.

28. L. Kyllönen; M. D'Este; M. Alini; D. Eglin; *Acta Biomater.*, **2015**, *11*, 412-434.

29. J. Li; X. L. Lu; Y. F. Zheng; *Appl. Surf. Sci.*, **2008**, *255*(*2*), 494-497.

30. W. Yang; G. Yin; D. Zhou; J. Gu; Y. Li; H. Zhang; *J. Mater. Sci. Technol.*, **2010**, *26*(*8*), 754-758.

31. P. Vashisth; J. R. Bellare; *Nanomedicine*, **2018**, *14*(*4*), 1325-1336.

32. Gh. Tomoaia; L. B. Pop; I. Petean; M. Tomoaia-Cotisel; *Mater. Plast.*, **2012**, *49*(*1*), 48-54.

33. Y. Shapovalova; D. Lytkina; L. Rasskazova; A. Gudima; V. Ryabov; A. Filimoshkin; I. Kurzina; J. Kzhyshkowska; *Eur. J. Cancer. Suppl.*, **2015**, *13*(*1*), 49-50.

34. P. Kubasiewicz-Ross; J. Hadzik; J. Seeliger; K. Kozak; K. Jurczyszyn; H. Gerber; M. Dominiak; C. Kunert-Keil; *Ann. Anat.*, **2017**, *213*, 83-90.

35. Gh. Tomoaia; M. Tomoaia-Cotisel; A. Mocanu; O. Horovitz; L. D. Bobos; M. Crisan; I. Petean; *J. Optoelectron. Adv. Mater.*, **2008**, *10*(*4*), 961-964.

36. M. Honda; K. Kikushima; Y. Kawanobe; T. Konishi; M. Mizumoto; M. Aizawa; *J. Mater. Sci. Mater. Med.*, **2012**, *23*(*12*), 2923–2932.
37. F. Yang; W. J. Dong; F. M. He; X. X. Wang; S. F. Zhao; G. L. Yang; *Oral Surg. Oral Med. Oral Pathol. Oral Radiol.,* **2012**, *113*(*3*), 313-318.
38. S. F. Zhao; Q. H. Jiang; S. Peel; X. X. Wang; F. M. He; *Clin. Oral Implants Res.*, **2013**, *24*(Suppl. A100), 34–41. doi.org/10.1111/j.1600-0501.2011.02362.x
39. R. Marom; I. Shur; R. Solomon; D. Benayahu; *J. Cell. Physiol*., **2005**, *202*(*1*), 41-48.
40. D. H. Yang; D. W. Lee; Y. D. Kwon; H. J. Kim; H. J. Chun; J. W. Jang; G. Khang; *J. Tissue Eng. Regen. Med*., **2015**, *9*(*9*), 1067-1077.
41. I. Manjubala; M. Sivakumar; R. V. Sureshkumar; T. P. Sastry; *J. Biomed. Mater. Res*., **2002**, *63*(*2*), 200-208.
42. S. Shetty; N. Kapoor; J. D. Bondu; N. Thomas; T. V. Paul; *Indian J. Endocrinol. Metab*., **2016**, *20*(*6*), 846-852.
43. S. Rammelt; M. Neumann; U. Hanisch; A. Reinstorf; W. Pompe; H. Zwipp; A. Biewener; *J. Biomed. Mater. Res. A*, **2005**, *73*(*3*)*,* 284-294.
44. J. Y. C. Choi; C. A. Choi; I. S. L. Yeo; *J. Periodontal Implant Sci*., **2018**, *48*(*4*), 202-212.
45. Z. S. Tao; B. L. Bai; X. W. He; W. Liu; H. Li; Q. Zhou; T. Sun; Z. L. Huang; K. K. Tu; Y. X. LV; W. Cui; L. Yang; *Med. Biol. Eng. Comput*., **2016**, *54*(*12*), 1959-1968.
46. Y. Liang; H. Li; J. Xu; X. Li; M. Qi; M. Hu; *Int. J. Mol. Sci*., **2014**, *15*(*6*), 9952–9962.
47. S. Galli; M. Stocchero; M. Andersson; J. Karlsson; W. He; T. Lilin; A. Wennerberg; R. Jimbo; *Osteoporos. Int*., **2017**, *28*(*7*), 2195–2205.
48. S. Rapuntean; P.T. Frangopol; I. Hodisan; Gh. Tomoaia; D. Oltean-Dan; A. Mocanu; C. Prejmerean; O. Soritau; L.Z. Racz; M. Tomoaia-Cotisel; *Rev Chim (Bucharest),* **2018**, *69*(*12*), 3537-3544.
49. C. Garbo; J. Locs; M. D'Este; G. Demazeau; A. Mocanu; C. Roman; O. Horovitz; M. Tomoaia-Cotisel; *Int. J. Nanomed*., **2020**, *15*, 1037-1058.
50. P. T. Frangopol; A. Mocanu; V. Almasan; C. Garbo; R. Balint; G. Borodi; I. Bratu; O. Horovitz; M. Tomoaia-Cotisel; *Rev. Roum. Chim.,* **2016**, *61*(*4-5*), 337-344.
51. A. Mocanu; O. Cadar; P. T. Frangopol; I. Petean; Gh. Tomoaia; G. A. Paltinean; Cs. P. Racz; O. Horovitz; M. Tomoaia-Cotisel; *R. Soc. Open. Sci*., **2021**, *8*(*1*), 201785.
52. J. Y. Wang; Y. C. Liu; G. S. Lin; H. H. Chang; Y. T. Li; Y. C. Yang; H. Matsuyama; B. S. Lee; Y. W. Chen; K. L. Tung; *Surf. Coat. Technol*., **2020**, *386*, 125452.

NATURAL POLYPHENOLS AS COMPOUNDS WITH BIOLOGICAL ACTIVITY[*]

VALENTIN I. POPA[a]

ABSTRACT. Plants produce thousands of phenolic and polyphenolic compounds as secondary metabolites. They are essential to the physiology of plants being involved in diverse functions such as lignification and structure, pigmentation, pollination, allelopathy, pathogen and predator resistance and growth. Approximately 8000 have been described to date, major classes being flavonoids, flavones, flavan-3ols, flavanones and anthocyanins. They can be isolated from biomass waste and cultivated and spontaneous plants by biorefining and used for their biological properties in different fields. In this paper some examples of uses such as: modulation agents of carbohydrates metabolism in diabetes and alcoholic fermentation, agents for regulation of physiological process in plants (germination, plant propagation and cultivation, tissue culture, bioremediation), modulation agents of metabolic processes in microorganisms (antifungal and antibacterial properties, antioxidants), models to study the influence of stress factors (hydrogen peroxide oxidation and UV irradiation and life span regulation), and carbon sources as substrates in medium cultivation of microorganisms, are presented.

Keywords: *polyphenols, sources, isolation and characterization, biological properties*

INTRODUCTION

Phenolic compounds posses an aromatic ring bearing one or more hydroxyl groups and their structures may range from that of a simple phenolic molecule to that of a complex high-molecular mass polymer. These compounds, one of the most widely occurring groups of phytochemicals, are of considerable physiological and morphological importance in plants. There are more than

---

[*] *This paper is dedicated to Professor Petre T. Frangopol, Honorary Member of the Romanian Academy, to remind us of the esteem in which this man is known for the fate of education and research in Romania.*
[a] *Technical University of Iasi, Faculty of Chemical Engineering and Environmental Protection, Bulevardul Profesor Dimitrie Mangeron 73, Iași 700050, Iasi, Romania, vipopa@tuiasi.ro*

8000 polyphenolic compounds identified, from which 4000 are flavonoids. For the polyphenols, the following properties were identified: antioxidant, prooxidant, anticancer agents, apoptosis-inducing, antibacterial, antiparasite, anti-HIV activities, amelioration of cardiovascular diseases, improvement of endothelial function, modulation of gamma-glutamylcysteine synthetase expression, improvement of health and survival on high fat diet, coloring agents, chelating agents, modulators of plant development. In the plants the phenolics may act as phytoalexins, antifeedants, attractants for pollinators, contributors to plant pigmentation, antioxidants and protective agents against UV light, amongst others. These bioactive properties made these compounds play an important role in plant growth and reproduction, providing an efficient protection against pathogens and predators, besides contributing to the colour and sensory characteristics of fruits and vegetables. In particular, natural phenols have been reported to have in particular, excellent properties as food preservatives as well as having an important role in the protection against a number of pathological disturbances, such as atherosclerosis, brain dysfunction and cancer. Many plant extracts and phytochemicals have been shown to have free radical scavenging properties, being known as antioxidants [1].

Interestingly, Denham Harman proposed *The free radical theory of aging* published in 1956 [2]. He proposed that free oxygen radicals produced in the body cause aging, and further stated that "reducing compounds" (what we would now call "antioxidants") might represent a "chemical means of prolonging effective life" and that these molecules "might be of benefit in the field of cancer chemotherapy and nutrition". At present, there is a lot of information regarding the role of natural compounds, such as polyphenols, which are tested *in vitro* and *in vivo* (animal, human, vegetable systems or microorganisms) to demonstrate their antioxidant properties [3].

The separation of polyphenols is carried out using an innovative technology proposed by us [4,5]. This technology allows separating the secondary and the main compounds of biomass, which can be used in different fields due to their biological activities [6,7].

This paper presents the results obtained in the separation of polyphenols from different sources and some examples to use them for their biological activities.

RESULTS AND DISCUSSION

Biological properties of polyphenols

Concerning polyphenols, in our research programs, the following directions have been undertaken: modulation agents of carbohydrates metabolism in diabetes and alcoholic fermentation, agents for regulation of

physiological process in plants (germination, plant propagation and cultivation, tissue culture, bioremediation), modulation agents of metabolic processes in microorganisms (antifungal and antibacterial properties, antioxidants), models to study the influence of stress factors (hydrogen peroxide oxidation and UV irradiation and life span regulation), and carbon sources as substrates in medium cultivation of microorganisms [8-26]. Polyphenols are large, complex molecules found almost exclusively in plant products. These molecules possess unique chemical characteristics, including the ability to powerfully scavenge reactive oxygen and nitrogen species, blocking oxidative damage that leads to inflammation and biological aging of tissue. Reactive oxygen species (ROS) and reactive nitrogen species (RNS), such as hydroxyl radical ($\cdot$OH), hydrogen peroxide (H_2O_2), superoxide ($O_2\cdot-$), nitric oxide (NO$\cdot$), peroxynitrite (ONOO-) and others are major sources of oxidative stress in cells, damaging proteins, lipids, and DNA. Oxidative DNA damage has been identified as a cause of cancer, aging and neurodegenerative diseases, such as Alzheimer's and Parkinson's, cardiovascular diseases, such as arteriosclerosis, and is the primary cause of cell death and tissue damage resulting from heart attack and stroke. Therefore, the prevention of oxidative stress caused by ROS and RNS has important implications for the prevention and treatment of diseases. LDL oxidation and platelet activation are two key events in atherogenesis, which lead to the formation of atherosclerotic lesion. These processes are interrelated, in that oxidized LDL can activate platelets, and activated platelets increase the susceptibility of LDL to oxidation. Atherosclerosis is associated with endothelial dysfunction, platelet activation, lipoprotein aggregation, macrophage foam cell formation, inflammation and thrombosis. These events are closely related and interact among themselves, finally leading to the formation of atherosclerotic lesions. Atherosclerosis involves both LDL oxidation and platelet formation and both processes can affect each other. Platelet activation is increased by oxidative stress, and oxidized LDL, in turn, was shown to enhance platelet activation. Activated platelets in turn can increase LDL oxidizability [27] any means of intervention that favorably affects the balance between the activity of the macrophage oxygenases and cellular antioxidants, as well as the elevation of LDL associated antioxidants or extrinsic antioxidants in plasma or extracellular space, can possibly contribute to the inhibition of the atherosclerotic process. Strategies to reduce LDL oxidation thus involve the use of various antioxidants, which synergistically act on the cells and/or on the LDL molecules. In very simple terms, flavonoids inhibit the oxidation of polyunsaturated fatty acid groups in LDL by intercepting the free radical propagation of LDL oxidation. However, polyphenols are more than just free radical scavengers. Depending on their specific type and source, they also potently modulate gene expression. It means that polyphenols with unique characteristics can be chosen to address specific disease processes [28].

The common yeast *Saccharomyces cerevisiae* is often used in laboratory experiments as a model for understanding the biology of higher organisms due to the great similarity of basic life processes. The yeast is ideal in detecting cancerous chemicals, because its DNA-damage response system is remarkably similar to human cells. It can also be used to detect other types of damage, such as oxidative stress with a high degree of accuracy. Furthermore, the yeast cultures increased the expression of sirtuins, molecules known to trigger calorie restriction-like effects in multiple tissues, contributing to longevity. When polyphenols were added to yeast cell cultures, it was found that the treated cultures lived an average of 2-3 generations longer than the control cultures. Sirtuins are involved in a wide range of cellular processes, such as aging, transcription, apoptosis, inflammation and stress resistance, as well as energy efficiency and alertness during low-calorie situations. Sirtuins can also control circadian clocks and mitochondrial biogenesis. When yeast cultures were treated with polyphenols from grape seeds and spruce wood bark, it was observed that the treatment enhanced the cells' resistance to oxidative stress, both by inhibiting the production of harmful reactive oxygen species and by ramping up gene expression of vital natural cellular antioxidant systems. Thus, it was observed that polyphenols protect the yeast cell against hydrogen peroxide and UV irradiation and they can be used to inhibit cancer development. Grape seeds are also appreciated due to their content of phenolic compounds, such as gallic acid, catechin and epicatechin, and a wide variety of procyanidins (mainly condensed tannin). Their biological activities include: antioxidant properties and radioprotective effects, prevention of cataract, antihyperglycemic effects, enhancement of postprandial lipemia, modulation of the expression of antioxidant enzyme systems, improvement of insulin sensitivity and prevention of hypertriglyceridemia, inhibition of aromatase and suppression of aromatase expression, inhibition of protein kinase activity of epidermal growth factor receptor, protective effects against oxidative damage in mouse brain cells and anti-inflammatory effects. Oxidative stress is a condition arising from an imbalance between oxidant and antioxidants, leading to excess production of ROS. ROS are natural by-products of mithocondrial electron-transport chain reactions. The mithocondria are the "power plant" of the cell, generating chemical energy by producing adenosine triphosphate (ATP), the body's "energy currency" [29].

When polyphenols are used as agents for regulation of physiological process in plants (germination, plant propagation and cultivation, tissue culture, bioremediation), they could have similar effects with auxine and citokinine, and their action is synergetic with that of the hormones biosynthesized by plants. Polyphenolic extracts exhibited antibacterial properties against *Staphylococcus aureus*, *Escherichia coli* and *Pseudomonas aeruginosa*.

The antimicrobial activity of the extracts against the tested microorganisms might be related to the presence of phenolic acids, such as gallic, protocatechuic, 3-hydroxybenzoic, chlorogenic acids and flavonoids, in the extracts [10]. Electrospun poly(2-hydroxyethyl methacrylate) (pHEMA) fibers, loaded with synthetic and natural antioxidants in the form of selected types of polyphenols, such as vanillic, gallic, syringic acids, catechin or natural spruce bark extract, were investigated with regard to their release behavior in terms of antioxidant activities [21,30]. At the same time it was developed poly(L-lactide-co-glycolide) (PLGA) bicomponent fibers, loaded with selected amounts of the catechin as natural polyphenolic antioxidant. The activity of the released catechin was assessed regarding its influence on multi-walled carbon nanotube (MWCNT) induced formation of reactive oxygen species (ROS) in the human alveolar epithelial cell line A549. As a proof of the concept, the activity of the released catechin in A549 cells stimulated with MWCNTs was determined, revealing a high reduction of ROS production in a dose dependent manner.

CONCLUSIONS

Polyphenolic compounds, along with other bioactive compounds, can be obtained from secondary resources or from cultivated plants using biorefining. There are numerous polyphenols with different structures and compositions, depending on the raw material and the techniques used for their extraction. Polyphenols are characterized by many interesting properties (antioxidant, antifungal and antibacterial, preventing and inhibiting agents of cancer, protection agents of the vascular system), which recommend their utilization in different biological systems. The biological properties of polyphenols have been demonstrated using different model systems: plant, animal and human cells and microorganisms. Polyphenols can be immobilized by electrospinning or included in different supports to be used in biological systems.

EXPERIMENTAL

Isolation and characterization of polyphenols

The separation of polyphenols can be carried out using a technology of biorefining that was previously proposed by us [4,5] some years ago. This innovative technology illustrated in Figure 1 allows separating the secondary and the main compounds of biomass, which can be further used in different fields due to their biological activities [6,7].

In our studies, for isolating polyphenols, we used wastes resulting from different industrial processes, as well as spontaneous and cultivated plants, as raw materials. Some of the raw materials we used are described below.

Spruce bark (*Picea abies*) is an abundant byproduct resulting from the wood processing industry. Spruce and pine barks are known by their rich content of proanthocyanidins and they have been used in folk medicine and as a dietary supplement.
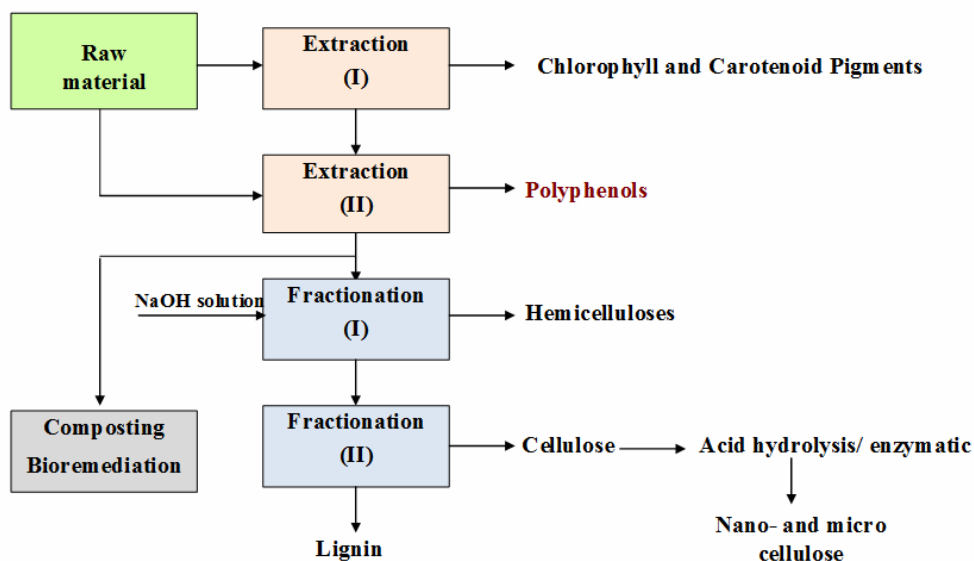

Figure 1. Separation of compounds with biological properties from biomass by biorefining

Grape seeds represent a considerable proportion of pomace, amounting to 40-50% on a dry matter. In recent years, naturally occurring plant phenolics in grape by-products have drawn a lot of interest, considering that grapes (*Vitis vinifera*) belong to the world's largest fruit crops. Grape seeds contain catechin, epicatechin, dimeric, trimeric and tetrameric proanthocyanidin, having antioxidant activity against reactive oxygen species (ROS). The grape seeds extract has proved helpful in various diseases, such as hepatic fibrosis, ischemia reperfusion injury (reducing the size of infarction in cardiac ischemia) and cancer. Also, it inhibits free radical production and has an important influence in the carbohydrate metabolism in fermentation and diabetes.

Hawthorn (*Crategus monogyna*) is a spontaneous plant known in traditional medicine for its many health benefits, especially in cardiovascular health.

Asclepias syriaca was selected and cultivated in our studies due to its energetic value, being rich in hydrocarbons. It is characterized by a complex composition comprising cellulose, hemicelluloses, lignin, polyphenols, sugars, alkaloids and hydrocarbons. It can be used as raw material to be processed by the biorefining technology proposed by us, allowing recovering all the compounds [4]. At the same time, hydrocarbons and unsaturated fatty acids could be used as an alternative to obtain triglycerides and biofuel.

Lingonberry (*Vaccinium myrtillus* L.) is a wild shrub, whose fruits and aerial parts are used as food and in traditional medicine, due to their richness in bioactive phenolic compounds. Seasonal variations of the phenolic constituents in bilberry leaves, stems and fruits have been observed and characterized from the viewpoint of antioxidant properties. The extraction of polyphenols can be performed using different techniques and solvents, which influence the composition and yields of the recovered compounds. Thus, the following techniques have been used: conventional Soxhlet extraction, ultrasounds, microwave and supercritical fluids assisted extractions. Water, methanol and ethanol have been used as extraction agents and their influence on the extracted total polyphenolic compounds (TPC) was determined by the Folin-Ciocalteu method. The content in phenolic compounds was correlated well with TPC and the 2,2-diphenyl-1-picrylhydrazyl (DPPH) radical scavenging activity. The total phenolic content was expressed in mg gallic acid equivalents (GAE) per g dried extract (d.e.), using a standard curve of gallic acid (0.1-2.0 µg/mL). The information concerning the polyphenol compositions was enhanced when we used HPLC associated with mass spectroscopy. At the same time, after alkaline hydrolysis, other polyphenolic acids were identified, which proved that some of them are present in glycoside form.

REFERENCES

1. I. Ignat; I. Volf; V. I. Popa; *Food Chem., ***2011**, *126,* 1821–1835
2. D. Harman; *J. Gerontol*., **1956,** *11(3)*, 298-300
3. I. Volf; V. I. Popa*;* Integrated Processing of Biomass Resources for Fine Chemical Obtaining: Polyphenols. In *Biomass as Renewable Raw Material to Obtain Bioproducts of High-Tech Value;* V. Popa, I. Volf, Eds.; Elsevier: Radarweg, Netherlands, **2018**, Chapter 4, pp. 113-160
4. Cr. I. Simionescu; V. Rusan; V. I. Popa; *Cellulose Chem. Technol*., **1987**, *21(1)*, 3 -16
5. O. C. Bujor; I. A. Talmaciu; I. Volf; V. I. Popa; *Tappi J*., **2015**, *14(3)*, 187-193

6. V. I. Popa; Hemicelluloses in Pharmacy and Medicine. In *Polysaccharides in medicinal and pharmaceutical applications*, V. Popa Ed.; Smithers Rapra, London, UK, **2011**, Chapter 2, pp.57-88

7. V. I. Popa; Lignin in Biological System, in *Polymeric Biomaterials, vol.1, Structure and function;* S. Dumitriu, V. Popa, Eds., CRC Press/Taylor & Francis, NW, USA, **2013**, Chapter 21, pp.709-738.

8. A.-R. Hainal; I. Ignat; I. Volf; V. I. Popa; *Cellulose Chem. Technol.*, **2011**, *45(3-4)*, 211-219

9. A.-R. Hainal; R. Diaconescu; I. Volf; V. I. Popa; *Rom. Biotechnol. Lett.*, **2012**, *17(2)*, 7084-7092

10. I. Ignat; D. G. Radu; I. Volf; A. I. Pag ; V. I. Popa ; *Cellulose Chem. Technol.*, **2013**, *47(5-6)*, 387-399

11. C. Tanase; I. Volf; S. Vintu; R. Gradinaru; V. I. Popa; *Cellulose Chem. Technol.*, **2013**, *47(7-8)*, 553-563

12. I. Volf; I. Ignat; M. Neamtu; V. I. Popa; *Chem. Pap.*, **2014**, *68(1)*, 121-129

13. C. Tanase; I. Boz; A. Stingu; I. Volf; V. I. Popa; *Ind. Crop. Prod.*, **2014,** *60*, 160-167

14. R.-E. Ghitescu; A.-M. Popa; V. I. Popa; R. M. Rossi; G. Fortunato; *Int. J. Pharm.*, **2015**, *494*, 278-287

15. R.-E. Ghitescu; I. Volf, C; Carausu; A.-M. Bühlmann; I. A. Gilca; V. I.Popa; *Ultrason. Sonochem.*, **2015**, *22*, 535-541

16. A. I. Talmaciu, I. Volf, V. I. Popa, *Chem. Biodivers.*, **2015**, *12*, 1635-1651

17. L. Lazar; A. I. Talmaciu; I. Volf; V. I. Popa; *Ultrason. Sonochem.*, **2016**, *32*, 191-197

18. C. Tanase; I. Boz; V. I. Popa; *Rom. Biotechnol. Lett.*, **2016**, *21(1)*, 11238-11245

19. A. I. Talmaciu; M. Ravber; I. Volf; Z. Knez; V. I. Popa; *J. Supercrit. Fluid.*, **2016**, *117*, 243-251

20. C. Tanase; S. Oroian; S.-L. Cosarca; V. I. Popa; *Cellulose Chem. Technol.*, **2016**, *50(5-6)*, 529-534

21. R.-E. Ghitescu; A.-M. Popa; A. Schipanski; C. Hirsch; G. Yazgan; V.I. Popa; R. M. Rossi; K. Maniura-Weber; G. Fortunato; *Eur. J. Pharm. Biopharm.*, **2018**, *122*, 78-86

22. O.-C. Bujor; C. Le Bourvellec; I. Volf; V. I. Popa; C. Dufour; *Food Chem.*, **2016**, *213*, 58-68

23. O.-C. Bujor; C. Giniès; V. I. Popa; C. Dufour; *Food Chem.*, **2018**, *252*, 356-365

24. C. Tanase; A. I. Talmaciu; C. I. Bara; I. Boz; I. Volf; V. I. Popa; *BioResources*, **2018**, *13(2),* 3994-4007

25. C. Tanase; L. Berta; A. Mare; A. Man; A. I. Talmaciu; I. Roșca; E. Mircia; I. Volf; V. I. Popa; *Eur. J. Wood Wood Prod.*, **2020**, *78*, 281-291

26. D. Jitaru (Ciobotariu); D. Ungureanu; M. Ciocoiu; M. Badescu; V. I. Popa; *Rev. Med. Chir. Soc. Med. Nat.*, Iasi, **2005**, *109*, supl. nr. 1, 33-37

27. M. Aviram; *Eur. J. Clin. Chem. Clin. Biochem.*, **1996**, *34,* 599-608

28. K. S. Panikar; R. A. Anderson; *Int. J. Mol. Sci.*, **2011**,*12*, 8181-8207

29. S. Davinelli; N. Sapere; M. Visentin; D. Zella; G. Scapagini; *Immunity & Ageing*, **2013**, *10*, 28 (5 pages)

30. R.-E. Ghitescu; A.-M. Popa; V. I. Popa; R. M. Rossi; G. Fortunato; *Intern. J. Pharm*, **2015**, *494*, 278-287

PHOTOVOLTAIC PERFORMANCES OF TWO TRIARYLAMINE-BASED DONORS IN VARIOUS INVERTED CELL CONFIGURATIONS

GAVRIL-IONEL GIURGI[a,b], LORANT SZOLGA[a,b,*], ANDREEA CRIȘAN[a], ION GROSU[a,*], JEAN RONCALI[a,*]

ABSTRACT. A complex analysis on the photovoltaic capabilities of two triarylamine-thienyl-based donors was conducted using different buffer layers in the structure of the cells, such as ZnO and MoO_3. The photovoltaic properties of the fabricated cells were characterized under simulated solar light, and monochromatic illumination. The analysis revealed a higher power conversion efficiency for the inverted-bulk-heterojunction structures.

Keywords: Organic solar cells, bilayer structure, bulk heterojunction, inverted structure, triarylamine derivatives

INTRODUCTION

Organic photovoltaics (OPV) is a focus of intensive research effort motivated by multiple advantages such as low environmental impact, low-cost, flexibility, lightweight, and possible semi-transparency [1-4].

OPV cells can be fabricated by various techniques including vacuum deposition of bi-layer planar heterojunction (PHJ) [3,4] and solution-processing of bulk heterojunction solar cells (BHJ) [12]. BHJ technology is the most developed and with best results so far but, although PHJ cells were surpassed in terms of power conversion efficiency (PCE) by BHJ cells, they are still valuable in the process of screening new active materials [5]. BHJ cells are fabricated at ambient temperature by spin-casting blend films from solutions of donor (**D**) and acceptor (**A**) materials. Two major cell architectures are proposed, a "direct" and an "inverted" one. In a direct cell, the active material

---

[a] *Babes-Bolyai University, Faculty of Chemistry and Chemical Engineering, Department of Chemistry and SOOMCC, Cluj-Napoca, 11 Arany Janos, 400028, Cluj-Napoca, Romania*

[b] *Optoelectronics Group, Base of Electronics Department, ETTI, Technical University of Cluj-Napoca, Str. Memorandumului, Nr.28, Cluj-Napoca, 400114, Romania*

[*] *Corresponding authors: lorant.szolga@bel.utcluj.ro, igrosu@chem.ubbcluj.ro, jeanroncali@gmail.com*

blend of **D** with **A** is spun-cast or PVD deposited on an indium-tin oxide (ITO) conducting electrode coated with a layer of poly(3,4-ethylenedioxythiophene): polystyrene sulfonate (PEDOT:PSS). A more stable cell could be obtained in an inverted structure in which solution-processed layers of ZnO and PVD deposited MoO_3 are inserted between the electrodes and the active material, replacing the PEDOT:PSS layer. The active layer in this case can be deposited by spin-casting or PVD technique. The literature that deals with direct and inverted cell fabrication underlines a higher efficiency and stability of inverted cells [5-8].

Even if conjugated polymers still represent a major class of donors for solution-processed BHJ cells, lately a significant contribution to the advance of OPVs was brought by use of small molecules due to their well-defined chemical structure, ease of synthesis and purification along easily tuned properties [9-13]. Triarylamine-based molecules as donors have already shown interesting photovoltaic performances [14-17].

We have recently reported on the synthesis of a dyad named DCV-C_{60} in which the connection between **D** block (**1**) containing a triarylamine-thienyl with an appended dicyanovinyl group and [6,6]-phenyl-C_{61}-butyric acid methyl ester ($PC_{61}BM$) as **A** is realized through position 3 of the thiophene moiety. The mentioned **D-A** dyad was also evaluated as active Single-Molecule Organic Solar Cell (SMOSC) material, tested out in inverted structure giving a cell characteristic of V_{oc}= 1 V, J_{sc}= 2.85 mA/cm^2, FF = 28% and *PCE* of 0.8% [14]. An analysis of bilayer and BHJ structures involving the donor **1** was not performed so far. To test if the presence of a hydroxymethyl group at the 3-positio of the thiophene unit would influence the characteristics of resulting cells, we have also synthesized the already reported unsubstituted compound **2** for comparison. In the case of donor **2,** only a direct bilayer analysis was reported previously [17].

In this context, the present work shows a comparative analysis of the cells fabricated in two different structures using the small molecular donors (**1**) and (**2**) and fullerene (C_{60}) or $PC_{61}BM$ as acceptor (Figure 1). Donors **1** and **2** were selected for their accessible synthesis and relevant properties among other small donors obtained in our group [15] [16].
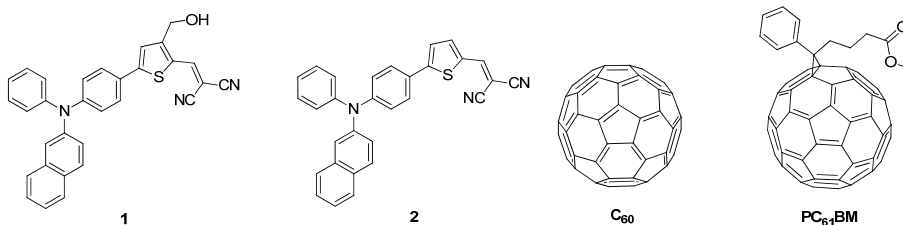

Figure 1. Chemical structures for donors (**1** and **2)** and the acceptors (C_{60} and $PC_{61}BM$)

RESULTS AND DISCUSSIONS

Figure 2 shows the two structures investigated in the present work: inverted-bilayer and inverted-BHJ. For both structures (bilayer and bulk), two buffer layers were used: a ZnO one with high capability for electron transport to the ITO electrode and a MoO_3 one as hole-transport layer to the Al electrode. At the same time, the MoO_3 presents very good properties for the encapsulation of the cells, protecting the active layer from the outside environment. Layers of C_{60}, MoO_3 and Al were always deposited in the vacuum by PVD (Physical Vapor Deposition) technique. The active layer in the case of the BHJ structures was deposited by spin-coating from solution and for the bilayer structures, donors **1** and **2** were deposited by PVD.
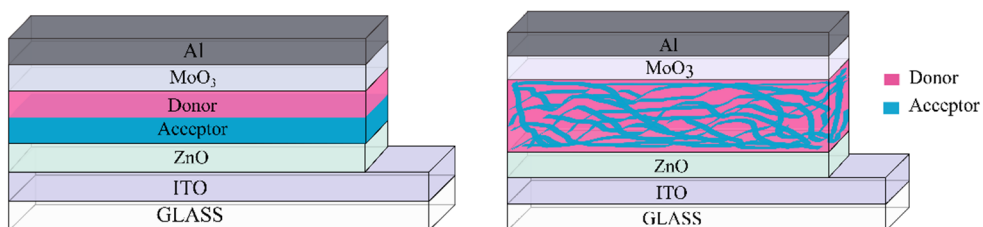

Figure 2. Simplified representations the OSC structures:
inverted-bilayer (left) and inverted-BHJ (right)

Inverted-bilayer structure (ITO/ZnO/C$_{60}$/Donor/MoO$_3$/Al)

To test out the inverted structures we spun-cast in each case a 30nm layer of ZnO on the ITO. The next layers were successively vacuum deposited using a thickness of 30nm of C_{60} followed up by a layer of 20nm of donor. The active layer was covered by a 10nm of MoO_3 before evaporating a 100nm thick Al electrodes. The best cell characteristics with donor **1** shows a V_{oc}=0.82V, J_{sc}=2.35 mA/cm^2, FF= 58 % and PCE=1.12%, after a temperature annealing at 70°C as presented in Table 1. The best cell characteristics with donor **2** shows a V_{oc}= 0.86 V, J_{sc}= 3.05 mA/cm2, FF=60% and PCE=1.56% for ambient conditions. Thermal annealing improves only the cells based on Donor **1**. The J vs V characteristics of the best cells are presented in Figure 3. The external quantum efficiency (EQE) spectra of the best devices are illustrated in Figure 4. The EQE spectra indicate that both C_{60} and Donors **1** or **2** contribute to the photocurrent generation.

Table 1. Inverted-bilayer solar cell electrical parameters using Donor **1**.

Cell Name	V_{oc} [V]	J_{sc} [mA/cm2]	FF [%]	PCE [%]	Average PCE [%]
P1_ambient	0.76	2.87	34.34	0.75	0.9
P2_ambient	0.81	2.24	57.90	1.05	
P1_50°C	0.79	2.22	53.88	0.94	1.01
P2_50°C	0.81	2.27	58.74	1.08	
P1_70°C	0.81	2.18	55.94	0.99	1.06
P2_70°C	**0.82**	**2.35**	**58.32**	**1.12**	
P1_90°C	0.83	2.36	56.81	1.11	1.04
P2_90°C	0.80	2.34	52.01	0.97	
P1_110°C	0.91	2.22	48.50	0.98	0.94
P2_110°C	0.81	2.20	50.77	0.90	

Table 2. Inverted-bilayer solar cell electrical parameters using Donor **2**.

Cell Name	V_{oc} [V]	J_{sc} [mA/cm2]	FF [%]	PCE [%]	Average PCE [%]
P1_ambient	0.85	3.07	57.65	1.51	1.54
P2_ambient	**0.86**	**3.05**	**59.81**	**1.56**	
P1_50°C	0.86	2.96	55.04	1.39	1.40
P2_50°C	0.85	2.98	55.57	1.42	
P1_70°C	0.85	2.49	58.02	1.22	1.26
P2_70°C	0.84	2.95	52.16	1.29	
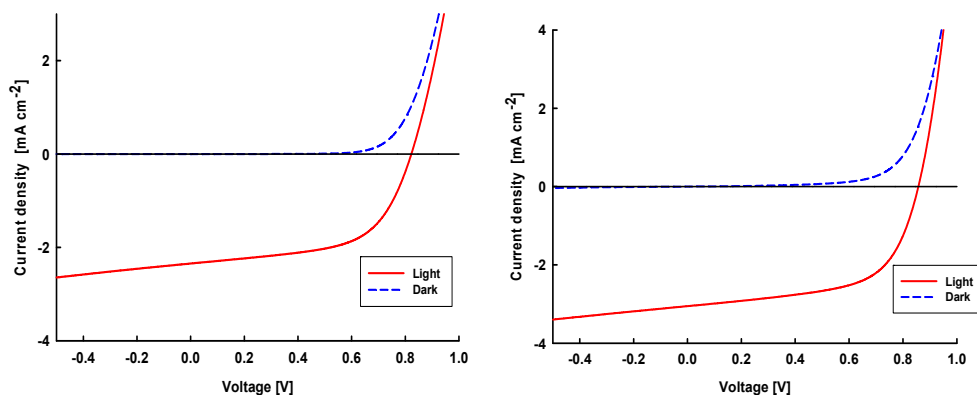
Figure 3. Current density *vs* voltage curves for best inverted-bilayer cell using Donor **1** (left) and Donor **2** (right).
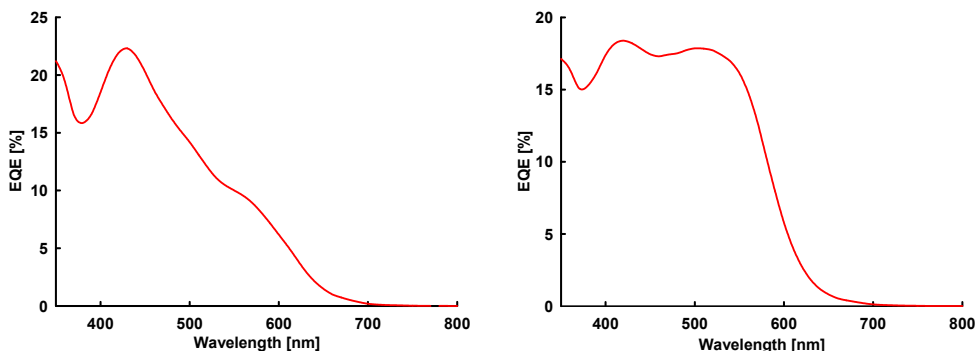
Figure 4. EQE characteristics for the best inverted-bilayer cell using
Donor **1** (left) and Donor **2** (right**)**.

Inverted-BHJ structure (ITO/ZnO/Donor:PC$_{61}$BM/MoO$_3$/Al)

From our previous testing of donor **1** in direct BHJ cells the best **D-A** ratio in solution proved to be the 1:2. Thus, we proceed our experiments in inverted-BHJ structures with donor **1** using this **D-A** ratio. The ZnO layer was kept at 30nm, the MoO$_3$ at 10nm and the Al electrodes at 100nm. The cell measurements results are presented in Table 3. The thermal annealing at 70°C proves to be beneficial for this inverted structure too, pushing the PCE up to 1.71%. The J-V and EQE characteristic for the best cells are presented in Figures 5, 6. In the case of donor **2**, in the absence of some previous BHJ tests, it was mandatory to discover the best **D-A** ratio. In the same fabrication stage, we tested out three **D-A** ratios: 1:1, 1:2 and 1:3. The solar simulator measurements presented in Table 4, revealed that the best **D-A** ratio for donor **2** is 1:2, just as in the case of donor **1**. The best cell characteristics for this ratio shows a V$_{oc}$=0.97V, J$_{sc}$=5.54 mA/cm^2, FF=35% and PCE=1.85%, in ambient conditions. Like in the case of the inverted-bilayer structure with the same donor thermal annealing does not improve the characteristics of the cells.

Table 3. Inverted-BHJ solar cell electrical parameters using Donor **1**.

Cell Name	V$_{oc}$ [V]	J$_{sc}$ [mA/cm^2]	FF [%]	PCE [%]	Average PCE [%]
P1_ambient	0.44	4.90	30.41	0.66	1.14
P2_ambient	1.02	4.88	32.71	1.63	
P1_50°C	1.02	4.88	32.72	1.63	1.35
P2_50°C	0.77	4.33	32.10	1.08	
P1_70°C	0.98	4.97	33.12	1.61	1.66
P2_70°C	**1.02**	**4.96**	**33.89**	**1.71**	
P1_90°C	1.00	4.76	34.91	1.66	1.62
P2_90°C	0.99	4.60	34.69	1.59	

Table 4. Inverted-BHJ solar cell electrical parameters using Donor **2**.

D-A Ratio	Cell Name	V_{oc} [V]	J_{sc} [mA/cm^2]	FF [%]	PCE [%]	Average PCE [%]
1:1	P1_ambient	1.02	4.05	34.68	1.43	1.44
	P2_ambient	**0.95**	**4.65**	**32.79**	**1.46**	
	P1_50°C	0.87	4.44	34.46	1.33	1.34
	P2_50°C	0.86	4.56	34.15	1.35	
	P1_70°C	0.81	4.22	35.51	1.22	1.27
	P2_70°C	0.86	4.41	34.57	1.31	
1:2	**P3_ambient**	**0.97**	**5.54**	**34.46**	**1.85**	1.82
	P4_ambient	0.97	5.40	34.13	1.79	
	P3_50°C	0.94	5.31	34.79	1.74	1.73
	P4_50°C	0.88	5.51	35.48	1.72	
	P3_70°C	0.89	5.20	35.56	1.47	1.49
	P4_70°C	0.75	5.47	37.25	1.52	
1:3	P5_ambient	**0.99**	**4.42**	**38.14**	**1.67**	1.65
	P6_ambient	0.97	4.40	38.00	1.63	
	P5_50°C	0.93	4.23	38.93	1.54	1.50
	P6_50°C	0.94	4.27	35.90	1.45	
	P5_70°C	0.90	4.28	37.04	1.43	1.41
	P6_70°C	0.87	4.27	37.30	1.39	
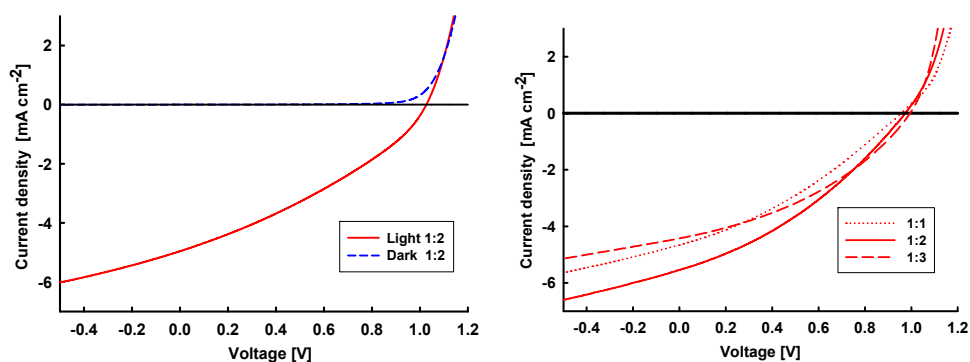
Figure 5. Current density *vs* voltage curves for best inverted-BHJ cells using Donor **1** (left) and Donor **2** (right).
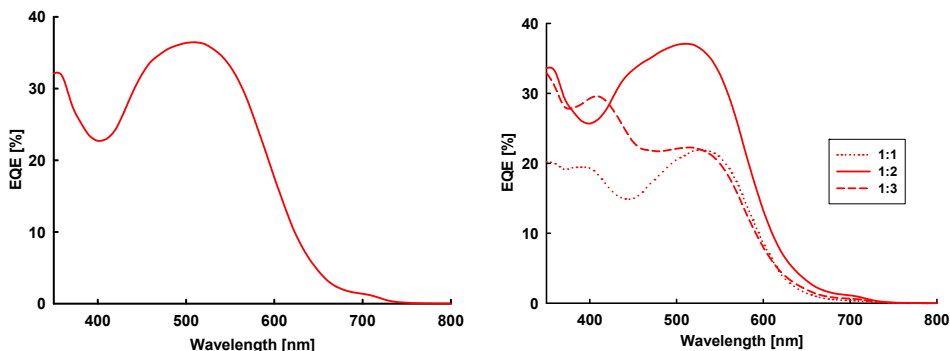
Figure 6. EQE characteristics for the best inverted-BHJ cell using
Donor **1** (left) and Donor **2** (right).

CONCLUSIONS

A comparative analysis was conducted on the photovoltaic performances of bilayer and BHJ cells in inverted structures using two small molecular donors. Comparing the best cell properties from each structure reveals that the BHJ structures presents better electrical characteristics than bilayer cells. We were able to raise the PCE of the cells with donor **1** from 1.12% in the case of the inverted-bilayer structure up to 1.71% in the case of the inverted-BHJ structure and for the cells fabricated with donor **2** from 1.56% in inverted-bilayer structure to 1.85% in inverted-BHJ structure, thus showing that the hydroxymethyl group at the 3-position 3 of the thiophene unit does not improve cell characteristics. With both donors, inverted BHJs show higher current densities than inverted-bilayer structures, but low fill factors. This unwanted effect could be countered by further investigations using different buffer layers which can also further improve the PCE.

EXPERIMENTAL PART

Materials and equipment

The cells were obtained using commercially available ITO-coated glass substrates of 24×25 mm. These substrates were sonicated for 10 minutes in distilled water, cleaned with Deconex (10 min), ethanol (10 min), isopropanol (10 min) and finally using an UV Ozone Cleaner for 20 minutes.

PC$_{61}$BM, PEDOT, PSS, MoO$_3$, CHCl$_3$, C$_6$H$_5$Cl and Al were commercially available. The active material and ZnO were prepared accordingly to literature data. [18] The deposition of different layers of the cells were carried out either using a classic spin-coater or a high vacuum deposition equipment (MANTIS DEPOSITION- model QUBE). The characterization of the cells was performed with an Artificial Sun system LCS-100 (94011A-ES) and a monochromator equipment IQE 200B Quantum Efficiency Measurement Solution, while the thickness of the layers was measured using a profilometer Tencor Alpha-Step D500. The absorption spectra of the film were analyzed by UV-VIS 1900 Shimadzu spectrometer

General procedure for the fabrication of inverted BHJs

A layer of 40 nm ZnO was deposited by spin-casting [S = 3000 rpm, t = 40 s) on clean ITO plates and then the plates were heated at 200°C for 10min. The films of **donor : PC$_{61}$BM** were spun-cast (t$_1$ = 40 s, S$_1$ = 1000 rpm, t$_2$ = 20 s, S$_2$ = 8000 rpm) on top of ZnO layer. The hole transporter layer (HTL) consisting in a 10 nm thick MoO$_3$ layer and the Al electrodes (100 nm) were deposited by thermal evaporation under high vacuum at 10^{-6} mbar.

ACKNOWLEDGEMENTS

REFERENCES

[1] S. Günes,H. Neugebauer, N. S. Sariciftci, *Chem. Rev.* **2007**,*107*, 1324-1338.
[2] C. J. Brabec, S. Gowrisanker, J. J. M. Halls, D. Laird, S. Jia, S. P. Williams, *Adv. Mater.* **2010**, *22*, 3839–3856.
[3] P. Peumans, A. Yakimov, S.R. Forrest, *J. Appl. Phys*. **2003**, *93*, 3693-3723.
[4] K. Walzer, B. Maennig, M. Pfeiffer, K. Leo, *Chem. Rev*. **2007**, *107*, 1223-1270.
[5] G.-I. Giurgi, L. Szolga, I. Kovacs, E. Bogdan, N.D. Hădade, A. Terec, I. Grosu, J. Roncali, *Studia UBB Chemia*, **2020**, *2*, 95-106.
[6] M. Abdallaoui, N. Sengouga, A. Chala, A.F. Meftah, & A. M. Meftah, *Opt.Mater.,* **2020**, *105*, 109916.
[7] S. Huang, B. Kang, L. Duan, & D. Zhang, *Colloid.Interface Sci*., **2020**, *583*, 178-187.
[8] Y. Wang, H. Cong, B. Yu, Z. Zhang, & X. Zhan, *Mater*., **2017**, *10*, 1064.
[9] A. Mishra, P. Bäuerle *Angew. Chem. Int. Ed*. **2012**, *51*, 2020-2068.

[10] J. Roncali, P. Leriche, P. Blanchard *Adv. Mater*. **2014**, *26*, 3821.

[11] D. Collins, N. A. Ran, M. C. Heiber, T.-Q. Nguyen, *Adv. Energy Mater*. **2017**, 1602242.

[12] A. Venkateswararao, K.-T. Wong, *Bull Chem. Soc. Jpn.* **2021**, *94*, 812-837.

[13] D. Demeter, S. Mohamed, A. Diac, I. Grosu, J. Roncali, *ChemSusChem,* **2014**, *7*, 1046-1050.

[14] J. Roncali, Acc. *Chem. Res*. **2009**, 42, 1719-1730.

[15] A.P. Diac, L. Szolga, C. Cabanetos, A. Bogdan, A. Terec, I. Grosu, J. Roncali, *Dyes Pigm*., **2019**, *171*, nr. 107748.

[16] A. Bogdan,L. Szolga, G.-I. Giurgi, A.P. Crişan, D. Bogdan, S. Hadsadee, S. Jungsuttiwong, R. Po, I. Grosu, J. Roncali, *Dyes Pigm*., **2021**, *184*, 108845.

[17] S. Mohamed, D. Demeter, J.-A. Laffitte, P. Blanchard, J. Roncali, *SciRep* **2015**, *5*, nr. 9031.

[18] M.I Nan, E. Lakatos, G.-I. Giurgi, L. Szolga, R. Po, A Terec, S. Jungsuttiwong I. Grosu, J. Roncali, *Dyes Pigm*., **2020**, 181, 108527.

[19] Y. M. Sun, J. H. Seo, C. J. Takacs, J. Seifter, A. J. Heeger, *Adv. Mater*, **2011**, *23*, 1679-1683.

POLYLACTIC ACID INTERACTIONS WITH BIOCERAMIC SURFACES

IZABELLA IRSAI[a], ADRIAN M.V. BRÂNZANIC[b], RADU SILAGHI-DUMITRESCU[a,*]

ABSTRACT. Molecular dynamics simulations were employed in order to analyze the interfacial interaction of polylactic acids with zirconia and hydroxyapatite surfaces. The interactions of polymers on five crystallographic planes were simulated. Silane coupling agents can improve the interactions between the bioceramic surfaces and the polylactic acids. The effects of the coupling agents are more evident in the presence of hydroxyapatite surfaces. Weak interactions hold together the polylactic acids and bioceramic systems. These interactions are formed between the hydrogen atoms from methyl groups or from the main chains of the polylactic acids and the oxygens of the surfaces. Polylactic acids change their conformations after molecular dynamics simulations due to the interactions. The conformation changes are more obvious when silane coupling agents are added to the polylactic acids and bioceramic systems.

Keywords: polylactic acid, hydroxyapatite, zirconia, molecular dynamics, weak interactions

INTRODUCTION

Biomaterials are biocompatible and non-toxic materials that are not recognized by the body as a potentially harmful foreign substances. They are classified as bioinert, resorbable and bioactive according to tissue response. Bioinert materials induce formation of a fibrous tissue of variable thickness, interfacial bond forms on bioactive materials and resorbable materials are replaced by the surrounding tissues [1]. Biomaterials belong to all 5 major

[a] *Babeş-Bolyai University, Faculty of Chemistry and Chemical Engineering, 11 Arany Janos str., RO-400028, Cluj-Napoca, Romania*
[b] *Babeş-Bolyai University, Institute of Interdisciplinary Research in Bio-Nano-Sciences, 42 Treboniu Laurian str., RO- 400271, Cluj-Napoca, Romania*
* *Corresponding author: radu.silaghi@ubbcluj.ro*

classes of materials: metals, ceramics, polymers, composites and natural materials. Bioceramics are a class of materials that satisfy most of these criteria in addition to their biocompatibility and sufficient mechanical strength close to that of bone. The bioceramics have low density, high hardness, low tensile strength and high compressive strength and they are characterized by chemical stability. Bioceramics induce a specific biological response at the interface of the material resulting in the formation of strong bond between the tissue and the material.

Hydroxyapatite (HA) is a highly biocompatible ceramic that is characteristically resorbable in body. In practice, hydroxyapatite is either used as a bioactive coating on implants, or reinforced by metal or ceramic phases. Zirconia is an inert ceramic in its pure form. The properties of interest to the engineer utilizing zirconia ceramics include strength, toughness, hardness, wear resistance and thermal properties [2,3].

Most polymers, especially thermoplastics, are non-polar (hydrophobic) substances, which are not compatible with polar (hydrophilic) surfaces, poor adhesion can result between polymer and material. To improve the adhesion between surfaces and polymers coupling agents have been employed [4–7]. Coupling agents are used in small quantities to treat a surface so that bonding occurs in the system. Bonding agents act as bridges that link the material and the polymer. Coupling agents are classified into organic (e.g. isocyanates, anhydrides, amides, imides), inorganic (e.g. silicates), and organic-inorganic groups (e.g. silanes). Silanes, represented as $R-Si(OR')_3$, have better performance in organic-inorganic coupling agents, because the attachment of silanes to hydroxy groups of cellulose or lignin is accomplished either directly to the alkoxy group (-OR') attached to silicon or via its hydrolyzed products (i.e. silanol) by the hydrogen bonds or ether linkage [8]. The functional group (R) in silanes also influences the coupling action [9–15].

Hydroxyapatite/polymer composites improve the HA mechanical properties.[16–18] HA polymer composites present good bioactivity due to the HA content [19]. The most intensively studied biopolymers are polyethylene [20, 21], polyamide [22, 23] and polylactic acid (PLA) [24–26]. These polymers are used as matrices in HA/polymer composites. The polyethylene/HA composites are used as hard tissue replacement. The chemical structure of polyamide is similar to the collagen structure; therefore polyamide can be utilized as a composite matrix. Polylactic acid /HA composites are employed in degradable internal bone fixation devices.

Reported here is a computational exploration of polylactic acid interactions with solid surfaces via non-covalent interactions, aiming to identify modes of binding and binding strengths.

RESULTS AND DISCUSSION

The interaction energies of polylactic acid/zirconia and PLA/silane/ zirconia systems are listed in Table 1. The negative values indicate that in all cases binding of the different types of PLA to the zirconia surface is favorable energetically.

Table 1. The interaction energies of polylactic(PLA)/zirconia and polylactic acid/silane/zirconia systems

h k l	PLA	$E_{interaction}$ (kcal/mol)	
		PLA/zirconia	PLA/silane/zirconia
(0 0 1)	α-L-LA$_{10}$	-7.35	-28.62
	π-L-LA$_{10}$	-9.93	-18.13
	3$_{10}$-L-LA$_{10}$	-13.11	-14.94
	β-L-LA$_{10}$	-21.11	-16.86
	DeSantis-LA$_{10}$	-12.47	-23.36
(1 0 0)	α-L-LA$_{10}$	-6.67	-19.36
	π-L-LA$_{10}$	-16.44	-22.04
	3$_{10}$-L-LA$_{10}$	-17.15	-26.15
	β-L-LA$_{10}$	-28.32	-20.78
	DeSantis-LA$_{10}$	-11.60	-18.49
(1 1 0)	α-L-LA$_{10}$	-8.96	-15.02
	π-L-LA$_{10}$	-13.65	-14.94
	3$_{10}$-L-LA$_{10}$	-9.23	-8.12
	β-L-LA$_{10}$	-25.56	-17.45
	DeSantis-LA$_{10}$	-12.04	-13.73
(1 1 1)	α-L-LA$_{10}$	-14.21	-22.67
	π-L-LA$_{10}$	-15.79	-21.83
	3$_{10}$-L-LA$_{10}$	-6.05	-21.26
	β-L-LA$_{10}$	-18.13	-29.00
	DeSantis-LA$_{10}$	-11.69	-24.00
(-1 0 0)	α-L-LA$_{10}$	-14.14	-28.26
	π-L-LA$_{10}$	-8.91	-19.10
	3$_{10}$-L-LA$_{10}$	-9.60	-29.23
	β-L-LA$_{10}$	-23.67	-28.28
	DeSantis-LA$_{10}$	-23.56	-18.52

Table 1 suggests that the optimized β sheets bind most strongly to the five surfaces. The interaction energies are above 20 kcal/mol except in the case of the (1 1 1) surface. The connections of α, π, 3$_{10}$ optimized helices and the DeSantis structure[27] to the (0 0 1) surface are two-three times

smaller than the binding of β sheet. In the case of (1 0 0) surface the lowest binding energy is obtained with the α helix is attached to zirconia. The binding energies of π and 3_{10} helices are nearly same, but with ~12 kcal/mol smaller than the interaction energy of the β sheet. The interaction energy differences between the β structure/(1 1 0) surface and the other structures/(1 1 0) surface are the largest. The α/(1 1 0) zirconia and 310/(1 1 0) zirconia have appropriate binding energy values. The same is valid for π/(1 1 0) zirconia and DeSantis/(1 1 0) zirconia. The interaction energy for optimized β-sheet/(1 1 1) zirconia is 18 kcal/mol. Three times lower than this is the interaction energy between optimized 3_{10} helix and (1 1 1) surface. The interaction energy of the optimized DeSantis structure and (-1 0 0) zirconia is very close to the value resulted from β sheet and (-1 0 0) interaction. The energy difference toward the less stable system is 14 kcal/mol.

Table 1 also shows that the coupling agents generally increase the interaction energies. The most striking increases were observed for optimized α and 3_{10} helices on zirconia surfaces. The interaction energies increase about three-four times in the case of optimized α helix/(0 0 1) surface, α helix/(1 0 0) surface and optimized 3_{10} helix/(1 1 1) surface, 3_{10} helix/(-1 0 0) surface. However, the silanes do not always increase the interaction energies – as ween e.g. in the β structure and (0 0 1), (1 0 0), (1 1 0) surface systems.

The top layers of the (0 0 1), (1 0 0), (1 1 1) and (-1 0 0) zirconia surfaces are constituted by zircon atoms. In contrast the oxygen atoms are on the interface of the bioceramic (1 1 0) surface. The polymer chains and the zirconia surfaces are held together by weak interactions. These interactions occur between the hydrogen atoms from methyl groups or from the main chains of the polymer and the oxygen atoms of the surfaces. Another attraction is formed between the carbonyl oxygen from the polylactic acid and the zirconium atoms of the bioceramic. These interactions influence the behavior of the polymer chains. The conformation changes after the simulations can be seen in Figure 1. In most cases the polymers remain parallel to the surfaces, but they change their positions compared to the reference surfaces. The conformations of the polymers undergo major changes when silane coupling agents are laid between the zirconia surfaces and the polylactic acids (Figure 2). These changes are influenced by interactions between the silane molecules and the polymers. Interactions occur between hydrogen atoms from methyl groups or from main chains of the polymers and the hydroxyl oxygens of the silane molecules. Another type of interaction takes place between the carbonyl or carboxyl oxygen atom of the polymer and the hydrogen atom of the silane molecule.
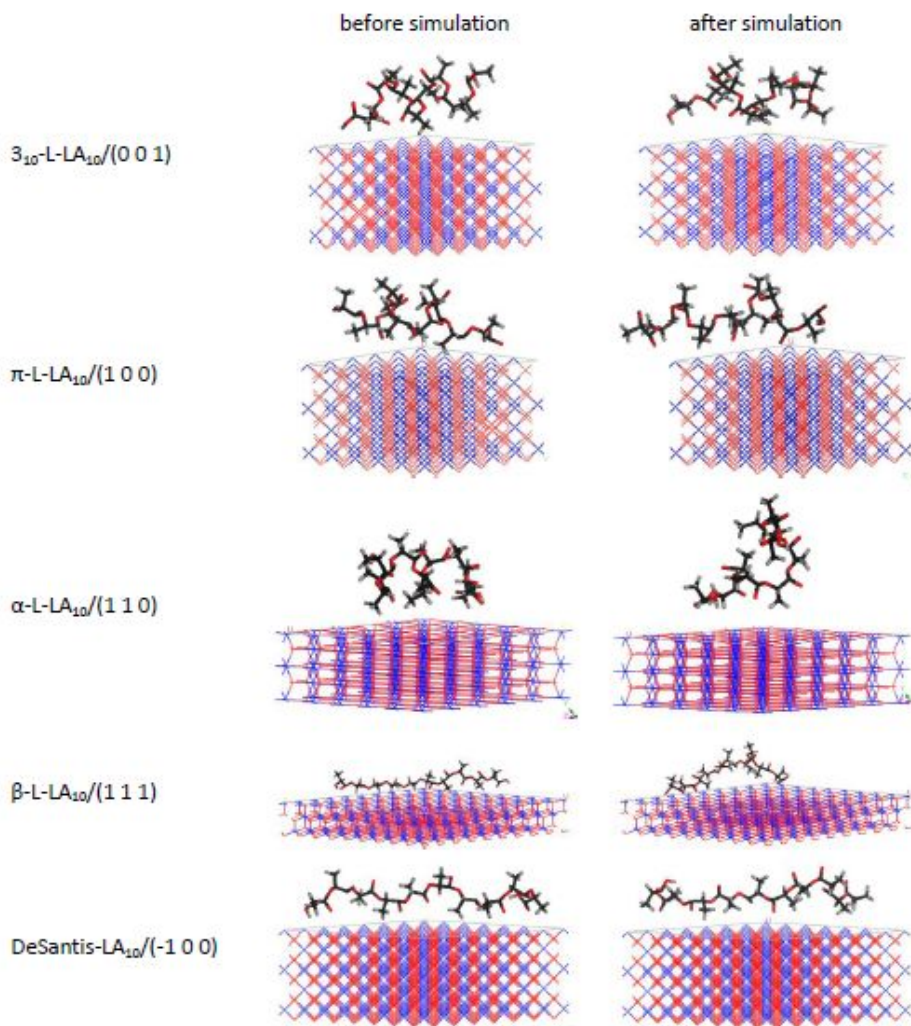
Figure 1. Snapshots of PLA on zirconia surfaces before and
after the molecular dynamics simulations

Table 2 shows the interaction energies of optimized PLA models and hydroxyapatite systems with and without coupling agents. The energy values are much smaller than in the polylactic acid/zirconia systems, nut still generally favorable – with one exception: the optimized α helix did not attach to the (1 1 1) hydroxyapatite surface. Overall, the interaction energies for PLA in Table 1 are relatively small and essentially degenerate – implying that no single type of secondary structure would be favored in these interactions.

The optimized π and β decameric units are hardly linked to (0 0 1) and (1 1 0) surfaces, respectively. The optimized DeSantis structure binds to (0 0 1), (1 1 0), (1 1 1) and (-1 0 0) hydroxyapatites with interaction energies above 4 kcal/mol. 3-6 kcal/mol interaction energies exist between optimized π helices and (1 1 0), (1 1 1) and (-1 0 0) surfaces. The interface energies are around 4-5 kcal/mol when the 3_{10} structures are connected to (1 1 0) and (-1 0 0) hydroxyapatite surfaces.
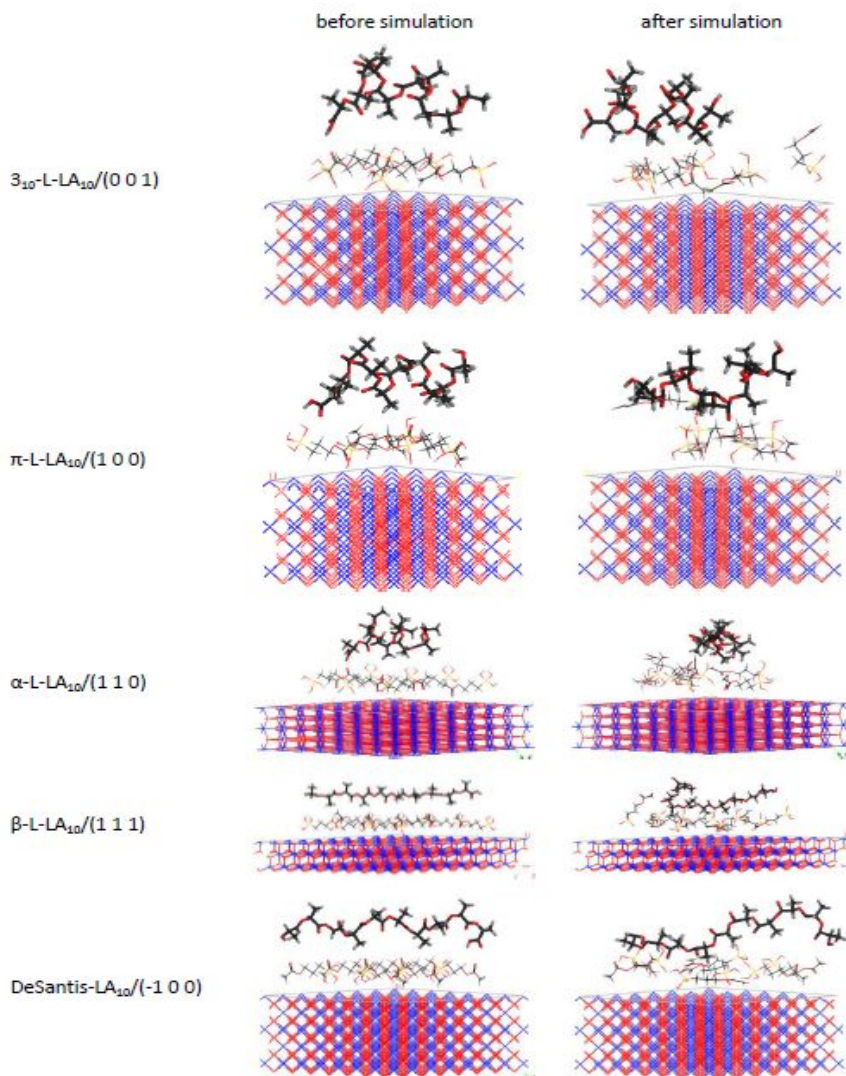

Figure 2. Snapshots of PLA on silane/zirconia surfaces before and after the simulations

Table 2. The interaction energies of polylactic (PLA) /hydroxyapatite (HA) and polylactic acid/silane/hydroxyapatite systems

		$E_{interaction}$ (kcal/mol)	
h k l	PLA	PLA/HA	PLA/silane/HA
(0 0 1)	α-L-LA$_{10}$	-0.79	-17.46
	π-L-LA$_{10}$	-0.07	-11.44
	3_{10}-L-LA$_{10}$	-1.52	-22.67
	β-L-LA$_{10}$	-1.95	-15.77
	DeSantis-LA$_{10}$	-3.90	-31.63
(1 0 0)	α-L-LA$_{10}$	-1.50	-11.78
	π-L-LA$_{10}$	-1.13	-18.54
	3_{10}-L-LA$_{10}$	-2.16	-10.57
	β-L-LA$_{10}$	-2.60	-29.59
	DeSantis-LA$_{10}$	-0.47	-12.48
(1 1 0)	α-L-LA$_{10}$	-0.84	-9.64
	π-L-LA$_{10}$	-4.76	-12.05
	3_{10}-L-LA$_{10}$	-4.96	-0.36
	β-L-LA$_{10}$	-0.18	-8.32
	DeSantis-LA$_{10}$	-6.63	-12.74
(1 1 1)	α-L-LA$_{10}$	0.46	-12.33
	π-L-LA$_{10}$	-3.13	-8.60
	3_{10}-L-LA$_{10}$	-1.24	-7.80
	β-L-LA$_{10}$	-2.74	-17.27
	DeSantis-LA$_{10}$	-6.16	-9.20
(-1 0 0)	α-L-LA$_{10}$	-1.84	-15.68
	π-L-LA$_{10}$	-5.98	-4.30
	3_{10}-L-LA$_{10}$	-3.99	-15.90
	β-L-LA$_{10}$	-3.68	-27.32
	DeSantis-LA$_{10}$	-5.41	-15.26

In most cases seen in Table 2, silanes have a much larger effect on the PLA/hydroxyapatite interactions than in the case of zirconia. Thus, the interaction energy of optimized π helix increases by two orders of magnitude with the addition of coupling agent. However the interaction energy decrease when the helix is attached to (-1 0 0) hydroxyapatite in the presence of silane.

The interactions energies between optimized β sheets and the hydroxyapatite surfaces increase in all cases with the addition of silanes.

Weak interactions hold together PLA and hydroxyapatite systems. The general formula of hydroxyapatite is $Ca_{10}(PO_4)_6(OH)_2$. The top layers of the surfaces have different atom compositions by cleaving the crystal along planes. Oxygen, calcium and phosphorus atoms are at the (1 0 0), (1 1 0) and (-1 0 0) surfaces. The interface of (0 0 1) hydroxyapatite contains oxygen and hydrogen molecules. Oxygen, hydrogen and phosphorus atoms constitute the top layers of (1 1 1) surface. The PLA/apatite interactions entail the hydrogen atoms from methyl groups or from the main chains of PLA and the oxygens of the surfaces. Interactions exist between oxygen from ester groups of PLA and hydroxyl groups in hydroxyapatite. PLA change their conformations after molecular dynamic simulations due to the interactions. The polymers did not remain parallel with the surface (Figure 3). Interactions between the polylactic acids and silane molecules exist when coupling agents are added to the system. The conformations of the decameric units were not preserved in these cases neither (Figure 4).

CONCLUSIONS

Molecular dynamics simulations were used to analyze the interfacial behaviors of polylactic acids and zirconia, hydroxyapatite surfaces. The interactions of polymers on five crystallographic planes were simulated. The interaction energies between the DFT optimized polymers and bioceramic surfaces was analyzed. The polylactic acids bind to the polymers in every situation. There is one exception, optimized α helix did not attach to the (1 1 1) hydroxyapatite surface. Optimized β sheets bind most strongly to the five zirconia surfaces, the interaction energies are above 20 kcal/mol. The energy values are much smaller in polylactic acid/hydroxyapatite systems than in the polylactic acid/zirconia systems. The silane coupling agents can improve the interactions between the bioceramic surfaces and the polylactic acids.

The effects of the coupling agents are more evident if the surface is hydroxyapatite.

Weak interactions hold together the polylactic acids and bioceramic systems. These interactions are formed between the hydrogen atoms from methyl groups or from the main chains of the polylactic acids and the oxygens of the surfaces. Polylactic acids change their conformations after molecular dynamics simulations due to the interactions. The conformation changes are more obvious when silane coupling agents are added to the polylactic acids and bioceramic systems.
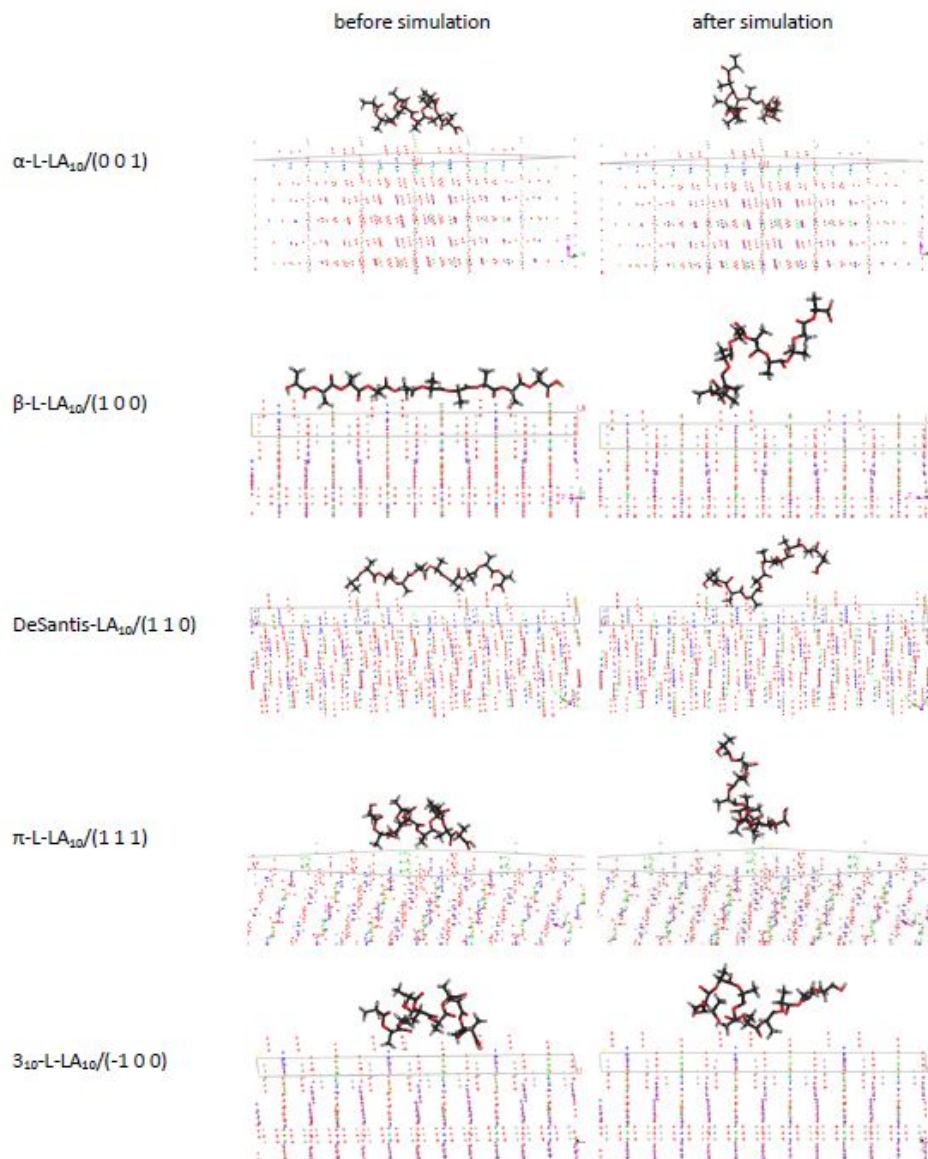
Figure 3. Snapshots of polylactic acids on hydroxyapatite surfaces before and after the simulations
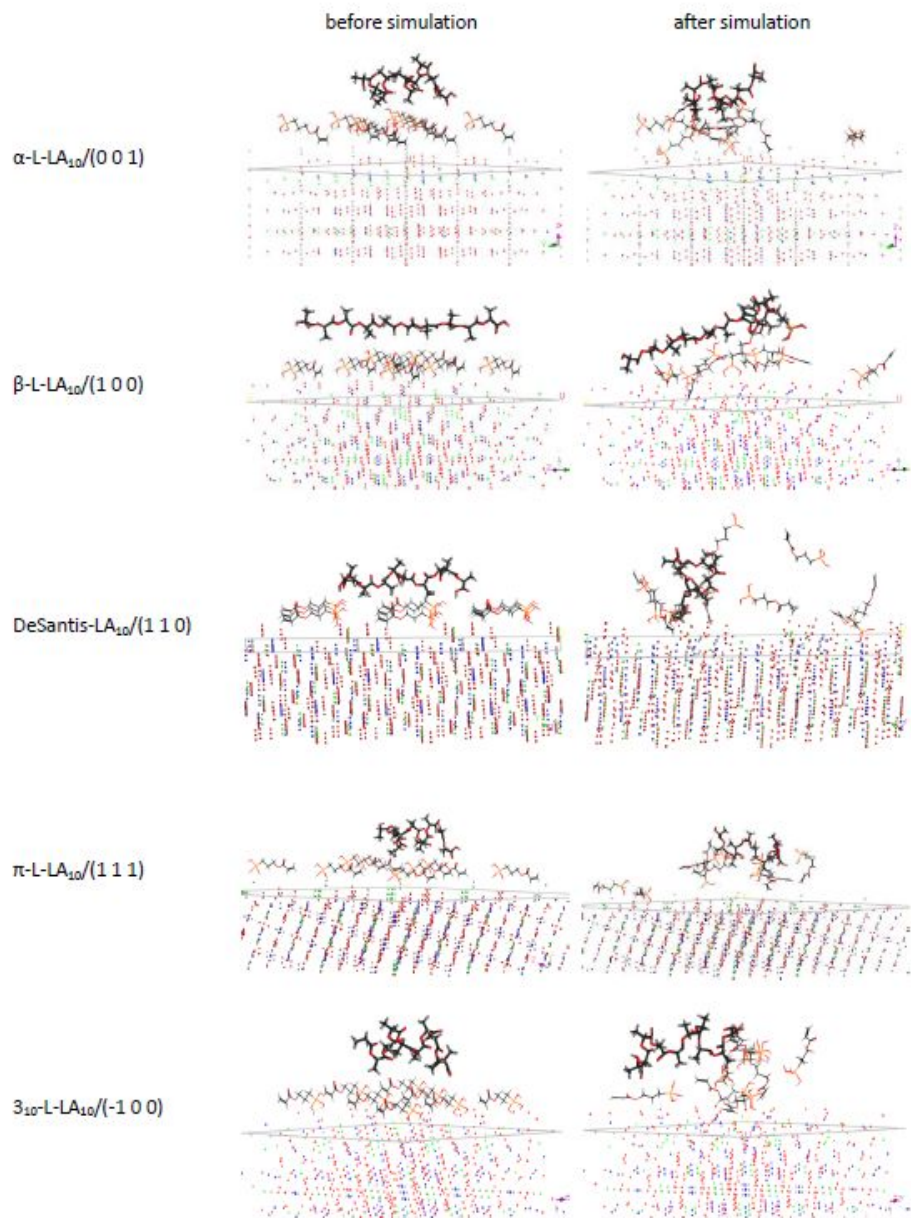
Figure 4. Snapshots of polylactic acids on silane/hydroxyapatite surfaces before and after the simulations

EXPERIMENTAL SECTION

Models of polymer molecules

Five PLA decameric units were employed throughout this study. The secondary-type structures (α, π, 3_{10}, β, DeSantis [27]) were optimized with at the M062x/6-311+G** level of theory [28] as previously described [29,30].

Models of bioceramic surfaces

The two bioceramics surfaces utilized in this study were hydroxyapatite and zirconia. The surfaces were cleaved along (0 0 1), (1 0 0), (1 1 0), (1 1 1) and (-1 0 0) planes, followed by minimizations under boundary conditions with a non-bond cut-off distance of 9.5 Å. The zirconia was created using built-in options of Material Studio software for creating ceramics (cf. Table 3). The hydroxyapatite surface was constructed based on crystallographic data (cf. Table 4) [31].

PLA/bioceramics interactions

The PLA/bioceramics models were constructed by placing the polymer chains on the surface. Molecular dynamic simulations were conducted on PLA/bioceramics interfacial model under NVT ensemble with a time step of 1 fs for 5 ps. The binding energies between the PLA and the surfaces were calculated after molecular dynamic simulations.

PLA/coupling agents/bioceramics interactions

Silane (3 acryloxypropyltrihydroxysilane) was used to investigate the effects of the coupling agents on the binding energies between the polylactic acid and bioceramics. The coupling agent models were built on all cleaved surfaces. 6-9 silane molecules were randomly distributed on the bioceramics surface. Geometry optimizations were performed on the surfaces /coupling agent systems. Then polylactic acid chains were placed on the systems. The molecular dynamic simulations were also conducted under NVT ensemble at 300 K temperature for 5 ps.

The adhesion between the polylactic acid and bioceramic surfaces can be evaluated by the interaction energy between them. The interaction energies were calculated through the following equation:

$$E_{interaction}=E_{surface+polymer} -(E_{surface}+E_{polymer}) \tag{1}$$

where $E_{surface+polymer}$ is the energy of the surface with PLA polymer, $E_{surface}$ is the energy of the surface and $E_{polymer}$ is the energy of the polymer. The binding energy is obtained by dividing the interaction energy to the number of monomers existing in the polymers. The high binding energy suggests high adhesive strength between the surface and the polymer.

The coupling agents increase molecular binding between bioceramics and polymers. The interaction energies in surface/coupling agent/polymer system:

$$E_{interaction} = E_{surface+coupling\ agent+polymer} - (E_{surface+coupling\ agent} + E_{polymer}) \quad (2)$$

where $E_{surface+coupling\ agent+polymer}$ is the energy of the surface with silane and PLA polymer, $E_{surface+coupling\ agent}$ is the energy of the surface with silane and $E_{polymer}$ is the energy of the polymer.

The molecular dynamics simulations were conducted using UFF force field [32] as implemented in the Forcite module of Materials Studio package [33]. The potential energy is expressed as a sum of valence or bonded interactions and non-bonded interactions.
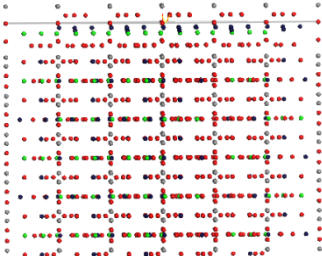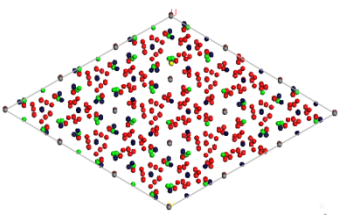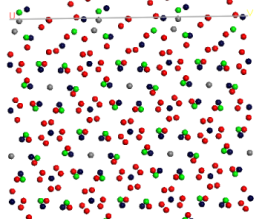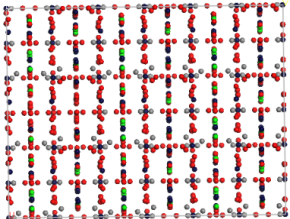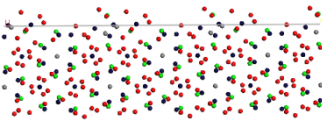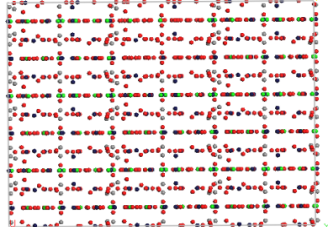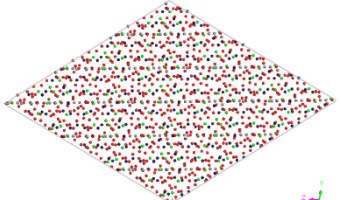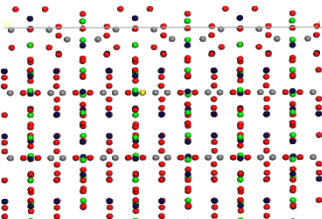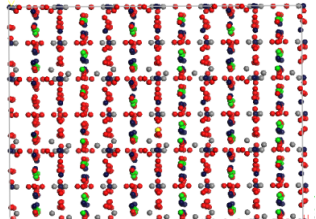
$$E = E_R + E_\theta + E_\Phi + E_\omega + E_{vdW} + E_{el} \quad (3)$$

The valence interactions consist of bond stretching (E_R) and angular distortions (Equation 3). Angular distortions include angle bending (E_θ), dihedral angle torsion (E_Φ) and inversion terms (E_ω). The non-bonded interactions involve van der Waals term (E_{vdW}) and electrostatic term (E_{el}).

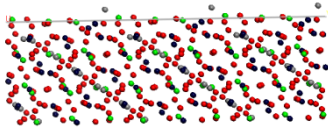**Table 3.** Models of zirconia surfaces. Color codes: blue represent zirconium atom and red the oxygen atom.

hhkl	front view	side view	top view
(0 0 1)			
(1 0 0)			
(1 1 0)			
(1 1 1)			
(-1 0 0)			

Table 4. Models of hydroxyapatite surfaces. Color codes: blue represent calcium, red oxygen, green phosphorus atom and gray hydrogen atoms

hkl	front view	top view
(0 0 1)		
(1 0 0)		
(1 1 0)		
(1 1 1)		
(-1 0 0)		

Molecular dynamics simulations were employed to study polylactic acid/bioceramics interface interactions. The study analyzed the binding energies between polylactic acid and two bioceramics: hydroxyapatite and zirconia. The interactions of polylactic acid on the surfaces crystallographic planes (0 0 1), (1 0 0), (1 1 0), (1 1 1) and (-1 0 0) were simulated. The effects of coupling agents on interfacial binding energies were also examined.

ACKNOWLEDGMENTS

REFERENCES

1. B. D. Ratner; A. S. Hoffman; F. J. Schoen; J. E. Lemons; *Biomaterials Science, An Introduction to Materials in Medicine* (Elsevier Academic Press, **2004**).
2. P. F. Manicone; P. Rossi Iommetti; L. Raffaelli; *J. Dent.* **2007**, *35,* 819–826.
3. J. R. Piascik; S. D. Wolter; B. R. Stoner; *Dent. Mater.* **2011**, *27,* e99–e105.
4. A. Attia; F. Lehmann; M. Kern; *Dent. Mater.* **2011**, *27,* 207–213.
5. R. L. Smith; C. Villanueva; J. K. Rothrock; C. E. Garcia-Godoy; B. R. Stoner; J. R. Piascik; J. Y. Thompson; *Dent. Mater.* **2011**, *27,* 779–785.
6. R. Amaral; M. Özcan; M. A. Bottino; L. F. Valandro; *Dent. Mater.* **2006**, *22,* 283–290.
7. S. Kitayama; T. Nikaido; R. Takahashi; L. Zhu; M. Ikeda; R. M. Foxton; A. Sadr; J. Tagami; *Dent. Mater.* **2010**, *26,* 426–432.
8. M. N. Aboushelib; H. Mirmohamadi; J. P. Matinlinna; E. Kukk; H. F. Ounsi; Z. Salameh; *Dent. Mater.* **2009**, *25,* 989–993.
9. J. P. Matinlinna; L. V. J. Lassila; P. K. Vallittu; *J. Dent.* **2006**, *34,* 740–746.
10. J. R. Piascik; E. J. Swift; J. Y. Thompson; S. Grego; B. R. Stoner; *Dent. Mater.* **2009**, *25,* 1116–1121.
11. J. P. Matinlinna; T. Heikkinen; M. Özcan; L. V. J. Lassila; P. K. Vallittu; *Dent. Mater.* **2006**, *22,* 824–831.
12. R. Di Maggio; S. Dirè; E. Callone; F. Girardi; G. Kickelbick; *Polymer (Guildf).* **2010**, *51,* 832–841.
13. R. P. Singh; J. D. Way; S. F. Dec; *J. Memb. Sci.* **2005**, *259,* 34–46.
14. J. Han; C. Zuo; Q. Gu; D. Li; X. Wang; G. Xue; *Appl. Surf. Sci.* **2008**, *255,* 2316–2321.
15. A. Casucci; E. Osorio; R. Osorio; F. Monticelli; M. Toledano; C. Mazzitelli; M. Ferrari; *J. Dent.* **2009**, *37,* 891–897.
16. J. F. Mano; R. A. Sousa; L. F. Boesel; N. M. Neves; R. L. Reis; *Compos. Sci. Technol.* **2004**, *64,* 789–817.
17. M. Darder; P. Aranda; E. Ruiz-Hitzky; *Adv. Mater.* **2007**, *19,* 1309–1319.

18. R. Murugan; S. Ramakrishna; *Compos. Sci. Technol.* **2005**, *65***,** 2385–2406.
19. J. Russias; E. Saiz; R. K. Nalla; K. Gryn; R. O. Ritchie; A. P. Tomsia; *Mater. Sci. Eng. C* **2006**, *26***,** 1289–1295.
20. L. Fang; Y. Leng; P. Gao; *Biomaterials* **2006**, *27***,** 3701–3707.
21. E. Smolko; G. Romero; *Radiat. Phys. Chem.* **2007**, *76***,** 1414–1418.
22. X. Zhang; Y. Li; G. Lv; Y. Zuo; Y. Mu; *Polym. Degrad. Stab.* **2006**, *91***,** 1202–1207.
23. Y. Zuo; Y. Li; J. Li; X. Zhang; H. Liao; Y. Wang; W. Yang; *Mater. Sci. Eng. A* **2007**, *452–453***,** 512–517.
24. M. Todo; S. D. Park; K. Arakawa; Y. Takenoshita; *Compos. Part A Appl. Sci. Manuf.* **2006**, *37***,** 2221–2225.
25. H. ping Zhang; X. Lu; Y. Leng; L. Fang; S. Qu; B. Feng; J. Weng; J. Wang; *Acta Biomater.* **2009**, *5***,** 1169–1181.
26. L. M. Mathieu; T. L. Mueller; P. E. Bourban; D. P. Pioletti; R. Müller; J. A. E. Månson; *Biomaterials* **2006**, *27***,** 905–916.
27. P. . De Santis; J. Kocacs; **1968**, *6***,** 299–306.
28. Y. Zhao; D. G. Truhlar; *Theor. Chem. Acc.* **2008**, *120***,** 215–241.
29. I. Irsai; A. Lupan; C. Majdik; R. Silaghi-Dumitrescu; *Stud. Univ. Babes-Bolyai Chem.* **2017**, *62***,** 495–513.
30. I. Irsai; C. Majdik; A. Lupan; R. Silaghi-Dumitrescu; *J. Math. Chem.* **2012**, *50***,** 703–733.
31. R. M. Wilson; J. C. Elliott; S. E. P. Dowker; *Am. Mineral.* **1999**, *84***,** 1406–1414.
32. A. K. Rappe; C. J. Casewit; K. S. Colwell; W. A. Goddard III; W. M. Skiff; *J. Am. Chem. Soc.* **1992**, *114***,** 10024–10035.
33. 2017 Dassault Systèmes BIOVIA, Materials Studio, 2017, San Diego: Dassault Systèmes.

A COMPUTATIONAL STUDY ON Ca^{2+} MODULATION OF ASIC 1 PHARMACOLOGIC PROPERTIES

RALUCA NICULAE[a], MARIA MERNEA[a*], LOREDANA GHICA[a], DAN FLORIN MIHĂILESCU[a]

ABSTRACT. Acid-sensing ion channel (ASIC) is involved in important processes like synaptic plasticity and learning, fear and anxiety, pain sensation. Due to its role in neurodegeneration and neuroinflammation, the channel is a viable pharmacological target. The channel is activated by acid pH pulses and it rapidly desensitizes; therefore the channel can exist in open, closed and desensitized states. Here we performed a molecular docking study of some ASIC1 ligands like amiloride, cocaine, histamine, ibuprofen, sinomenine and Zn^{2+} in the transmembrane region of ASIC1 channel models in different states (closed, open and desensitized). Also, since channel properties are influenced by Ca^{2+}, we performed a set of calculations when Ca^{2+} is present in the channel pore. In addition, we modelled mutant channels in different states with substitutions of residues forming Ca^{2+} binding sites. The interaction of ligands with mutant channel models was investigated in the presence and absence of Ca^{2+}. Our results show an affinity of ASIC1 for ibuprofen, followed by Zn^{2+}, histamine and amiloride. Sinomenine and cocaine do not appear as ASIC1 ligands regardless of channel state. Overall, Ca^{2+} enhances the interactions of ligands with the channels, including the interactions of cocaine that is not recognized as an ASIC1 ligand. The effect of mutations is to reduce the favourable interactions with ligands. The results obtained on the three channel states are consistent, showing that results are not significantly influenced by the choice of model. Our results bring new information on ASIC1 pharmacological modulation by showing that Ca^{2+} presence in the pore enhances channel affinity for ligands.

Keywords: *ASIC1, molecular docking, protein-ligand interaction, pharmacology*

INTRODUCTION

Acid-sensing ion channels (ASICs) are proton-activated ion channels that are part of the Na$^+$ channel superfamily along with sodium epithelial channel (ENaC), *Caenorhabitis elegans* degenerines (DEG), *Drosophila*

[a] *University of Bucharest, Faculty of Biology, Splaiul Independentei, 91-95, 050095, Bucharest, Romania*
[*] *Corresponding author: maria.mernea@bio.unibuc.ro*

melanogaster channels, „orphan" bile acid-activated channels BLINaC and INaC [1] and FMRF (Phe-Met-Arg-Phe-NH2) – activated sodium channels (FaNaC) of invertebrates [2].

The expression of ASIC channels in the nervous system is both central (ASIC 1a, -2a, -2b and -4) and peripheral (ASIC1-3), being involved in synaptic plasticity and learning [3], fear and anxiety [4], pain sensation [5], mechanosensation [6], ischemic stroke [7] and axonal degeneration in multiple sclerosis [8].

ASIC channels are highly expressed in the brain (ASIC1-4), especially in the hippocampus, amygdala, cerebellum and pituitary gland [9], but are also present in other regions like the cervix, uterus, endometrium, smooth muscles (ASIC2) [10]. They are mainly localized in the plasma membrane and the Golgi apparatus (ASIC1-4), nucleoplasm and cytosol (ASIC3), centriolar satellites and nucleoplasm (ASIC4) [3].

ASIC1a has a high selectivity for sodium ions, transports lithium ions with high efficiency and potassium ions with low efficiency. It mediates glutamate-independent entry of calcium into neurons under acidic conditions. Ca^{2+} overload is toxic to neurons and may be partly responsible for ischemic brain damage [11]. Injuries, inflammation, or ischemia are associated with a decrease of extracellular pH that has an activating role on ASIC channels [12].

ASIC1a works as a postsynaptic proton receptor that contributes to the postsynaptic excitatory current. In this case, ASIC channels sense the pH changes in the synaptic cleft upon neurotransmission [13]. A sudden drop of extracellular pH will produce a transient activation of ASICs followed by a rapid desensitization. Two types of desensitization were described in the case of ASIC, namely a low pH desensitization in which channels are shut from the open state and a steady-state desensitization that shuts the channel from a pre-open closed state [2]. ASIC1a properties are modulated by Ca^{2+}, the cation being responsible for a reduction in amplitude of ASIC1a currents and for shifting the activation pH to more acidic values [14, 15].

Previous studies have shown that the inhibition of ASIC1a by psalmotoxin 1 (PcTx1) reduced the infarct volume in the experimental stroke model by > 60% [12] and intracerebroventricular administration of PcTx1 up to 5 hours after transient occlusion of the middle cerebral artery reduced the infarct volume by 0.50% [16], thus demonstrating an important contribution of ASIC1a to stroke-induced ischemic neurodegeneration and the beneficial outcome of ASIC1a inhibition in such a situation. Moreover, disruption of ASIC gene or inhibition of ASIC function has shown a protective effect in several neurodegenerative diseases, including multiple sclerosis (MS), Huntington's disease and Parkinson's [17] or a reduced clinical deficit and axonal degeneration in experimental autoimmune encephalomyelitis [8]. Due

to its involvement in before mentioned pathological processes, ASIC represents a viable target in neurodegeneration and neuroinflammation [18].

Also, ASIC1 is considered a target in pain and inflammatory processes [18]. In the inflammation process, histamine potentiates ASIC1, leading to hypersensitivity [18]. ASIC1 can be inhibited by anti-inflammatory drugs like ibuprofen, contributing to the analgesic effect and limiting the inflammation [19].

In the present study we performed molecular docking calculations to investigate the interaction of ASIC1 with six possible ligands: a metal ion, namely Zn^{2+} and five small molecules, namely amiloride, ibuprofen, sinomenine, histamine and cocaine. The selected molecules present different affinities for ASIC1 (Zn^{2+} > sinomenine > amiloride > ibuprofen > histamine > cocaine) and different effects, being inhibitors (Zn^{2+}, sinomenine, amiloride, ibuprofen), activators (histamine) or with unknown effect (cocaine). Zn^{2+} is the single metal ion that we considered in the study. In comparison to other metal ions that inhibit ASIC1, like Cu^{2+}, Pb^{2+}, Cd^{2+} or Ni^{2+} (in µM concentrations or undetermined) [20], Zn^{2+} is the strongest inhibitor, acting on ASIC1a in nM concentrations (IC$_{50}$ = ~0.007 µM) [21]. Sinomenine, a bioactive alkaloid, is a strong inhibitor of ASIC1 (IC$_{50}$ of ~0.3 µM [22]) with a broad spectrum analgesic efficacy [23]. Amiloride, a K$^+$-sparing diuretic, is a strong blocker of ASIC1a channels, with an IC$_{50}$ value of ~10 µM [24], while ibuprofen, a non-steroid anti-inflammatory drug is a low potency inhibitor of ASIC1a, with a IC$_{50}$ of ~350 µM [25]. Histamine is an endogenous compound that induces a voltage-independent potentiation of ASIC1a homomers [26], with an IC$_{50}$ of ~480 µM [27]. In the case of cocaine, recent data obtained on rats showed an association between the overexpression of ASIC1a in nucleus accumbens and the enhancement of cocaine–seeking behaviour [28]. Even if there is no evidence of a direct interaction between cocaine and ASIC1 [29], the compound was included in the present study since lidocaine, a cocaine derivative, inhibits ASIC1 when found in large concentrations (IC$_{50}$ = ~12 mM) [19].

Since multiple crystal structures of ASIC1 are available in Protein Data Bank (PDB) [30], we performed docking calculations using three ASIC1 structures in different states, namely open [31], closed [32] and desensitized [14]. Considering Ca^{2+} effect on ASIC1 functioning, we performed calculations on native structures and on structures with a Ca^{2+} ion placed in the transmembrane (TM) region of the pore, as performed in a previous study [33]. Paukert et al. [15] reported two mutations that render ASIC1a insensitive to Ca^{2+}, namely D433 and E426. Here we also considered the docking of ligands to mutant channels presenting a single mutation at E426 or two mutations at E426 and D433, with and without Ca^{2+}.

Previous molecular docking studies performed on ASIC1 have focused on two regions: the "acidic pocket" (cluster of acidic residues) found in the extracellular region of the channel that is targeted by compounds that modify channel gating [34, 35] and the TM channel pore that is targeted by pore blocking compounds [36, 37]. Amiloride and ibuprofen appear to bind in the TM pore [38, 39], therefore we explore the binding of all selected compounds in the same region. Histamine binding to ASIC1 was previously investigated by molecular docking, but it was docked in the "acidic pocket" [34]. The binding of amiloride to ASIC1 was determined by X-ray crystallography [38], a comparison between the experiment and our results is found in Results and Discussion section. In the case of the other compounds, their docking to ASIC1 is performed here for the first time. In the present study we systematically investigate the binding of ligands on ASIC1a channels with different TM pores conformations according to their activation state, in the presence and absence of Ca^{2+}, resulting in new information on the binding sites of compounds and on the interference of Ca^{2+} with ASIC1a pharmacologic blockade.

RESULTS AND DISCUSSION

Native and mutant ASIC1 structures in different states

In the present study we considered three ASIC1 structures in different states. Information on the structures is summarized in Table 1. 2QTS represents the channel in a closed, desensitized-like state [19], 4FZ0 represents the channel activated by PcTx1, in an open state [18] and 6CMC represents the structure in a desensitized state [20].

Table 1. Description of ASIC1 structures used in the present study

PDB ID	Description	Ligands	pH	Resolu-tion (Å)	Organism	Function	Refer-ence
4FZO	ASIC1a structure with plasmatoxin 1 at 5.5 pH	PcTx1	5.5	2.8	*Gallus gallus*	Functional, open state	[31]
2QTS	ASIC1a structure at low pH	N/A	5.6	1.9	*Gallus gallus*	Nonfunctional, closed state	[32]
6CMC	Barium sites in the structure of a desensitized acid sensing ion channel	Barium	6.9	3.67	*Gallus gallus*	Functional, desensitized	[14]

The architecture of TM pore regions is particular in each state, as presented in Figure 1. In the case of 2QTS, the TM pore is occluded around kinks in the second TM helices (TM2) of two subunits (A and B), near the selectivity filter represented by the GAS motif. Toward the extracellular, the pore opens in a wide outer vestibule [19]. Due to the interaction with PcTx1 in 4FZ0 structure, the outer vestibule is larger, and the TM pore is stabilized in an open conformation, being selective to Na^+ ions. Residues forming the GAS motif are exposed to the extracellular side of the membrane and TM2 helices of subunits A and B are slightly tilted, a resemblance with 2QTS structure [18]. In 6CMC structure, the TM2 helices of ASIC subunits are discontinuous, being interrupted by the residues in the selectivity filter that form a belt-like structure. After the interruption, the cytoplasmic regions of TM2 helices are swapped between adjacent subunits, these features being described in [18].
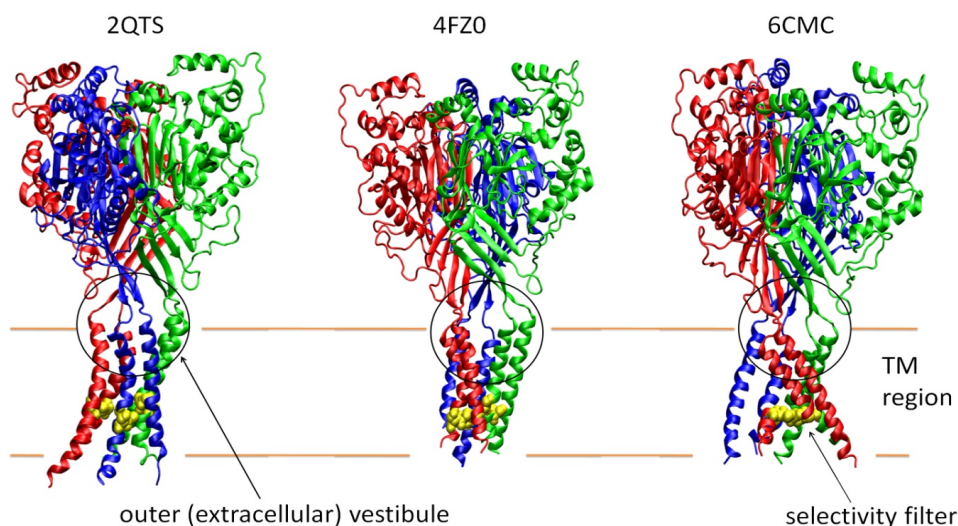

Figure 1. 3D structures of ASIC1 channel in different states: closed, desensitized-like (2QTS structure), open (4FZ0) and desensitized (6CMC). The channels are homotrimers, subunits A are coloured with blue, subunits B are coloured with red and subunits C are coloured in green. The residues from the selectivity filter are represented as van der Waals spheres coloured in yellow. The plasma membrane is schematically represented with orange lines in order to highlight the TM regions of channels. The outer vestibules representing the location where Ca^{2+} and ligands were docked are circled with black.

Mutant channel models were built by changing the residues D433 and E426 that represent Ca^{2+} binding sites [22]. These are located in the TM regions of the channels, in the outer vestibules. The mutations that we modelled are E426G and D433C, meaning that we replaced the negatively charged residues with neutral residues. This has an important impact on the electrostatics of the outer vestibules, as presented in Figure 2. In the case of all three crystal structures, the outer vestibule is electronegative, being coloured with red. The introduction of a single mutation and of two mutations renders the outer vestibule increasingly electropositive, which can be seen as an increase in areas coloured in blue. Even more, we prepared a set of structures with Ca^{2+} in the pore. The ion additionally perturbs the electrostatics of the TM pores. The ion brings two positive charges that on top of the replacement of negative residues leads to a channel pore that is strongly electropositive (in Figure 2 we represented the electrostatics of the double mutant channels with Ca^{2+}). We expect these changes to have an important impact on the interaction between ASIC1 and the six ligands that we considered.
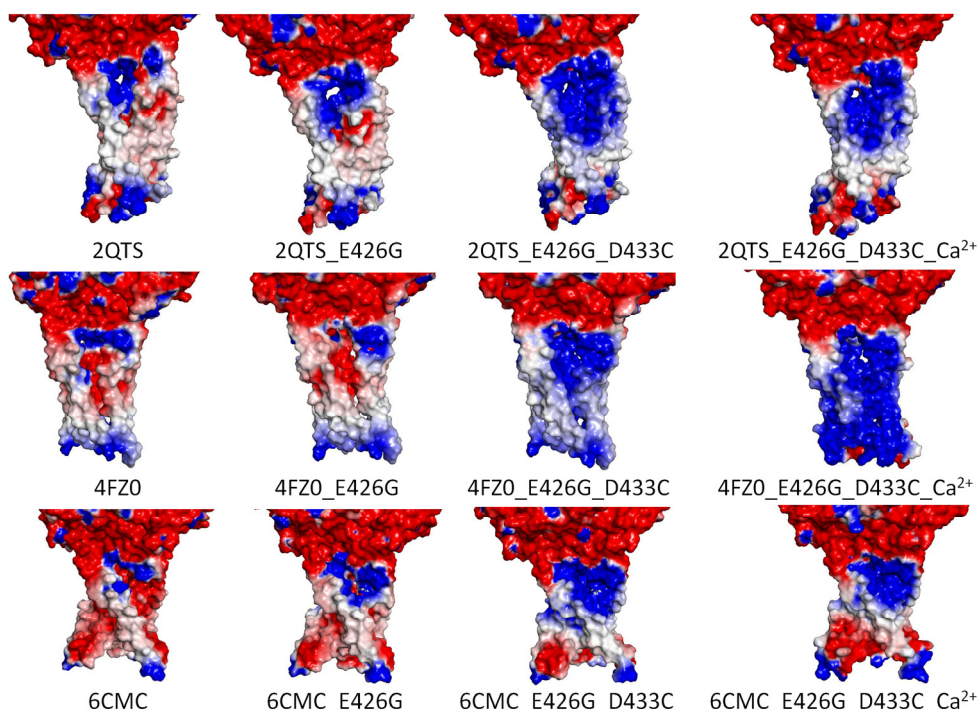

Figure 2. Details on TM regions of native, mutant ASIC1 models and double mutant model with Ca^{2+} represented as surfaces coloured according to the distribution of electrostatic potential. Red is used to highlight electronegative regions and blue is used for electropositive regions.

Physicochemical properties of considered ASIC1 ligands

In our study we considered six ligands: amiloride, cocaine, histamine, ibuprofen, sinomenine and Zn^{2+}. The properties of the ligand molecules that we considered are presented in Table 2. It can be seen that compounds present a variable number of hydrogen bonds donors and acceptors, from a total of 3 in the case of cocaine and ibuprofen, to a total of 12 in the case of amiloride. Amiloride is the most rigid molecule, presenting only 1 rotable bond while cocaine is the most flexible molecule, presenting 5 rotable bonds. Ibuprofen presents the smallest polar surface area (37.3 Å^2), followed by cocaine, histamine and sinomenine (~55 Å^2) and the largest polar surface area was seen in the case of amiloride (156.79 Å^2). According to logP (partition coefficient) values, cocaine, ibuprofen and sinomenine are hydrophobic while amiloride and histamine are hydrophilic. The differences in the physicochemical properties of ligands suggest differences in their interaction with ASIC1 channel models.

Table 2. Physicochemical properties of considered ASIC1 ligands. The data was retrieved from DrugBank [40], except for sinomenine, whose properties were retrieved from PubChem [41].

Ligand	No. of H-bonds donors	No. of H-bonds acceptors	No. of rotable bonds	No of aromatic rings	Polar surface area (PSA, in Å^2)	LogP
Amiloride	5	7	1	1	156.79	-0.5
Cocaine	0	3	5	3	55.84	2.28
Histamine	2	2	2	1	54.7	-0.7
Ibuprofen	1	2	4	1	37.3	3.84
Sinomenine	1	5	2	4	59	2.2

Docking of ligands to native ASIC1 structures in the absence of Ca^{2+}

Initially amiloride, cocaine, histamine, ibuprofen, sinomenine and Zn^{2+} were docked at the native channel structures in the three states. CDOCKER algorithm has generated 10 poses for each ligand at each structure, but only the top ranking pose was analysed here. CDOCKER energies of these poses were retrieved and compared in order to estimate which ligands present the strongest interaction. These are represented in Figure 3 and values are reported in Table 3.

In the closed state (2QTS structure), the best binding ligand is ibuprofen (CDOCKER energy = -34.17 kcal/mol), followed by Zn^{2+} (CDOCKER energy = -29.45 kcal/mol), histamine (CDOCKER energy = -11.57 kcal/mol)

and amiloride (CDOCKER energy = -2.35 kcal/mol). Unfavourable interactions were obtained for sinomenine (CDOCKER energy = 5.10 kcal/mol) and cocaine (CDOCKER energy = 10.86 kcal/mol). In the case of ASIC1 in open state (4FZ0 structure), the compounds ordered from the most favourable to the most unfavourable binding are: Zn2+ (CDOCKER energy = -45.28 kcal/mol) > ibuprofen (CDOCKER energy = -31.36 kcal/mol) > histamine (CDOCKER energy = -11.41 kcal/mol) > amiloride (CDOCKER energy = 2.75 kcal/mol) > sinomenine (CDOCKER energy = 13.20 kcal/mol) > cocaine (CDOCKER energy = 16.78 kcal/mol). The order of ligands based on the interaction with ASIC1 in desensitized state (6CMC structure) is: ibuprofen (CDOCKER energy = -31.78 kcal/mol) > histamine (CDOCKER energy = -24.64 kcal/mol) > Zn^{2+} (CDOCKER energy = -18.79 kcal/mol) > amiloride (CDOCKER energy = -18.75 kcal/mol) > sinomenine (CDOCKER energy = -1.30 kcal/mol) > cocaine (CDOCKER energy = 0.94 kcal/mol).

Table 3. CDOCKER Energy determined for the ligands docked at native, simple and double mutation ASIC1 channel models in the three states: closed (2QTS), open (4FZO) and desensitized (6CMC). Results are given for the two datasets: without and with Ca^{2+}.

Ligand name	Receptor structure	CDOCKER energy (kcal/mol)					
		wt		E426G		E426G_D433C	
		no Ca^{2+}	with Ca^{2+}	no Ca^{2+}	with Ca^{2+}	no Ca^{2+}	with Ca^{2+}
Amiloride	2qts	-2.36	-9.40	-2.79	-10.07	-3.83	-8.21
	4fzo	2.75	-16.45	2.77	-9.19	-2.11	-12.77
	6cmc	-18.75	-28.26	-12.00	-13.04	-8.95	-13.09
Cocaine	2qts	10.86	-1.61	9.43	4.24	5.16	4.54
	4fzo	16.78	-3.92	15.75	-0.43	9.98	-1.56
	6cmc	0.94	-4.83	-0.52	4.34	-0.53	-6.48
Histamine	2qts	-11.57	-19.39	-13.59	-18.58	-13.30	-14.76
	4fzo	-11.41	-20.80	-9.25	-18.54	-11.83	-22.77
	6cmc	-24.64	-25.61	-20.58	-16.34	-18.22	-23.43
Ibuprofen	2qts	-34.17	-50.13	-29.14	-48.66	-29.95	-44.89
	4fzo	-31.36	-55.00	-15.65	-47.08	-32.55	-52.63
	6cmc	-31.78	-49.27	-34.89	-45.69	-39.60	-50.84
Sinomenine	2qts	5.10	2.15	4.35	-2.91	4.19	4.35
	4fzo	13.20	5.02	15.41	-4.01	11.39	0.83
	6cmc	-1.30	30.01	-0.04	-4.98	2.59	4.00
Zinc	2qts	-29.45	-16.87	-9.10	-21.75	-13.01	-6.79
	4fzo	-45.28	-14.83	-6.40	-15.95	-8.69	5.37
	6cmc	-18.79	0.98	-45.31	-9.49	-6.51	5.34

By comparing the results we observe that ibuprofen presents the most favourable interaction with ASIC1 independent of channel state. A similar situation can be seen in the case of histamine, but the interaction is less favourable than in the case of ibuprofen and in the case of Zn^{2+} where the interaction with the open channel structure is more favourable than the interactions with the closed or desensitized channels.

Amiloride presents the most favourable interactions with the desensitized channel and even unfavourable interactions with the open channel. The binding of amiloride in ASIC1 TM pore of the desensitized state structure is confirmed by the X-ray diffraction study of Baconguis et al [38] on ASIC1 crystals soaked in amiloride. They identified that the TM pore of ASIC1 is partially occluded by three amiloride molecules bound at superficial locations. The authors suggested that pore blockage should occur when amiloride is bound in a deeper location [38]. In the same study, the authors identified amiloride molecules bound in the extracellular domains, in the "acid pockets" [38], confirming the existence of a second amiloride binding site in the extracellular domain [2]. In the case of closed and open state channels, there is no structural evidence on the binding of amiloride into the TM pores.
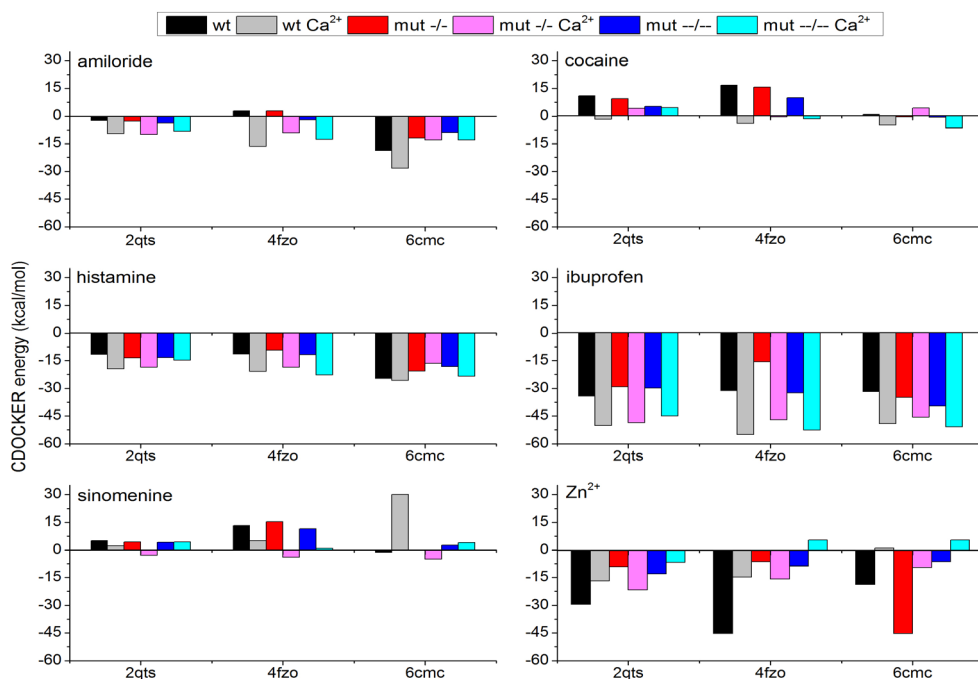

Figure 3. CDOCKER energies associated to the best docking pose of considered ligands at native and mutant ASIC1 channel structures, with and without Ca^{2+}. Docking of ligands to native ASIC1 structures in the presence of Ca^{2+}.

Sinomenine presents unfavourable binding with the closed and open channels and slight favourable binding with the desensitized channel structure. This data suggests that sinomenine does not bind in ASIC1 TM pore. Since data from the literature support the inhibitory effect of sinomenine on ASIC1 [26], we could assume that its binding site was not sampled here and it might be located elsewhere.

In the case of cocaine, it presents unfavourable interactions with all structures, but especially with the closed and open channels. This result was expected, as there are no indications to cocaine being an ASIC1 ligand.

Docking of ligands to native ASIC1 structures in the presence of Ca^{2+}

As can be seen in Figure 3 and according to the data in Table 3, the presence of Ca^{2+} mostly enhances the favourable interactions, with some exceptions that will be discussed below. In the case of the closed channel, we observe that Ca^{2+} facilitates the interaction with ibuprofen (CDOCKER energy = -50.13 kcal/mol), histamine (CDOCKER energy = -19.39 kcal/mol), amiloride (CDOCKER energy = -9.40 kcal/mol), cocaine (CDOCKER energy = -1.61 kcal/mol) and even renders more favourable the interaction with sinomenine (CDOCKER energy = 2.15 kcal/mol). It is worth mentioning that cocaine presents an unfavourable interaction with the channel in the absence of Ca^{2+}, but the presence of Ca^{2+} stabilizes the interaction. Also, as expected due to the positive charge of Ca^{2+}, the interaction with Zn^{2+} becomes less favourable (CDOCKER energy = -16.87 kcal/mol).

The interaction of the open channel model with the ligands (except for Zn^{2+}) becomes more favourable in the presence of Ca^{2+}, in a similar manner as observed in the case of the closed channel. The ligands ordered based on their affinity to the channel bound to Ca^{2+} is: ibuprofen (CDOCKER energy = -55.00 kcal/mol), histamine (CDOCKER energy = -20.80 kcal/mol), amiloride (CDOCKER energy = -16.45 kcal/mol), Zn^{2+} (CDOCKER energy = -14.83 kcal/mol), cocaine (CDOCKER energy = -3.92 kcal/mol). Due to the presence of Ca^{2+} the interactions with amiloride and cocaine have become favourable, while the interaction with Zn^{2+} has become less favourable than in the absence of Ca^{2+}. Less unfavourable interaction energies can be seen in the case of sinomenine (CDOCKER energy = 5.02 kcal/mol).

In the case of the channel in desensitized state, the presence of Ca^{2+} also changes the interactions. These become more favourable for ibuprofen (CDOCKER energy = -49.27 kcal/mol), amiloride (CDOCKER energy = -28.26 kcal/mol), histamine (CDOCKER energy = -25.61 kcal/mol) and cocaine (CDOCKER energy = -4.83 kcal/mol). The interactions with Zn^{2+} (CDOCKER energy = 0.98 kcal/mol) and sinomenine (CDOCKER energy = 30.01 kcal/mol) become unfavourable.

Ca^{2+} is important for ASIC1 activity as it was proved to be an allosteric modulator and channel blocker [42]. Therefore, we considered appropriate to investigate the interaction with ligands in the presence of Ca^{2+}. Overall, regardless of channel state, our results suggest that Ca^{2+} enhance the interactions with ibuprofen, histamine, amiloride and cocaine. This is especially interesting for cocaine that presented unfavourable binding to the channels in the absence of Ca^{2+}. The interactions with sinomenine become more favourable in the presence of Ca^{2+}, except for the structure in desensitized state. Zn^{2+} also presents less favourable interactions with the channels and even unfavourable interactions with the channel in desensitized state with Ca^{2+}.

Docking of ligands to mutant ASIC1 models

According to CDOCKER energies presented in Table 3 and Figure 3, the mutations impact the interactions with ligands, both in the absence and in the presence of Ca^{2+}. The results depend on the state of the channel. For instance, in the case of ibuprofen, in comparison to the native channel, the interaction is slightly less favourable with mutant channel models in closed state in the absence (CDOCKER energy = -29.14 kcal/mol for simple mutation and -29.95 kcal/mol for double mutation) and presence of Ca^{2+} (CDOCKER energy = -48.66 kcal/mol for single mutation and -44.89 kcal/mol for double mutation), Ca^{2+} having the same effect on enhancing CDOCKER energies. In the open state models, relative to the native channel, the single mutation model presents less favourable interaction energies (CDOCKER energy = -15.65 kcal/mol without Ca^{2+} and -47.08 kcal/mol with Ca^{2+}), while the double mutant model presents slightly more favourable interaction energies (CDOCKER energy = -32.55 kcal/mol without Ca^{2+} and -52.63 kcal/mol with Ca^{2+}). In the desensitized state, mutant channels present enhanced favourable interaction energies relative to the native channel (CDOCKER energy for single mutation model = -34.89 kcal/mol without Ca^{2+} and -45.69 kcal/mol with Ca^{2+}; CDOCKER energy for double mutation model = -39.60 kcal/mol without Ca^{2+} and -50.84 kcal/mol with Ca^{2+}).

Amiloride docking at mutant channels in closed states resulted in more favourable GDOCKER energies, especially in the presence of Ca^{2+}. The docking of amiloride to native and single mutation models leads to positive CDOCKER energies (loss of inhibition), only the double mutant channel model in open conformation presents favourable interactions with amiloride. The presence of Ca^{2+} results in favourable interactions between mutant channel models in open state and amiloride. The tendency is inverse in the case of desensitized mutant channel models, where the interactions with amiloride become less favourable, without significant differences in the presence of Ca^{2+}.

The docking of cocaine to mutant channel models results in positive GDOCKER energies (unfavourable) in the absence of Ca^{2+}. Only the mutant channels in open conformation and the double mutant channel in desensitized state, all in the presence of Ca^{2+}, present slightly favourable interactions with cocaine. Histamine presents favourable interactions with mutant channel models regardless of state and the addition of Ca^{2+} enhances the interactions, except for the interaction with single mutation channel in desensitized state. Sinomenine presents unfavourable interactions with ASIC1 mutant channel models, especially with the mutants in open state. It appears that favourable interactions can be seen only in the case of single mutation channels with Ca^{2+}, regardless of channel state. The interaction with Zn^{2+} is less favourable in the case of mutant channel models regardless of state, except for the single mutation channel model in desensitized state, where the interaction with Zn^{2+} is significantly enhanced.

Based on above presented results, it appears that the change in pore electrostatics trough mutations has different effects of the affinity for ligands, increasing the affinity toward some of them, like amiloride or decreasing the affinity for others, like Zn^{2+}. The affinity toward the ligand used as negative control increases in mutant channel models and in the presence of Ca^{2+}.

CONCLUSIONS

Here we performed a systematic investigation on the interaction between six ligands (amiloride, cocaine, histamine, ibuprofen, sinomenine and Zn^{2+}) and ASIC1 channel models in different states (closed, open, desensitized), with and without a Ca^{2+} ion placed in the outer vestibule of the pore. In the study we sampled the outer channels vestibules; sampling other sites in the extracellular domain being a future perspective.

Our results point towards ibuprofen as a high affinity ligand that binds in the TM regions of the channels, regardless of state. Other ligands showing an affinity for this region are Zn^{2+}, histamine and amiloride. Sinomenine and cocaine do not present a favourable binding in TM pores of ASIC1 models. The result was expected in the case of cocaine. In the case of sinomenine, a proved inhibitor of ASIC1, we hypothesize that its binding site is located in a different region than the TM pore.

Obtained results are consistent in the case of channels in the three states for cocaine, histamine, ibuprofen, sinomenine and Zn^{2+} showing that the choice of model doesn't significantly impact results. Differences were obtained in the case of amiloride, where our docking calculations show a strong favourable interaction with the channel in desensitized state, a weak favourable interaction with the channel in closed state and an unfavourable interaction with the channel in open state.

Adding of Ca^{2+} ion enhances the favourable energies in the case of all ligands except for Zn^{2+} that is also a divalent cation. Changing the electrostatics of the pore by mutations has altered the interaction with ligands, mostly making them less favourable. In the case of some ligands like amiloride, mutant channel models present an increased affinity.

Our study brings new information of the pharmacological modulation of ASIC1, as we showed that the presence of Ca^{2+}, a channel modulator and blocker, enhances the affinity for ligands.

EXPERIMENTAL SECTION

Preparation of protein structures for docking

The crystal structures of ASIC1 under the PDB codes 2QTS, 4FZO and 6CMC were retrieved from Protein Data Bank and were used to generate the coordinates of the receptor. All water molecules and other hetero atoms were removed from the structures. The following operations performed on the structures, including refinement, modelling of mutations, and adding of Ca^{2+} were performed in Biovia Discovery Studio (BIOVIA Inc., https://www.3ds.com).

Initially, the native structures were checked for valence, lack of hydrogen and any structural disturbances of connectivity or connection order. Energy minimization was performed to achieve a stable protein conformation. Mutant channel models starting from each of the three crystal structures were built by considering a single mutation, namely E426G (single mutation models) and two mutations, namely E426G and D433C (double mutations models). Mutant channels were modelled as previously described in [33].
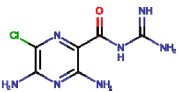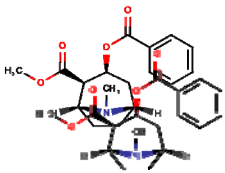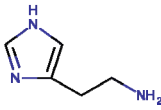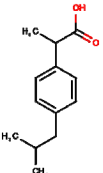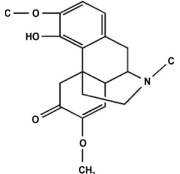
Native and mutant structures with Ca^{2+} were obtained by placing an ion in the transmembrane pore of the channel. As a reference region for placing Ca^{2+} and afterwards the ligands we considered the selectivity filter of the channels represented by the "GAS" motif [32]. The selectivity filters in each structure are marked in Figure 1, as well as the area considered for Ca^{2+} and ligands binding, located above the selectivity filter, in a region called the outer vestibule [18-20]. Ca^{2+} was placed in an optimal position identified by docking calculations using the CDOCKER algorithm implemented in Biovia Discovery Studio.

At the end of structure preparation stage of our study we obtained 18 starting structures representing native and mutant channels modelled according to the three 3D structures (2QTS, 4FZ0 and 6CMC), with and without Ca^{2+} bound in their outer vestibules. The following stage was represented by docking the six ligands to all these models, resulting in a total of 108 docking models.

Molecular docking

Molecular docking is a computational method that predicts the affinity of a ligand for a receptor. The docking of six ligands (amiloride, cocaine, histamine, ibuprofen, sinomenine and Zn^{2+}) in the outer vestibule of ASIC1a native and mutant models was performed using CDOCKER, in Biovia Discovery Studio. The chemical structures of the six ligands are presented in Table 4. Their physicochemical properties were also retrieved from DrugBank. The structures of compounds were retrieved from Drug Bank [30]. Their 3D structures and parameters in CHARMm force field were generated using Biovia Discovery Studio.

Table 4. Details of inhibitors

Molecule name	Chemical structure	Molecular formula	Molecular weight g/mol
Amiloride		$C_6H_8ClN_7O$	229.63
Cocaine		$C_{17}H_{21}NO_4$	303.35
Histamine		$C_5H_9N_3$	111.08
Ibuprofen		$C_{13}H_{18}O_2$	206.28
Sinomenine		$C_{19}H_{23}NO_4$	329.4
Zinc cation	Zn^{++}	Zn^{2+}	65.4
Calcium cation	Ca^{++}	Ca^{2+}	40.08

CDOCKER is a molecular dynamics simulated-annealing-based algorithm, using CHARMm force field (HARvard Macromolecular Mechanical Chemistry) for refining the structure [43]. CDOCKER algorithm involved 2000 steps of structure heating up to 700 K followed by 5000 steps of structure cooling to 300 K. The output of CDOCKER was represented by a set of 10 possible docking poses ranked by their CDOCKER energies (interaction energy between receptor and ligand and internal ligand strain energy) and CDOCKER interaction energies (nonbonded energy between receptor and ligand). More negative values are associated with a more favourable interaction. The best ranked pose in all cases was retained for further analysis.

ACKNOWLEDGMENTS

REFERENCES

1. M. Paukert, E. Babini, M. Pusch,S. Grunder, *J Gen Physiol*, **2004**. 124(4): p. 383-94.
2. S. Kellenberger,L. Schild, *Pharmacol Rev,* **2015**. 67(1): p. 1-35.
3. J. Du, L. R. Reznikov,M. J. Welsh, *PLoS One*, **2014**. 9(12): p. e115310.
4. A.E. Ziemann, J.E. Allen, N.S. Dahdaleh, Drebot, II, M.W. Coryell, A.M. Wunsch, C.M. Lynch, F.M. Faraci, M.A. Howard, 3rd, M.J. Welsh, J.A. Wemmie. *Cell*, **2009**. **139**, 1012-21.
5. N.K. Isaev, E.V. Stelmashook, E.Y. Plotnikov, T.G. Khryapenkova, E.R. Lozier, Y.V. Doludin, D.N. Silachev,D.B. Zorov, *Biochemistry* (Mosc), **2008**. 73(11): p. 1171-5.
6. C.C. Chen,C.W. Wong, *J Cell Mol Med,* **2013**. 17(3): p. 337-49.
7. S. Chai, M. Li, D. Branigan, Z.G. Xiong,R.P. Simon, *J Biol Chem*, **2010**. 285(17): p. 13002-11.
8. M.A. Friese, M.J. Craner, R. Etzensperger, S. Vergo, J.A. Wemmie, M.J. Welsh, A. Vincent,L. Fugger, *Nat Med,* **2007**. 13(12): p. 1483-9.
9. O. Alijevic,S. Kellenberger, *J Biol Chem*, **2012**. 287(43): p. 36059-70.
10. Y.Z. Wang, J.J. Wang, Y. Huang, F. Liu, W.Z. Zeng, Y. Li, Z.G. Xiong, M.X. Zhu,T.L. Xu, *Elife*, **2016**. 5.
11. X.P. Chu,Z.G. Xiong, *Adv Exp Med Biol,* **2013**. 961: p. 419-31.
12. Z.G. Xiong, X.M. Zhu, X.P. Chu, M. Minami, J. Hey, W.L. Wei, J.F. MacDonald, J.A. Wemmie, M.P. Price, M.J. Welsh,R.P. Simon, *Cell*, **2004**. 118(6): p. 687-98.

13. D.M. MacLean,V. Jayaraman, *Proc Natl Acad Sci USA*, **2017**. 114(12).
14. N. Yoder,E. Gouaux, *PLoS One*, **2018**. 13(12): p. e0209147.
15. M. Paukert, X. Chen, G. Polleichtner, H. Schindelin,S. Grunder, *J Biol Chem,* **2008**. 283(1): p. 572-81.
16. G. Pignataro, O. Cuomo, E. Esposito, R. Sirabella, G. Di Renzo,L. Annunziato, *Int J Physiol Pathophysiol Pharmacol,* **2011**. 3(1): p. 1-8.
17. J.A. Wemmie, R.J. Taugher,C.J. Kreple, *Nat Rev Neurosci,* **2013**. 14(7): p. 461-71.
18. R.V. A. O. Ramírez, E. Soto, *Mediators Inflamm*., **2017**.
19. A. Baron,E. Lingueglia, *Neuropharmacology*, **2015**. 94: p. 19-35.
20. S. Gründer,X. Chen, *International journal of physiology, pathophysiology and pharmacology*, **2010**. 2(2): p. 73-94.
21. K.A. Sluka, O.C. Winter,J.A. Wemmie, *Curr Opin Drug Discov Devel*, **2009**. 12(5): p. 693-704.
22. D.I. Osmakov, T.A. Khasanov, Y.A. Andreev, E.N. Lyukmanova,S.A. Kozlov, *Frontiers in pharmacology*, **2020**. 11: p. 991-991.
23. W. Jiang, W. Fan, T. Gao, T. Li, Z. Yin, H. Guo, L. Wang, Y. Han,J.-D. Jiang, *Pain Research and Management*, **2020**. 2020: p. 1876862.
24. R. Waldmann, G. Champigny, F. Bassilana, C. Heurteaux,M. Lazdunski, *Nature*, **1997**. 386(6621): p. 173-7.
25. S. Ugawa, Y. Ishida, T. Ueda, K. Inoue, M. Nagao,S. Shimada, *Biochem Biophys Res Commun*, **2007**. 363(1): p. 203-8.
26. O.I. Barygin, M.S. Komarova, T.B. Tikhonova, A.S. Korosteleva, M.V. Nikolaev, L.G. Magazanik,D.B. Tikhonov, *Channels*, **2017**. 11(6): p. 648-659.
27. C. González-Inchauspe, M.N. Gobetto, O.D. Uchitel, *Neuroscience*, **2020**. 439: p. 195-210.
28. A.L. Gutman, C.V. Cosme, M.F. Noterman, W.R. Worth, J.A. Wemmie,R.T. LaLumiere, *Addict Biol*, **2020**. 25(2): p. e12690.
29. C.J. Kreple, Y. Lu, R.J. Taugher, A.L. Schwager-Gutman, J. Du, M. Stump, Y. Wang, A. Ghobbeh, R. Fan, C.V. Cosme, L.P. Sowers, M.J. Welsh, J.J. Radley, R.T. LaLumiere,J.A. Wemmie, *Nature Neuroscience*, **2014**. 17(8): p. 1083-1091.
30. H.M. Berman, J. Westbrook, Z. Feng, G. Gilliland, T.N. Bhat, H. Weissig, I.N. Shindyalov, P.E. Bourne, *Nucleic Acids Research*, **2000**. 28: p. 235-242.
31. I. Baconguis,E. Gouaux, *Nature*, **2012**. 489(7416): p. 400-5.
32. J. Jasti, H. Furukawa, E.B. Gonzales,E. Gouaux, *Nature*, **2007**. 449(7160): p. 316-23.
33. M.M. L. L. Ghica, R. Niculae, D. F. Mihailescu, *rpj*, **2020**. 65: p. 9-10.
34. V.S. Korkosh,D.B. Tikhonov, *Dokl Biochem Biophys*, **2019**. 485(1): p. 111-114.
35. Y. Liu, J. Ma, R.L. DesJarlais, R. Hagan, J. Rech, D. Lin, C. Liu, R. Miller, J. Schoellerman, J. Luo, M. Letavic, B. Grasberger,M. Maher, *Communications Biology*, **2021**. 4(1): p. 174.
36. A.V. Ilyaskin, A. Diakov, C. Korbmacher,S. Haerteis, *Physiological reports,* **2017**. 5(3): p. e13132.

37. A. Schmidt, G. Rossetti, S. Joussen,S. Gründer, *Mol Pharmacol*, **2017**. 92(6): p. 665-675.
38. I. Baconguis, C.J. Bohlen, A. Goehring, D. Julius, E. Gouaux, *Cell*, **2014**. 156(4): p. 717-29.
39. T. Lynagh, J.L. Romero-Rojo, C. Lund, S.A. Pless, *Journal of Medicinal Chemistry,* **2017**. 60(19): p. 8192-8200.
40. D.S. Wishart, C. Knox, A.C. Guo, S. Shrivastava, M. Hassanali, P. Stothard, Z. Chang, J. Woolsey, *Nucleic Acids Res,* **2006**. 34(Database issue): p. D668-72.
41. S. Kim, J. Chen, T. Cheng, A. Gindulyte, J. He, S. He, Q. Li, B.A. Shoemaker, P.A. Thiessen, B. Yu, L. Zaslavsky, J. Zhang, E.E. Bolton, *Nucleic Acids Research,* **2020**. 49(D1): p. D1388-D1395.
42. P. Zhang, F.J. Sigworth,C.M. Canessa, J Gen Physiol, **2006**. 127(2): p. 109-17.
43. G. Wu, D.H. Robertson, C.L. Brooks III,M. Vieth, *Journal of Computational Chemistry*, **2003**. 24(13): p. 1549-1562.

BIOMIMETIC NANOCOMPOSITE STRUCTURES DESIGNED FOR COATING OF ORTHOPEDIC IMPLANTS: AFM INVESTIGATION

**REKA BALINT[a], IOAN PETEAN[a], PETRE T. FRANGOPOL[&],
AURORA MOCANU[a], GEORGE ARGHIR[b], SORIN RIGA[a,c],
GHEORGHE TOMOAIA[c,d], OSSI HOROVITZ[a],
MARIA TOMOAIA-COTISEL[a,c*]**

ABSTRACT. Titanium implants are highly resistant to external forces and have affordable prices but the contact between Ti metal and surrounding native tissue could provoke an immunological response. The developing of biomimetic coating onto the Ti surface proves to be a smart choice to enhance the osseointegration and ensure an optimal healing process, due to the creation of nanostructured biomaterials like those in native bone. Thus, we designed a composite coating based on multi-substituted hydroxyapatite (noted ms-HAP or HAPc) nanoparticles, NPs, doped with essential elements: Mg, Zn and Si, functionalized with collagen type 1 (COL), embedded into poly lactic acid, PLA, matrix, and finally covered with COL layer to achieve biomimetic structures. Thin layers of biomimetic composite were self-assembled onto Ti surface via dip-coating method. Both, initial and coated Ti implants were investigated by atomic force microscopy (AFM), which allows surface investigation at high resolution of nano-level. COL amount in composite might self-assemble as COL fibers assuring a biomimetic structure, characterized by important features, like suitable porosity to facilitate the delivery of nutrients to osteoblasts and proper nano-topography and surface roughness to promote cell adhesion and proliferation. The outermost layer is of pure collagen which could assure a natural attachment to the bone tissue promoting osseo-integration.

Keywords: biomimetic structure, bio-composite, multi-substituted hydroxyapatite, collagen, PLA, AFM images, surface roughness

---

[a] *Babeş-Bolyai University, Faculty of Chemistry and Chemical Engineering, Research Center of Physical Chemistry, 11 Arany Janos str., RO-400028, Cluj-Napoca, Romania*
[b] *Technical University of Cluj-Napoca, Faculty of Materials and Environment Engineering, 103-105 Muncii Boulevard, RO-400641, Cluj-Napoca, Romania*
[c] *Academy of Romanian Scientists, 3 Ilfov Str., RO-050044, Bucharest, Romania*
[d] *Iuliu Hatieganu University of Medicine and Pharmacy, Department of Orthopedics and Traumatology, 47 Gen. Traian Mosoiu Str., RO-400132, Cluj-Napoca, Romania*
[&] *Deceased on December 11, 2020*
[*] *Corresponding author: mcotisel@gmail.com*

REKA BALINT, IOAN PETEAN, PETRE T. FRANGOPOL, AURORA MOCANU, GEORGE ARGHIR, SORIN RIGA, GHEORGHE TOMOAIA, OSSI HOROVITZ, MARIA TOMOAIA-COTISEL

INTRODUCTION

The body hard tissue trauma could affect mobility of the patients for long time, even if their life is not in danger. Some difficult cases lead to the patient's invalidity. Therefore, orthopedic research is focused on the improvement of bone trauma healing which often imply usage of nano-biomaterials as bone substitutes [1-10] and artificial implants [11-13].

The implants need to be strong enough and not so heavy to assure a good function of restored bone and to be biocompatible with the host tissue [14, 15]. The foreign body reaction occurs if the implant materials have a bad interaction with the native tissue [16, 17]. It could generate local stress and possibly infection which may lead to the removal of the implant [17]. A possible solution for surpassing these drawbacks would be the developing of biomimetic structures similarly to those in natural healthy bone.

Metallic implants are easy to be worked into the desired shape, have great mechanic and wearing resistance but have a lower biocompatibility and often are heavier than common bone tissue. Also, they have lower production costs than other complex materials. Several alloys like special stainless steel [18-20] and titanium [21-23] prove to have good characteristics as mechanical resistance and weight and are inert enough in contact with living tissues. Despite these good characteristics the wounded bone has a long time of healing and needs to accept the implant. Therefore, it is important to increase the biocompatibility of the metallic surface of implants using different methods to avoid high increases of production costs.

The coating needs to contain several components of the natural bone such as collagen (COL) [24, 25] and hydroxyapatite (HAP) [26, 27] to assure a proper connection between implant and the native tissue. It is not enough to put COL and HAP into the coating layers on Ti implants to assure a biomimetic coating. A synergism between them is needed to generate a biomimetic coating with a similar structure to those of natural bone. The data in literature show that the most important fact to obtain a biomimetic coating is to use the HAP/COL ratio as in natural bone [28, 29] and to use a biocompatible polymer matrix which could be reticulate by the natural compounds [30, 31]. Polylactic acid (PLA) proves to be a biocompatible polymer which was successfully used into biomimetic composites implanted in vivo [32, 33].

Titanium is lighter than stainless steel assuring better mechanical properties and is further considered as target implant for developing biomimetic coatings for an improved osseointegration with natural bones. This purpose needs special investigation technique able to visualize the composite structure at finest details [34-36].

Atomic force microscopy (AFM) is one of the most powerful investigation methods of the composite surface within high resolution at nano-level [37-42]. In this work, the focus is on the application of nanotechnology in tissue engineering research highlighting nano-engineered composites designed to coat the Ti implants.

The goal of this work is related to developing innovative coatings, which can mimic the natural bone structure and reinforce in vivo tissue repair strategies [32]. In the last years, important advances in tissue engineering have been achieved, especially on usage of multi-substituted hydroxyapatites, ms-HAPs [32, 42, 43].

Thus, we designed a biomimetic composite coating based on multi-substituted HAP (noted ms-HAP or HAPc) nanoparticles, NPs, doped with essential elements: Mg, Zn and Si, functionalized with collagen type 1 (COL), embedded into poly lactic acid, PLA, matrix, and finally covered with COL layer achieving biomimetic structures, like ms-HAP/COL@PLA/COL.

RESULTS AND DISCUSSION

Ti rods were tested by X-ray diffraction (XRD), and the XRD pattern is shown in Figure 1. The obtained pattern evidences the diffraction peaks only for titanium proving the highest purity of Ti rods.
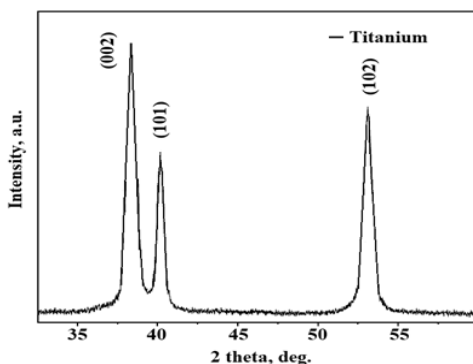

Figure 1. XRD patterns of the Ti rod with Miller indices
in the brackets for diffracting planes.

The developed peaks are strong and intense corresponding to the crystalline state of Ti rods and diffracting planes corresponding to Miller indices (002), (101) and (102).
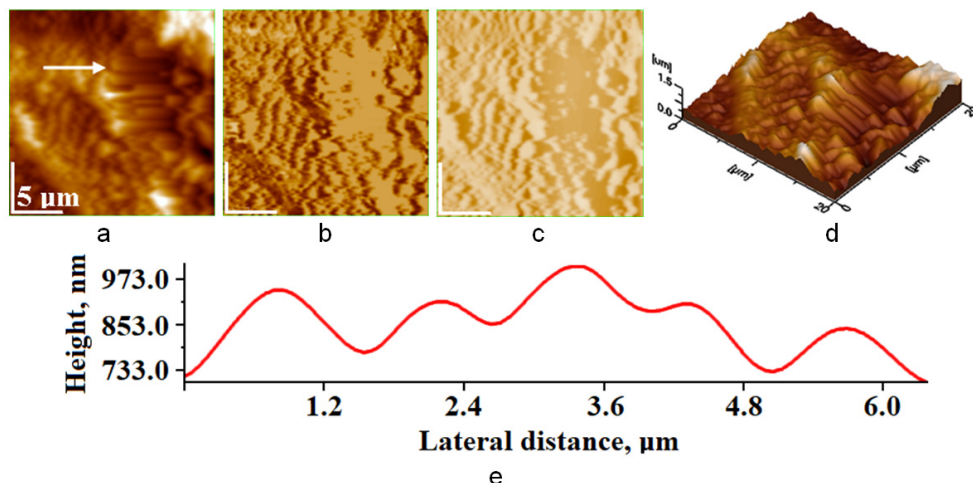
REKA BALINT, IOAN PETEAN, PETRE T. FRANGOPOL, AURORA MOCANU, GEORGE ARGHIR, SORIN RIGA, GHEORGHE TOMOAIA, OSSI HOROVITZ, MARIA TOMOAIA-COTISEL

Figure 2. AFM images of Ti surface after the cold pressing: a) two-dimensional (2D) topographic image, b) phase image, c) amplitude image, d) tridimensional (3D) image, and e) profile along the arrow in panel (a). Scanned area 20 μm x 20 μm; Ra 265 nm; Rq (RMS: root mean square) 330 nm.

The Ti surface changing towards the preparation steps was investigated by AFM.

The Ti rod after cold pressing presents an irregular surface due to the metal interaction with press dies, Figure 2. It looks like the micro-structural Ti grains were pinched, fact which increases the Ra roughness from 141 nm as received to 265 nm. This Ti surface is not suitable for biomimetic coatings. This is sustained by the significant irregularities reveled by phase and amplitude images, Figures 2b and 2c. The lack of proper Ti surface is more evident in the tridimensional (3D) image, Figure 2d, in good agreement with the cross profile shown in Figure 2e.

Therefore, a texture was induced by grinding with P500 abrasive paper and the Ti surface changes are observed in Figure 3a. The irregularities were removed, and a ditch structure was formed. Some fine debris particles were observed on the surface and were removed by ultrasound cleaning. The surface uniformity is clearly sustained by the phase and amplitude images, Figure 3b and 3c. The surface texturing is more evident in Figure 3d. The ditch structure formation on the surface is sustained by the profile in Figure 3e. Some irregularities still appear on the edges of ditches, which require an acid treatment.
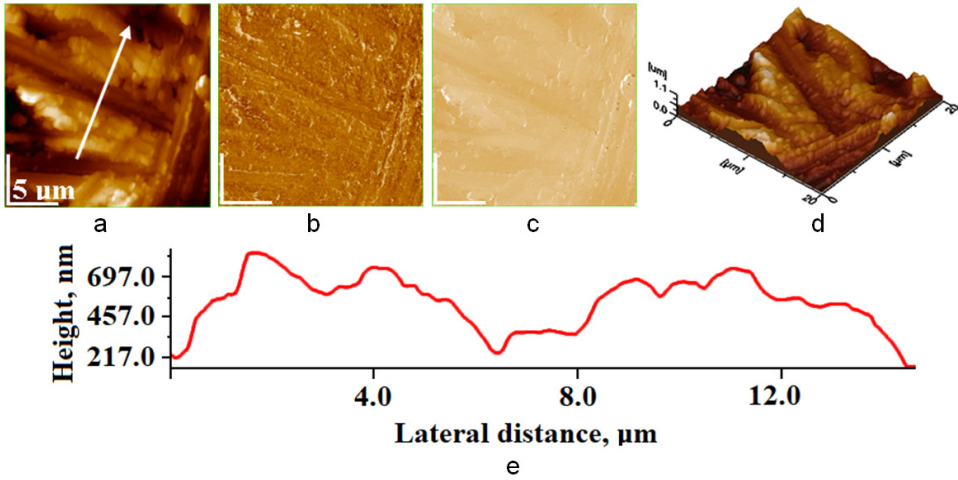
Figure 3. AFM images of Ti grinded with P500: a) topographic image, b) phase image, c) amplitude image, d) 3D image, and e) profile along the arrow in panel (a). Scanned area 20 μm x 20 μm; Ra 154 nm; Rq 186 nm.

Finally, the Ti rod surface was chemically activated with ortho-phosphoric acid and presents well-formed ditches with sharp edges which are perfectly cleaned and degreased, Figure 4a. The proper preparation of the Ti surface is also proven by the phase image, Figure 4b.
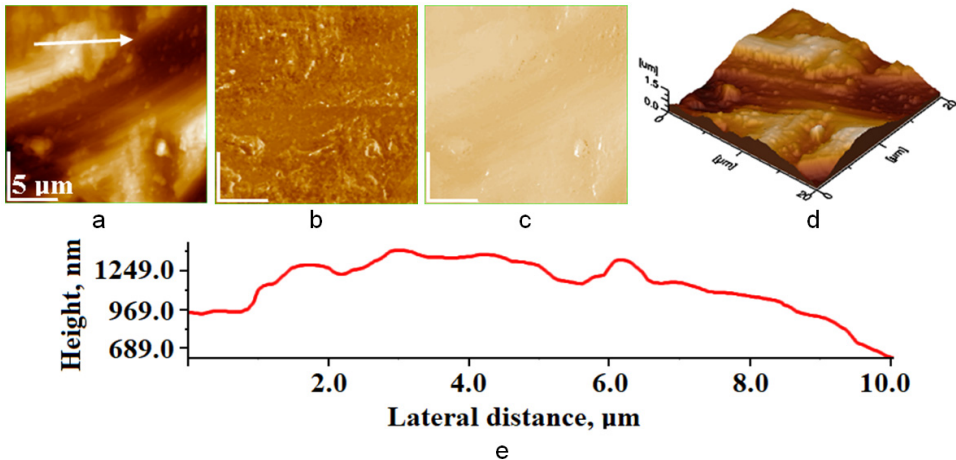

Figure 4. AFM images of Ti grinded with P500 and etched with ortho-phosphoric acid: a) topographic image, b) phase image, c) amplitude image, d) 3D image, and e) profile along the arrow in panel (a). Scanned area 20 μm x 20 μm; Ra 176 nm; Rq 218 nm.

145

Amplitude image in Figure 4c shows that the Ti surface is free of defects and is optimal for coating with composite material. Overall, the AFM investigation proves that this surface morphology is suitable for biomimetic coating. The less viscous dispersion 1 will flow easily into the ditches and fits the edges and leads to a strong attachment of the composite to the Ti surface after drying.
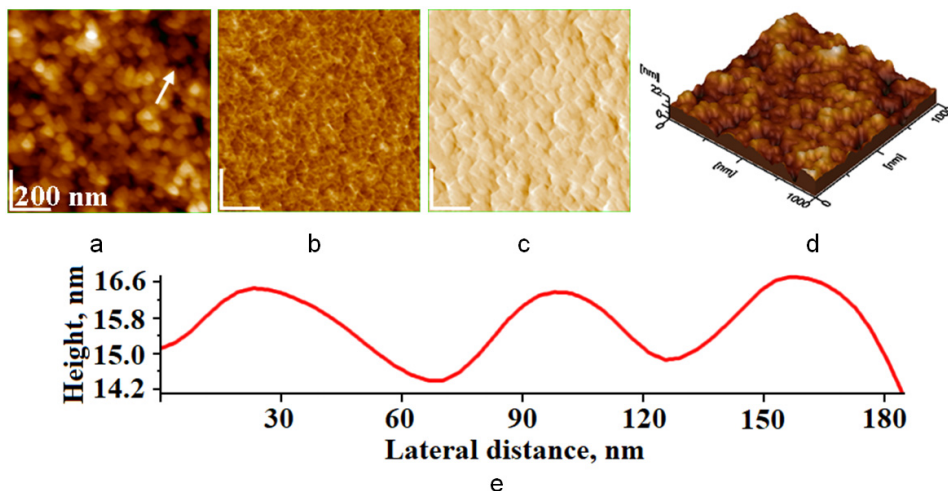

Figure 5. AFM images of HAPc-6%COL (core-shell) nanoparticles: a) topographic image, b) phase image, c) amplitude image, d) 3D image, and e) profile along the arrow in panel (a). Scanned area 1 μm x 1 μm; Ra 2.29 nm; Rq 2.89 nm.

The major component in our coating material is the freeze dried ms-HAP/6%COL core-shell NPs which provide both biomimetic components of the coating, namely nanostructured ms-HAP particles, noted also HAPc = HAP-1.5wt% Mg-0.2wt% Zn-0.2wt% Si, functionalized with 6% collagen. The HAPc NPs were investigated by AFM, Figure 5, and appear well individualized particles adsorbed on the Ti surface (Fig. 5a-d). The HAPc NPs have rounded shape and a diameter of about 50 nm as observed in profile, Figure 5e. Usually HAPc nanoparticles have around 40 nm, but the presence of collagen on HAPc NPs increases their diameter.

Collagen capping of HAPc nanoparticles is more evident in the phase image, Figure 5b, where the coating pellicle is observed in yellow nuance meanwhile HAPc nanoparticles appears in brown nuance. The adsorbed HAPc-6%COL film is smooth and uniform having a Ra of about 2.29 nm and Rq of about 2.89 nm, in good agreement with tridimensional observation, in Figure 5d, and cross profile in Figure 5e.

The XRD patterns in Figure 6 reveal less intense and broadened peaks due to the fine diameter of HAPc particles and to the presence of collagen corona. The crystallite size determined with Scherrer formula shows a diameter of about 42 nm. It is a good correlation with the AFM observation proving that the observed nanoparticles have a crystalline core of about 40 nm which is coated with collagen corona.
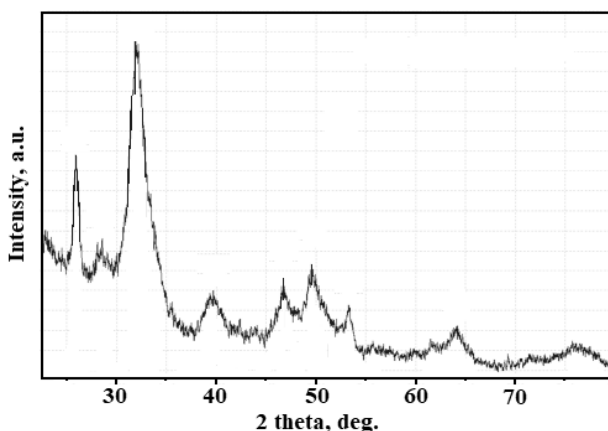

Figure 6. XRD pattern for HAPc-6%COL (core-shell) nanoparticles.

The nanostructure in Figure 5 is usual for a lyophilized powder but far away from a biomimetic coating. The biomimetic structure needs to be promoted. Collagen is the thread that holds together the living bodies. Therefore, its natural forms represent guidance for the biomimetic patterning. The collagen structure involved in hard tissue is of great interest for present paper. Literature results show that bones contain collagen type I fibers having rounded section and diameters varying from fibrils (e.g. 67 nm) to large formations of about 10 µm strongly mineralized with HAP [44-49].

As a first step to establish biomimetic structure, a simpler task was performed. Collagen, as the one in HAPc-6%COL NPs, was dispersed at alkaline pH and self-assembled on the solid substrate (e.g. three successive layers transferred by vertical adsorption onto glass) to observe the natural, biologic assemblies of COL fibers. The resulted structures were observed by AFM at a scan size of 20 µm x 20 µm, in Figure 7.

Clearly, collagen self-assembled from alkaline dispersion onto solid substrate produces a biomimetic display like the one required for bone regeneration [44]. A 10 µm diameter pore is observed in the center of the image in Figure 7a. A denser area of interconnected collagen fibers is observed in the left side of the pore. A significant number of collagen fibers begin from the dense area to the pore border.

REKA BALINT, IOAN PETEAN, PETRE T. FRANGOPOL, AURORA MOCANU, GEORGE ARGHIR, SORIN RIGA, GHEORGHE TOMOAIA, OSSI HOROVITZ, MARIA TOMOAIA-COTISEL

The inside area of the pores is visibly distinct in phase image having brown nuance, Figure 7b. The network of COL fibers is clearly observed in the amplitude image, Figure 7c. These collagen fibers have similar shape and size with the natural collagen generated by osteoblast cells [44, 45]. The profile takes over three almost parallel COL fibers, Figure 7e, and reveals a diameter of fibers of about 600 nm, being in good agreement with published data.
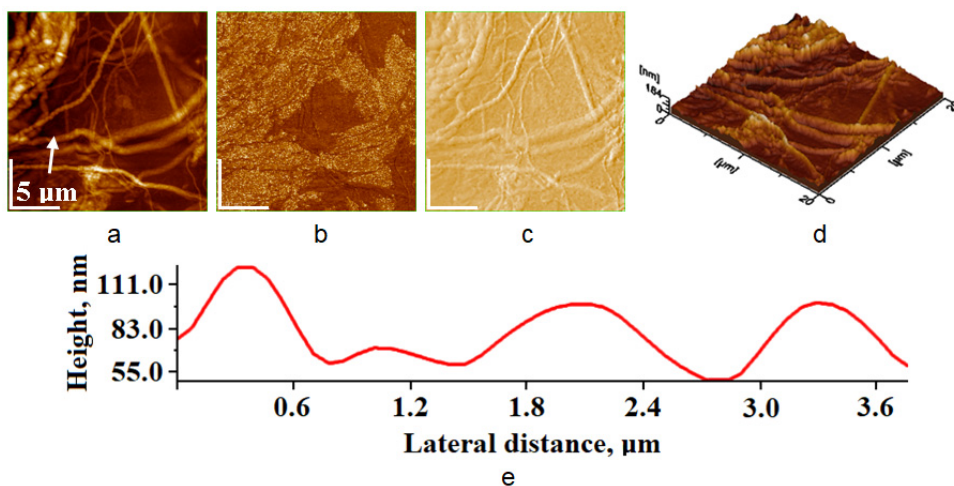

Figure 7. AFM images of collagen fibers self-assembled on glass from COL alkaline dispersion: a) topographic image, b) phase image, c) amplitude image, d) 3D image, and e) profile along the arrow in panel (a). Scanned area 20 μm x 20 μm; Ra 22.2 nm; Rq 27.3 nm.

The presence of HAPc is required as mineralizer of network of collagen fibers to generate biomimetic bone like structure. The HAPc-6%COL nanoparticles contain the natural ratio between HAP and COL and it is expected to generate the biomimetic structure during the drying of the applied layers on the Ti surface.

Porosity is an important requirement for a bone biomimetic structure to assure enough space for osteoblasts adhesion and proliferation [44, 45]. The acetone addition (beside the main role as fluidizer) in the first dispersion used for coating presents the benefit of significant pore generation during evaporation of HAPc-6%COL@PLA. The significant pore creation in the first three layers is important because the second dispersion used for coatings covers with composite the bottom of pores preventing Ti contact with osteoblasts. The interlocking of the second dispersion used for coating into these pores of the basal layers results in a rough surface of the coating.

Therefore, the pores network is a useful structure as observed in Figure 8, for HAPc-6%COL@PLA coating on Ti implant. These pores are of submicron size and are lastly generate by the slower evaporation of dichloromethane (DCM) under drying process of bio-composite. Such morphology could be useful to facilitate the adhesion of osteoblasts to the coating surface on Ti implant.
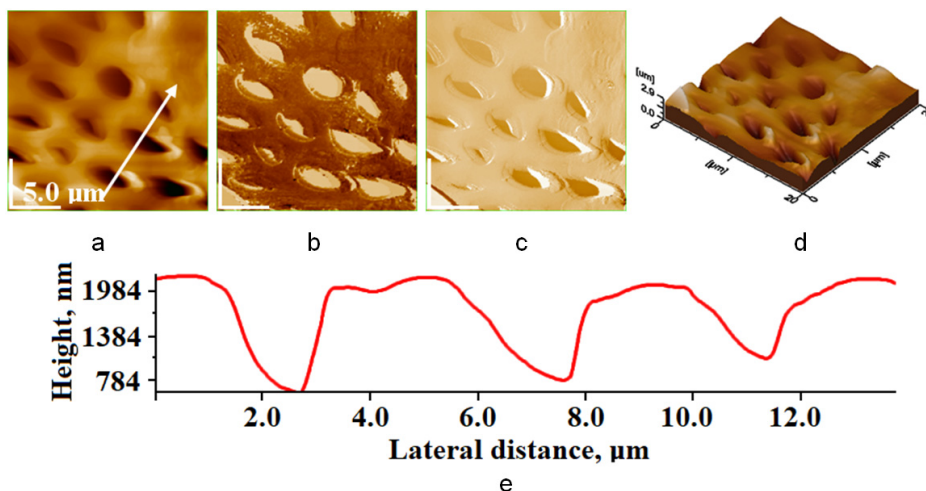

Figure 8. AFM images of pores network on HAPc-6%COL@PLA surface: a) topographic image, b) phase image, c) amplitude image, d) 3D image, and e) profile along the arrow in panel (a). Scanned area 20 μm x 20 μm; Ra 289 nm; Rq 360 nm.

A network with relative parallel pores lines is observed at area of 20 μm x 20 μm in Figure 8a. Also, Figures 8b, 6c and 8d show that the pores are distinctly evidenced.

The roughness of the composite HAPc-6%COL@PLA surface is relatively high. The nano-topography proves the HAPc-6%COL@PLA composite to be a biomimetic structure which can be a promoter for the osteoblast's adhesion on the surface.

Therefore, a closer look to the pores is required. Figure 9 indicates the constitution of a well-developed pore having a diameter of about 2.5 μm. The material around the pore is dense and compact showing an optimum bonding of ms-HAP crystals with COL and PLA, as observed in phase image, Figure 9b, and in amplitude image, Figure 9c. The intermediary layers are still visible on the pore wall in the 3D image, Figure 9d. The pore profile, Figure 9e, has a parabolic conformation with flat bottom. The depth of the pore is about 1 μm.
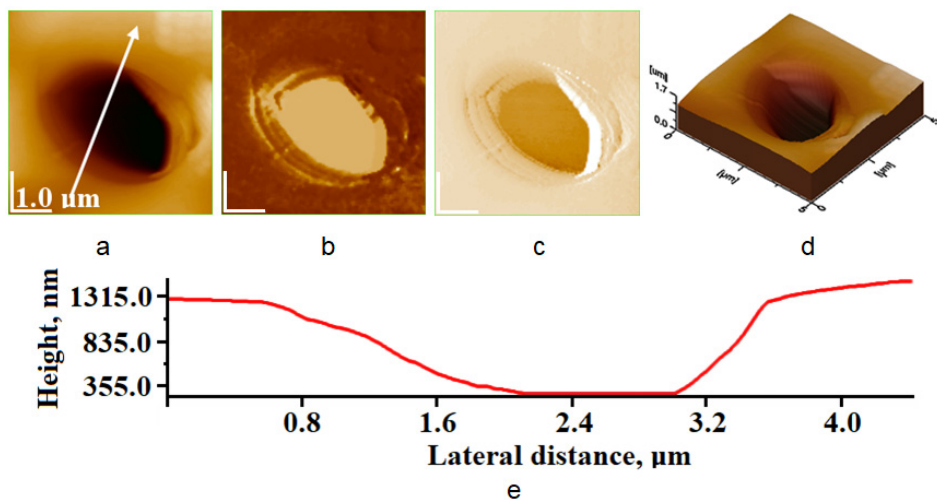
REKA BALINT, IOAN PETEAN, PETRE T. FRANGOPOL, AURORA MOCANU, GEORGE ARGHIR, SORIN RIGA, GHEORGHE TOMOAIA, OSSI HOROVITZ, MARIA TOMOAIA-COTISEL

Figure 9. AFM images of a single pore on HAPc-6%COL@PLA composite surface: a) topographic image, b) phase image, c) amplitude image, d) 3D image, and e) profile along the arrow in panel (a). Scanned area 5 µm x 5 µm; Ra 342 nm; Rq 434 nm.
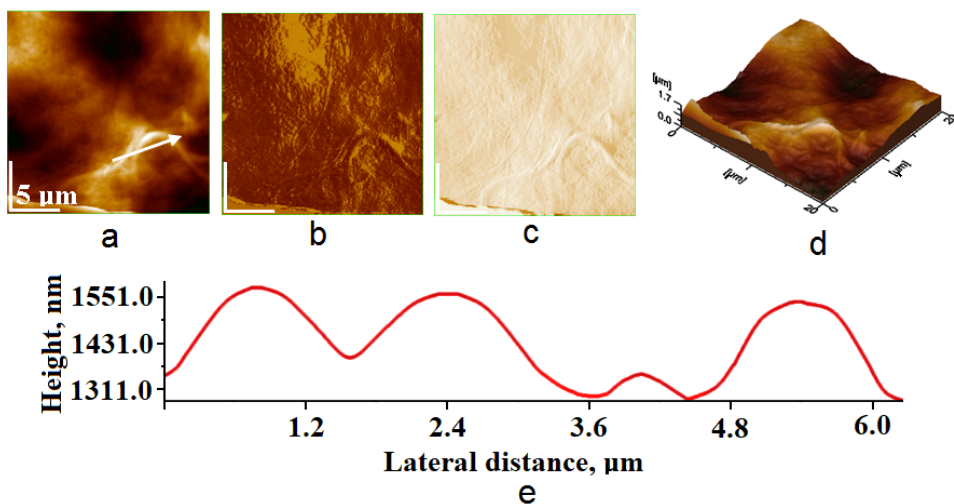

Fig. 10. AFM images of the surface of HAPc-6%COL@PLA/COL composite self-assembled on Ti implant: a) topographic image, b) phase image, c) amplitude image, d) 3D image, and e) profile along the arrow in panel (a). Scanned area 20 µm x 20 µm; Ra 256 nm; Rq 304 nm.

150

The morphology of the HAPc-6%COL@PLA/COL composite surface is illustrated in AFM images, Figure 10, at scanned area of 20 µm x 20 µm. The formation of COL fibers on the surface of this biomimetic structure is revealed particularly in Figure 10a, 10c and 10e. The porosity of this biomimetic HAPc-6%COL@PLA/COL surface is also high. The surface roughness of the HAPc-6%COL@PLA/COL composite is smaller than for the HAPc-6%COL@PLA composite structure. The surface roughness can be controlled in the preparation process of all this coating.

A central feature of this HAPc-6%COL@PLA/COL surface is observed in Figure 11 at a scanned area of 5 µm x 5 µm. Surface topography reveals a divergent bunch of collagen fibers which reach the surface top on the left side of the image and spreads radially in the upper right side of the image. The COL fibers are well developed being distinctly observed in phase and amplitude images, Figures 11b and 11c, and very well horizontally attached on the surface as observed in 3D image in Figure 11d. A rounded profile of the collagen fibers with diameter varying from about 200 µm to 400 µm is given in Figure 11e. The COL fibers formation might appear also inside of the composite and this aspect cannot be ruled out.

Figure 11. AFM images of the HAPc-6%COL@PLA/COL coating on Ti implant:
a) topographic image, b) phase image, c) amplitude image, d) 3D image,
e) profile along the arrow in panel (a). Scanned area 5 µm x 5 µm;
Ra 51.0 nm; Rq 65.4 nm.

Further, Figure 12 illustrates a bunch of three collagen fibers, with diameter ranges from 90 to 300 nm. The tropocollagen rings of the COL fibers are visible at the highest magnification of scanned area of 1 µm x 1 µm, in all

REKA BALINT, IOAN PETEAN, PETRE T. FRANGOPOL, AURORA MOCANU, GEORGE ARGHIR, SORIN RIGA, GHEORGHE TOMOAIA, OSSI HOROVITZ, MARIA TOMOAIA-COTISEL

Figures 12a-12d. The tropocollagen rings are perfectly visible in the topographic image, Figure 12a, and their periodicity of about 67 nm is observed in the profile, given in Figure 12e.
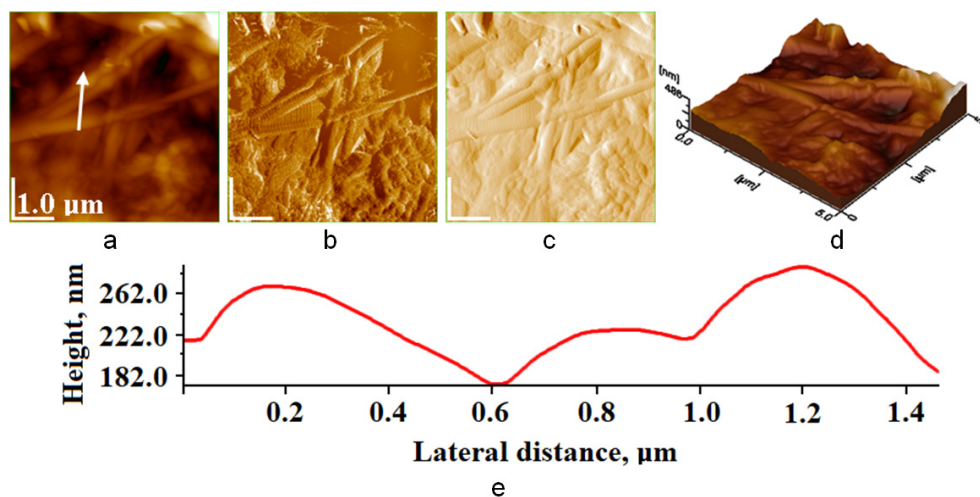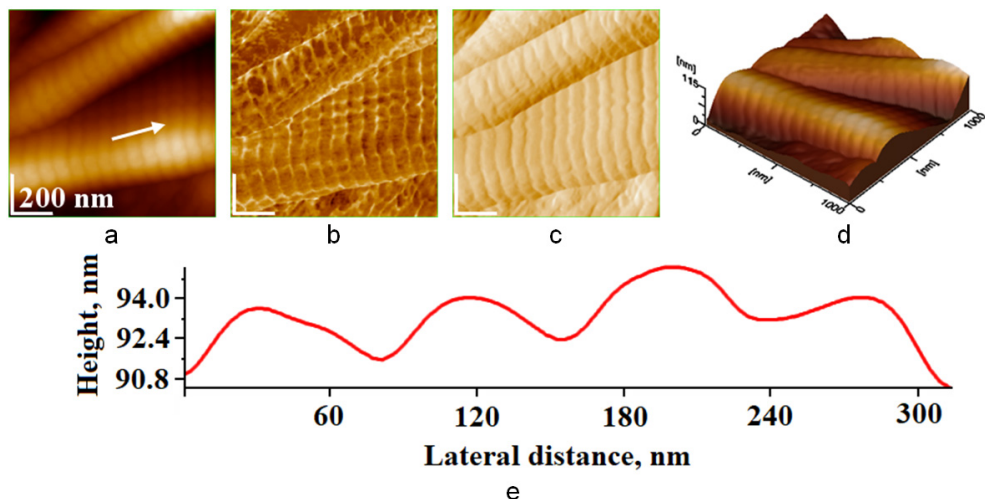

Figure 12. AFM images of the HAPc-6%COL@PLA/COL coating on Ti implant: a) topographic image, b) phase image, c) amplitude image, d) 3D image, and e) profile along the arrow in panel (a). Scanned area 1 μm x 1 μm; Ra 16.2 nm; Rq 18.2 nm.

Certainly, collagen fibers network formation on the HAPc-6%COL@PLA/COL composite surface assures the major transformation from a simple nano-composite material to a biomimetic bio-composite structure, carrying COL branching bundles.

AFM probing the HAPc-6%COL@PLA/COL surface reveals collagen fibers self-assembled on the surface of bio-composite. Furthermore, Figure 13 illustrates another feature, namely a bunch of two collagen fibers, perpendicularly oriented to each other.

The characteristics of COL fibers visualized in Figure 13 are comparable with those given in Figure 12. They adhere on the surface of biomimetic composite increasing the biocompatibility of whole coating surface on Ti implant.

The topography, Figure 13a, evidences a collagen fiber with diameter of about 400 nm (Figure 13e). The structural periodicity is better observed in Figures 13a, 13b, 13d and 13f. Profiles in Figure 13e evidence the fibers diameter and the periodicity of rings on the COL fiber, Figure 13f, which are in good agreement with related data [32, 44].
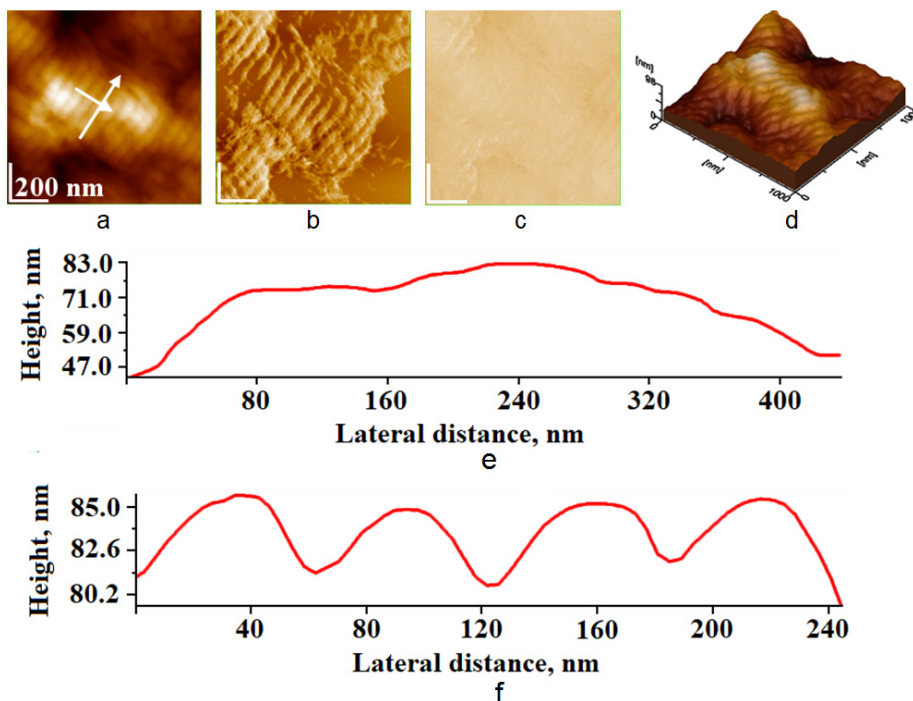
Figure 13. AFM images of the HAPc-6%COL@PLA/COL biomimetic coating on Ti implant, view at highest magnification: a) topographic image, b) phase image, c) amplitude image, d) 3D image; e) the profile along the arrow in panel (a, perpendicular on the axis of COL fiber); f) the profile along the arrow in panel (a, on the COL fiber axis). Scanned area 1 μm x 1 μm; Ra 15.1 nm; Rq 18.3 nm.

In this investigation, the fibrillary structure of type 1 collagen has been revealed in detail, Figures 12 and 13. Thus, artificial collagen fibres display some properties of natural collagen fibrils and are now accessible using self-assembly technique, as shown in Figure 12. The understanding of the structural properties of native collagen fibres will guide the further development of fibrous biomimetic collagenous composites for biomedicine using nanotechnology.

This composite coating on Ti implant was recently investigated *in vivo* studies on femoral fracture rat model [32] and demonstrated a strong support for osteoblasts activity in the new bone formation and fracture healing. Also, recently *in vivo* study, this biomimetic composite coating on Ti implants showed a strong osseointegration with the native bone, in the same rat model. Our histological studies demonstrated the formation of trabecular bone and compact bone at 8 weeks after the implantation in the rat model [50].

REKA BALINT, IOAN PETEAN, PETRE T. FRANGOPOL, AURORA MOCANU, GEORGE ARGHIR, SORIN RIGA, GHEORGHE TOMOAIA, OSSI HOROVITZ, MARIA TOMOAIA-COTISEL

Our preliminary *in vitro* studies on these biomimetic composite structures used as scaffolds in stem cells culture displayed minimal degradation of scaffolds after one month, and all the scaffolds contained small amounts of woven bone and considerable amounts of osteoid in the process of mineralization. The ability of these biomimetic composite scaffolds to promote *in vitro* bone growth discloses a new property of these nanomaterials, named osteoinductivity, which might have a great impact in biomedical applications (*unpublished results*). Certainly, more studies are requested for clinical applications.

The surface roughness values, Ra (arithmetical roughness) and Rq (RMS: root mean square roughness), with their standard deviations are given in Table 1 for Ti surface before coating and in Table 2 for biomimetic coatings on Ti implants, for the same scanned area of 20 µm x 20 µm measured by AFM. The standard deviation, SE, was calculated from at least 3 different areas scanned at 20 µm x 20 µm.

Table 1. The surface roughness, Ra and Rq (RMS),
of Ti implants before coatings, evaluated by AFM.

Ti	Ti Cold pressed		Ti Grinded		Ti Grinded and etched with acid	
Fig.	Ra±SD nm	RMS±SD nm	Ra±SD nm	RMS±SD nm	Ra±SD nm	RMS±SD nm
2	265±25	330±30	-	-	-	-
3	-	-	154±17	186±19	-	-
4	-	-	-	-	176±18	218±20

Table 2. The surface roughness, Ra and Rq (RMS), of biomimetic
coatings on Ti implants measured by AFM.

Composite	HAPc-6%COL@PLA		HAPc-6%COL@PLA/COL	
Fig.	Ra±SD nm	RMS±SD nm	Ra±SD nm	RMS±SD nm
8	289±24	360±27	-	-
10	-	-	256±15	304±26

Ra and Rq values were processed with Microcal Origin 6.0 analysis soft (Microcal Software Inc., Northampton M.A., USA) providing the standard deviation display. The resulted plots are presented in Figure 14.
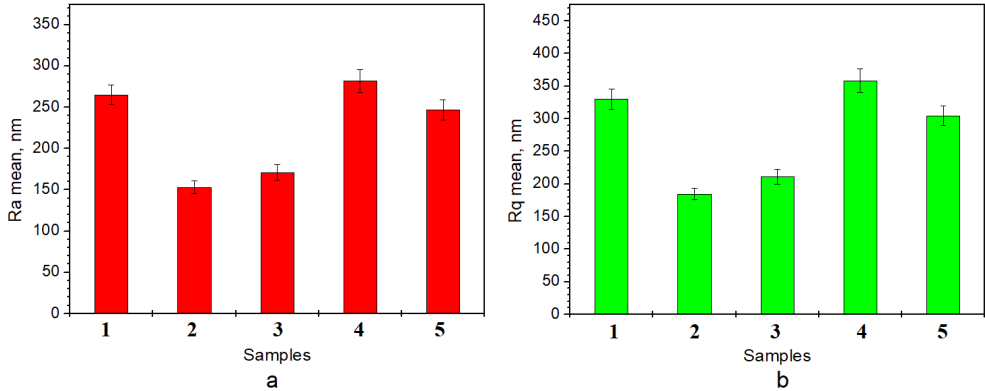
Figure 14. Mean roughness Ra (a) and Rq (RMS, b) for Ti surface before coating:sample 1 (Ti, after the cold pressing); 2 (Ti, grinded with P500); 3 (Ti, grinded with P500 and etched with ortho-phosphoric acid) and after coating: 4 (Ti, sample 3 coated with HAPc-6%COL@PLA composite); 5 (Ti, sample 3 coated with HAPc-6%COL@PLA/COL biomimetic structure); all values estimated at scanned area of 20 μm x 20 μm; all values are statistically significant at $p<0.05$.

Both Ra (Figure 14a) and Rq (Figure 14b) values show the same trend during the processes developed in current study. Titanium implant samples 2-4 have an increased roughness due to the Ti surface treatment. The porosity formed in the HAPc-6%COL@PLA coating on Ti implant leads to a strong increasing of surface roughness. The surface roughness is very well exemplified on the two-dimensional topographic images. The collagen layer added to the coating, resulted in HAPc-6%COL@PLA/COL biomimetic composite coating, and leads to a sensitive decrease of the surface roughness due to some pore occlusion with collagen fibers. All samples have a controlled surface roughness, which can easily be modified as requested by the clinical applications; all the surface roughness values are statistically significant different at $p<0.05$.

CONCLUSIONS

AFM is a powerful tool for investigation of the biomimetic composite coating on the titanium surface of implants. It proves that the collagen amount in the nano-composite material can reticulate. The AFM images revealed a biomimetic network of collagen fibers like the one in natural bone formed on the surface of nano-composite layers. The nano-topography and surface roughness are evidenced by AFM microscopy in the coating layers

REKA BALINT, IOAN PETEAN, PETRE T. FRANGOPOL, AURORA MOCANU, GEORGE ARGHIR, SORIN RIGA, GHEORGHE TOMOAIA, OSSI HOROVITZ, MARIA TOMOAIA-COTISEL

on Ti implants and are suitable for osteoblasts attachment to the surface increasing the cells viability. Adding an extra layer of pure collagen could be a facile enhancer of osteoblasts activity to generate new bone on the revealed biomimetic structures.

EXPERIMENTAL SECTION

The titanium rods were purchased from Goodfellow Cambridge Limited, Huntingdon, England and machined in our laboratory to the desired surface condition. Materials for the coating are: polylactic acid PLA 3051 D, obtained from Nature Works, Minnetonka, MN, USA; dichloromethane high purity (DCM), acetone ≥99.5%, type 1 COL from bovine Achilles tendon lyophilized powder, and an 85% phosphoric acid aqueous solution, 99.99% purity, all purchased from Sigma–Aldrich (St Louis, MO, USA).

Titanium samples preparation: The rounded titanium rods were flattened with a 20 TF hydraulic press to obtain a rectangular section of 3 mm width and 1.5 mm thick and cut into sticks with a 20 mm length. The plan parallel shape of the sticks is required for a proper AFM investigation. Both sides of the sticks were grinded with P500 abrasive paper for 10 minutes to obtain a proper texture of the active surface. The grinding debris was removed by intense washing with bi-distilled water, followed by an ultrasound cleaning. An ultrasound device Sonic Vibra-Cell VCX 750 Watt was used for this purpose. After cleaning the rods were chemically activated for 30 min with orto-phosphoric acid to obtain a perfectly clean and degreased surface.

Preparation of the coating dispersions: There were prepared two dispersions for the sticks coating. The first one is more fluid to assure a strong bonding to the titanium surface and to become the resistant layers. Second dispersion is more viscous to assure a better structuring among HAP and COL to promote the biomimetic aspect of the composite. The granular matter of the composite is a complex HAP based powder functionalized with 6% collagen synthesized by a wet precipitation method described in our previous papers [37, 39]. This powder is further noted as HAPc-6%COL. PLA solution was prepared by PLA dissolution in dichloromethane (DCM). PLA was dissolved in DCM under strong magnetic agitation in ratio of 4.8% (e.g. 1 g of PLA in 15 ml of pure DCM). Two dispersions were prepared when PLA was completely dissolved into DCM. The first contains 76 % HAPc-6%COL and 24 % PLA solution. The fluidity of this dispersion is enhanced by adding acetone. The second dispersion contains 71 % HAPc-6%COL and 29 % PLA solution.

156

Coating: The titanium surface prepared as described was coated with successive layers using dip coating method. Three successive layers of dispersion 1 were transferred: 30 seconds of adsorption followed by a slow retraction of sample from dispersion tank and followed by 10 minutes of natural drying. Afterwards, three successive layers of dispersion 2 were transferred in the same condition. It results the titanium sample coated with composite material in which we expect to develop biomimetic structure (further marked as HAPc-6%COL@PLA). A similar sample was prepared, and a pure collagen layer was transferred via vertical adsorption 5 seconds from rich COL solution at pH 12, resulting HAPc-6%COL@PLA/COL biomimetic structure on Ti implant.

X ray diffraction (XRD) was performed on a D8 ADVANCE X-ray diffractometer from Bruker AXS GmbH, Karlsruhe, Germany (Bragg-Brentano geometry) using Cu Kα radiation. Diffraction peaks were indentified using Match 1.0 data base powered from Crystal Impact Co.

AFM microscopy was performed on a JSPM 4210 Scanning Probe Microscope, Jeol, Japan. The surface morphology and roughness were estimated as previously presented by us [51-56]. The images were scanned in tapping mode using NSC 15 Hard cantilevers produced by Micromesh Co, Estonia. The resonance frequency of the cantilever is about 325 kHz and the force constant of 40 N/m. The obtained images were processed in the standard manner using the specific soft Win SPM2.0 Processing, Jeol, Japan.

Statistical analysis: For statistical analysis GraphPad Prism 6 for Windows was used. The values of surface roughness, Ra and Rq (RMS), were estimated as the mean value ± standard deviation (SD). Statistical significance was identified using one-way ANOVA test followed by Tukey post-hoc test.

ACKNOWLEDGMENTS

REKA BALINT, IOAN PETEAN, PETRE T. FRANGOPOL, AURORA MOCANU, GEORGE ARGHIR, SORIN RIGA, GHEORGHE TOMOAIA, OSSI HOROVITZ, MARIA TOMOAIA-COTISEL

REFERENCES

1. R. Balint; G. A. Paltinean; Gh. Tomoaia; D. Oltean-Dan; A. Mocanu; M. Tomoaia-Cotisel; *Ann. Ser. Biol. Sci*., **2021**, *10(1)*, 90 – 145, ISSN 2285 – 4177.
2. I. Cacciotti; *Int J Appl Ceram Technol*., **2019**, *16(5)*, 1864-1884.
3. M.H. Santos; P. Valerio; A.M. Goes; M.F. Leite; L.G.D. Heneine; H.S. Mansur; *Biomed. Mater*., **2007**, *2(2)*, 135–141.
4. I.V. Antoniac; A. Antoniac; E. Vasile; C. Tecu; M. Fosca; V. G. Yankova; J.V. Rau; *Bioact. Mater.,* **2021**, *6(10)*, 3383–3395.
5. I. Ullah; M. A. Siddiqui; S. K. Kolawole; H. Liu; J. Zhang; L. Ren; K. Yang; *Ceram. Int*., **2020**, *46(10)*, 14448–14459.
6. T. Kumai; N. Yui; K. Yatabe; C. Sasaki; R. Fujii; M. Takenaga; H. Fujiya; H. Niki; K. Yudoh; *Int. J. Nanomedicine*., **2019**, *14*, 1283–1298.
7. H. Liu; M. Lin; X. Liu; Y. Zhang; Y. Luo; Y. Pang; H. Chen; D. Zhu; X. Zhong; S. Ma; Y. Zhao; Q. Yang; X. Zhang; *Bioact. Mater*., **2020**, *5(4)*, 844–858.
8. T. G. Kim; S.-H. Park; H. J. Chung; D.-Y. Yang; T. G. Park*; J. Mater. Chem.*, **2010**, *20*, 8927–8933.
9. P. Pan; X. Chen; K. Metavarayuth; J. Su; Q. Wang; *Curr. Opin. Colloid Interface Sci*., **2018**, *35*, 104–111.
10. Z. Wang; Y. Yan; T. Wan; *Sci. Eng. Compos. Mater*., **2012**, *19(2)*, 177–182.
11. T. Albrektsson; B. Chrcanovic; M. Jacobsson; A. Wennerberg; *JSM Dent Surg*, **2017**, *2(3)*, 1022, 1-6.
12. A. Cappella; H.H. de Boer; P. Cammilli; D. De Angelis; C. Messina; L M. Sconfienza; F. Sardanelli; C. Sforza; C. Cattaneo; *Forensic Sci. Int.,* **2019**, *302*, 109909, 1-9.
13. E.N. L'Abbé; S.A. Symes; D.E. Raymond; D.H. Ubelaker; *Forensic Sci. Int*., **2019**, *299*, 187 – 189.
14. L.H. Li; H.W. Kim; S.H. Lee; Y.M. Kong; H.E. Kim; *J. Biomed. Mater. Res*, **2005**, *73A (1),* 48-54.
15. N.S. Manam; W.S.W. Harun; D.N.A. Shri; S.A.C. Ghani; T. Kurniawan; M.H. Ismail; M.H.I. Ibrahim; *J Alloys. Compd*., **2017**, *701*, 698-715.
16. R. Trindade; T. Albrektsson; P. Tengvall; A. Wennerberg; *Clin Implant Dent Relat Res*, **2017,** *18(1)*, 192 -203.
17. D. van Steenberghe; *Eur J Oral Implantol*.; **2018**, *11(Suppl1)*, S15 – S20.
18. A. Dziubinska; K. Majerski; E. Siemionek; *Procedia Manuf*., **2018**, *15*, 411-418.
19. S. Cicek; A. Karaca; I. Torun; M. S. Onses; B. Uzer; *Mater. Today: Proc*., **2019**, 7(1), 389–393.
20. N. Madhumitha; R.K. Bharath; *J. World Fed. Orthod*., **2017***, 6(4),* 171-176.
21. K. Patka; R. Pokrowiecki; *Adv. Eng. Mater.,* **2018**, *20(5)*, 1700648, 1-18.
22. W. Chen; K. Xu; B. Tao; L. Dai; Y. Yu; C. Mu; X. Shen; Y. Hu; Y. He; K. Cai; *Acta Biomater*., **2018**, *74*, 489–504.
23. Y. Li; C. Wong; J. Xiong; P. Hodgson; C. Wen; *J Dent Res*, **2010**, *89(5),* 493-497.

24. M. D. Shoulders; R.T. Raines; *Annu. Rev. Biochem., **2009**, 78,* 929–958.
25. R.J. DeVolder; I.W. Kim; E.S. Kim; H. Kong; *Tissue Eng. Part A*, **2012**, *18* (*15-16)*, 1642-1651.
26. H.W. Kim; Y.H. Koh; L.H. Li; S. Lee; H.E. Kim; *Biomaterials*, **2004**, *25(13),* 2533–2538.
27. L.A. Sena; M.C. Andrade; A.M. Rossi; G. Almeida Soares; *J. Biomed. Mater. Res*, **2002**, *60(10),* 1-7.
28. X. Cai; H. Follet; L. Peralta; M. Gardegaront; D. Farlay; R. Gauthier; B. Yu; E. Gineyts; C. Olivier; M. Langer; A. Gourrier; D. Mitton; F. Peyrin; Q. Grimal; P. Laugier; *Acta Biomater., **2019**, 90,* 254-256.
29. F.A. Shah; S. Sayardoust; P. Thomsen; A. Palmquist; *Bone*, **2019**, *127,* 244-249.
30. J. Wang; C. Liu; *J. Bionic Eng*., **2014**, *11(4),* 600–609.
31. S. Minardi; F. Taraballi; F.J. Cabrera; J. Van Eps; X. Wang; S.A. Gazze; J. S. Fernandez-Mourev; A. Tampieri; L. Francis; B.K. Weiner; E. Tasciotti; *Mater. Today Bio*., **2019**, *2, 100005,* 1-11.
32. D. Oltean-Dan; G.B. Dogaru; M. Tomoaia-Cotisel; D. Apostu; A. Mester; H.R.C. Benea; M.G. Paiusan; E.M. Jianu; A. Mocanu; R. Balint; C.O. Popa; C. Berce; G.I. Bodizs; A.M. Toader; Gh. Tomoaia; *Int. J. Nanomed*., **2019**, *14,* 5799-5816.
33. I. Izquierdo-Barba; L. Santos-Ruiz; J. Becerra; M.J. Feito; D. Fernandez-Villa; M.C. Serrano; I. Diaz-Guemes; B. Fernandes Tome; S. Enciso; F.M. Sanches Margallo; D. Monopoli; H. Alfonso; M.T. Portoles; D. Arcos; M. Vallet-Regi; *Acta Biomater., **2019**, 83,* 456-466.
34. Gh. Tomoaia; L.B. Pop; I. Petean; M. Tomoaia-Cotisel; *Mater. Plast*., **2012**, *49(1),* 48-54.
35. C. Garbo; M. Sindilaru; A. Carlea; Gh. Tomoaia; V. Almasan; I. Petean; A. Mocanu; O. Horovitz; M. Tomoaia-Cotisel; *Part. Sci. Technol*., **2017**, *35(1),* 29-37.
36. F. Goga; E. Forizs; A. Avram; A. Rotaru; A. Lucian; I. Petean; A. Mocanu; M. Tomoaia-Cotisel; *Rev. Chim*., **2017**, *68(6),* 1193-1200.
37. Gh. Tomoaia; O. Soritau; M. Tomoaia-Cotisel; L.B. Pop; A. Pop; A. Mocanu; O. Horovitz and L.D. Bobos; *Powder Technol., **2013**, 238,* 99-107.
38. S. Rapuntean; P.T. Frangopol; I. Hodisan; Gh. Tomoaia; D. Oltean-Dan; A. Mocanu; C. Prejmerean; O. Soritau; L.Z. Racz; M. Tomoaia-Cotisel; *Rev. Chim*., **2018**, *69(12*), 3537-3544.
39. Gh. Tomoaia; A. Mocanu; I. Vida-Simiti; N. Jumate; L.D. Bobos; O. Soritau; M.Tomoaia-Cotisel; *Mater. Sci. Eng. C*, **2014**, *37*, 37-47.
40. A. Mocanu; G. Furtos; S. Rapuntean; O. Horovitz; C. Flore; C. Garbo; A. Danisteanu; Gh. Rapuntean; C. Prejmerean; M. Tomoaia-Cotisel; *App. Surf. Sci.,* **2014**, *298,* 225–235.
41. P.T. Frangopol; A. Mocanu; V. Almasan; C. Garbo; R. Balint; G. Borodi; I. Bratu; O. Horovitz; M. Tomoaia-Cotisel; *Rev. Roum. Chim*., **2016**, *61(4-5*), 337-344.

42. C. Garbo; J. Locs; M. D'Este; G. Demazeau; A. Mocanu; C. Roman; O. Horovitz; M. Tomoaia-Cotisel; *Int. J. Nanomed*., **2020**, *15*, 1037-1058.

43. A. Mocanu; O. Cadar; P.T. Frangopol; I. Petean; Gh. Tomoaia; G.A. Paltinean; C.P. Racz; O. Horovitz; M. Tomoaia-Cotisel; *R. Soc. Open Sci.,* **2021**, *8(1)*, 201785, 1-25.

44. A.M. Ferreira; P. Gentile; V. Chiono; G. Ciardelli; Acta Biomater., **2012**, 8(9), 3191–3200.

45. P. Fratzl; Collagen: Structure and Mechanics, an Introduction, of the chapter 1. In *Book Collagen: Structure and Mechanics*; P. Fratzl_Editor; Springer: Boston, MA, U.S., **2008**; pp. 1-13. DOI: 10.1007/978-0-387-73906-9.

46. X. Chen; L. Zhou; H. Xu; M. Yamamoto; M. Shinoda; I. Tad; S. Minami; K. Urayama; H. Yamane; *Int. J. Biol. Macromol.,* **2019**, *135*, 959–968.

47. K. Saini; D. Discher; N. Kumar; *J Mech. Behav. Biomed.,* **2019**, *91*, 315–325.

48. V. Baranauskas; I. Garavello; Z. Jingguo; M. A. da Cruz-Hofling; *Appl. Surf. Sci*., **2005**, *248(1-4),* 492–498.

49. T. Kreller; F. Sahm; R. Bader; A.R. Boccaccini; A. Jonitz-Heincke; R. Detsch; *Materials*, **2021**, *14*, 3516, 1-18.

50. D. Oltean-Dan; P.T. Frangopol; R. Balint, Gh. Tomoaia; A. Mocanu; M. Tomoaia-Cotisel; *Studia. Univ. Babes-Bolyai. Chem.,* **2021,** *66(3),* i*n print.*

51. I. Petean; Gh. Tomoaia; O. Horovitz; A. Mocanu; M. Tomoaia-Cotisel; *J. Optoelectron. Adv. M*., **2008**, *10(9),* 2289-2292.

52. L. Barbu-Tudoran; Gh. Tomoaia; O. Horovitz; A. Mocanu; M. Tomoaia-Cotisel; *J. Optoelectron. Adv. M.,* **2008**, *10(9),* 2293-2297.

53. P.T. Frangopol; D.A. Cadenhead; M. Tomoaia-Cotisel; A. Mocanu; *Studia. Univ. Babes-Bolyai. Chem.,* **2009**, *54(*1), 23-35.

54. M. Tomoaia-Cotisel; A. Tomoaia-Cotisel; T. Yupsanis; Gh. Tomoaia; I. Balea; A. Mocanu; C.P. Racz; R*ev. Roum. Chim*, **2006**, *51(12),* 1181-1185.

55. M. Tomoaia-Cotisel; A. Mocanu; *Rev. Chim. (Bucharest),* **2008**, *59(11),* 1230-1233.

56. Gh. Tomoaia; O. Horovitz; A. Mocanu; A. Nita; A. Avram; C.P. Racz; O. Soritau; M. Cenariu; M. Tomoaia-Cotisel; *Colloids Surf. B,* **2015**, *135*, 726-734.

SINGLE-MOLECULE DETECTION AND MANIPULATION WITH BIOLOGICAL NANOPORES

IRINA SCHIOPU[a,*], ALINA ASANDEI[a], LOREDANA MEREUTA[b], ISABELA DRAGOMIR[a], CEZARA BUCATARU[b], TUDOR LUCHIAN[b,*]

ABSTRACT. Single-molecule electrophysiology techniques using protein-based or solid-state nanopores as nanoreactors were proven incredibly useful as platforms for sensing and biophysical characterisation of biological molecules (e.g., peptides, proteins), DNA detection and sequencing in a label-free, low-cost, rapid and high signal-to-noise ratio manner. Herein we present a number of discoveries in this field, developed over the years in our laboratory, including: (i) the pH-mediated, fine-tuning of peptides passage through the α-hemolysin nanopore; (ii) increase of the capture rate and dwell times of polypeptides inside the nanopore, through engineering dipole-like polypeptides; (iii) the implication of a nanopore-AuNP (citrate anion-coated gold nanoparticles) platform to selectively detect nanomolar concentrations of target ssDNA.

Keywords: *single-molecule, peptides, electrophysiology, detection, sensing, nanopore, DNA, PNA*

INTRODUCTION

Wild-type or genetically modified biological nanopores [1], [2], have been used as nanoreactors in various applications involving detection [3], sensing and identification [4], quantification [5], and physical characterization of single small molecules [6], [7].

Presently, among the most common biological nanopores we mention aerolysin [8]–[10], M. smegmatis porin A (MspA) [11], outer membrane protein G (OmpG) [12], [13], fragaceatoxin C (FraC) [14], cytolysin A (ClyA) [15], 29 phage DNA packaging motor [16], outer membrane protein F (OmpF) [17]–[20].

---

[a] *Alexandru Ioan Cuza University, Interdisciplinary Research Institute, Sciences Department, 54 Lascar Catargi str., RO-700107 Iasi, Romania*

[b] *Alexandru Ioan Cuza University, Department of Physics, 11 Carol I bvd., RO-700506 Iasi, Romania*

* *Corresponding authors: iri.schiopu@gmail.com, luchian@uaic.ro*

IRINA SCHIOPU, ALINA ASANDEI, LOREDANA MEREUTA, ISABELA DRAGOMIR,
CEZARA BUCATARU, TUDOR LUCHIAN

The alpha-hemolysin (α-HL), secreted by the human pathogen *Staphylococcus Aureus*, is one of the most often used nanopore in single-molecule analysis techniques. A homo-heptameric (232.4 kDa) transmembrane channel is formed spontaneously when its water-soluble monomers bind to the surface of lipid membranes [21]. The resolved crystal structure of the α-HL nanopore revealed three main structural componens: (i) the vestibule, with a ~2.6 nm diameter opening; (ii) the lumen, a β-barrel segment having a ~2 nm diameter opening, and (iii) the constriction region, with the narrowest diameter of 1.4 nm delimiting the vestibule from the lumen [22].

The interaction pathway of the studied molecules inside the nanopore depends greatly on which opening of the nanopore they enter. For example, based solely on steric considerations, the α-HL nanopore's vestibule region allows entry of a B-form DNA-DNA duplex (diameter of ~ 2 nm), while the nanopore's β-barrel allows only single-stranded DNAs (diameter of ~ 1 nm) capture and passage [23], [24]. In the realm of nucleic acids analysis and among others, the α-HL nanopore has proven efficient for the identification of individual microRNAs through the detection of a complex formed by the microRNA with a complementary RNA probe [25], base-pair energies calculus [26], in the determination of a DNA hairpin or a DNA-PNA duplex strength and in discriminating between hairpins or duplexes that differ by one base pair only [27]–[29].

The technique uses an external applied electric force to capture the molecule of interest inside the nanopore and, thus, reveal the specific features of the molecule (e.g., binding rate constants, apparent occupied volumes, binding energy, hybridization state, mismatching of base-pairs). In brief, the detection paradigm implicates the existence of a nanopore embedded in a stable artificial lipid bilayer [30] that separates the two sides of the recording cell, conventionally named, *cis*-side, ground connected, and *trans*-side, where the reference electrode is placed. Once a potential difference is applied on the protein-lipid system, the electrically charged particles from the buffer solution present in the two chambers will move across the nanopore driven by the generated electric field (Figure 1A, panel a) and a constant ionic current will be recorded (this represents the baseline of every control experiment, Figure 1A, panel c). As the molecule of interest is captured by the nanopore (Figure 1A, panel b), it will transiently block it and such events are seen as reversible decreases in the ionic current flow. The main parameters important to be monitored and analyzed in this context, which shed light of molecule's features or its interaction with the nanopore, are: (1) τ_{on} – the average inter-blocking events time; (2) τ_{off} – the dwell time of the molecule inside the nanopore and (3) ΔI – the average current blockade caused by the presence of a single molecule inside the nanopore, which is usually calculated as the modulus of the difference between the baseline current (I_{open}) and the value of the blockage values ($I_{blocked}$) (Figure 1A, panel d).
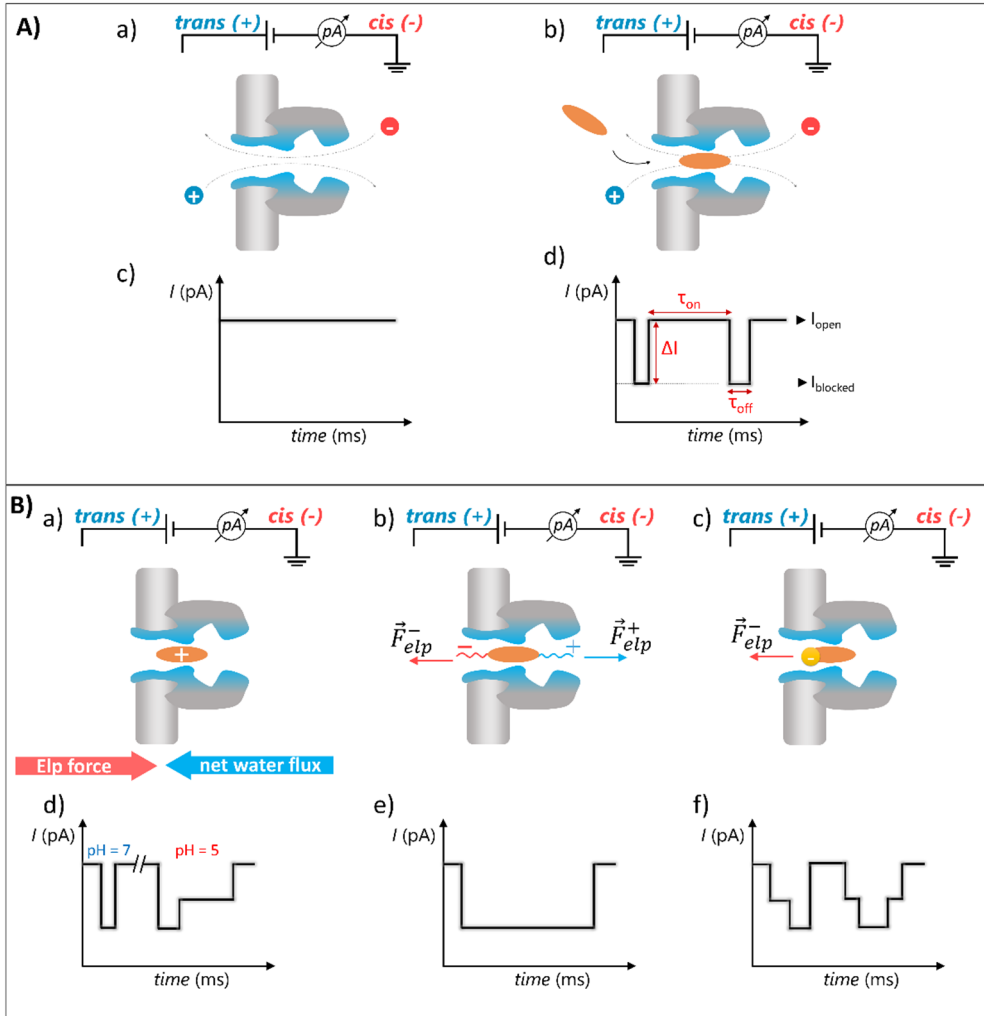
Figure 1. A) Schematic representation of the single-molecule detection technique using the α-HL nanopore. The main principle of detection relies on monitoring the ionic current through the nanopore (panels a and c) and observing the fluctuations in the ionic current determined by the passing of a molecule through the nanopore (panels b and d) and analyzing the specific interaction parameters (panel d) B) Schematic representations of ways to optimize the single-molecule detection technique: slowing down the passage of the studied molecule through the nanopore by enhancement of the electro-osmotic flow via pH fine-tuning (panel a and d); functionalization of the biomolecule with oppositely charged segments (panels b and e); using citrate anion-coated gold nanoparticles (yellow circles in panel c) in order to reveal the specific fingerprint of single molecules or molecular complexes (e.g., ssDNA, DNA-PNA duplex) (panel f).

163

Several enhancement strategies can be used in order to improve the sensitivity and the resolution of the detection approach. As investigated in our laboratory, these 'gimmicks' imply slowing down the passage of the molecule through the nanopore or make use of charged ligands to enhance the detection of the target molecule.

The first approach focuses on keeping the molecule inside the nanopore for a longer period of time either by modifying the pH values of the solution in which the protein-lipid system is placed, thus altering the electro-osmotic flow and rendering it opposite to the electrophoretic flow at acidic pH values and thereby exerting a better control over the molecule translocation across the nanopore (Figure 1B, panels a and d). Alternatively, by engineering biomolecules (e.g., polypeptides or peptide-nucleic acids - PNAs) with oppositely charged amino acids segments at both termini, their collective interaction with the applied transmembrane potential determine electrophoretic forces pulling oppositely on the nanopore-captured biopolymer and prolong its dwell times inside the nanopore (Figure 1B, panels b and e).

The second approach focuses on the specific ionic current signature of the molecule upon interaction with the nanopore (Figure 1B, panel c and f). The use of unmodified citrate anion-coated gold nanoparticles (AuNPs) can help detect small quantities of target molecules like ssDNA of more complex compounds like hybridize DNA-PNA molecules.

Regardless of the chosen approach, the main purpose of such enhancement strategies is to lead to a rapid, real-time, low-cost, label-free detection technique with high sensitivity and resolution.

STRATEGIES FOR SLOWING DOWN MOLECULES THROUGH A PROTEIN NANOPORE

pH-mediated fine-tuning of forces exerted on the nanopore-captured peptide reveals intermediate states in peptide translocation

The principle of this strategy was applied in our lab in the study of chimeric peptides termed CAMA, a merge between the sequences of the antimicrobial peptides cecropin A (CA) and magainin (MA) (**Table 1**). By varying the solution pH ranging from neutral to mildly acidic values (pH = 7.1, 3.3, 4.5, 5.1) the translocation speed of the peptide is decreased and different sub-states of the peptide's pathway inside the α-HL nanopore were identified (i.e., β-barrel vs. vestibule).

Table 1. The amino acid sequences of the peptides

Peptides	Sequence
CAMA P1	KWKLFKKIGIGKHFLSAKKF-NH$_2$
CAMA P5	KWKHLKKIGIGKHFLSAKKF-NH$_2$
CAMA P6	KWKLFKKIGIGKFLQSAKKF-NH$_2$

This approach led to the following findings: (1) the revealing of two-sub-states corresponding to the location of the peptide inside the nanopore; (2) the capture rate of the peptide can be controlled by modifying the pH; (3) the dwell time of the last sub-state, corresponding to the peptide in the vestibule part of the nanopore, increases at acidic pH [31].

The two main sub-states observed when decreasing the pH value of the solution, which are invisible at neutral pH, are denoted in Figure 2 with B1, representing the blockade produced by the presence of the peptide inside the lumen (β-barrel) part of the nanopore, and B2, representing the blockade of the vestibule part of the nanopore by the peptide's presence. As the CAMA P6 peptide was added in the *trans*-part of the lipid-nanopore system, the B1 blockade arises first, followed sequentially by the smaller B2 blockade sub-state, the direction of the peptide's movement inside the nanopore being trans→lumen→vestibule→cis. As the buffer pH is lowered from 5.1 to 3.3, the second B2 blockade sub-state becomes more distinguishable (Figure 2, panel a and b).
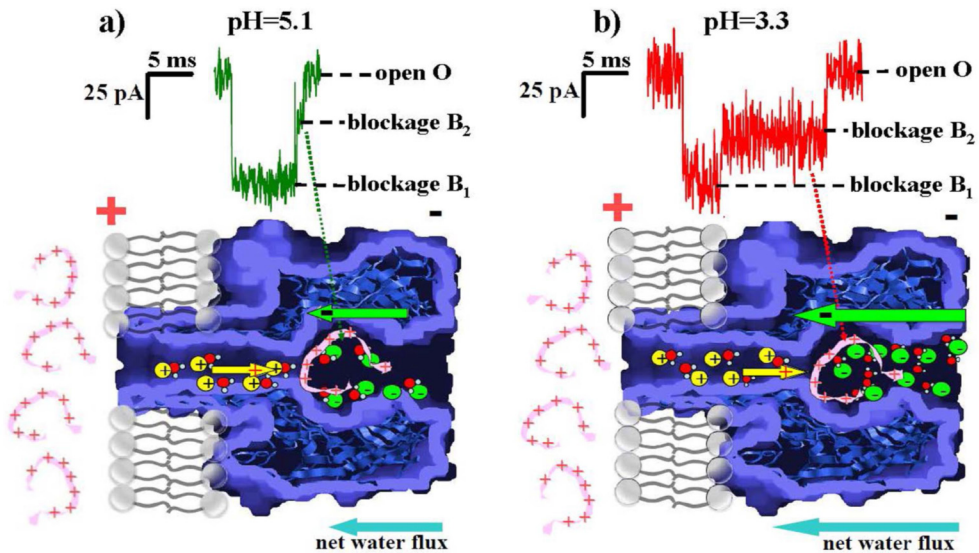

Figure 2. Representation of the two distinct blockade substates revealed by lowering the electrolyte's pH from 5.1 (panel a) to 3.3 (panel b). The open states are marked (open O) and the blockade sub-states by B1 (associated with a single CAMA peptide lodged inside the α-HL's β-barrel) and respectively B2 (associated with a single CAMA peptide lodged inside the α-HL's vestibule). The trans-added cationic CAMA peptide is depicted in pink. When the lipid membrane-isolated nanopore is positively biased, the peptides are electrophoretically driven inside the nanopore, while by lowering the pH, the flux of anions transported in the opposite direction is higher than that of cations, rendering the overall net water flux opposite to the trans-to-cis movement of the peptide, thus increasing the translocation duration. Adapted from [31].

IRINA SCHIOPU, ALINA ASANDEI, LOREDANA MEREUTA, ISABELA DRAGOMIR,
CEZARA BUCATARU, TUDOR LUCHIAN

The peptide capture by the nanopore can be controlled by modulating the pH value in the electrolyte

A side observation related to the pH-controlled trafficking of studied peptides across the α-HL nanopore, is a visible decrease in the CAMA peptide association rate with the nanopore at low pH values (Figure 3, panel a). This is a direct consequence of the repulsive electrostatic interactions which manifest at acidic pH between the positively charged peptide and the positive charges found at the mouth of the α-HL β-barrel.

The peptide residence time inside the α-HL vestibule increase at acidic pH

The B2 sub-state (Figure 3, panel c) which is associated with the peptide's dwelling inside the α-HL's vestibule, increases dramatically at acidic pH values. In figure 3, panel b, the statistical analysis of the dissociations rate (rate$_{off}$ B2 = τ_{off} B2^{-1}) as a function of pH are represented. Two main causes were proposed account for these observations: (1) the role of electrostatic repulsions forces between the cationic peptide and the protein inner surface positive charges or, (2) the increase of the electro-osmotic flow which opposes the electrophoretic force that drives the peptide through the nanopore.
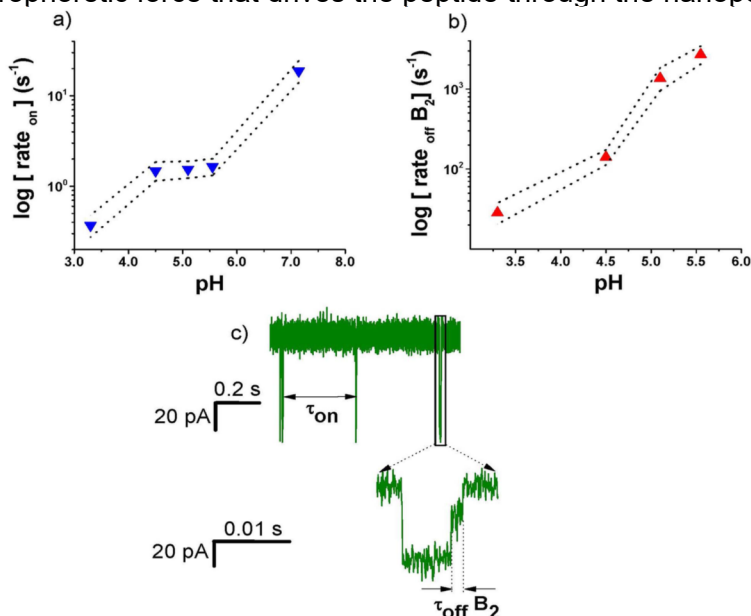

Figure 3. The effect of lowering the electrolyte's pH on the association rate (panel a) and dissociation rate (panel b), respectively, characterizing the reversible interactions between the cationic peptide and the vestibule region of the α-HL nanopore (denoted by B2 in panel c). Adapted from [31].

The main role of the electrophoretic and electro-osmotic forces in slowing down the peptide drift velocity along the vestibule region of the α-HL nanopore

To explain how the interplay of the electrophoretic and electro-osmotic forces leads to the slowdown of the peptide movement inside the nanopore's vestibule, the following facts are to be considered: (1) the cationic peptide moves across the nanopore in the trans-to-cis direction, driven by the external applied electrophoretic force; (2) the α-hemolysin nanopore is slightly anion selective at neutral pH, and this augments at acidic pH, causing the net water flow carried by anions to move in the cis-to-trans direction, making the electro-osmotic water flow to oppose electrophoresis. Collectively, the drift velocity of a peptide (v_{drift}) can therefore be expressed as the vector sum of the electrophoretic and electro-osmotic components [31]:

$$v_{\text{drift}} = v_{\text{electrophoretic}} - v_{\text{electroosmotic}} = \mu \frac{\Delta V}{l_{\text{pore}}} - \frac{(P_{Cl-} - P_{K+})}{(P_{Cl-} + P_{K+})} N_h I / \left(|e^-| \, S_{\text{pore}} [H_2 O] \right) \quad (1)$$

where μ – peptide's electrophoretic mobility, ΔV – the applied potential difference, I_{pore} and S_{pore} – length and average cross-section of the α-HL nanopore vestibule, P_{K+} and P_{Cl-} - ionic permeabilities, N_h - number of water molecules associated with each mobile ion, I - net ionic current through the nanopore while a peptide resides within the vestibule (i.e., B2 sub-state in figure 3, panel c), $|e^-|$ - electronic charge, $[H_2O]$ - water concentration. The formula (1) clearly shows that as the nanopore increases its anion selectivity, the electro-osmosis flow will also increase, causing the drift velocity of the peptide to decrease. By tuning the pH value of the solution in which the lipid-nanopore system is immersed, and thus modifying the net output between the electrophoretic and the electro-osmotic flow, it is possible to trap and identify in a very effective way nanoparticles [32], DNA fragments [33] or dendrimers [34], [35]. Also, further studies showed that at extreme acidic pH values the cationic peptides reveal a back-and-forth movement between the vestibule and the lumen region of the α-HL, before being released [36].

Oppositely charged segments engineered on polypeptides slow-down their passage across the nanopore

This strategy makes use of a design in the primary structure of polypeptides, by placing opposite charged groups (glutamic acids and arginines) at their N- and C- termini (Table 2).

Table 2. The primary sequences of the modified polypeptides

Peptides	Sequence
CP2a	Ac – (E)$_{12}$ – (N)$_{12}$ – (R)$_{12}$ – NH$_2$
CP2b	Ac – (E)$_{12}$ – (Q)$_{12}$ – (R)$_{12}$ – NH$_2$

In this case, all studies were carried out at neutral pH (7.3) and the peptides were added in the *trans*-side of lipid membrane-nanopore system. The experiments revealed significant details about the kinetics of such new designed peptides while interacting with the nanopore: (1) the capture rate of peptide were enhanced by increasing the applied potential across the nanopore; (2) the main cause of the increase capture rate is the presence of the electrostatic attraction interactions between the polypeptide and the entry of the nanopore's β-barrel; (3) the dwell time of the captured peptide was increased by augmenting the applied transmembrane value [37].
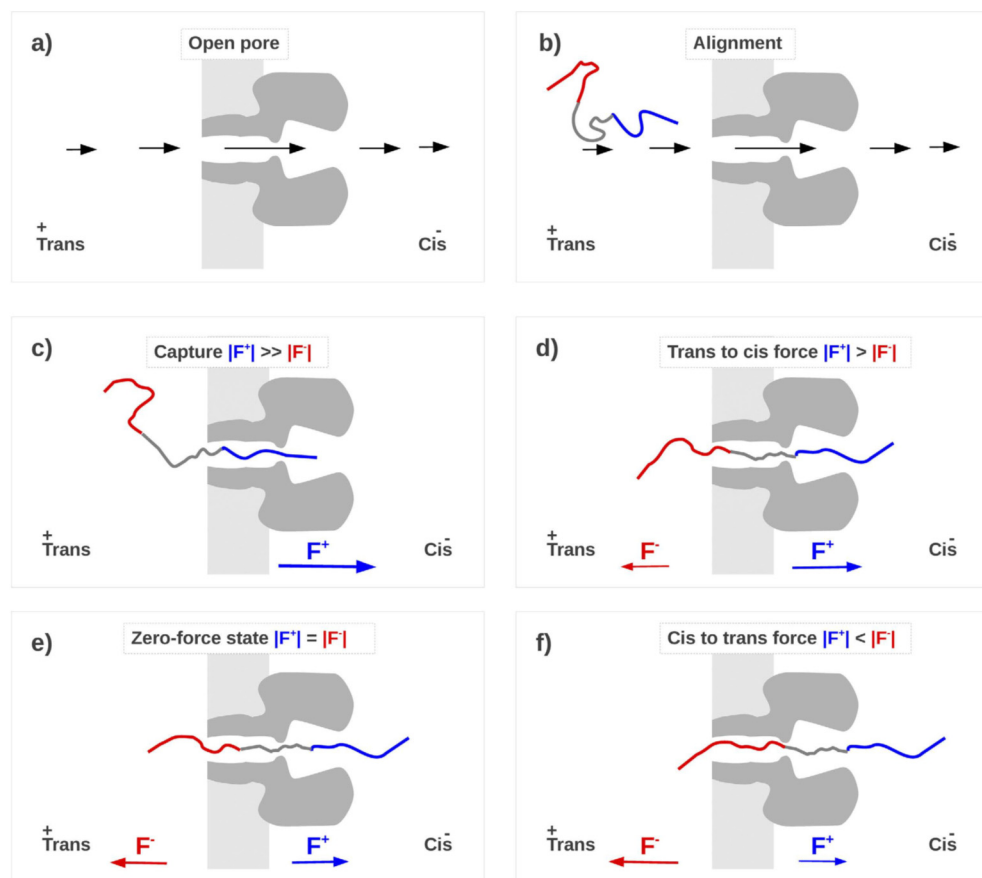

Figure 4. Descriptive model of a macrodipole-like polypeptide (red – negatively charged moiety, blue – positively charged moiety) movement inside the α-HL nanopore isolated in a lipid membrane, under the influence of an applied transmembrane potential. Adapted from [37].

In Figure 4, the peptide's motion across the nanopore is illustrated in a simplest embodiment, depicting its journey across the nanopore's distinct regions. When the polypeptides were added in the *trans*-side of the nanopore, a positively applied transmembrane potential will orient a nanopore approaching polypeptide, to enter the β-barrel with its negative tail head on (i.e., glutamic acids segment) (Figure 4, panel b). Note that the electro-osmotic flow effects can be neglected, as such the experiments were carried out at neutral pH [31]. This event marks the polypeptide capture (Figure 4, panel c), continued by its movement inside the nanopore, driven by a net electric force stemming from components acting on the two oppositely charged tails (Figure 4, panel d). When a balance between the two electric forces acting on the captured polypeptide is reached (zero-force state), a metastable state ensues (Figure 4, panel e) that can be maintained until thermal fluctuations break it and lead to the polypeptide's escape (Figure 4, panel f). Through entrapping a captured polypeptide for a longer time inside the nanopore, this strategy facilitated monomers discrimination on the polypeptide sequence [38-40].

We have also shown that the capture rate and the residence time of the different biomolecules can be controlled by applying a salt gradient across the nanopore. By using a lower salt concentration in the side where the molecules were being added, the detection of the biomolecules can be significantly enhanced without reducing the residence times [41] and even increase the detection sensitivity in the nanomolar range of studied molecule [27].

STRATEGIES FOR DETECTING SINGLE-STRANDED DNA AND PNA MOLECULES

The nanopore-based strategy enabling single-stranded DNA (ssDNA) and DNA-PNA molecular complexes detection with unmodified citrate anion-coated gold nanoparticles (AuNPs), is based upon the following pillars: (1) each specific molecule or molecular complex has its own distinguishable signature in the recorded ionic current across the nanopore; (2) the AuNPs undergo aggregation upon interacting with the neutrally charged PNA molecules, thus changing the pattern of the ionic current fluctuations as compared to control experiments (present only AuNPs); (3) the PNA-DNA hybridization process disrupts the AuNPs aggregation, and this is distinguishable via electric current measurements through the nanopore (Figure 5 I) [42]. The selected PNA and ssDNAs sequences chosen for such experiments are presented in Table 3, where HCV is a specific sequence to the hepatitis C virus and H1N1 is a specific ssDNA sequence to a type of influenza A virus [43].

IRINA SCHIOPU, ALINA ASANDEI, LOREDANA MEREUTA, ISABELA DRAGOMIR,
CEZARA BUCATARU, TUDOR LUCHIAN

Table 3. The primary sequences of the polynucleotides (PNA and ssDNA)

Polynucleotide	Sequence
PNA2	5′ -CCCACCCGCAGCCCTCATTA-3′
HCV (ssDNA complementary to PNA2)	5′-TAATGAGGGCTGCGGGTGGG-3′
H1N1 (ssDNA non-complementary to PNA2)	5′-ACG GAAGGA GTGCCAA-3′

We envisioned that ionic current fluctuations recorded through the nanopore were specific to the cis-side addition of AuNP alone (Figure 5II, panel a), PNA2 (Figure 5II, panel b), HCV and H1N1 (Figure 5II, panel c). Moreover, to preclude the fast salt-induced aggregation of AuNPs and enhance at the same time the sensitivity of the detection process [44], a salt-gradient was maintained across the nanopore (trans 3 M KCl, cis 0.1 M KCl).
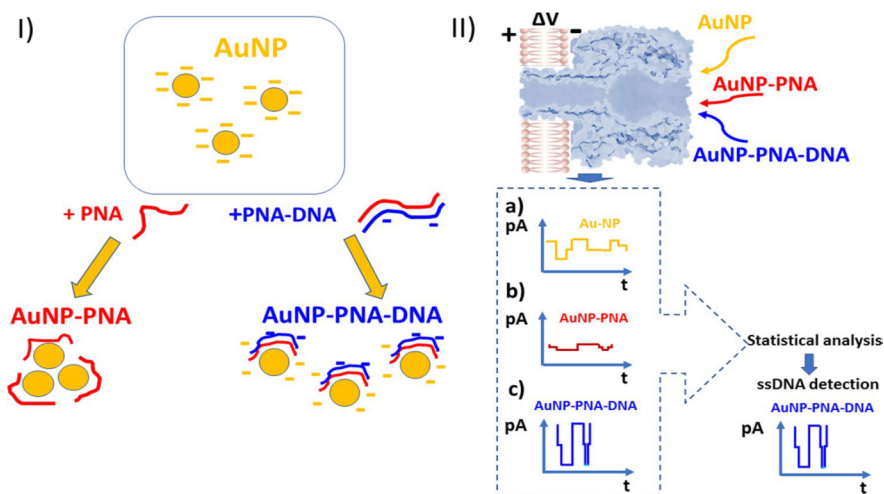

Figure 5. The ssDNAs and DNA-PNA complexes detection strategy using an AuNP-nanopore platform. (I) AuNP-PNA form aggregates that can be disrupted by the hybridization process of PNAs molecules with the complementary ssDNAs. (II) Each analyte entails a distinguishable ionic current blockade signature through the α-HL nanopore (AuNPs - panel a AuNP-PNA aggregates – panel b and AuNP-PNA-DNA complexes – panel c), thus facilitating ssDNA detection when using PNA with a complementary sequence. Adapted from [42].

As evidenced in figure 6, summarizing experiments whereby the analytes were added successively in the *cis*-side of the membrane (AuNPs (panel a), PNA2 (panel b), H1N1 (panel c) and HCV (panel d), distinct patters in the current fluctuations can be observed, visible from the amplitude analysis and the average dwell times (Table 4).

Table 4. Concentration values, ionic current blockages and dwell times for AuNP, and the consecutively added PNA2, H1N1 and HCV

	Concentration	ΔI (pA)	τ_{off} (s)
AuNP	5 nM	48.1 ± 0.85	0.001 ± 5E−4
AuNP/PNA2*	5 nM	-	-
AuNP/PNA2/H1N1	15 nM	57.3 ± 0.8	0.0016 ± 0.001
AuNP/PNA2/H1N1/HCV	50 nM	15.4 ± 0.4	0.12 ± 0.01

* no values recorded, because the AuNP/PNA aggregates were precluded from entering the nanopore, due to steric exclusion

The recorded data demonstrate the possibility of detecting single-stranded HCV fragments in the presence of other ssDNA sequences (i.e., H1N1), mimicking a heterogenous nucleic acids sample.
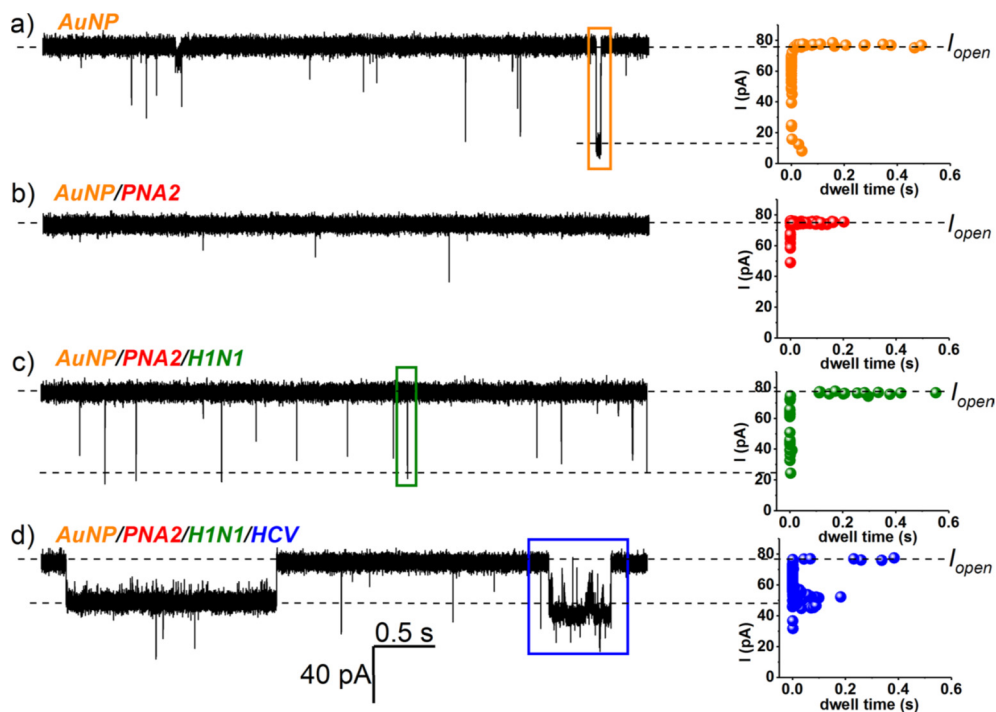

Figure 6. Ionic current fluctuation recorded at ΔV = + 70 mV in the presence of the cis-added AuNPs alone (5 nM) (a), AuNPs mixed with PNA (5 nM) (b), AuNPs/PNA aggregates in the presence of H1N1 (15 nM) (c) and AuNPs/PNA in the presence of both H1N1 (15 nM) and HVC (50 nM) (d), as well as their corresponding current amplitude histograms. Adapted from [42].

The minimum concentration detection limit for PNA2, HCV and H1N1 was established in the nanomolar range (5 nM).

CONCLUSIONS

Unlike other simple, conventional approaches to probing biopolymers properties and function in reconstituted lipid membranes [45], a grand challenge in today's proteomics and genomics is to correlate structure with function, via single-molecule studies. An essential step to achieve individual biopolymers detection and sequencing with single monomer resolution, lies in the specific capturing and holding of polymers inside the nanopore for sufficiently long periods of time, to enable accurate sequence readout. Herein we presented only a few selected from the emerging technologies developed in our laboratory, still in the proof-of-concept stage, yet holding a promise to that end. In the realm of nucleic acids detection, the AuNP aggregation strategy working in conjunction with PNA fragments and nanopore sensing, may enable the rapid and reliable nucleic acid diagnosis, with minimum number of specialized reagents involved.

We dedicate this work to the memory of Professor Petre T. Frangopol, whose work, struggle and dedication made possible the introduction of Biophysics and Medical Physics fields at the Faculty of Physics, 'Alexandru I. Cuza' University of Iasi.

REFERENCES

1. J. J. Kasianowicz; J. W. F. Robertson; E. R. Chan; J. E. Reiner; V. M. Stanford, *Annu. Rev. Anal. Chem.* **2008**, 1, 737−766
2. S. W. Kowalczyk; T. R. Blosser; C. Dekker; *Trends Biotechnol.*, **2011**, *29*, 607–614
3. Z.-L. Hu; M.-Z. Huo; Y.-L. Ying; Y.-T. Long; *Angew. Chem. Int. Ed.*, **2021**, 10.1002/anie.202013462
4. A. Asandei; S. Iftemi; L. Mereuta; I. Schiopu; T. Luchian; *J. Membr. Biol.*, **2014** *247(6)*, 523-530

5. J. J. Kasianowicz; E. Brandin; D. Branton; D. W. Deamer; *Proc. Natl. Acad. Sci. USA*, **1996**, *93*, 13770–13773
6. T. Luchian; Y. Park; A. Asandei; I. Schiopu; L. Mereuta; A. Apetrei; *Acc. Chem. Res.,* **2019**, *52 (1)*, 267–276
7. A. Asandei; I. Schiopu; S. Iftemi; L. Mereuta; T. Luchian; *Langmuir*, **2013**, *29*, 15634–15642
8. A. Fennouri; R. Daniel; M. Pastoriza-Gallego; L. Auvray; J. Pelta; L. Bacri; *Anal. Chem.*, **2013**, *85*, 8488–8492
9. C. Cao; J. Yu; Y.-Q. Wang; Y.-L. Ying; Y.-T. Long; *Anal. Chem.*, **2016**, *88*, 5046–5049
10. C. Cao; M.-Y. Li; N. Cirauqui; Y.-Q. Wang; M. Dal Peraro; H. Tian; Y.-T. Long; *Nat. Commun.*, **2018**, *9*, 2823
11. T. Z. Butler; M. Pavlenok; I. M. Derrington; M. Niederweis; J. H. Gundlach; *Proc. Natl. Acad. Sci. USA*, **2008**, *105*, 20647–20652
12. S. Conlan; Y. Zhang; S. Cheley; H. Bayley; *Biochemistry*, **2000**, *39*, 11845–11854
13. M. Chen; S. Khalid; M. S. P. Sansom; H. Bayley; *PNAS*, **2008**, *105*, 6272–6277
14. G. Huang; K. Willems; M. Soskine; C. Wloka; G. Maglia; *Nat. Commun.*, **2017**, *8*, 1
15. M. Soskine; A. Biesemans; B. Moeyaert; S. Cheley; H. Bayley; G. Maglia; *Nano. Lett.*, **2012**, *12*, 4895–4900
16. F. Haque; J. Lunn; H. Fang; D. Smithrud; P. Guo; *ACS Nano*, **2012**, *6*, 3251–3261
17. E. M. Nestorovich; T. K. Rostovtseva; S. M. Bezrukov; *Biophys. J.*, **2003**, *85*, 3718–3729
18. E. M. Nestorovich; C. Danelon; M. Winterhalter; S. M. Bezrukov; *Proc. Natl. Acad. Sci. USA*, **2002**, *99*, 9789–9794
19. A. Apetrei; A. Asandei; Y. Park; K.-S. Hahm; M. Winterhalter; T. Luchian; *J. Bioenerg. Biomembr.*, **2010**, *42*, 173–180
20. J. Wang; J. A. Bafn; S. P. Bhamidimarri; M. Winterhalter; *Angew. Chem. Int. Ed.*, **2019**, *58*, 4737–4741
21. K. Yamashita; Y. Kawai; Y. Tanaka; N. Hirano; J. Kaneko; N. Tomita; M. Ohta; Y. Kamio; M. Yao; I. Tanaka; *Proc. Natl. Acad. Sci. USA*, **2011**, *108*, 17314–17319
22. L. Song; M. R. Hobaugh; C. Shustak; S. Cheley; H. Bayley; J. E. Gouaux; *Science*, **1996**, *274*, 1859–1865
23. L.-Q. Gu; J. W. Shim; *Analyst*, **2010**, *135*, 441–451
24. R. T. Perera; A. M. Fleming; A. M. Peterson; J. M. Heemstra; C. J. Burrows; H. S. White; *Biophys. J.*, **2016**, *110*, 306–314
25. Y. Wang; D. Zheng; Q. Tan; M. X. Wang; L.-Q. Gu; *Nat. Nanotechnol.*, **2011**, *6*, 668–674
26. A. Ciuca; A. Asandei; I. Schiopu; A. Apetrei; L. Mereuta; C. H. Seo; Y. Park; T. Luchian; *Anal. Chem.*, **2018**, *90*, 7682–7690
27. L. Mereuta; A. Asandei; I. Schiopu; Y. Park; T. Luchian; *Anal. Chem.*, **2019**, *91*, 8630–8637

28. W. Vercoutere; S. Winters-Hilt; H. Olsen; D. Deamer; D. Haussler; M. Akeson; *Nat. Biotechnol.*, **2001**, *19*, 3
29. Y. Ding; A. M. Fleming; H. S. White; C. J. Burrows; *J. Phys. Chem. B*, **2014**, *118*, 12873–12882
30. M. Montal; P. Mueller; *Proc. Natl. Acad. Sci. USA*, **1972**, *69*, 3561–3566
31. L. Mereuta; M. Roy; A. Asandei; J. K. Lee; Y. Park; I. Andricioaei; T. Luchian; *Sci. Rep.*, **2014**, *4*, 3885
32. M. Tsutsui; Y. Maeda; Y. He; S. Hongo; S. Ryuzaki; S. Kawano; T. Kawai; M. Taniguchi; *Appl. Phys. Lett.*, **2013**, *103*, 013108
33. Y. He; M. Tsutsui; C. Fan; M. Taniguchi; T. Kawai; *ACS Nano*, **2011**, *5*, 5509–5518
34. A. Asandei; A. Ciuca; A. Apetrei; I. Schiopu; L. Mereuta; C. H. Seo; Y. Park; T. Luchian; *Sci. Rep.*, **2017**, *7*, 6167
35. A. Asandei; I. Schiopu; C. Ciobanasu; Y. Park; T. Luchian; *J. Membr. Biol.*, **2018**, *251*, 405–417
36. A. Asandei; I. Schiopu; M. Chinappi; C. H. Seo; Y. Park; T. Luchian; *ACS Appl. Mater. Interfaces*, **2016**, *8*, 13166–13179
37. A. Asandei; M. Chinappi; J. -K. Lee; C. H. Seo; L. Mereuta; Y. Park; T. Luchian; *Sci. Rep.*, **2015**, *5*, 10419
38. I. S. Dragomir; A. Asandei; I. Schiopu; I. C. Bucataru; L. Mereuta; T. Luchian; *Polymers (Basel)*, **2021**, *13*, 1210
39. A. Asandei; G. Di Muccio; I. Schiopu; L. Mereuta; I. S. Dragomir; M. Chinappi; T. Luchian; *Small Methods*, **2020**, *4*, 1900595
40. A. Asandei; I. S. Dragomir; G. Di Muccio ;M. Chinappi; Y. Park; T. Luchian; *Polymers (Basel)*, **2018**, *10*, 885
41. M. Wanunu; W. Morrison; Y. Rabin; A. Y. Grosberg; A. Meller; *Nat. Nanotechnol.*, **2010**, *5*, 160–165
42. L. Mereuta; A. Asandei; I. S. Dragomir; I. C. Bucataru; J. Park; C. H. Seo; Y. Park; T. Luchian; *Sci. Rep.*, **2020**, *10*, 11323
43. Z. Guan; J. Liu; W. Bai; Z. Lv; X. Jiang; S. Yang; A. Chen; G. Lv; *PLOS ONE*, **2014**, *9*, e108401
44. L. Mereuta; A. Asandei; C. H. Seo; Y. Park; T. Luchian; *ACS Appl. Mater. Interfaces*, **2014**, *6*, 13242–13256
45. L. Mereuta; T. Luchian; Y. Park; K.-S. Hahm; *Biochem. Biophys. Res. Commun.*, **2008**, *373*, 467-472

174

NEW MERCURY(II) COMPLEXES OF POLYDENTATE LIGANDS

**CĂTĂLIN ŞALGĂU[a], ANDREA DOBRI[a],
ANCA SILVESTRU[a,*]**

ABSTRACT. The mercury(II) complexes $[Hg(SCN)_2\{PPh[C_6H_4(CH_2NMe_2)-2]_2\}]$ (**1**) and $[2,6-(Me_2NCH_2)_2C_6H_3Se][HgCl_3]$ (**3**) were prepared and structurally characterized in solution by multinuclear NMR and ESI mass spectrometry. The reactions performed to obtain the complex $[2,6-(Me_2NCH_2)_2C_6H_3SeHgCl]$ (**2**) failed and we could isolate only a mixture of **3** and $[(HgCl_2)_3\{2,6-(Me_2NCH_2)_2C_6H_3\}]$ (**4**). Compounds **1** and **4** were characterized by single-crystal X-ray diffraction.

Keywords: mercury(II) complexes, triarylphosphane, organoselenium ligand; intramolecular coordination; solution behavior, solid state structure.

INTRODUCTION

The necessity to obtain metal complexes with a better thermal and hydrolytic stability and significantly improved specific activity for catalytic or biological applications determined a permanently increased interest for new ligands, capable to stabilize both main group and transition metals. Various organic groups capable to act as *C,N*-chelating moieties towards phosphorus or chalcogens were used in order to design new ligands bearing both *hard* (N) and *soft* (P or chalcogen) donor atoms in their molecules, thus providing the appropriate conditions for *P,N-* or *E,N*-coordination (E = S, Se, Te) to metal centers [1,2]. Such species include bulky phosphanes, *e.g.* $PPh_x[C_6H_4(CH(R)NR'_2)-2]_{3-x}$ (R = H, Me, R' = Me, x = 0 – 2 [3-7], R = H, R' = Et [8]), $PPh_x[C_6H_3(CH_2NMe_2)_2-2,6]_{3-x}$ (x = 0, 2) [9] or diphosphanes, *e.g.* $2,6-(PR_2CH_2)_2py$ (R = ^tBu, Ph, py = pyridine) [10] and diorganochalcogenides, *e.g.* $[2-(R_2NCH_2)C_6H_4]_2E$ (E = Se, Te) [11], $[2-(Me_2NCH_2)C_6H_4][Me_2C(OH)CH_2]E$ (E = S, Se, Te) [12].

---

[a] *Babeş-Bolyai University, Faculty of Chemistry and Chemical Engineering, Department of Chemistry, Supramolecular Organic and Organometallic Chemistry Centre (SOOMCC), 11 Arany Janos str., RO-400028 Cluj-Napoca, Romania*
** Corresponding author: anca.silvestru@ubbcluj.ro*

During the last years we reported several group 12 metal complexes stabilized by *P,N*-chelating ligands, *e.g.* [MCl$_2$(PPh$_x$R$_{3-x}$)] [M = Zn, Cd, Hg, R = 2-(Me$_2$NCH$_2$)C$_6$H$_4$, x = 0 – 3) [13], organoselenolato groups, *e.g.* [2-(Me$_2$NCH$_2$)C$_6$H$_4$Se]$_2$M (M = Zn, Cd) [14] or by ligands of type [2-(Me$_2$NCH$_2$)C$_6$H$_4$][Me$_2$C(OH)CH$_2$]E (E = S, Se) [15]. As a continuation of our work, we report here about the new mercury(II) complexes [Hg(SCN)$_2${PPh[C$_6$H$_4$(CH$_2$NMe$_2$)-2]$_2$}] (**1**) and [2,6-(Me$_2$NCH$_2$)$_2$C$_6$H$_3$Se][HgCl$_3$] (**3**). Our attempts to synthesize the complex [2,6-(Me$_2$NCH$_2$)$_2$C$_6$H$_3$SeHgCl] (**2**), as well as the crystal and molecular structure of the serendipitously obtained [(HgCl$_2$)$_3${2,6-(Me$_2$NCH$_2$)$_2$C$_6$H$_3$}] (**4**) are also discussed.

RESULTS AND DISCUSSION

Synthesis and solution behavior

The complex [Hg(SCN)$_2${PPh[C$_6$H$_4$(CH$_2$NMe$_2$)-2]$_2$}] (**1**) was obtained by reacting [HgCl$_2${PPh[C$_6$H$_4$(CH$_2$NMe$_2$)-2]$_2$}] and KSCN in a 1:2 molar ratio, using a mixture of solvents (CH$_2$Cl$_2$ and methanol), as depicted in equation 1.

$$[HgCl_2\{PPh[C_6H_4(CH_2NMe_2)\text{-}2]_2\}] \xrightarrow[\text{-2 KCl}]{\text{+2KSCN}} [Hg(SCN)_2\{PPh[C_6H_4(CH_2NMe_2)\text{-}2]_2\}] \quad (1)$$
$$\textbf{1}$$
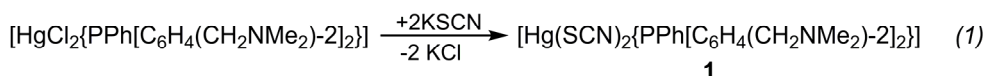
For the synthesis of the complex [HgCl{SeC$_6$H$_3$(CH$_2$NMe$_2$)$_2$-2,6}] (**2**) we employed a multistep procedure based on the lithiation of 1,3-(Me$_2$NCH$_2$)$_2$C$_6$H$_4$, insertion of selenium into the newly formed C–Li bond and subsequent reaction of the lithium organoselenolate with HgCl$_2$ in a 1:1 molar ratio, as displayed in Scheme 1.
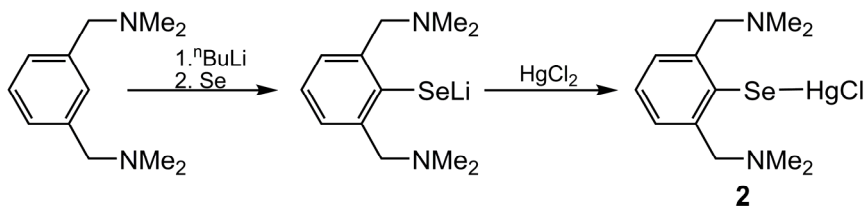
Scheme 1

Instead of the desired product **2**, we obtained a yellowish solid which is only poorly soluble in chlorinated organic solvents. The multinuclear NMR spectra of this solid, recorded in DMSO-d_6, revealed a mixture containing [{2,6-(Me$_2$NCH$_2$)$_2$C$_6$H$_3$}Se][HgCl$_3$] (**3**) and [(HgCl$_2$)$_3${2,6-(Me$_2$NCH$_2$)$_2$C$_6$H$_3$}] (**4**). Recrystallization of the obtained solid resulted in a mixture of crystals

and we could separate only mechanically crystals of the two species. We succeeded to prepare compound **3** by reacting [2,6-(Me$_2$NCH$_2$)$_2$C$_6$H$_3$Se]Cl with HgCl$_2$ in a 1:1 molar ratio (eq. 2).

$$[2,6-(Me_2NCH_2)_2C_6H_3]SeCl + HgCl_2 \longrightarrow [\{2,6-(Me_2NCH_2)_2C_6H_3\}Se]^+[HgCl_3]^- \quad (2)$$
$$\textbf{3}$$
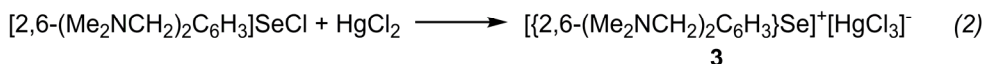
The isolated compound **1** and compound **3** obtained in eq. 2, as well as the mixture of **3** and **4**, isolated as a product obtained after performing the reactions in Scheme 1, were characterized in solution by multinuclear NMR. The ^{1}H NMR spectrum of compound **1** shows in the aliphatic region a broad singlet and an AB spin system, which were assigned to the N(CH_3)$_2$ and the CH_2N protons, respectively, thus suggesting an intramolecular coordination, either N→P or N→Hg. Anyway, the ^{1}H NMR spectrum shows that the two aryl groups with pendant arms are equivalent in solution, at room temperature. In the aromatic region were observed multiplet resonances for the expected non-equivalent protons in the phenyl and the C$_6$H$_4$ groups, with multiplicity determined by ^{1}H-^{1}H and ^{31}P-^{1}H couplings. The ^{31}P and the ^{199}Hg NMR spectra of **1** are consistent with the coordination of phosphorus to Hg(II). They appear as a singlet accompanied by ^{199}Hg satellites and a doublet, respectively, with very close values of the observed ^{31}P-^{199}Hg coupling constants (6200 and 6211 Hz, respectively).

The ^{1}H NMR spectrum of compound **3** shows two singlet resonances in the aliphatic region for the N(CH_3)$_2$ and the CH_2N protons, respectively, thus suggesting the equivalence of the two pendant arms of the 2,6-(Me$_2$NCH$_2$)$_2$C$_6$H$_3$ group. The aliphatic region suggests either no N→Se or N→Hg intramolecular coordination or a dynamic behaviour based on decoordination, inversion at nitrogen and re-coordination, too fast to be observed at room temperature [16]. In the aromatic region of the spectrum are displayed multiplet resonances for the three non-equivalent protons in the C$_6$H$_3$ group. The ^{77}Se and the ^{199}Hg NMR spectra of **3** show singlet resonances at 1185 ppm and at -1353 ppm, respectively. These values are consistent with an ionic structure in solution, containing [{2,6-(Me$_2$NCH$_2$)$_2$C$_6$H$_3$}Se]$^+$ cations and [HgCl$_3$]$^-$ anions. The ESI+ and the ESI– mass spectra of this species contain peaks of high intensity at *m/z* 271.07133 (100%) and at 306.87647 (100%), with a characteristic pattern for the [{2,6-(Me$_2$NCH$_2$)$_2$C$_6$H$_3$}Se]$^+$ cation and the [HgCl$_3$]$^-$ anion, respectively, thus suggesting the formation of the ionic species **3**.

The formation of compound **4** is supported by mass spectrometry. The ESI+ spectrum of the mixture obtained as depicted in Scheme 1 shows,

besides the peaks at *m/z* 271.07133 (77%) and at 306.87647 (92%), another one at *m/z* 193.17054 (36%), corresponding to the cation $[2,6\text{-}(Me_2NCH_2)_2C_6H_3 + H]^+$.

We suppose that the formation of these species, instead of the desired product **2**, was determined by incomplete lithiation of $2,6\text{-}(Me_2NCH_2)_2C_6H_4$, followed by secondary reactions between the species present in solution. Unfortunately, at this moment we don't have a certain reaction mechanism for the whole process which lead to the mixture of **3** and **4**. We can only have a certain explanation for the formation of **4** in the reaction between not lithiated $2,6\text{-}(Me_2NCH_2)_2C_6H_4$ and $HgCl_2$ in a 1:3 molar ratio.

Single-crystal X-ray diffraction studies

The ORTEP-like diagram of **1** and **4** with the atom numbering schemes are depicted in Figure 1 and Figure 2, respectively, while selected interatomic distances and angles for the two compounds are given in Table 1.
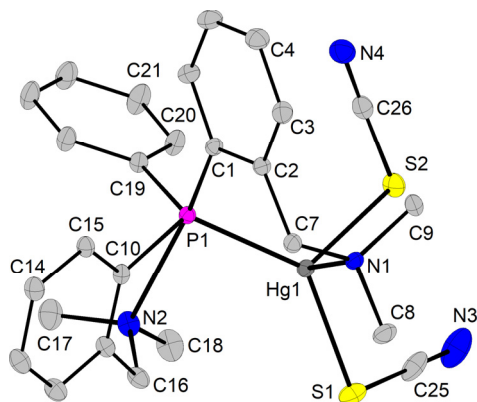
Figure 1. Thermal ellipsoids representation at 30% probability and atom numbering scheme of $C_Pδ_Pλ_{Hg}$-**1**. Hydrogen atoms are omitted for clarity.
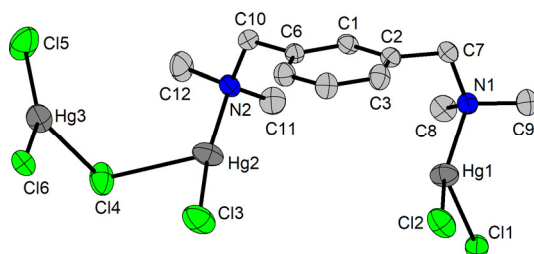

Figure 2. Thermal ellipsoids representation at 30% probability and atom numbering scheme of **4**. Hydrogen atoms are omitted for clarity.

Table 1. Selected interatomic distances [Å] and angles [°] in **1** and **4**

1			
Hg1–P1	2.4602(4)	N1–Hg1–S1	99.78(3)
Hg1–S1	2.5012(5)	N1–Hg1–S2	102.34(3)
Hg1–S2	2.5459(4)	S1–Hg1–S2	101.26(1)
N1···Hg1	2.457(1)	N1–Hg1–P1	91.08(3)
N2···P1	2.96	S1–Hg1–P1	117.43(1)
		S2–Hg1–P1	136.48(2)
4			
		N1–Hg1–Cl1	95.4(3)
		N1–Hg1–Cl2	150.6(3)
N1···Hg1	2.237(10)	N1–Hg1–Cl1'	101.7(3)
N2···Hg2	2.162(7)	Cl1–Hg1–Cl2	105.8(3)
Hg1–Cl1	2.636(5)	Cl1–Hg1–Cl1'	87.61(17)
Hg1–Cl2	2.354(4)	Cl2–Hg1–Cl1'	99.3(3)
Hg1···Cl1'	2.763(6)	Hg1–Cl1–Hg1'	92.39(17)
		Hg1–Cl2–Hg3'''	95.78(5)
		N2–Hg2–Cl3	166.2(2)
Hg2–Cl3	2.280(3)	N2–Hg2–Cl4	101.5(2)
Hg2–Cl4	2.888(3)	Cl3–Hg2–Cl4	90.97(11)
		Cl5–Hg3–Cl6	149.71(16)
		Cl5–Hg3–Cl4	103.62(14)
Hg3–Cl5	2.370(3)	Cl6–Hg3–Cl4	106.67(13)
Hg3–Cl6	2.406(3)	Cl5–Hg3–Cl6''	98.32(15)
Hg3···Cl6''	2.988(3)	Cl6–Hg3–Cl6''	82.83(10)
Hg3···Cl4	2.546(3)	Cl4–Hg3–Cl6''	88.98(10)
		Hg3–Cl4–Hg2	103.92(9)
		Hg3–Cl6–Hg3''	97.17(10)

Symmetry equivalent positions 1-x,-y,1-z; -x,1-y,1-z; and 1+x,1/2-y,1/2+z are given by *prime, double prime* and *triple prime*, respectively.

In compound **1**, the triarylphosphane behaves as a *P,N*-chelating ligand, while the SCN groups act as thiocyanato ligands, thus resulting in a tetrahedral coordination geometry about Hg(II). The second 2-(Me$_2$NCH$_2$)C$_6$H$_4$ group behaves as a *C,N*-chelating moiety towards phosphorus. In this way phosphorus became pentacoordinate, with a distorted trigonal bipyramidal coordination geometry (N2–P1–C1 174.35º) and with the phosphorus atom placed at 0.48 Å above the C10C19Hg1 trigonal plane. The two chelate rings, Hg1N1C7C2C1P1 and P1N2C16C11C10, formed by the N→Hg and N→P, respectively, intramolecular coordination are not planar. The six-membered ring Hg1N1C7C2C1P1 has a boat conformation, with P1 and C7 in apices, while the five-membered ring P1N2C16C11C10 is folded about the P1···C16

imaginary axis. As a result of the intramolecular coordination of the two pendant arms, one to Hg and the other to P, the crystal of compound **1** contains a racemic mixture of $A_P\delta_P\lambda_{Hg}$, $C_P\delta_P\lambda_{Hg}$, $A_P\lambda_P\lambda_{Hg}$ and $A_P\lambda_P\delta_{Hg}$ isomers, where λ and δ refer to the chirality determined by the formation of the six- and five-membered rings about mercury and phosphorus, respectively, while A and C refer to the chirality determined by the phosphorus atom in a trigonal bipyramidal environment [17]. A similar behavior of the triarylphosphane ligand and a close magnitude of the P→Hg, N→Hg and N→P interactions were observed previously for the related [HgCl$_2$\{PPh[C$_6$H$_4$(CH$_2$NMe$_2$)-2]$_2$\}] [13].

The nitrogen atoms of the two SCN ligands are involved in weak N···H interactions (N4···H5 2.56 Å and N3···H9A 2.64 Å, *vs.* Σr$_{vdW}$(N,H) 2.86 Å [18]) with neighbor molecules, thus resulting in a ribbon-like polymeric structure, as depicted in Figure 3.
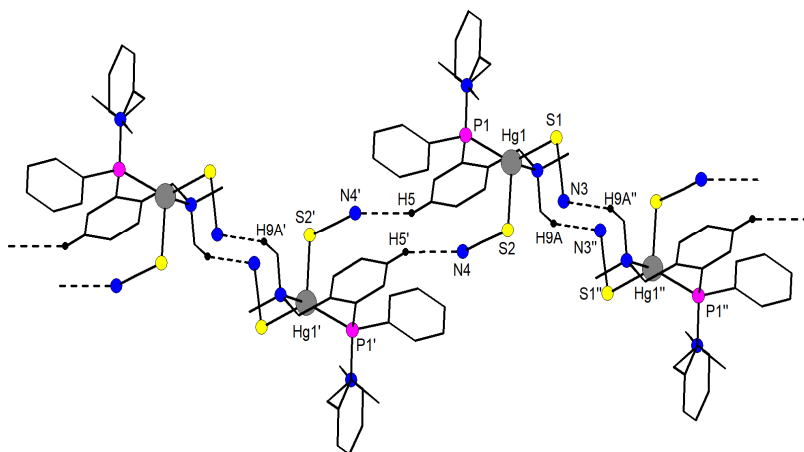

Figure 3. Ribbon-like association in the crystal of **1**. Hydrogen atoms, except those involved in intermolecular interactions are omitted for clarity.

The crystal of **4** contains three HgCl$_2$ independent molecules which are connected in a 3D supramolecular network by a *N,N* bridging 2,6-(Me$_2$NCH$_2$)$_2$C$_6$H$_4$ ligand. The HgCl$_2$ molecules based on Hg1 and Hg3 form parallel polymeric chains of Hg$_2$Cl$_4$ dimers interconnected through chlorine bridges (Cl2···Hg3 3.08 Å). The 2,6-(Me$_2$NCH$_2$)$_2$C$_6$H$_4$ molecules act as *N,N* bridging, neutral ligands between Hg2 and Hg1 atoms (N1→Hg1 2.22 Å and N2→Hg2 2.15 Å, vs. Σr$_{vdW}$(N,Hg) 4.01 Å [18]), while the Hg3 atoms are not involved in any N→Hg interaction. In this way the polymeric chains are connected in 2D layers (Figure 4).
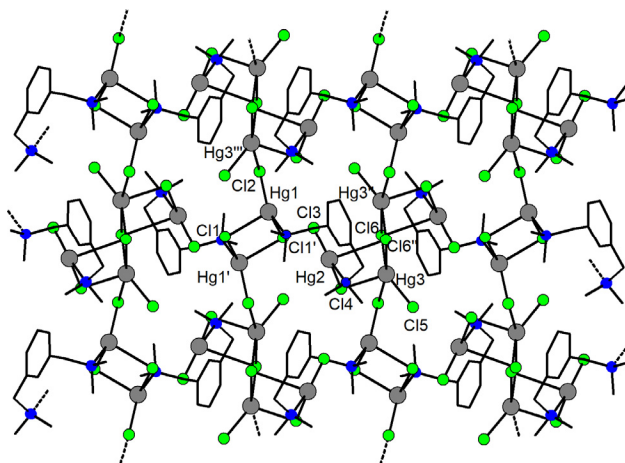
Figure 4. A 2D layer in the crystal of **4**. Hydrogen atoms are omitted for clarity.

Such layers are further connected by weak Cl···Hg interactions (Cl5···Hg2 3.24 Å, vs. Σr_{vdW}(Cl,Hg) 4.27 Å [18]) in a 3D supramolecular network.

EXPERIMENTAL SECTION

The starting materials [HgCl$_2${PPh[C$_6$H$_4$(CH$_2$NMe$_2$)-2]$_2$}] [13] and 2,6-(Me$_2$NCH$_2$)$_2$C$_6$H$_3$SeCl [19] were prepared as previously described. All the other reagents were commercially provided and used as received.

Solvents were dried and distilled under argon prior to use. Melting points were measured on an Electrothermal 9200 apparatus. ^{1}H, ^{31}P{^{1}H}, ^{77}Se{^{1}H} and ^{199}Hg{^{1}H} NMR spectra were recorded in CDCl$_3$ on a BRUKER Avance 400 instrument, operating at 400.1 (^{1}H), 161.9 (^{31}P), 76.3 (^{77}Se) and 71.6 (^{199}Hg) MHz. The chemical shifts are reported in δ units (ppm) relative to TMS (^{1}H, ref. CDCl$_3$ 7.26 ppm, DMSO-d_6 2.50 ppm), H$_3$PO$_4$ 85% (^{31}P), Me$_2$Se (^{77}Se) and Me$_2$Hg (^{199}Hg), respectively. The NMR data were processed using the MestReNova software [20]. ESI mass spectra were recorded on a Thermo Scientific Orbitrap XL spectrometer equipped with a standard ESI/APCI source.

Synthesis of [Hg(SCN)$_2${PPh[C$_6$H$_4$(CH$_2$NMe$_2$)-2]$_2$}] (1)

A solution of KSCN (0.021 g, 0.22 mmol) în MeOH (15 mL) was added at room temperature to a solution of [HgCl$_2${PPh[C$_6$H$_4$(CH$_2$NMe$_2$)-2]$_2$}] (0.07 g, 0.11 mmol) în CH$_2$Cl$_2$ (15 mL). The reaction mixture was stirred for 12 hours.

Subsequently, the solvents were removed under reduced pressure and the remained sticky product was washed with n-hexane (2 x 5 mL), when a colorless solid was formed. Hexane was removed by filtration and the solid was dried under reduced pressure. Yield: 0.07 g (51%). M.p. 156°C. ^{1}H NMR (CDCl$_3$): δ = 2.10 (s, br., 6H, N(CH_3)$_2$), AB spin system with δ$_A$ 3.28 and δ$_B$ 4.00 (4H, CH_2N, $^2J_{HH}$ 12.9 Hz), 7.02 (dd, 2H, P–C$_6H_4$, $^3J_{HH}$ = 7.3, $^3J_{PH}$ = 12.2 Hz), 7.38 (t, 2H, P–C$_6H_4$, $^3J_{HH}$ 7.1 Hz), 7.43 (t, 2H, P–C$_6H_4$, $^3J_{HH}$ 6.8 Hz) 7.53-7.64 (m, 3H P–C$_6H_5$-*meta+para* + 2H P–C$_6H_4$); 7.69 (br., 2H P–C$_6H_5$-*ortho*). ^{31}P NMR (CDCl$_3$): δ = 19.4 (s, $^1J_{HgP}$ 6200 Hz). ^{199}Hg NMR (CDCl$_3$): δ = -597.12 (d, $^1J_{HgP}$ 6211 Hz).

Synthesis of [2,6-(Me$_2$NCH$_2$)$_2$C$_6$H$_3$Se][HgCl$_3$] (3)

A suspension of HgCl$_2$ (0.136 g, 0.50 mmol) in methanol (15 mL) was added to a solution of 2,6-(Me$_2$NCH$_2$)$_2$C$_6$H$_3$SeCl (0.153 g, 0.50 mmol) in CH$_2$Cl$_2$ (15 mL), under stirring, at room temperature. After 12 hours the solvents were removed in vacuum and the remained solid was washed with hexane (2x10 mL) and dried at reduced pressure, when the title compound resulted as a yellowish solid. Yield: 0.266 g (92%). M.p. 148-149 ^{o}C (dec.). ^{1}H NMR (DMSO-d_6), δ = 2.83 [s, 12H, N(CH_3)$_2$], 3,48 [s, 4H, (CH_2N)], 7,24-7,31 (m, 3H, C$_6$H$_3$); ^{77}Se NMR (DMSO-d_6), δ = 1185 (s); ^{199}Hg NMR (DMSO-d_6), δ = -1353 (s). ESI+ MS (MeOH), *m/z* (%): 271.07133 (100) [2,6-(Me$_2$NCH$_2$)$_2$C$_6$H$_3$Se]$^+$, ESI– MS (MeOH), *m/z* (%): 306.87647 (100) [HgCl$_3$]$^-$.

Formation of [2,6-(Me$_2$NCH$_2$)$_2$C$_6$H$_3$Se][HgCl$_3$] (3) and [(HgCl$_2$)$_3${2,6-(Me$_2$NCH$_2$)$_2$C$_6$H$_3$}] (4)

A solution of n-BuLi in n-hexane (1.6 M, 1.46 mL, 2.34 mmol) was added dropwise, under stirring, to a solution of 1,3-(Me$_2$NCH$_2$)$_2$C$_6$H$_4$ (0.450 g, 2.34 mmol) in n-hexane (50 mL). Stirring continued over night, then n-hexane was removed under vacuum and the reaction mixture was dissolved in THF (50 mL). Selenium powder (0.185 g, 2.34 mmol) was added and stirring continued for other 4 hours. To the resulted red solution, HgCl$_2$ (0.635 g, 2.34 mmol) was added and stirring continued overnight. THF was removed under reduced pressure and the product was dissolved in CH$_2$Cl$_2$ (50 mL). Then CH$_2$Cl$_2$ was removed in vacuum and the product was washed with n-hexane and dried, when a yellowish solid was obtained. The NMR and the MS spectra suggested the formation of a mixture containing mainly [{2,6-(Me$_2$NCH$_2$)$_2$C$_6$H$_3$}Se][HgCl$_3$] (**3**) and [(HgCl$_2$)$_3${2,6-(Me$_2$NCH$_2$)$_2$C$_6$H$_3$}] (**4**). ESI+ MS (MeOH), *m/z* (%):193.17054 (36) [RH+H]$^+$, 271.07133 (77) [RSe]$^+$, R = 2,6-(Me$_2$NCH$_2$)$_2$C$_6$H$_3$; ESI– MS (MeOH), *m/z* (%): 306.87647 (92) [HgCl$_3$]$^-$.

X-ray structure determination

The details of the crystal structure determination and refinement for compounds **1** and **4** are given in Table 2. Data were collected on a Bruker D8 VENTURE diffractometer at 100 K, by using a Mo-K_α radiation (λ = 0.71073 Å) from a IµS 3.0 microfocus source with multilayer optics. The structure was refined with anisotropic thermal parameters for non-H atoms. Hydrogen atoms were placed in fixed, idealized positions and refined with a riding model and a mutual isotropic thermal parameter. For structure solving and refinement the Bruker APEX3 Software Package was used [21]. The drawings were created with the Diamond program [22].

Table 2. Crystallographic data for **1** and **4**

	1	4
Empirical formula	$C_{26}H_{29}HgN_4PS_2$	$C_{12}H_{20}Cl_6Hg_3N_2$
Formula weight	693.21	1006.77
Temperature (K)	100(2)	295(2)
Wavelength (Å)	0.71073	0.71073
Crystal system	monoclinic	monoclinic
Space group	P21/n	P21/c
a (Å)	9.0428(2)	11.3141(2)
b (Å)	14.9881(4)	13.5832(2)
c (Å)	20.2953(6)	14.4866(3)
α (°)	90	90
β (°)	102.2860(10)	107.9830(10)
γ (°)	90	90
Volume, ($Å^3$)	2687.71(12)	2117.56(7)
Z	4	4
Density (calculated) (g/cm^3)	1.713	3.158
Absorption coefficient (mm^{-1})	5.963	22.452
F(000)	1360	1792
Crystal size, mm	0.23 x 0.12 x 0.097	0.140 x 0.110 x 0.090
θ range for data collections, °	2.054 to 28.288	1.892 to 28.282
Reflections collected	22055	58817
Independent reflections	6477, [R(int) = 0.0163]	5258 [R(int) = 0.0412]
Refinement method	Full-matrix least-squares on F^2	
Data / restraints / parameters	6477 / 0 / 314	5258 / 0 / 747
Goodness-of-fit on F^2	1.031	1.036
Final R indicies [I>2sigma(I)]	R1 = 0.0134, wR2 = 0.0301	R1 = 0.0276, wR2 = 0.0659
R indicies (all data)	R1 = 0.0148, wR2 = 0.0306	R1 = 0.0372, wR2 = 0.0710
Largest diff. peak and hole, $eÅ^{-3}$	0.407 and -0.527	1.477 and -2.542

CONCLUSIONS

The new metal complexes [Hg(SCN)$_2${PPh[C$_6$H$_4$(CH$_2$NMe$_2$)-2]$_2$}] (**1**) and [2,6-(Me$_2$NCH$_2$)$_2$C$_6$H$_3$Se][HgCl$_3$] (**3**) were isolated as pure species, with good yields, by replacing Cl$^-$ with SCN$^-$ in [HgCl$_2${PPh[C$_6$H$_4$(CH$_2$NMe$_2$)-2]$_2$}] and by extracting Cl$^-$ from 2,6-(Me$_2$NCH$_2$)$_2$C$_6$H$_3$SeCl by HgCl$_2$, respectively. Unfortunately, we could not obtain the complex [2,6-(Me$_2$NCH$_2$)$_2$C$_6$H$_3$SeHgCl] (**2**) by a succession of reactions based on the lithiation of 2,6-(Me$_2$NCH$_2$)$_2$C$_6$H$_4$, but we could prove by multinuclear NMR and ESI mass spectrometry the formation of a mixture of **3** and [(HgCl$_2$)$_3${2,6-(Me$_2$NCH$_2$)$_2$C$_6$H$_3$}] (**4**), as a result of incomplete lithiation and subsequent insertion of selenium. The room temperature ^{1}H NMR spectra gave no clear evidence for N→Hg, N→P or N→Se intramolecular interactions in compounds **1** and **3**, respectively. The X-ray diffraction studies revealed that both aryl groups with pendant arms act as *C,N*-chelating groups in **1**, one of them coordinated to mercury and the other to phosphorus, while in the crystal of **4** the 2,6-(Me$_2$NCH$_2$)$_2$C$_6$H$_4$ molecules act as *N,N* bridging, neutral ligands.

ACKNOWLEDGMENTS

SUPPLEMENTARY DATA

CCDC 2107690 and 2107691 contain the supplementary crystallographic data for compounds **1** and **4**. These data can be obtained free of charge *via http://www.ccdc.cam.ac.uk/conts/ retrieving.html*, or from the Cambridge Crystallographic Data Centre, 12 Union Road, Cambridge CB2 1EZ, UK; fax: +44 1223 336 033; or e-mail: deposit@ccdc.cam.ac.uk.

REFERENCES

1. S. Maggini, *Coord. Chem. Rev.*, **2009**, *253*, 1793-1832.
2. A. J. Mukherjee, S. S. Zade, H. B. Singh, R. B. Sunoj, *Chem. Rev.*, **2010**, *110*, 4357-4416.
3. C. Chuit, R. J. P. Corriu, P. Monforte, C. Reye, J. P. Declercq, A. Dubourg, *Angew. Chem. Int. Ed. Engl.*, **1993**, *32*, 1430-1432.

4. M. A. Alonso, J. A. Casares, P. Espinet, K. Soulantica, *Inorg. Chem.*, **2003**, *42*, 3856-3864.
5. A. Chandrasekaran, N. V. Timosheva, R. O. Day, R. R. Holmes, *Inorg. Chem.*, **2002**, *41*. 5235-5240.
6. I. Yamada, M. Ohkouchi, M. Yamaguchi, T. Yamagishi, *J. Chem. Soc., Perkin Trans.*, **1997**, *1*, 1869-1874.
7. L. Horner, G. Simons, *Phosphorus Sulfur Silicon Relat. Elem.*, **1983**, *15*, 165-175.
8. R. Șuteu, S. Shova, A. Silvestru, *Inorg. Chim. Acta*, **2018**, *475*, 105-111.
9. R. Kreiter, J. J. Firet, M. J. J. Ruts, M. Lutz, A. L. Spek, R. J. M. Klein Gebink, G. Van Kotten, *J. Organomet. Chem.*, **2006**, *691*, 422-432.
10. S. Y. de Boer, Y. Gloaguen, M. Lutz, J. I. Van der Vlugt, *Inorg. Chim. Acta*, **2012**, *380*, 336-342.
11. A. Panda, G. Mugesh, H. B. Singh, R. J. Butcher, *Organometallics*, **1999**, *18*, 1986-1993.
12. A. Pop, R. Mitea, A. Silvestru, *J. Organomet. Chem.*, **2014**, *768*, 121-127.
13. A. Dobri, Al. Covaci, A. Covaci, A. Silvestru, *Polyhedron*, **2020**, *182*, 114511.
14. A. Pölnitz, A. Rotar, A. Silvestru, C. Silvestru, M. Kulcsar, *J. Organomet. Chem.*, **2010**, *695,* 2486-2492*.*
15. A. Pop, C. Bellini, R. Șuteu, V. Dorcet, T. Roisnel, J.-F. Carpentier, A. Silvestru, Y. Sarazin, *Dalton Trans.*, **2017**, *46*, 3179-3191.
16. M. Iwaoka, S. Tomoda, *J. Am. Chem. Soc.*, **1996**, *118*, 8077-8084.
17. N. G. Connelly, T. Damhus, R. M. Hartshorn, A. T. Hutton (Eds.), Nomenclature of Inorganic Chemistry-IUPAC Recommendations 2005, RSC Publishing, Cambridge**, 2005**.
18. S. Alvarez, *Dalton Trans.*, **2013**, *42*, 8617-8636.
19. A. Pop, A. Silvestru, *Polyhedron*, **2019**, *160*, 279-285.
20. MestReC and MestReNova, Mestrelab Research S.L., A Coruña 15706, Santiago de Compostela.
21. G. M. Sheldrick, *Acta Crystallogr. Sect. C*, **2015**, 71, 3-8.
22. DIAMOND-Visual Crystal Structure Information System, Crystal Impact, Postfach 1251, D-53002 Bonn, Germany, **2015**.

THE COMPLEMENTARY ROLE OF THE RAMAN MICROSPECTROSCOPY TO THE OXIDATIVE STRESS ASSAYS IN THE NEONATAL SYNAPTOSOMES CHARACTERIZATION

VLAD-ALEXANDRU TOMA[a,b,c], ALIA COLNIȚĂ[a], IOANA BREZEȘTEAN[a,d], BOGDAN DUME[b], IOANA ROMAN[c], IOAN TURCU[a*]

ABSTRACT. Raman microspectroscopy was tested as an alternative/ complementary method for biochemical evaluation of the synaptosomes obtained from neonatal rat brain prenatally exposed to sodium valproate and treated with allicin. Spectrophotometric assays of several oxidative stress markers (catalase, superoxide dismutase, total thiols) and acetylcholine esterase activity revealed the redox balancing function and pro-cholinergic effect of the allicin as compared to the valproate effect. Raman evaluation showed no significant changes in our experimental conditions. Different concentrations and volumes of the synaptosomes vesicles must be tested for the optimal Raman examination of these purified synaptosomes.

Keywords: Raman, synaptosomes, brain, vesicles, sensitive method, redox status

INTRODUCTION

The structural diversity of the nervous system frequently needs multidisciplinary perspectives in order to evaluate a phenomenon in a more accurate manner. As described by Frisch et al. [1], prenatally exposure of Wistar rats to high dosages of sodium valproate induced in newborn individuals

[a] *National Institute for Research and Development of Isotopic and Molecular Technologies, Donath str. No. 67-103, 400293 Cluj-Napoca, Romania*
[b] *Babeș-Bolyai University, Faculty of Biology and Geology, Clinicilor str. No. 5-7, 400006 Cluj-Napoca, Romania*
[c] *National Institute of Research and Development for Biological Sciences, Institute of Biological Research, Republicii str. No. 48, 400015 Cluj-Napoca, Romania*
[d] *Babeș-Bolyai University, Faculty of Physics, Kogalniceanu str. No.1, 400084, Cluj-Napoca, Romania*
[*] *Corresponding author: ioan.turcu@itim-cj.ro*

cognitive teratogenicity that might be associated with the autism spectrum disorders (ASDs). ASDs were characterized by redox imbalance based on the down-regulation of the factor erythroid-derived 2-like 2 (Nrf2). Alongside, in ASDs were observed arterial hypertension by endothelial NO synthetase (eNOS) deficiency, DNA hyperacetylation, neuronal hyperconnectivity with increased ATP cycle, and synaptic deficiency of postsynaptic density protein 95 (PSD-95). The allicin (which can be easily obtained from garlic and onion) acts as an antioxidant, NRF2 activator, increases the concentration of the S-allyl-mercapto-glutathione [2] in brain, liver, or plasma and increases the NO concentration in blood. Until now, ASDs are established just after the appearance of the symptoms at 2-3 years old. The context of ASDs manifestation greatly restricts the investigation methods, many of these being invasive or applied too late. As a prototype idea, the investigation of the synaptic feature with very sensitive methods could form a basis for the early identification of an ASDs-related pattern in newborns. The synaptosomes are vesicles that contain pre/post-synaptic densities, mitochondria, and whole synaptic neurochemical complex. These vesicles, like the exosomes, pass over the cellular membranes and can be identified in the bloodstream [3]. Based on these pieces of evidence, we tested as a first step, the Raman microspectroscopy on the neonatal brain synaptosomes associated with redox-cholinergic status evaluation.

Raman microspectroscopy is a noninvasive and nondestructive label-free technique that uses the inelastically scattered light to rapidly provide biochemical and structural information from molecules [4, 5]. Each molecule is characterized by a unique "spectral fingerprint" which comprises its vibrational pattern dependent on its constituent chemical bonds and structure [5]. Recently, the Raman technique has been recognized as a very powerful analytical tool to help advance the field of neuroscience [6]. It has been used to characterize fundamental biological molecules in cells [4, 7] to discriminate normal cells from cancer cells on the basis of their biochemical differences [4, 8, 9, 10] and to detect protein misfolding and aggregation, key modifications that take place in the early stage of neurodegenerative diseases [5, 10, 11, 13]. To further enhance its helpfulness, Raman microspectroscopy has been multiplexed with other analytical methods (such as advanced statistical techniques) to shed light on the relative abundance of various molecules in the brain [13].

In this work we employed Raman spectroscopy for the rapid characterization of synaptosomes (SYN) prepared from neonatal Wistar rat brains and as a detection tool to identify the vibrational changes induced into the SYN samples treated with either sodium valproate (SYN@VAL), allicin (SYN@ALI) or both (ALI@SYN@VAL). Mizuno et al. [14] reported an early

study focused on the use of Fourier Transform (FT) Raman spectroscopy in monitoring the relative changes of proteins and lipids. Moreover, the study was able to reveal the structural changes and the component content ratio from the synaptosomal fraction of the rat brain. Ajito et al. [7] applied a laser trapping technique combined with near-infrared (NIR) Raman spectroscopy (LTRS) for the analysis of SYN isolated from the rat brain, dispersed in the phosphate buffer solution [7, 15]. Their results indicated that the laser-trapped synaptosomes include some types of lipids and proteins. In another study [16], the same group describes in situ detection of glutamate released from a single SYN using LTRS. As far as we know no Raman spectroscopic investigations were reported until now on SYN@VAL, SYN@ALI, and ALI@SYN@VAL.

RESULTS AND DISCUSSION

The oxidative stress measurements have revealed that valproate treatment in adults decreased ($P < 0.01$) the catalase (CAT) activity (**Fig. 1a**) in newborns as well as allicin administration ($P < 0.05$). Combined therapy normalized the CAT activity as compared to Control but remained slightly decreased ($P < 0.05$). Superoxide dismutase (SOD) (**Fig. 1b**) activity was unchanged after valproate exposure but allicin administration slightly increased the enzyme activity ($P < 0.05$). The oxidative stress enzymes and other non-enzymatic antioxidants such as reduced glutathione (GSH) or ascorbate cannot be described as standard parameters which are in direct relationship with oxidative stress increasing or decreasing. Our data suggest firstly that CAT decreasing was not associated with SOD decreasing and secondly, the antioxidants such as allicin reduced the CAT activity and induced a high activity of the SOD, according to our previous results [17]. As was noticed by Loyd [18], valproate administration reduced the activity of several antioxidants such as CAT, SOD, or peroxidase via the NRF2 down-regulation effect. Our results partially confirm these findings by decreasing the CAT activity whereas SOD remained unchanged.

The nonenzymatic antioxidant potential of the synapses was evaluated by measuring the concentration of the total -SH groups (**Fig. 1c**). Valproate administration did not change the level of the thiols in synaptosomes while allicin treatment significantly decreased ($P < 0.001$) the total -SH concentration. Decreasing of the -SH groups after allicin administration was noticed in blood and liver by Rabinkov et al. [19] and confirmed by our previous results [17]. Briefly, the allicin reacts with GSH and forms a new

compound, S-allyl-mercapto-glutathione which is not detected by Ellman reaction. Based on this evidence, although the concentration of GSH and -SH groups decreased after allicin treatment, a new thio-compound, S-allyl-mercapto-glutathione [17, 19] restore the thio-compounds pool. These findings demonstrated that prenatally administration of sodium valproate will expose the newborns to oxidative stress by reducing the antioxidant enzymes. In contrast, prenatally administration of allicin maintained or increased the antioxidant capacity in the synaptic complex. Various relationships between oxidative stress and chemical signaling of the neurons were described in literature [20, 21]. Our experimental context was correlated to the valproate signaling effect by increasing γ-aminobutiric acid (GABA) concentration [22]. Since GABA is an inhibitory molecule, we evaluate the opposite effect by measuring the acetylcholine esterase (AChE) activity in the purified synaptosomes (**Fig. 1d**).

Allicin administration slightly increased ($P < 0.05$) AChE whereas valproate significantly decreased the activity of this enzyme ($P < 0.001$) and the combined therapy normalized the AChE activity as compared to Control. Our results confirm several previous findings of the stimulated cholinergic effect of the allicin [23] and argue the positive cognitive effect of the allicin consumption [24]. These results were then associated with Raman microspectroscopy in order to evaluate the complementary role of the spectroscopic methods in the synaptosome characterization. The Raman results are shown in **Fig. 2.** Very similar spectra are the ones of the control sample and the SYN@ALI sample, while SYN@VAL and ALI@SYN@VAL also present identical features.

The Raman spectra of SYN and SYN@ALI samples are dominated by the sharp, intense peak at 669 cm^{-1}/678 cm^{-1} which can be assigned to C-S stretching mode or to deformations in cysteine [5]. Another well-defined but low-intensity Raman band is at 705 cm^{-1}/714 cm^{-1}, coming from cholesterol [5]. The same authors assign the Raman bands located in the spectral range 1480-1554 cm^{-1} to C-H/C=N deformation and to amide II, while the band at 1716 cm^{-1}/1721 cm^{-1} could come from esters or amide groups [7, 15]. The last one in also present in the Raman spectra of the SYN@VAL and ALI@SYN@VAL samples with little to no shift. Furthermore, the dominant band at 669 cm^{-1}/678 cm^{-1} from the first two samples is missing. This could be an indication of the induced autism and the local molecular disruption/degradation upon treatment with sodium valproate.
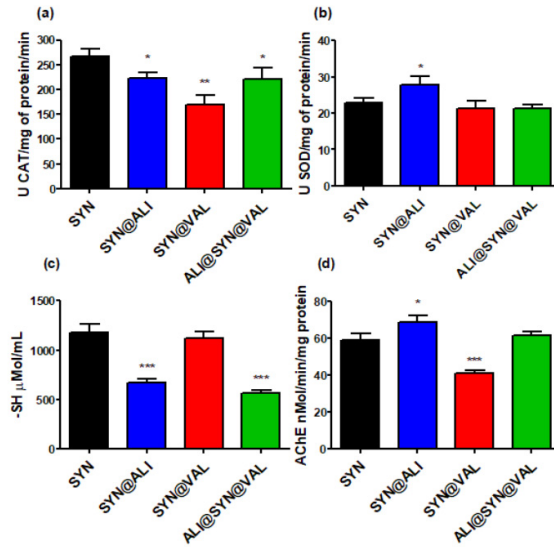
Figure 1. Assessment of CAT (a), SOD (b), -SH (c) and AChE (d) in purified synaptosomes of control (SYN) and experimental groups. Values are expressed as mean ± SEM. *$P < 0.05$, **$P < 0.01$, ***$P < 0.001$.
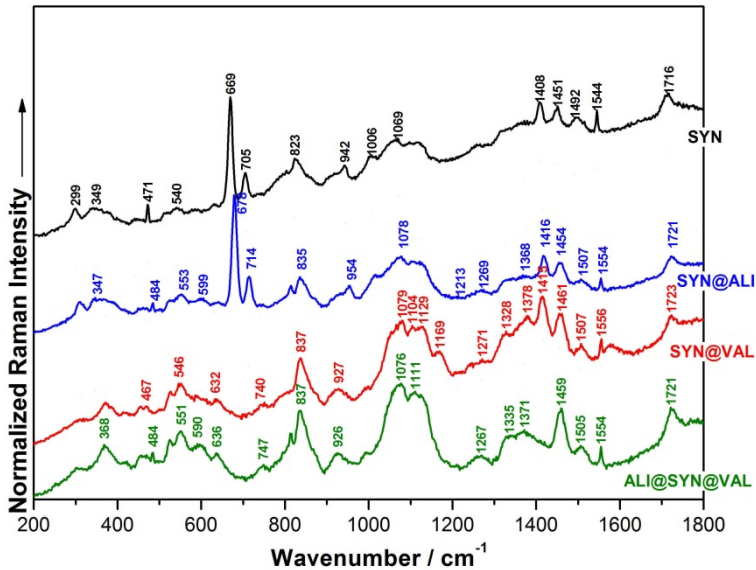

Figure 2. Normalized Raman spectra of the investigated samples.

CONCLUSIONS

Overall, the Raman analysis indicated a similar spectral fingerprint in the case of all four tested samples. The major difference lies in the absence of the 669 cm^{-1}/678 cm^{-1} in the case of the treated samples with sodium valproate, suggesting an intense structural modification. Based on the spectral features of the investigated samples, one can conclude that the treatment with allicin at the used concentration has no significant influence on the studied synaptosomes. In opposition with these findings, the biochemical measurements depict redox balancing reactions after allicin administration, despite the lack of spectroscopic fingerprint. Further Raman analyses must be done with new different concentrations and volumes.

EXPERIMENTAL SECTION

Animals

Adult Wistar female rats (3-month-old) weighing 120-150 g were provided *ad libitum* access to standard rat chow and water. Animals have been maintained in a light/temperature-controlled room with a light/dark cycle of 12/12 h under 22°C constant temperature. Rats were housed 3/cage and all rats in the same cage corresponded to one of the experimental groups. After 3 days of habituation, one male was moved in each cage for the next 5 days. At the end of this period, the males were removed and the first day after male removal was considered as E1 (embryonic day 1). The experimental groups were: Control (SYN), Allicin (SYN@ALI), Valproate (SYN@VAL) and Allicin + Valproate (ALI@SYN@VAL).

Treatment procedures

In E10 (gestational day 10), the rats were intraperitoneally injected with sodium valproate 550 mg/kg b.w. in saline solution 0.9%. Concomitantly, the allicin treatment was enteral administered, until the birth of the pups (E20-E21), in all groups without Control. The allicin dose was 2.5 mg/kg b.w. Animal care and procedures were carried out in accordance to the European Communities Council Directive 2010/63/UE. The procedures of the current work have been approved by the Ethical Committee of Babeș-Bolyai University (IRB no. 2012/03.02.2016).

Neonatal brain sampling and synaptosomes purification

12h after birth, the corresponding pups of the experimental groups were slightly narcotized with diethyl ether and 3 whole brains/group were dissected out, weighting and placed in Syn-PER buffer (Thermo Fischer, 87793) for synaptosomal purification. The whole tissue was lysed 1:1 w/v with

Syn-PER buffer and the sample was then centrifugated at +4°C, for 10 min, at 1500 rpm. The supernatant was collected and spun at 13.500 rpm at +4°C for 20 min. The pellet obtained was the required synaptosomal preparation. For the next measurements, the pellet was resuspended in 5 mL Syn-PER buffer solution and kept at -80°C.

Raman measurements

Raman measurements were performed on a number of 4 liquid samples: SYN, SYN@VAL, SYN@ALI and ALI@SYN@VAL. The Raman spectra were recorded using a Renishaw InVia Reflex Raman confocal spectrometer with a 532 nm excitation line. The laser power on the samples was 200 mW. The signal was collected in the range 200-1800 cm^{-1} using an edge filter >100 cm^{-1}. The spectral resolution was 1 cm^{-1}. A Leica microscope with a 20× objective was used to focus and to visualize the liquid samples. The measurements were conducted on 10 µL.

Biochemical assays

The isolated synaptosomes were used to assay the activity of CAT, SOD, AChE and the concentration of -SH groups. CAT was assayed by the spectrophotometric measure of the decreasing absorbance of the hydrogen peroxide at 240 nm. SOD was assayed by the method with pyrogallol. The superoxide catalyzes the pyrogallol oxidation and this reaction was measured at 420 nm. The oxidation of the pyrogallol was inversely proportional to the SOD activity. AChE was determined also by a kinetic method using the Ellman reagent (DTNB, dithionitrobenzoic acid) with acetylthiocoline iodide 0.0745 M at 412 nm. Total -SH groups were colorimetrically assayed with Ellman reagent at 412 nm.

Statistical analyses

All results are expressed as mean ± SEM. Comparisons between multiple groups were made using one-way ANOVA followed by Bonferroni's post-hoc test. $P < 0.05$ was considered statistically significant and was interpreted as follows: *$P < 0.05$, **$P < 0.01$, ***$P < 0.001$. Statistical analyses were done using GraphPad Prism 5.

ACKNOWLEDGMENTS

REFERENCES

1. C. Frisch; K. F. Hüsch; A. Angenstein; W. Kudin; C. E. Kunz; C. Elger Helmestaedter; *Epilepsia*, **2009**, *50*, 1432-1441.
2. J. Borlinghaus; F. Albrecht; M. C. H. Gruhlke; I. D. Nwachukwu; A. J. Slusarenko; *Molecules*, **2014**, *19*, 12591-12618.
3. C. Hacioglu; F. Kar; G. Kanbak; *Med. Sci. Discovery*, **2018**, *5*, 192-197.
4. M. Lasalvia; G. Perna; V. Capozzi; *Appl. Spectrosc.*, **2014**, *68*, 1123-1131.
5. G. Devitt; K. Howard; A. Mudher; S. Mahajan; *ACS Chem. Neurosci.*, **2018**, *9*, 404-420.
6. T. D. Payne; A. S. Moody; A. L. Wood; P. A. Pimiento; J. C. Elliott; B. Sharma; *Analyst,* **2020**, *145*, 3461-3480.
7. K. Ajito; C. Han; K. Torimitsu; *Microsc. Microanal.*, **2003**, *9*, 1062-1063.
8. H. Wang; T. S. Tsai; J. Zhao; A. M. D. Lee; B. K. K. Lo; M. Yu; H. Lui; D. I. McLean; H. Zeng; *Photodermatol. Photoimmunol. Photomed.*, **2012**, *28*, 147-152.
9. P. Donfack; M. Rehders; K. Brix; P. Boukamp; A. Materny; *J. Raman Spectrosc.*, **2010**, *41*, 16-26.
10. Y. Li; Z. N. Wen; L. J. Li; M. L. Li; N. Gao; Y. Z. Guo; *J. Raman Spectrosc.*, **2010**, *41*, 142-147.
11. H. M. Schipper; C. S. Kwok; S. M. Rosendahl; D. Bandilla; O. Maes; C. Melmed; D. Rabinovitch; D. H. Burns; *Biomarkers Med.*, **2008**, *2*, 229-238.
12. M. Muratore; *Anal. Chim. Acta*, **2013**, *793*, 1-10.
13. D. Sun; X. Chen; *ACS Cent. Sci.*, **2020**, *6*, 459-460.
14. A. Mizuno; T. Hayashi; K. Tashibu; S. Maraishi; K. Kawauchi; Y. Ozaki; *Neurosci. Lett.*, **1992**, *141*, 47-52.
15. K. Ajito; K.Torimitsu; *Lab. Chip.*, **2002**, *2*, 11-14.
16. K. Ajito; C. Han; K. Torimitsu; *Anal. Chem.*, **2004**, *76*, 2506-2510.
17. V. Toma; A. B. Tigu; A. D. Farcaș; B. Sevastre; M. Taulescu; A. M. Gherman; I. Roman; E. Fischer-Fodor; M. Pârvu; *Int. J. Mol. Sci.*, **2019**, *20*, 1-18.
18. K. A. Loyd; *Biosci. Horiz.*, **2013**, *6*, 1-10.
19. A. Rabinkov; T. Miron; D. Mirelman; M. Wilchek; S. Glozman; E. Yavin; L. Weiner; *Biochim. Biophys. Acta*, **2000**, *1499*, 144-153.
20. A. L. Christianson; N. Chesler; J. G. Kromberg; *Dev. Med. Child. Neurol.*, **1994**, 30, 161-171.
21. M. Kuwagata; T. Ogawa; S. Shioda; T. Nagata; *Int. J. Devl. Neuroscience*, **2009**, *27*, 399-405.
22. C. H. Kim; P. Kim; H. S. Go; G. S. Choi; J. H. Park; H. E. Kim; S. J. Jeon; I. C. Pena; S. H. Han; J. H. Cheong; J. H. Ryu; C. Y. Shin; *J. Neurochem.*, **2013**, *124*, 832-843.
23. S. Kumar; *Indian J. Pharmacol.*, **2015**, *47*, 444.
24. H. Zhang; P. Wang; Y. Xue; L. Liu; Z. Li; Y. Liu; *Tissue and Cell*, **2018**, *50*, 89-95.

HIGUCHI MODEL APPLIED TO IONS RELEASE
FROM HYDROXYAPATITES

**AURORA MOCANU[a], PETRE T. FRANGOPOL[&], REKA BALINT[a],
OANA CADAR[b], IULIA MARIA VANCEA[a], ROZALIA MINTĂU[a],
OSSI HOROVITZ[a], MARIA TOMOAIA-COTISEL[a,c*]**

ABSTRACT. In this study, the ions release of physiological elements from pure stoichiometric hydroxyapatite, HAP, and from multi-substituted hydroxyapatite, ms-HAPs, containing 1.5%Mg, 0.2%Zn, 0.2%Si and 5 %Sr, noted HAPc-5%Sr, and from HAPc-10%Sr, in water and in simulated body fluid, SBF, was studied by inductively coupled plasma optical emission spectrometry, ICP-OES, both in static and simulated dynamic regimes. The HAP and ms-HAP nanoparticles, NPs, were prepared by wet chemical precipitation and lyophilized powders were physicochemical characterized as presented elsewhere. The *in vitro* cations and anions release mechanism was investigated by applying a modified Higuchi model, which fits well the experimental results, particularly for simulated dynamic conditions. The predominant role of diffusion in the release of ions from the hydroxyapatites was confirmed. The sustained ions release from these nanomaterials recommends the investigated ms-HAPs for therapeutic applications.

Keywords: multi-substituted hydroxyapatites; ions release; static conditions, simulated dynamic conditions; Higuchi model

INTRODUCTION

Hydroxyapatite, HAP, and multi-substituted hydroxyapatites, ms-HAPs are frequently used as bone substitutes [1-9]. As physiological elements Mg, Zn, Sr and Si were employed due to their role in bone regeneration [10, 11] and multiple biomedical applications in orthopedy and in stomatology [12-16]

---

[a] *Babeş-Bolyai University, Faculty of Chemistry and Chemical Engineering, Research Center of Physical Chemistry, 11 Arany Janos Str., RO-400028, Cluj-Napoca, Romania.*

[b] *INCDO INOE 2000, Research Institute for Analytical Instrumentation, 67 Donath Str., RO-400293 Cluj-Napoca, Romania.*

[c] *Academy of Romanian Scientists, 3 Ilfov Str., RO-050044, Bucharest, Romania.*

[&] *Deceased on December 11, 2020.*

[*] *Corresponding author: mcotisel@gmail.com.*

AURORA MOCANU, PETRE T. FRANGOPOL, REKA BALINT, OANA CADAR, IULIA MARIA
VANCEA, ROZALIA MINTĂU, OSSI HOROVITZ, MARIA TOMOAIA-COTISEL

as coatings on metallic implants for enhanced osseointegration in the fracture healing. The structure of ms-HAP nanomaterials is the unchanged HAP structure, as demonstrated previously [2, 17-19] by complimentary methods XRD, SEM, AFM, BET, IR, Raman [11], as well TG, DTG, DTA and DSC showing a superior thermal stability [2, 7].

Hydroxyapatite and other calcium phosphates were also used as carriers for various drugs, and the drug release in water and physiological liquids was investigated [20-26]. However, HAPs powders, containing physiological elements, Mg, Zn, Si and Sr, have not been actively studied for simultaneously ions release in immersion liquids. One reason for the lack of research is that ions release requires extended investigation in time for evaluation of the ions release profile which might be related with the optimal therapeutic effect of these nanomaterials [11, 27, 28].

The behavior of synthesized stoichiometric hydroxyapatite (HAP) $Ca_{10}(PO_4)_6(OH)_2$ and of two multi-substituted hydroxyapatites (ms-HAPs), both containing 1.5 wt% Mg, 0.2 wt% Zn, 0.2 wt% Si and different Sr amounts: HAPc-5%Sr , respectively HAPc-10%Sr when immersed in water and in simulated body fluid (SBF) was recently investigated [11, 27]. The theoretical formulas for the ms-HAP materials are: $Ca_{8.76}Mg_{0.63}Zn_{0.03}Sr_{0.58}(PO_4)_{5.93}(SiO_4)_{0.07}(OH)_{1.93}$ for HAPc-5%Sr and $Ca_{8.12}Mg_{0.65}Zn_{0.03}Sr_{1.20}(PO_4)_{5.93}(SiO_4)_{0.07}(OH)_{1.93}$ for HAPc-10%Sr. The release of Ca^{2+}, Mg^{2+}, Sr^{2+}, as well as of P (phosphate) in water and the variation of ions content in SBF in contact with soaked HAPs was measured using inductively coupled plasma optical emission spectrometry (*ICP-OES*). Zn^{2+} and silicate ions could not be detected in the solutions, since they were under the detection limit of ICP-OES. A static method was applied, where the HAP samples were maintained in the immersion liquid in closed flasks for different time frames, from 1 to 90 days, and a simulated dynamic method, when the immersion liquid was changed daily with a fresh one, for 7 days.

Some conclusions about the release kinetics were obtained by applying the Korsmeyer-Peppas equation to our results [11, 27] when a complex mechanism, variable in time, including diffusion, but also incongruent dissolution effects was evidenced. For the samples soaked in SBF, only strontium release can be considered, since in SBF calcium, phosphate and magnesium ions are present, and an uptake of these ions takes place on the solid HAPs, with formation of new apatite. Therefore in the case of these ions the release in SBF is counteracted by their deposition, which can even overcome the release.

In order to better understand the role of diffusion and dissolution, we decided to further explore the release mechanism with a different mathematical model. The Higuchi model [29-31] was largely applied and compared with other

models mostly for the release of drugs from polymeric matrices [32-37], but also from inorganic matrices, particularly hydroxyapatites and other calcium phosphates [38-40]. It is based on Fickian diffusion, so it should work when inner diffusion of ions from the particle to the surrounding liquid is the rate determining step and the released species is uniformly distributed in a homogeneous matrix [38]. Then, the released amount of a species should be proportional to the square root of time. The simplest form of the Higuchi equation is:

$$M_t = k_H \, t^{1/2} \qquad\qquad (1)$$

where M_t is the cumulative ions release at time t. The Higuchi release rate constant k_H is determined for given conditions both by characteristics of the solid matrix and by the characteristics of the released species.

RESULTS AND DISCUSSION

For a verification of the role of inner diffusion in the ion release from HAPs, the applicability of the Higuchi equation (1) was tested. The ion release profile from HAP, HAPc-5%Sr and HAPc-10%Sr, both noncalcined and calcined, is represented in Figure 1 against the square root of time ($t^{1/2}$), with time measured in days ($d^{1/2}$) for 90 days in static conditions. In Figure 2 the cumulated ion release is represented against $time^{1/2}$($days^{1/2}$) for 7 days in simulated dynamic conditions (replacement of the immersion liquid after each day).

It is evident from Figures 1 and 2 that the first point (for day 0) is an outlier. The regression lines for the linearization $M_t = f(t^{1/2})$ do not pass through the origin of coordinates, in agreement with the finding that diffusion is not the main process in the early stages of ion release. Therefore a modified form of equation (1) was tried:

$$M_t = a + Kt^{1/2} \qquad\qquad (2)$$

where M_t is the cumulative ions release at time t and K is a release rate constant, which depends both on the characteristics of HAP nanoparticles and on the properties of the released species, but also on the nature of the immersion medium or temperature. Some of the regression lines can be seen in Figure 3 on the example of the noncalcined HAPc-5%Sr sample, for the release of Mg^{2+} ions in water and Sr^{2+} ions both in water and SBF, in static and simulated dynamic conditions.

In Table 1 the parameters of the regression lines according to eq. (2) are given for days 1-90 in static conditions: the y-intercept, a-value, and the release rate constant, K, with their standard errors and the coefficients of determination (r^2).
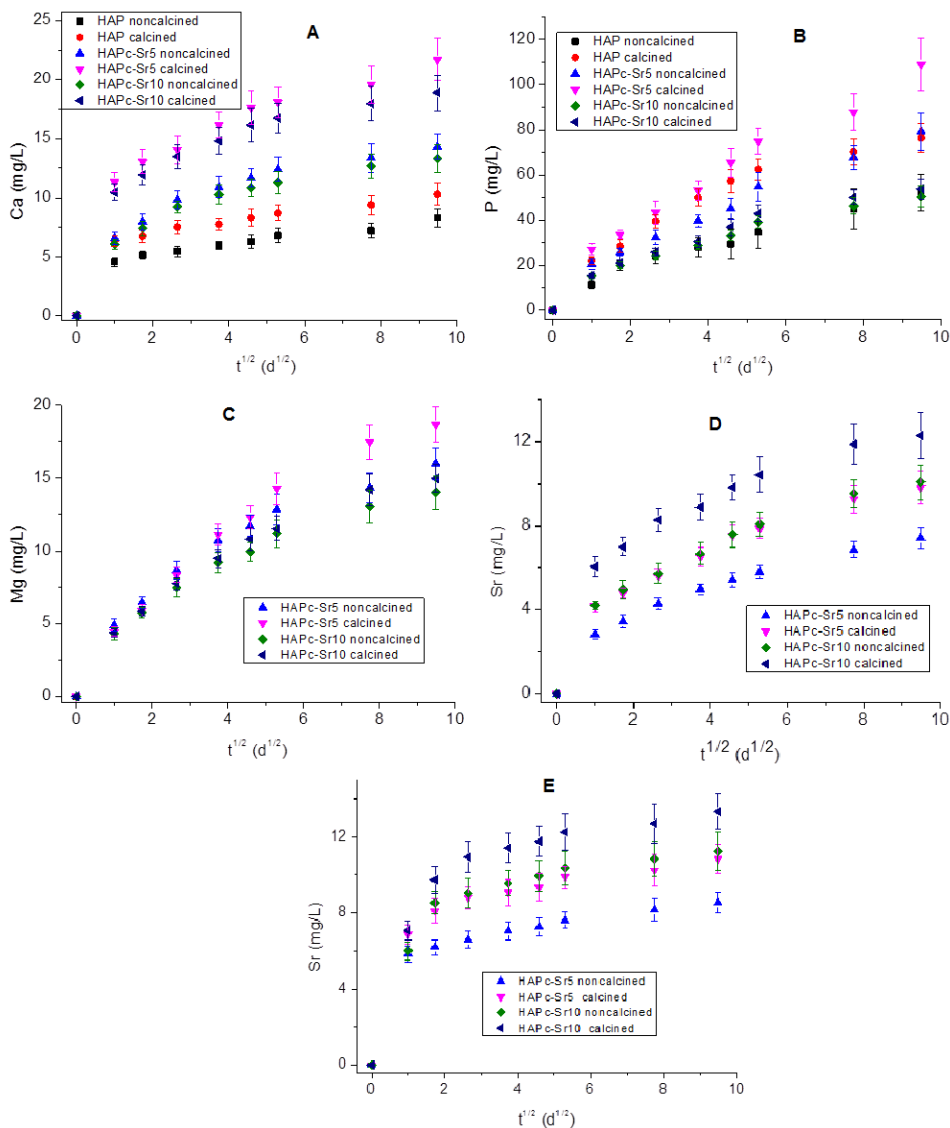
AURORA MOCANU, PETRE T. FRANGOPOL, REKA BALINT, OANA CADAR, IULIA MARIA
VANCEA, ROZALIA MINTĂU, OSSI HOROVITZ, MARIA TOMOAIA-COTISEL

Figure 1. Ion release vs. square root of time (days$^{1/2}$) for 90 days in static conditions from noncalcined and calcined samples of HAP, HAPc-5%Sr (HAPc-Sr5) and HAPc-10%Sr (HAPc-Sr10). Release in water of Ca^{2+} (A), P (phosphate ions, B), Mg^{2+}(C), Sr^{2+}(D), and Sr^{2+} in SBF (E). Vertical bars represent the standard deviations of the measured values.
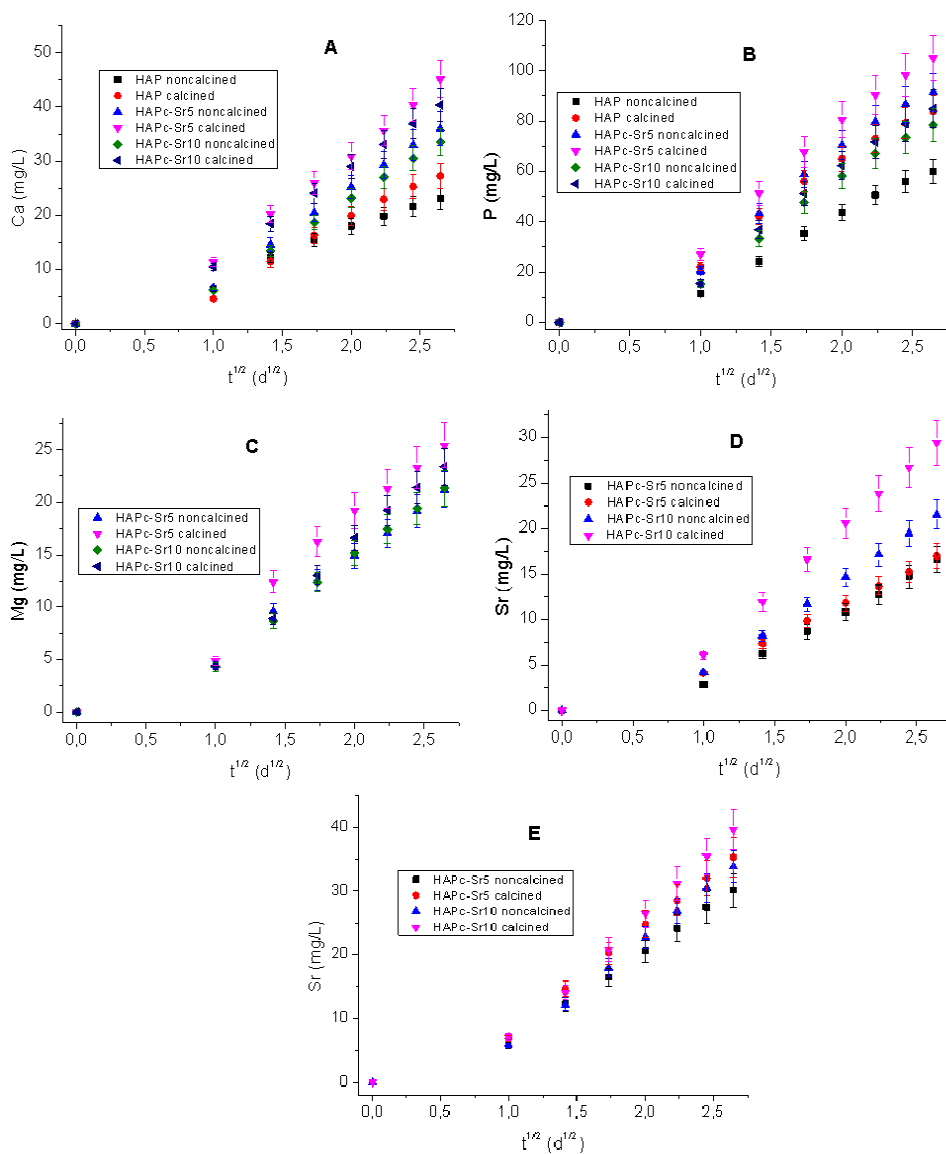
Figure 2. Cumulated ion release vs. time$^{1/2}$ (days$^{1/2}$) for 7 days in simulated dynamic conditions from noncalcined and calcined samples of HAP, HAPc-5%Sr (HAPc-Sr5) and HAPc-10%Sr (HAPc-Sr10). Release in water of Ca^{2+} (A), P (phosphate ions, B), Mg^{2+}(C), Sr^{2+} (D), and Sr^{2+} in SBF (E). Vertical bars represent the standard deviations of the measured values.

AURORA MOCANU, PETRE T. FRANGOPOL, REKA BALINT, OANA CADAR, IULIA MARIA
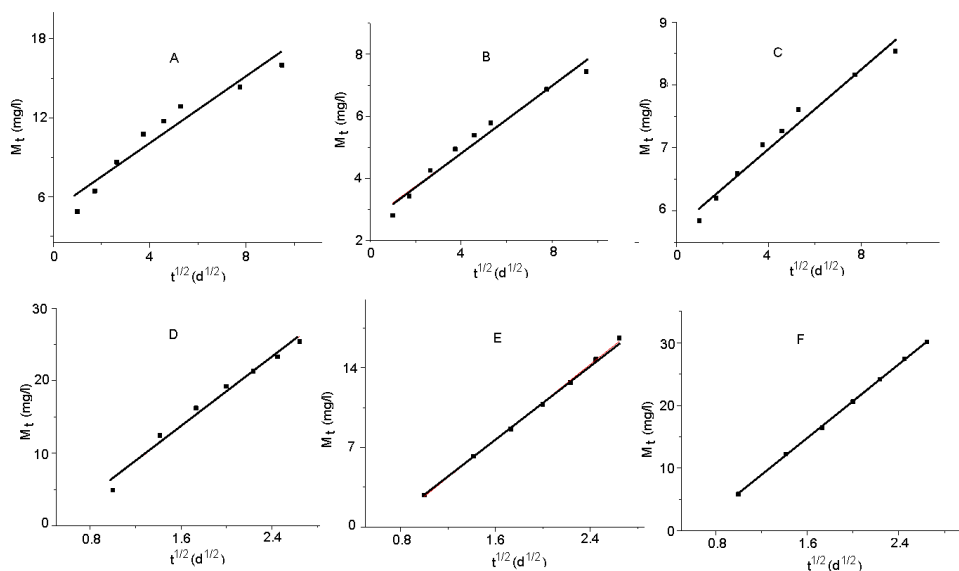VANCEA, ROZALIA MINTĂU, OSSI HOROVITZ, MARIA TOMOAIA-COTISEL

Figure 3. Regression lines for ions release from noncalcined HAPc-5%Sr (HAPc-Sr5) of Mg^{2+} (A, D) and Sr^{2+} (B, E) in water, and of Sr^{2+} in SBF (C, F) in static conditions, for 90 days (A-C), and in simulated dynamic conditions for 7 days (D-F).

The equation (2) applies satisfactory; most r^2 values are over 0.9. The Higuchi equation works better for Ca and P, the main constituents of the HAPs, and best for the unsubstituted HAP. The equation (2) fails for Sr release from HAPc-10%Sr in SBF, where ions exchange processes can appear, between Ca^{2+} and Mg^{2+} ions from the solution, and Sr^{2+} ions from the solid sample. However, for days 28-90, the regression lines have determination coefficients of over 0.99 for noncalcined HAPc-10%Sr and 0.94 for the calcined one. Thus diffusion becomes the major mechanism also in this case for later immersion times, when ion exchange would be expected to slow down.

Generally, the linearity is not strictly maintained through the entire domain of values. For not substituted HAP the highest coefficient of determination is found for the values for days 14-90 of calcium and P release, with a sensibly lower K value than for the first days. That could mean that after a period of more rapid dissolution, the inner diffusion (characterized by the $t^{1/2}$ rate law) becomes preponderant. Higher r^2 values for the later days of interaction between HAPs and water are observed for most ions and samples, the linearity of the $M_t = f(t^{1/2})$ plots becoming more

200

marked, as observed also in Figure 1. For example, for Ca^{2+} release from noncalcined HAP $r^2 = 0.997$, from noncalcined HAPc-5%Sr: 0.999 in days 7-28, from calcined HAPc-10%Sr over 0.99 in days 21-90; for P from noncalcined HAP $r^2 = 0.99$ for days 14-90. For the substituted HAPs and for the release of Mg and Sr, the $t^{1/2}$ law seems to be applicable earlier, starting from the first days of immersion in water.

Considering the K parameter as a measure of the diffusion rate, it appears that the diffusions of Ca and P process faster from substituted HAPs than from the unsubstituted one, while for HAPc-10%Sr the rate is lower than for HAPc-5%Sr. This could be explained by the distortion of the crystal lattice by substitution of Ca^{2+} with differently sized cations, which favors inner diffusion. On the other hand, the *a*-values (y-intercepts) can be considered an extrapolation of the ion release at time 0 and a measure of initial solubility. For Ca^{2+} they are also higher in substituted HAPs, thus confirming the solubility increase by substitution in HAPs [41, 42].

In order to compare the diffusion rates of different cations we have to use K values calculated in $mmol\ L^{-1}d^{-1/2}$ instead of $mg\ L^{-1}d^{-1/2}$ as shown in Table 1. For instance, in calcined samples the values are:

HAPc - 5%Sr: 0.029 for Ca^{2+}; 0.071 for Mg^{2+}; 0.0079 for Sr^{2+}

HAPc-10%Sr: 0.024 for Ca^{2+}; 0.052 for Mg^{2+}; 0.0084 for Sr^{2+}.

Therefore the diffusion rate of Mg is much higher as for Sr, and also over the value for Ca. This could be due to the lower size of Mg^{2+} ions (ionic radius 86 pm) as compared to Sr^{2+} (132 pm) and Ca^{2+} (114 pm), and thus to their higher mobility. The *a*-values (recalculated in % to the initial content of the element in the sample) indicate also a higher release of Mg^{2+} ions (2.49% from calcined HAPc-5%Sr and 2.77% from HAPc-10%Sr), as compared with the corresponding values for Ca^{2+}; (0.33% and 0.35% respectively), and Sr^{2+} (0.76% and 0.60% in water, 1.47% and 0.85% in SBF). This stronger magnesium release from substituted HAPs is known in literature [43, 44]. It is also worth noting the higher strontium release in SBF than in water, also observed by Beuvelot et al. [45], which can be assigned to the ion exchange with Ca^{2+} and Mg^{2+} ions, components of the SBF.

It is interesting that K values for strontium in SBF are lower than in water (Table 1), while the ion release, as measured by *a*-values, is higher. The cause should be the interference of ion exchange with the cations present in SBF. The different release rates for different ions determine a different composition of the dissolved material than the original solid one, i.e. an incongruent dissolution of HAPs [11, 46].

AURORA MOCANU, PETRE T. FRANGOPOL, REKA BALINT, OANA CADAR, IULIA MARIA
VANCEA, ROZALIA MINTĂU, OSSI HOROVITZ, MARIA TOMOAIA-COTISEL

Table 1. Parameters of equation (2) for ions release from HAPs in water and in SBF in static conditions (90 days).

Ion	Sample	Me-dium	a (mg/L)	K (mg L^{-1}d$^{-1/2}$)	r^2
Ca^{2+}	HAP noncalcined	Water	4.41±0.14	0.405±0.026	0.9723
	HAP calcined		6.13±0.13	0.445±0.025	0.9779
	HAPc-5%Sr noncalcined		7.01±0.61	0.86±0.11	0.8868
	HAPc-5%Sr calcined		11.2±0.5	1.16±0.10	0.9484
	HAPc-10%Sr noncalcined		6.5±0.6	0.80±0.11	0.8900
	HAPc-10%Sr calcined		10.7±0.6	0.96±0.12	0.9069
P (phos-phate)	HAP noncalcined	Water	10.5±1.4	4.44±0.27	0.9746
	HAP calcined		21.7±3.9	6.4±0.7	0.9133
	HAPc-5%Sr noncalcined		14.0±1.2	6.98±0.22	0.9932
	HAPc-5%Sr calcined		18.6±2.3	9.51±0.44	0.9852
	HAPc-10%Sr noncalcined		13.0±1.4	4.21±0.27	0.9723
	HAPc-10%Sr calcined		13.6±2.0	4.62±0.37	0.9559
Mg^{2+}	HAPc-5%Sr noncalcined	Water	4.9±0.7	1.27±0.14	0.9208
	HAPc-5%Sr calcined		3.7±0.8	1.73±0.14	0.9540
	HAPc-10%Sr noncalcined		4.2±0.6	1.14±0.20	0.9426
	HAPc-10%Sr calcined		4.2±0.6	1.26±0.11	0.9481
Sr^{2+}	HAPc-5%Sr noncalcined	Water	2.68±0.20	0.538±0.038	0.9653
	HAPc-5%Sr calcined		3.81±0.28	0.690±0.053	0.9606
	HAPc-10%Sr noncalcined		3.88±0.27	0.71±0.05	0.9648
	HAPc-10%Sr calcined		5.99±0.36	0.74±0.07	0.9416
Sr^{2+}	HAPc-5%Sr noncalcined	SBF	5.73±0.11	0.315±0.021	0.9704
	HAPc-5%Sr calcined		7.33±0.32	0.40±0.06	0.8588
	HAPc-10%Sr noncalcined		7.2±0.6	0.49±0.11	0.7205
	HAPc-10%Sr calcined		8.5±0.7	0.59±0.14	0.7114

In Table 2, the same parameters of eq. (2) as in Table 1 are given, for the cumulated dynamic ion release in days 1-7.

Here the linearity of the relation (2) for days 1-7 is very good, as seen also in Figure 3; all the coefficients of determination are above 0.95, most of them about 0.99.

Table 2. Application of equation (2) for ions release from HAPs in water and in SBF in simulated dynamic conditions (days 1-7); noncalc stands for noncalcined.

Ion	Sample	Me-dium	a (mg/L)	K mg L^{-1}d$^{-1/2}$	r^2
Ca^{2+}	HAP noncalcined	Water	-0.8 ±0.7	9.14±0.40	0.9867
	HAP calcined		-2.8 ± 1.7	11.1±0.9	0.9556
	HAPc-5%Sr noncalc.		-3.7 ± 2.1	14.5±1.1	0.9587
	HAPc-5%Sr calcined		-3.0 ± 1.7	17.3±0.9	0.9803
	HAPc-10%Sr noncalc.		-10.33 ± 0.27	16.67±0.13	0.9996
	HAPc-10%Sr calcined		-7.32 ± 0.26	18.07±0.13	0.9997
P (phos-phate)	HAP noncalcined	Water	-18.0±1.8	30.2 ± 0.9	0.9948
	HAP calcined		-11.9 ±3.9	37.4 ± 2.0	0.9837
	HAPc-5%Sr noncalc.		-19.9 ± 4.5	43.3 ± 2.2	0.9841
	HAPc-5%Sr calcined		-16.8 ± 4.0	47.3 ± 2.0	0.9892
	HAPc-10%Sr noncalc.		-21.7 ± 3.0	38.9 ± 1.5	0.9913
	HAPc-10%Sr calcined		=23.8 ± 3.2	42.1 ± 1.6	0.9913
Mg^{2+}	HAPc-5%Sr noncalc.	Water	-5.5 ± 1.5	12.0±0.8	0.9759
	HAPc-5%Sr calcined		-4.9 ± 0.5	9.86±0.27	0.9956
	HAPc-10%Sr noncalc.		-5.89 ± 0.37	10.38±0.18	0.9956
	iHAPc-10%Sr calcined		-7.41 ± 0.49	11.78±0.24	0.9974
Sr^{2+}	HAPc-5%Sr noncalc.	Water	-5.62 ± 0.29	8.30 ± 0.15	0.9981
	HAPc-5%Sr calcined		-3.63 ± 0.11	7.76 ± 0.06	0.9997
	HAPc-10%Sr noncalc.		-6.68 ± 0.21	10.66 ± 0.10	0.9994
	HAPc-10%Sr calcined		-8.11 ± 0.25	14.24±0.13	0.9995
Sr^{2+}	HAPc-5%Sr noncalc.	SBF	-8.86 ±2 0.24	14.75 ± 0.12	0.9996
	HAPc-5%Sr calcined		-9.83 ± 0.48	17.16 ± 0.24	0.9988
	HAPc-10%Sr noncalc.		-11.53±0.42	17.13±0.21	0.9991
	HAPc-10%Sr calcined		-13.5 ± 0.62	19.99±0.31	0.9985

CONCLUSIONS

Considering the validity ranges of the Higuchi model for the ions release from the investigated HAPs, we can affirm that, while diffusion is important throughout the entire process of ion release in static conditions, from day 1 to 90, dissolution has also a significant contribution in the initial phase of the process. After the dissolution of the outer, more soluble, shell of particles, the internal diffusion of ions from the bulk to the interface with

AURORA MOCANU, PETRE T. FRANGOPOL, REKA BALINT, OANA CADAR, IULIA MARIA
VANCEA, ROZALIA MINTĂU, OSSI HOROVITZ, MARIA TOMOAIA-COTISEL

the immersion medium will be the main process. Moreover, in time a saturation of the solution is approached due to the low solubility, so diffusion remains predominant.

In simulated dynamic condition, when the immersion liquid is daily renewed, no saturation could occur, so both dissolution and diffusion contribute to the ion release.

Nonetheless, the ions exchange process cannot be ruled out, both in static and in simulated dynamic conditions.

EXPERIMENTAL SECTION

The synthesis of HAP and multi-substituted HAPs (HAPc-5%Sr and HAPc-10%Sr, both containing 1.5 wt% Mg, 0.2 wt% Zn, 0.2 wt% Si and 5 wt%, respectively 10 wt% Sr) was carried out as shown elsewhere [2, 6, 7, 11] by a wet chemical method. Shortly, an aqueous solution containing the calculated amounts of cations (Ca^{2+}, Mg^{2+}, Zn^{2+}, Sr^{2+} as nitrates) and another solution for the anions phosphate and silicate (containing $(NH_4)_2HPO_4$ and tetraethyl orthosilicate, TEOS) were prepared and ammonia solution was added to assure an alkaline pH (11.5). The solutions were mixed at room temperature, to assure a stoichiometric ratio cations/anions = 5/3, and after maturation the precipitate was separated by filtration. Two series of powdered samples were used: lyophilized (noncalcined) and calcined at 300 °C (1 h).

The ion release was studied in ultrapure deionized water (pH 5.6) and in simulated body fluid (Kokubo's SBF) [47] containing (mmol/L): Na^+ (142.0); K^+ (5.0); Mg^{2+} (1.5); Ca^{2+} (2.5); Cl^- (147.8); HCO_3^- (4.2); HPO_4^{2-} (1.0); SO_4^{2-} (0.5), buffered at the physiologic pH 7.40 at 37 °C, with tris(hydroxymethyl)amino methane and hydrochloric acid. Samples of 0.15 g for each of the 6 solid HAPs were soaked in 15 mL liquid (HAPs content 10 g/L) at 37°C [11]. For the study in static conditions, these samples were kept in closed flasks at 37 °C for 1; 3; 7; 14; 21; 30; 60, and 90 days, and afterwards the filtrated solutions were analyzed. In simulated dynamic conditions (7 days) the immersion liquid for each sample was analyzed daily and then changed with the same volume of fresh liquid.

In the filtrates, the Ca, Mg, Sr, Zn, P and Si content was measured with an inductively coupled plasma optical emission spectrometer (*ICP-OES*) OPTIMA 5300DV (Perkin-Elmer, USA), using calibration solutions prepared from multi-element IV storage solutions [11, 27]. The results were calculated as mg/L (ppm). Zn and Si could not be determined in the solutions, because their concentration was under the limit of quantification of the method.

The graphics and the data analysis for linear fitting to obtain the regression lines and their parameters were performed by means of the Origin 8.5® software from OriginLab®.

ACKNOWLEDGEMENTS

REFERENCES

1. P. T. Frangopol; A. Mocanu; V. Almasan; C. Garbo; R. Balint; G. Borodi; I. Bratu; O. Horovitz; M. Tomoaia-Cotisel; *Rev. Roum. Chim.,* **2016**, *61(4-5)*, 337-344.
2. E. Forizs; F. Goga; A. Avram; A. Mocanu; I. Petean; O. Horovitz; M. Tomoaia-Cotisel; *Studia UBB Chemia*; **2017**, *62*(4, Tom I), 173-180.
3. S. Rapuntean; P. T. Frangopol; I. Hodisan; Gh. Tomoaia; D. Oltean-Dan; A. Mocanu; C. Prejmerean; O. Soritau; L. Z. Racz; M. Tomoaia-Cotisel; *Rev. Chim. (Bucharest)*, **2018**, *69*(12), 3535-3544.
4. Gh. Tomoaia; M. Tomoaia-Cotisel; L.-B. Pop; A. Pop; O. Horovitz; A. Mocanu; N. Jumate; L.-D. Bobos; *Rev. Roum. Chim.* **2011***, 56(10-11)*, 1039-1046.
5. Gh. Tomoaia; O. Soritau; M. Tomoaia-Cotisel; L.-B. Pop; A. Pop; A. Mocanu; O. Horovitz; L.-D. Bobos; *Powder Technol.,* **2013***, 238*, 99-107.
6. Gh. Tomoaia; M. Tomoaia-Cotisel; L.B. Pop; A. Mocanu; A. Pop; *Nanopowders of hydroxyapatite and its substituted derivatives with medical applications and their fabrication procedure*, Romanian Patent, OSIM, Bucharest, Romania, no. 125817 B1, BOPI, **2013**, *6*, 123.
7. F. Goga; E. Forizs; A. Avram; A. Rotaru; A. Lucian; I. Petean; A. Mocanu; M. Tomoaia-Cotisel; *Rev. Chim. (Bucharest),* **2017**, *68(6)*, 1193-1200.
8. Gh. Tomoaia; L.B. Pop; I. Petean; M. Tomoaia-Cotisel; *Mater. Plast.*, **2012**, *49(1)*, 48-54.
9. Gh. Tomoaia; A. Mocanu; I. Vida-Simiti; N. Jumate; L.-D. Bobos; O. Soritau; M. Tomoaia-Cotisel; *Mater. Sci. Eng.* C, **2014**, *37*, 37–47.
10. D. Oltean-Dan; G. B. Dogaru; M. Tomoaia-Cotisel; D. Apostu; A. Mester; H. R. C. Benea; M. G. Paiusan; E. M. Jianu; A. Mocanu; R. Balint; C. O. Popa; C. Berce; G. I. Bodizs; A. M. Toader; Gh. Tomoaia; *Int. J. Nanomed.,* **2019**, *14*, 5799-5816.
11. C. Garbo; J. Locs; M. D'Este; G. Demazeau; A. Mocanu; C. Roman; O. Horovitz; M. Tomoaia-Cotisel; *Int. J. Nanomed.,* **2020**, *15*, 1037-1058.
12. C. Lindahl; W. Xia; J. Lausmaa; H. Engqvist; *Biomed. Mater.*, **2012**, *7*, 045018; doi:10.1088/1748-6041/7/4/045018.

AURORA MOCANU, PETRE T. FRANGOPOL, REKA BALINT, OANA CADAR, IULIA MARIA
VANCEA, ROZALIA MINTĂU, OSSI HOROVITZ, MARIA TOMOAIA-COTISEL

13. B. Colovic; S. Pasalic; V. Jokanovic; *Ceram. Int*., **2012**, *38(8)*, 6181–6189.
14. M.-S. Wu; W. I. Higuchi; J. L. Fox; M. Friedman; *J. Dent. Res*., **1976**, *55(3)*, 496-505.
15. Q. Liu; W. Guo; M. Yang; K. Wang; W. Liu; F. Wu; *Adv. Polym. Technol*., **2019**, Article ID 9562437; https://doi.org/10.1155/2019/9562437.
16. M. Rohnke; S. Pfitzenreuter; B. Mogwitz; A. Henß; J. Thomas; D. Bieberstein; T. Gemming; S. K. Otto; S. Ray; M. Schumacher; M. Gelinsky; V. Alt; *J. Control. Release*, **2017**, *262*, 159–169.
17. A. Mocanu; G. Furtos; S. Rapuntean; O. Horovitz; C. Flore; C. Garbo; A. Danisteanu; Gh. Rapuntean; C. Prejmerean; M. Tomoaia-Cotisel; *Appl. Surf. Sci*., **2014**, *298*, 225–235.
18. Gh. Tomoaia; A. Mocanu; L.-D. Bobos; L.-B. Pop; O. Horovitz; M. Tomoaia-Cotisel; *Studia UBB Chemia*, **2015**, *60(3),* 265-272.
19. C. Garbo; M. Sindilaru; A. Carlea; Gh. Tomoaia; V. Almasan; I. Petean; A. Mocanu; O. Horovitz; M. Tomoaia-Cotisel; *Particul. Sci. Technol,* **2017**, *35(1)*, *29*-37.
20. M.-P. Ginebra; C. Canal; M. Espanol; D. Pastorino; E. B. Montufar; *Adv. Drug Deliv. Rev*, **2012**, *64(12)*, 1090-1110.
21. M. H. Alkhraisat; C. Rueda; J. Cabrejos-Azama; J. Lucas-Aparicio; F. T. Mariño; J. Torres García-Denche; L. B. Jerez; U. Gbureck; E. L. Cabarcos; *Acta Biomater*., **2010**, *6(4)*, 1522–1528.
22. U. Gbureck; E .Vorndran; J. E. Barralet. *Acta Biomater*., **2008**, *4(5)*, 1480–1486.
23. E. Vidal; J. Buxadera-Palomero; C. Pierre; J. M. Manero; M.-P. Ginebra; S. Cazalbou; C. Combes; E. Rupérez; D. Rodríguez; *Surf. Coat. Technol*., **2019**, *358*; 266-275.
24. G. R. Mahdavinia; M. H. Karimi; M. Soltaniniya; B. Massoumi*; Int. J. Biol. Macromol*., **2019**, *126*, 443-453.
25. G. Vidhya; G. S. Kumar; V. S. Kattimani; E. K. Girija; *Mater. Today: Proceedings*, **2019**, *15(2)*, 344-352.
26. C. Luo; S. Wu; J. Li; X. Li; P. Yang; G. Li; *Int. J. Biol. Macromol*., **2020**, *155*, 174-183.
27. A. Mocanu; O. Cadar; P. T. Frangopol; I. Petean; Gh. Tomoaia; G. A. Paltinean; C. P. Racz; O. Horovitz; M. Tomoaia-Cotisel; *Roy. Soc. Open Sci*., **2021**, *8(1),* 201785; https://doi.org/10.1098/rsos.201785.
28. O. Cadar; R. Balint; Gh. Tomoaia; D. Florea; I. Petean; A. Mocanu; O. Horovitz; M. Tomoaia-Cotisel; *Studia UBB Chemia*, **2017**, *62* (*4*; Tom II), 269-281.
29. T. Higuchi; *J. Pharm. Sci*., **1963**, *52(12)*, 1145–1149.
30. S. Dash; P. N. Murthy; L. Nath; P. Chowdhury; *Acta Pol. Pharm*., **2010**, *67(3)*, 217-223.
31. J. Siepmann; N. A. Peppas; *Int. J. Pharm*., **2011**, *418(1)*, 6-12.
32. Y. Fu; W. J. Kao;. *Expert Opin. Drug Deliv*.; **2010**, *7(4)*, 429-444.
33. M. Golshan; M. Salami-Kalajahi; H. Roghani-Mamaqani; M. Mohammadi;. *Polymer*, **2017**, *117*, 287-294.
34. R. Gouda; H. Baishya; Z. Qing**;** *J. Develop. Drugs*, **2017**, *6*(2), 1000171; https://doi.org/10.4172/2329-6631.1000171.

35. G. Nikravan; V. Haddadi-Asl; M. Salami-Kalajahi; *e-Polymers*, **2019**, *19(1)*, 203-214.
36. H.-G. Lee; Y.-S. Park; J.-H. Jeong; Y.-B. Kwon; D. H. Shin; J.-Y. Kim; Y.-S. Rhee; E.-S. Park; D.-W. Kim; C.-W. Park; *Drug Des., Devel. Ther.,* **2019**, *13*, 2459–2474.
37. M. M. Leena; M. G. Antoniraj; J. A. Moses; C. Anandharamakrishnan; *J. Drug Deliv. Sci. Technol.*, **2020**, *57*, 101678; https://doi.org/10.1016/j.jddst.2020. 101678.
38. S. Bose; S. Tarafder; *Acta Biomater.*, **2012**, *8(4)*, 1401-1421.
39. M. M. Mailafiya; K. Abubakar; A. Danmaigoro; S. M. Chiroma; E. B. A. Rahim; M. A. M. Moklas; Z. A. B. Zakaria; *Biomed. Res. Ther.*, **2019**, *6*(12), 3518-3540.
40. S. Mondal; G. Hoang; P. Manivasagan; H. Kim; J. Oh; *Ceram. Int.*, **2019**, *45(14)*, 17081-17093.
41. E. Landi; A. Tampieri; G. Celotti; S. Sprio; M. Sandri; G. Logroscino; *Acta Biomater.,* **2007**, *3(6)*, 961-969.
42. E. Boanini; M. Gazzano; A. Bigi; *Acta Biomater.,* **2010**, *6(6)*, 1882-1894.
43. N. C. Andres; N. L. D'Elía; J. M. Ruso; A. E. Campelo; V. L. Massheimer; P. V. Messina; *ACS Appl. Mater. Interfaces,* **2017**, *9(18)*, 15698-15710.
44. S. Chen; Y. Shi; X. Zhang; J. Ma; *J. Biomed Mater Res A.*, **2019**, *107(11)*, 2512-2521.
45. J. Beuvelot; Y. Mauras; G. Mabilleau; H. Marchand-Libouban; D. Chapparda; *Dig. J. Nanomater. Biostruct.*, **2013**, *8(1)*, 207-217.
46. S. V. Dorozhkin; *J. Colloid. Interf. Sci.,* **1997**, *191(2)*, 489-497.
47. T. Kokubo; *Biomaterials*, **1991**, *12(2)*, 155-163.

CURCUMIN-WHEY PROTEIN SOLID DISPERSION SYSTEM WITH IMPROVED SOLUBILITY AND CANCER CELL INHIBITORY EFFECT

LEVENTE RÁCZ[a], MARIA TOMOAIA-COTIŞEL[a], CSABA-PAL RÁCZ[a], PAULA BULIERIS[b], IOANA GROSU[b], SEBASTIAN PORAV[b], ALEXANDRA CIORÎŢĂ[b], XENIA FILIP[b], FLAVIA MARTIN[b], GEORGETA SERBAN[c], IRINA KACSÓ[b],*

ABSTRACT. The solid dispersion system containing a high amount of the natural compound curcumin was prepared with whey protein concentrate by spray-drying method in 5:1 molar ratio. X-ray powder diffraction and DSC techniques show the formation of the solid dispersion system in amorphous state, and the presence of weak hydrogen bond type interactions between the components was established by FTIR analysis. SEM images show highly homogeneous donut-like spherical microparticles morphology for the system. The solubility of curcumin from the system was enhanced compared to practically insoluble raw curcumin, reaching a value of 70 µg/mL in aqueous buffer solution at pH=8 similar with intestinal environment. The synthesized material had better effects against skin melanoma cells, compared to lung adenocarcinoma cells, but in both cases the effect was promising, and through further and more complex analyses the antitumoral potential of CUC-WPC_SD could be exploited.

Keywords: curcumin, whey protein concentrate, complexation, enhanced solubility, anticarcinogenic effect

INTRODUCTION

Curcumin (CUC) (1*E*,6*E*)-1,7-Bis(4-hydroxy-3-methoxyphenyl)-hepta-1,6-diene-3,5-dione), with a diferuloylmethane structure was first isolated from rhizomes of *Curcuma longa* in 1815 as a yellow compound which exhibits

---

[a] *Babeş-Bolyai University, Faculty of Chemistry and Chemical Engineering, 11 Arany Janos str., RO-400028, Cluj-Napoca, Romania*
[b] *National Institute of Research&Development for Isotopic and Molecular Technologies, 67-103 Donath str., RO-400293 Cluj-Napoca, Romania*
[c] *University of Oradea, Faculty of Medicine and Pharmacy, 29 Nicolae Jiga str., RO-410028, Oradea, Romania*
* *Corresponding author: irina.kacso@itim-cj.ro*

biological and pharmaceutical activities. It has been used in traditional Chinese and Indian medicines for treatment of various diseases [1]. More and more research results show the efficiency of curcumin in the treatment of many medical conditions, as a result of the antioxidant, anti-inflammatory [2], antimicrobial [3], antiviral [4], neuroprotective [5] and, last but not least, anti-carcinogenic effect [6].

The chemical structure of CUC ($C_{21}H_{20}O_6$) (Figure 1) consists in two aryl rings containing *o*-methoxy phenolic OH–groups symmetrically linked in conjugation through a *β*-diketone moiety which gives particular characteristics, such as intramolecular hydrogen atom transfer which determines the existence of keto-enol tautomerism, with important role in its physical-chemical properties [7]. The CUC molecule hydrophobicity is responsible for the very low solubility in aqueous medium, poor absorption, bioavailability and stability [8] that limit its therapeutic effectiveness. Thus, a large number of researches have been carried out and published in the last decade in attempt to improve the solubility and bioavailability of CUC, and to demonstrate its therapeutic effect in treatment of various diseases. Crystal engineering studies have led to the obtaining of polymorphs and co-crystals [9, 10] with higher solubility and dissolution rate compared to pure starting CUC. Inclusion complexes and different incorporation strategies of CUC into various carrier molecules, including but not limited to nanoparticles [11, 12], polymers [13], cyclodextrins [14], liposomes [11] or different proteins [15, 16] have been obtained and characterized, as well as micelles and solid dispersions [10, 11, 17], respectively.
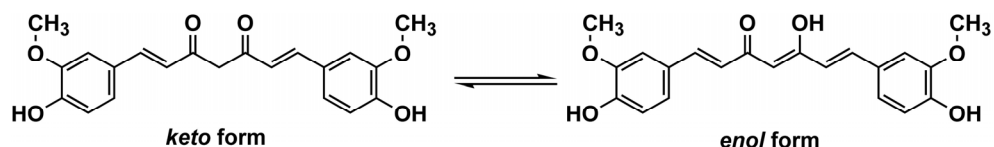
Figure 1. Chemical structure of curcumin

One of the most used protein for increasing the solubility and bioavailability of CUC is whey protein. This protein possesses important nutritional and biological properties [18], antimicrobial, antiviral, anticarcinogenic activity and other metabolic features that have been associated with it [19]. It's being used in the whey protein concentrate (WPC) or isolate (WPI) form, that contains 65-90% *β*-lactoglobulin [18]. In addition to the *β*-lactoglobulin main component the whey protein also contains α-lactalbumin, immunoglobulin, serum albumin, casein and other components. The amino acid sequence and three-dimensional structure confer to the *β*-lactoglobulin the ability to

bind small hydrophobic ligands and therefore it can act as a specific transporter for them [20]. This ability is also supplemented by its antioxidant potential [21].

The solubility, stability and bioavailability improvement of CUC with whey protein or *β*-lactoglobulin was performed by different ways. CUC was loaded in WPI obtaining whey protein aggregates in emulsion [16] or whey protein hydrolysate in suspension [22]. Other studies reported the complexation of CUC and WPI in form of micro- or nano-encapsulates [23-25] or nano-emulsions [26], the β-lactoglobulin being also used for the same purpose [27-29]. In addition, the biological activity of CUC, such as the antioxidant [16, 23, 30] and anticancer [25] effect, was enhanced, thus encouraging the use of these complexes in pharmaceutical, nutraceutical or food [16] applications.

Most studies on CUC with whey protein or *β*-lactoglobulin complexation have been performed on 1:1 molar ratio [16, 27, 28, 31]. Few studies investigate the complexation using an excess of CUC, as in the case of nano-encapsulates [25].

The aim of our study is to prepare an enhanced solubility solid-state curcumin-whey protein concentrate dispersion system (CUC-WPC_SD) with high amount of curcumin content by spray drying (SD) method, whose efficiency is proved by the literature data [15, 24, 30].

Curcumin – whey protein solid dispersion systems were prepared in different molar ratios, from 1:1 to 20:1, whose preliminary analysis regarding the solubility and stability showed that 5:1 stoichiometry (CUC-WPC_SD) is the optimal formula for the proposed purpose. The identification of the system was highlighted by X-ray powder diffraction (XRPD), Fourier transform infrared spectroscopy (FTIR) and differential scanning calorimetry (DSC). The morphological characterization was realized by scanning electron microscopy (SEM) and the dissolution by UV spectrophotometry. The *in vitro* cytostatic activity was tested on several cancer cell types.

RESULTS AND DISCUSSION

CUC-WPC_SD complex characterization

X-ray powder diffraction (XRPD)

In order to prove the solid disperse system CUC-WPC_SD obtained by CUC incorporation into WPC, in the optimized molar ratio 5:1, first it was analyzed by XRPD.
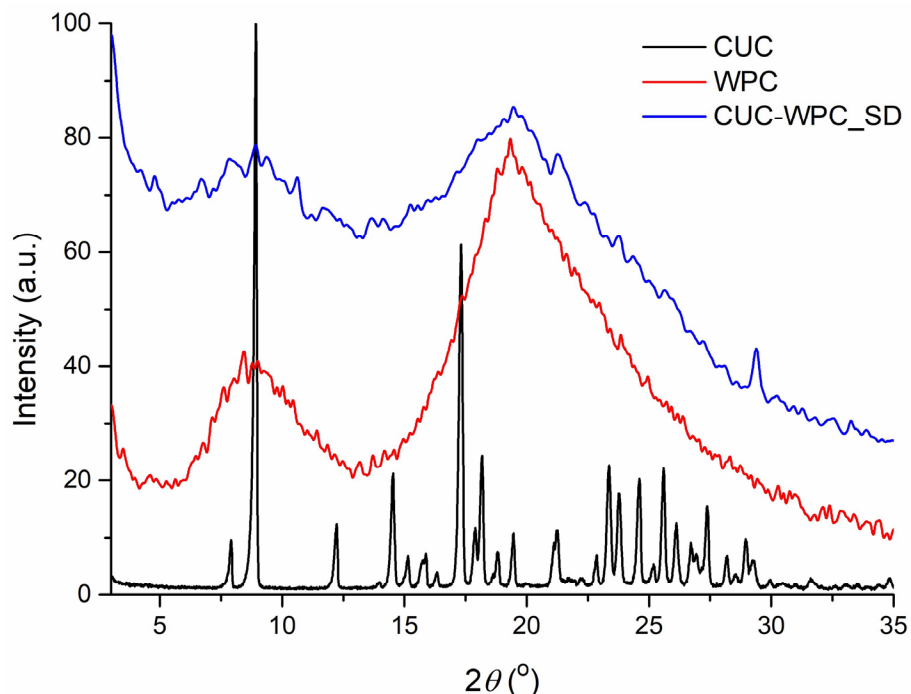
Figure 2. The compared PXRD patterns of CUC, WPC and CUC-WPC_SD

The diffractograms of raw CUC and WPC were compared with CUC-WPC_SD one (Figure 2). It was observed that the analyzed sample is in an amorphous state, without being able to distinguish the characteristic diffraction lines of CUC, which suggests its loading in WPC and a homogeneous dispersion system formation.

Differential scanning calorimetry (DSC)

The DSC curve of CUC (Figure 3) shows a sharp endothermic melting signal with $T_{on}=172.6°C$, $T_{peak}=177.8°C$ and $\Delta H=-194.6$ J·g^{-1}, and presents thermal stability up to 200°C. The DSC trace of WPC shows an amorphous material, without significant thermal events, observing only one broad endothermic signal between 40-100°C, corresponding to the unbounded water elimination.
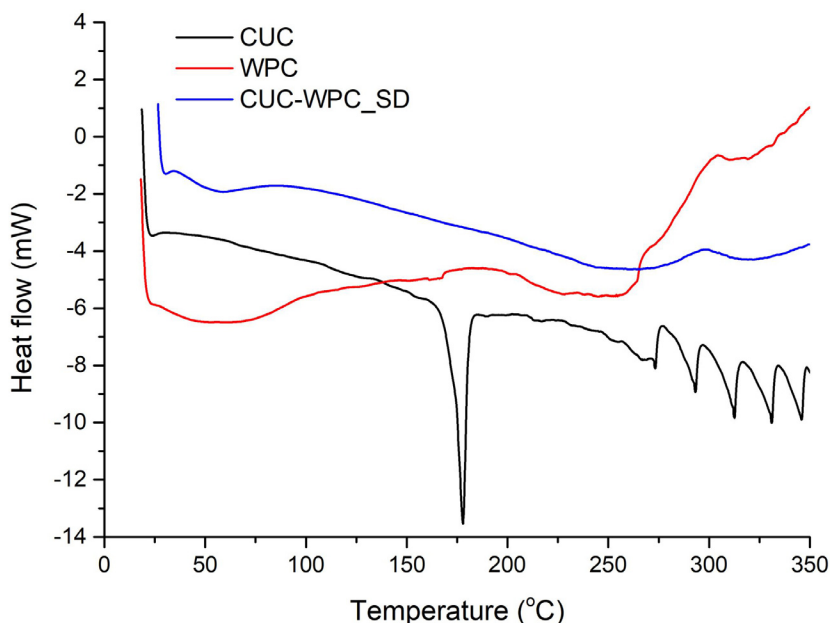
Figure 3. The compared DSC curves of CUC, WPC and CUC-WPC_SD

Analyzing the DSC curve of CUC-WPC_SD one can observe one low intensity broad endotherm signal between 40 and 90°C due to the residual unbounded water elimination, but the melting signal of CUC does not appears, which indicates that the loading of curcumin in whey protein in 5:1 stoichiometric ratio occurs.

Fourier transform infrared spectroscopy (FTIR)

The changes in the position, intensity or width of the characteristic vibrational bands of curcumin and whey protein on the CUC-WPC_SD system FTIR spectrum could be explained by the transformations and interactions that occur during the incorporation process. On the CUC-WPC_SD dispersion system FTIR spectrum one can identify the most important absorption bands of CUC [32] and those of WPC with certain modifications (Figure 4).

Regarding the characteristic vibrational bands of CUC in the spectrum of CUC-WPC_SD sample the following changes appear: the C=O stretching from 1627 cm^{-1} and the aromatic C=C stretching from 1602 cm^{-1} disappear; the aromatic ring bending vibration from 1509 cm^{-1} shift to 1516 cm^{-1}; the CH_2 bending from 1429 cm^{-1} and the C-O stretching from 1207 cm^{-1} shift to 1431 cm^{-1} and 1210 cm^{-1}, respectively and both appear as a shoulder; the C-O stretching from 1154 cm^{-1} and 1121 cm^{-1} shift to 1163 cm^{-1} and

1127 cm^{-1}, respectively; the C-OH stretching from 1028 cm^{-1} and the benzoate *trans*-CH vibration from 963 cm^{-1} shift to 1034 cm^{-1} and at 970 cm^{-1}, respectively.
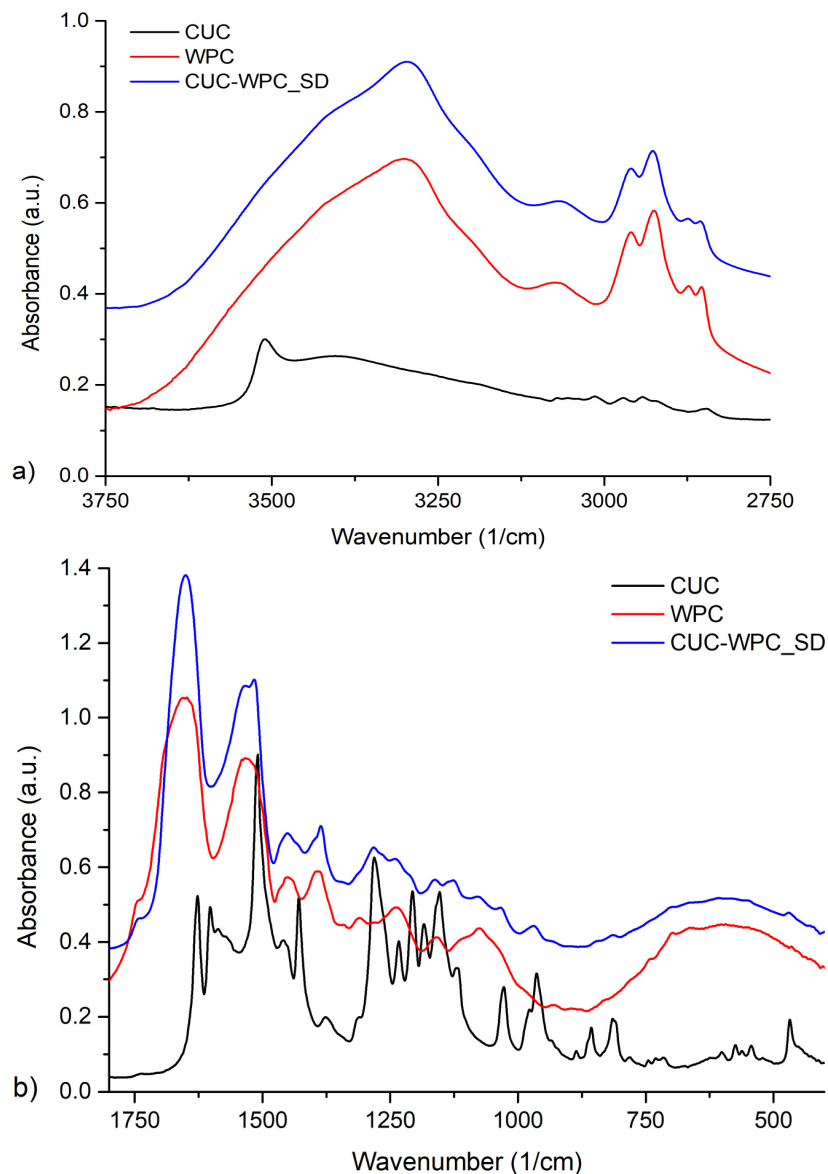

Figure 4. The compared FTIR spectra of CUC, WPC and CUC-WPC_SD, spectral domain a) 3750-2750 cm^{-1} and b) 1800-400 cm^{-1}

As a result of the loading with CUC, the characteristic vibrational bands of WPC have undergone the following changes: the shoulder at 1694 cm^{-1}, assigned to protein aggregates [33], no longer appears; the amide I band, due to the stretching vibrations of C=O in the peptide bonds [34] from 1657 cm^{-1} shift to 1650 cm^{-1} and becomes narrower; the vibration bands from 1533 and 1392 cm^{-1} were shifted to 1517 cm^{-1} and to 1386 cm^{-1} respectively; the low intensity vibration band from 1309 cm^{-1} was shifted and appears as a shoulder at 1314 cm^{-1}, the medium intensities sharp vibration bands from 1237 and 1158 cm^{-1} shifts to 1240 and 1162 cm^{-1}, respectively. The outlined changes of some vibration bands, especially those characteristics of the OH and COOH groups, suggest the existence of some weak hydrogen bond- and electrostatic-type interactions between the two components of the CUC-WPC_SD dispersion system.

Scanning electron microscopy (SEM)

Morphological analysis of CUC-WPC_SD sample, presented in Figure 5, revealed an amorphous state without any crystalline features. In terms of shape, the sample is highly homogeneous, the particles adopting a donut-like form.
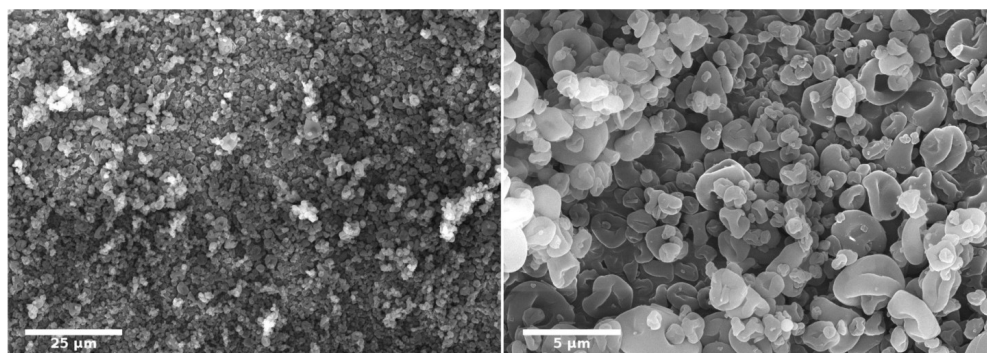
Figure 5. SEM images of the particle size distribution in the CUC-WPC_SD sample

The particle size distribution showed a relatively large interval, varying between 0.17 μm to 4.9 μm and having a mean size of 1.5 μm. Despite the wide range, the size distribution follows a Gaussian curve (Figure 6).
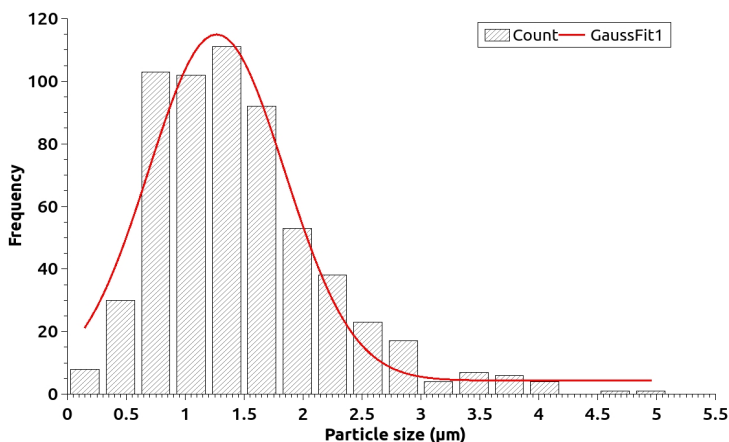
Figure 6. The Gaussian curve of particle size distribution

Powder dissolution measurements

The solid dispersion system CUC-WPC_SD was subjected to the dissolution experiment in deionized water and in aqueous buffer at 1.8 and 8 physiologically pH values, respectively. The curcumin concentration in the CUC-WPC_SD solution was monitored over time, by recording the absorption intensity for a period of 160 min (Figure 7). On figure 7 the dissolution profile of raw curcumin, practically insoluble in water, was also represented.
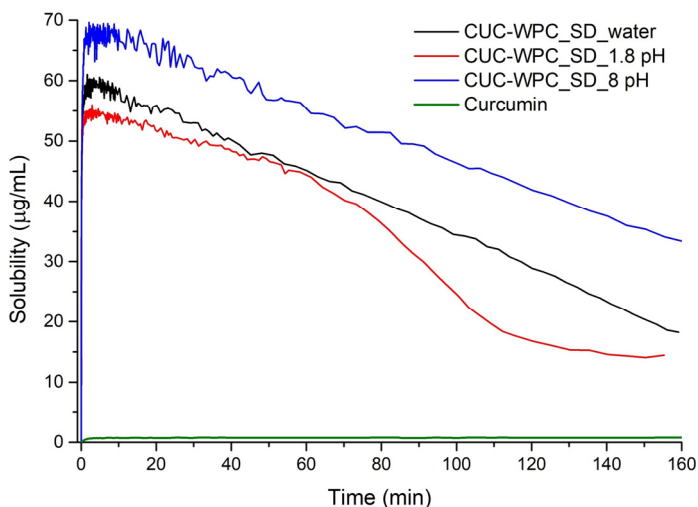
Figure 7. Variation of curcumin concentration in aqueous solutions of CUC-WPC_SD compared with the solubility of pure curcumin

The dissolution profile of CUC contained in the CUC-WPC_SD system in water (concentration of CUC (μg/mL) as a function of time (min)), shows the maximum concentration of ~60 μg/mL almost instantaneously, after which a linear decreasing trend in the curcumin concentration in solution is manifested, due to CUC precipitation over time.

In aqueous buffer with pH=1.8 (similar with gastric liquid) the maximum concentration of CUC reaches a value of ~55 μg/mL. In the first 60 minutes of the dissolution experiment a linear decreasing tendency to a value of 45 μg/mL was observed, after which there is a sudden decrease of the amount of dissolved curcumin.

The dissolution profile in buffer with pH=8 (similar to the pH of the intestinal environment) shows instantaneously dissolution of CUC to the maximum concentration of ~70 μg/mL, after which there is a linear decreasing tendency due to CUC precipitation. After 160 min, the final CUC concentration was ~35 μg/mL.

No decomposition of curcumin at all the pH values in the performed dissolution tests was observed.

Cytotoxicity tests

The obtained CUC-WPC_SD dispersion system was tested *in vitro* against skin melanoma (A375) and lung adenocarcinoma (A549) cells. The A375 cells were affected to a higher extent compared to A549 cells (p<0.0001, Figure 8a), aspect indicated also by the IC_{50} concentration. The results showed that CUC-WPC_SD has an IC_{50} value of 45.5 μg/mL against A375 cells and 203.6 μg/mL against A549. Compared to the untreated control, A375 cells were significantly more affected (p<0.0001) starting with the concentration of 30 μg/mL, whereas for A549 the concentrations of 200 μg/mL and 300 μg/mL, were the most effective. However, at the lowest concentration tested (10 μg/mL), both cell lines had a proliferative response, with registered values above those of the untreated controls (119% for A549, and 120% for A375, respectively).

The LDH values calculated herein, show no significant difference between the two cell lines (Figure 8b). Compared to the cells treated with Tween 20, no necrosis was observed, however, the negative values registered could indicate a membrane blockage [35].

A direct dose dependent reaction was observed in A375 cells that registered high NO values at concentrations above 30 μg/mL. The results are consistent with the observed effects on the MTT assay. A dose dependent reaction was observed for A549 cells as well, however the trend was more chaotic (Figure 8c), compared to the skin melanoma cells. Nevertheless, the highest value registered for the NO concentration, was associated with the lowest value registered for the MTT assay, in both cell types.
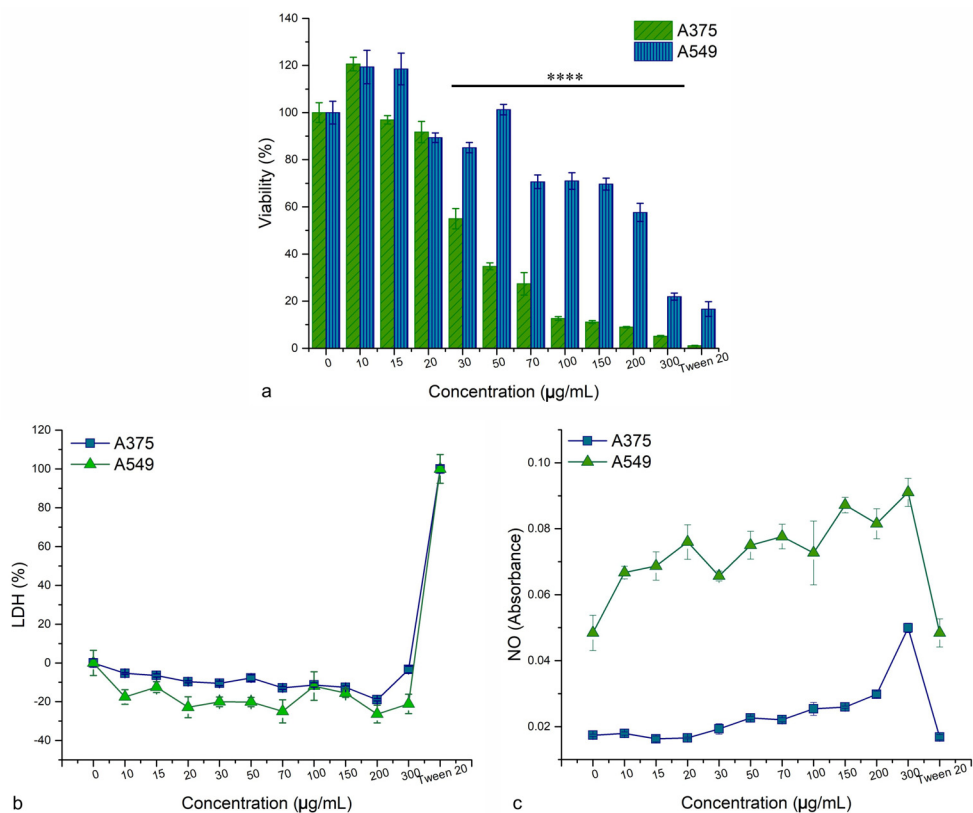
Figure 8. Cytotoxicity assays performed on A375 and A549 cells, treated with CUC-WPC_SD. a) MTT assay showing the extend of damages induced in the cells' viability in 24 h. b) LDH assay showing the amount of LDH released in the culture media of the cells treated with the drug for 24 h. c) NO assay revealing the amount of nitric oxide released in the culture media of the treated cells.

The NO concentration has a controversial background, as it can indicate both apoptotic and proliferative effects. This means that at low concentrations detected, the apoptosis could be rescued, but tumor inhibition through apoptosis has also been reported for the same scenario [36]. Therefore, the Griess assay is associated with other biochemical analyses such as LDH and MTT, considered for this study, to be able to correlate the events observed. Herein, for both A375 and A549 cells a moderate negative correlation (r = -0.7) was observed between the viability and NO assay test results. This indicates that at high concentrations (starting with 30 µg/mL drug concentration), the inhibition of the cancer cells tested was achieved through apoptosis, rather than necrosis.

Similar results were obtained in other previous studies. By testing nano-encapsulated curcumin with whey protein against different cancer cell lines (colon, prostate, and pancreatic cancers), a better inhibitory capacity was observed compared to pure curcumin [25]. When polyethylene glycol was used to enhance the solubility of curcumin, a strong inhibitory capacity against multiple pancreatic cancer cells was obtained [37]. The IC_{50} values of curcumin alone ranged from 7 to 18 µM, whereas for the PEG-loaded curcumin, the values decreased to more than half. Also, the incorporated curcumin in catanionic lipid nano-systems was tested for its effect against Lewis lung cancer, the IC_{50} value of curcumin nano-systems (20.2 µM) was almost half of that of curcumin used alone (39.7 µM) [38].

CONCLUSIONS

The CUC-WPC_SD solid dispersion system was prepared by spray-drying in 5:1 molar ratio. Combining the XRPD, DSC, FTIR and SEM analysis results highlight the formation of the amorphous material whose components are joined by weak electrostatic interactions, being highly homogeneous, and adopting a donut-like spherical form.

The dissolution process of curcumin from this system shows a maximum solubility value of 70 µg/mL in aqueous buffer solution at pH=8, similar of intestinal fluid, and the active component being stable in this environment.

The obtained dispersion system manifested better effects against skin melanoma cells, compared to lung adenocarcinoma cells, but in both cases the effect was promising, and through further and more complex analyses the antitumoral potential of CUC-WPC_SD could be exploited. The inhibition of skin melanoma cells (A375) is dose dependent in 24 h. However, at low concentrations (10 µg/mL) the effect was proliferative, with values above the untreated control. The LDH release was constant at all tested concentrations. The nitric oxide (NO) concentration increased in a dose dependent manner, with values above the negative control (cells treated with Tween 20).

EXPERIMENTAL SECTION

Materials

All chemicals used for CUC-WPC_SD preparation and testing: curcumin, ethanol, propanol, DMEM F-12, L-glutamine, penicillin-streptomycin solution, Tris base, lithium lactate, NAD solution, sulfanilamide, formazan

salt, and *N*-(1-naphthyl) ethylene-diamine were purchased from Sigma-Aldrich, Germany; the weight protein concentrate (WPC) was from Merck, Germany, and the fetal bovine serum from HyClone, Thermo Fisher Scientific, UK. All these chemicals were used without further purification. The cells used in cytotoxicity studies, A549 (ATCC CCL-185) and A375 (ATCC CRL-1619), were purchased from Lomianki, Poland.

Preparation of CUC-WPC_SD solid dispersion system

The solid starting compounds, CUC (M_W=368.38 g/mol) and WPC (M_W=~18400 g/mol), were weighed for a molar ratio of CUC:WPC of 5:1 (1:10 w/w). Curcumin was dissolved in ethanol and the WPC in distilled water. Before mixing the solutions, the WPC aqueous solution was filtered, the volume was corrected with distilled water for a concentration of ≤4% in ethanol. The obtained yellow, slightly milky solution was processed using a SF-1500LAB spray dryer, applying the following parameters: T_{in}=165°C and T_{out}=49°C, ventilator frequency 58 Hz, solution flow rate 5 mL/min. In the end a fine, homogeneous yellow-orange powder was obtained.

X-ray powder diffraction (XRPD)

Data collection was acquired with the DIFFRAC plus XRD Commander using a Brucker D8 Advance Diffractometer with the tube set at 40 kV and 40 mA, equipped with a germanium (1 1 1) monochromator, used to obtain Cu Kα_1 radiation and a LYNKSEYE detector. The measurements were recorded in Bragg-Brentano geometries – variant in reflections- in 3-35° 2θ range, employing a scan rate of 0.02°/s.

Differential scanning calorimetry (DSC)

Thermal measurements were performed with a DSC-60 Shimadzu differential scanning calorimeter in standard aluminum crimped pans as sample holders and alumina as reference sample. Samples have been analyzed in the 20-350°C temperature range under dry nitrogen flow (3.5 L·h^{-1}) with a 10°C·min^{-1} heating rate. For data collection and analysis, the Shimadzu TA-WS60 and TA60 2.1 software were employed. The DSC calorimeter was calibrated with reference standards of zinc and indium.

Fourier-Transform Infrared Spectroscopy (FTIR)

FT-IR spectra were obtained using a JASCO 6100 FTIR spectrometer in the 4000 to 400 cm^{-1} spectral domain, with a resolution of 4 cm^{-1} by employing the KBr pellet technique. Each sample has been dispersed in

about 300 mg of anhydrous KBr and the resulting powder was ground in an agate mortar. The pellet was obtained by pressing the ground mixture into an evacuated die. The spectra were collected and analyzed with Jasco Spectra Manager v.2 software.

Scanning electron microscopy (SEM)

Samples provided for SEM analysis were prepared in the same fashion, briefly. The spray-dried samples were spread over the double-sided conductive tape (12 mm) fixed on aluminum stubs and coated with a 10 nm layer of gold. Image acquisition was conducted on a Hitachi SU8230 High Resolution Scanning Electron Microscope equipped with a cold field emission gun and a 80 X-Max system from Oxford Ins. for EDS analysis. For this analysis the microscope was operated at 30 kV in high mag. mode. Approximately 85% of the carbon disk was scanned to give a realistic overview of the sample and only a few representative areas were captured.

Powder Dissolution Experiments

The absorbance values for curcumin and CUC-WPC_SD system in deionized water and buffer solutions were detected by a pION µDISS Profiler apparatus, consisting of an integrated diode array spectrophotometer connected to a fiber optic UV probe located directly in the reaction vessel and is able of measuring the concentration as a function of time without having to filter the solution. Measurement of dissolution kinetics and equilibrium solubility was carried out at 470 nm, where the used protein has no absorption, and the concentration of curcumin was calculated by means of a standard curve. In a typical experiment, 10 mL of solvent (deionized water, pH 5.8 or buffer solutions with pH 1.8 and 8.0) was added to a flask containing 10 mg of sample, and the resulting mixture was stirred at 25 °C and 600 rpm. The dissolution experiment with 160 min monitoring time was carried out in triplicate. The calibration curve was performed at 470 nm, a value at which WPC does not show an absorption signal, using a solution of curcumin in ethanol (Figure 9). The linear equation (y = 0.0331x + 0.0149) derived from the calibration curve was used to calculate the amount of dissolved CUC during the dissolution process.
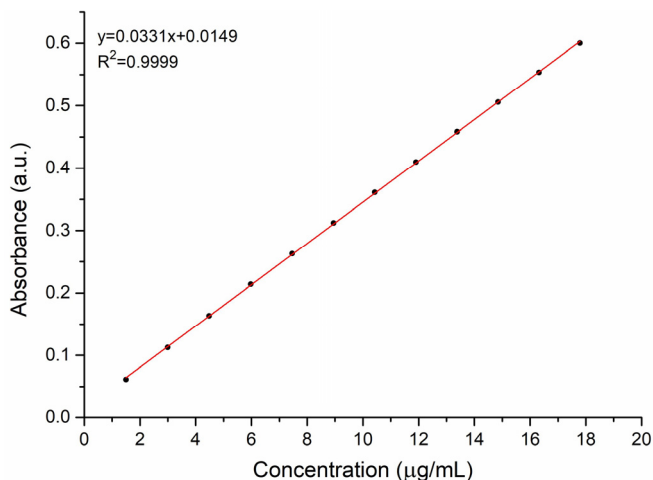
Figure 9. Calibration curve of curcumin concentration in ethanol

Cytotoxicity experiments

Cell culture. CUC-WPC_SD was tested in vitro against lung adenocarcinoma A549 (ATCC CCL-185) and skin melanoma A375 (ATCC CRL-1619) cells. A549 cells were maintained in DMEM F-12 media, supplemented with 10% fetal bovine serum, and A375 cells was kept in DMEM F-12 media supplemented with 10% fetal bovine serum, 1% L-glutamine and 1% penicillin-streptomycin solution. Both cell lines were grown in 25 mL flasks, at 37°C and 5% CO_2 in humified atmosphere.

Treatment. Three types of biochemical analyses were performed according to the ISO 10993-5 standard. Briefly, at an 80% confluence, the cells were transferred in 96 well plates and left for 24 h to attach. After this period, the treatment with CUC-WPC_SD was applied in increasing concentrations (10 – 300 µg/mL) for an additional 24 h.

Cell viability was assessed through the MTT assay and the value at which 50% of the cells is affected (IC_{50}) was calculated. The media from the treated cells was analysed for lactate dehydrogenase release (LDH assay) and for nitric oxide production (NO Griess assay). The work flow was as follows: 150 µL of LDH regent (Tris base 20 mM, lithium lactate, and NAD solution) was mixed with 50 µL of media, and 100 µL of NO regent (sulphanilamide and *N*-1-napthylethylenediamine) was mixed with 50 µL of media. The reagents were left with the media for 10 min in dark, at room temperature, after which the absorbances were read at 630 nm and 490 nm for LDH, and 548 nm for NO.

The cells remaining in the wells were incubated for an additional 1.5 h with 100 μL MTT solution. Forward, the formazan salt was dissolved with acidified propanol for 5 min, and the absorbance was read at 630 nm and 550 nm. The BioTek plate reader, coupled with Gen5 Software was used (Epoch, Germany), and each plate contained a positive untreated control, a negative control (cells treated with 2% Tween 20), and vehicle controls (media mixed with reagents and CUC-WPC_SD, without cells).

Statistical analyses. Each experiment had six replicates and the mean was calculated from at least three independent experiments. One-way ANOVA and Students test were performed using the OriginPro 9.3 Software, and P values of ≤0.05 were considered significant.

ACKNOWLEDGMENTS

REFERENCES

1. B. B. Aggarwal, Curcumin: the Indian solid gold, In *The Molecular Targets and Therapeutic Uses of Curcumin in Health and Disease*, B. B. Aggarwal, Y. J. Surh, S Shishodia, Springer, Boston, MA, **2007**, Vol 595, Chapter 1, pp. 1-75
2. S. J. Hewlings, D. S. Kalman, *Foods*, **2017**, *6(10)*, 92; doi:10.3390/foods 6100092
3. A. Adamczak, M. Ozarowski, T. M. Karpinski, *Pharmaceuticals,* **2020**, *13(7)*, 153; doi:10.3390/ph13070153
4. D. C. Mathew, W.-L. Hsu, *J. Funct. Foods,* **2018**, *40(692),* 692-699
5. A. Askarizadeh, G. E. Barreto, N. C. Henney, M. Majeed, A. Sahebkar, *Int. J. Pharm*., **2020**, *585*, 119476; doi.org/10.1016/j.ijpharm.2020.119476 R
6. M. A. Tomeh, R. Hadianamrei, X. Zhao, *Int. J. Mol. Sci.*, **2019**, *20*, 1033; doi:10.3390/ijms20051033
7. S. Mondal, S. Ghosh, S. P. Moulik, *J. Photochem. Photobiol. B: Biol*., **2016**, *158*, 212–218
8. M. L. A. D. Lestari, G. Indrayanto, Chapter three. Curcumin, In *Profiles of Drug Substances, Excipients, and Related Methodology*, First ed., H. Britain Ed., Academic Press, Elsevier Inc., **2014**, Vol. 39, pp.113-204,
9. P. Sanphui, G. Bolla, *Cryst. Growth Des*., **2018**, *18,* 5690−5711
10. K. Suresh, A. Nangia, *Cryst. Eng. Comm*., **2018**, *20*, 3277-3296
11. Z. Liu, J. D. Smart, A. S. Pannala, *J. Drug Deliv. Sci. Technol*., **2020**, *60*, 102082; doi: 10.1016/j.jddst.2020.102082 R
12. K. Ahmed, Y. Li, D. J. McClements, H. Xiao, *Food Chem*., **2012**, *132*, 799–807

13. Y. He, H. Liu, W. Bian, Y. Liu, X. Liu, S. Ma, X. Zheng, Z. Du, K. Zhang, D. Ouyang, *Pharmaceutics*, **2019**, *11*, 442; doi:10.3390/pharmaceutics11090442

14. A. Celebioglu, T. Uyar, *Food Chem.*, **2020**, *317*, 126397; doi:10.1016/j.foodchem.2020.126397 R

15. U. Kannamangalam Vijayan, N. Nitin Shah, A. Bhimrao Muley, R. S. Singhal, *J. Food Eng.*, **2021**, *292*, 110258; doi:10.1016/j.jfoodeng.2020.110258 R

16. M. Mohammadian, M. Moghadam, M. Salami, Z. Emam-Djomeh, F. Alavi, S. Momen, A. A. Moosavi-Movahedi, *J. Drug Deliv. Sci. Technol.*, **2020**, *56*, 101531; doi:10.1016/j.jddst.2020.101531 R

17. A. M. Chuah, B. Jacob, Z. Jie, S. Ramesh, S. Mandal, J. K. Puthan, P. Deshpande, V. V. Vaidyanathan, R. W. Gelling, G. Patel, T. Das, S. Shreeram, *Food Chem.*, **2014**, *156*, 227–233

18. A. R. Madureira, C. I. Pereira, A. M. P. Gomes, M. E. Pintado, F. X. Malcata, *Food Res. Int.*, **2007**, *40*, 1197–1211

19. R. A. McGregor, S. D. Poppitt, Chapter 19 - Milk Proteins and Human Health, In *Milk proteins: from expression to food*, 2nd ed., H. Singh, M. Boland, A. Thompson Eds., Academic Press, **2014**, pp. 541-555

20. G. Kontopidis, C. Holt, L. Sawye, *J. Dairy Sci.*, **2004**, *87*, 785–796

21. H. C. Liu, W. L. Chen, S. J. T. Mao, *J. Dairy Sci.*, **2007**, *90*, 547–555

22. Y. Pan, Q.-T. Xie, J. Zhu, X.-M. Lia, R. Menga, B. Zhanga, H.-Q. Chena, Z.-Y. Jin, *Food Chem.*, **2019**, *287*, 76–84

23. R. A. Awad, Z. M. R. Hassan, A. F. Farrag, M. M. El-Sayed, T. N. Soliman, *IJFANS*, **2015**, *4(3)*, 125-131

24. W. Liu, X. D. Chen, Z. Cheng, C. Selomulya, *J. Food Eng.*, **2016**, *169*, 189-195

25. G. K. Jayaprakashaa, K. N. Chidambara Murthya, B. S. Patil, *Eur. J. Pharmacol.*, **2016**, *789*, 291-300.

26. M. Li, Y. Ma, J. Cui, *LWT - Food Science and Technology*, **2014**, *59(1)*, 1-10

27. A. H. Sneharani, J. V. Karakkat, S. A. Singh, A. G. Appu Rao, *J. Agric. Food Chem.*, **2010**, *58*, 11130–11139

28. M. Li, Y. Ma, M. O. Ngadi, *Food Chem.*, **2013**, *141*, 1504–1511

29. C. D. Kanakis, P. A. Tarantilis, M. G. Polissiou, H. A. Tajmir-Riahi, *J. Biomol. Struct. Dyn.*, **2013**, *31(12)*, 1455–1466

30. M. I. Landin Neves, S. Desobrybanon, I. T. Perrone, S. Desobry, J. Petit, *Powder Technol.*, **2019**, *345*, 601-607

31. M. Mohammadian, M. Salami, F. Alavi, S. Momen, Z. Emam-Djomeh, A. A. Moosavi-Movahedi, *Food Biophys.*, **2019**, *14*, 425–436

32. C. Siregar, S. Martono, A. Rohman, *J. Appl. Pharm. Sci.*, **2018**, *8(08)*, 151-156

33. S. M. Beck, K. Knoerzer, J. Arcot, *J. Food Eng.*, **2017**, *214*, 166-174

34. R. Arunkumar, C. J. Drummond, T. L. Greaves, *Front. Chem.*, **2019**, *7*, 74; doi: 10.3389/fchem.2019.00074

35. A. Ciorîță, M. Suciu, S. Macavei, I. Kacso, I. Lung, M. L. Soran, M. Parvu, *Molecules*, **2020**, *25(4)*, 819; doi:10.3390/molecules25040819

36. R. M. Levytskyy, Y. Z. Filyak, R. S. Stoika, *Exp. Oncol.*, **2004**, *26*, 217-220

37. J. Li, Y. Wang, C. Yang, P. Wang, D. K. Oelschlager, Y. Zheng, D.-A. Tian, W. E. Grizzle, D. J. Buchsbaum, M. Wan, *Mol. Pharmacol.*, **2009**, *76*, 81–90

38. S. Li, C. Fang, J. Zhang, B. Liu, Z. Wei, X. Fan, Z. Sui, Q. Tan, *Nanomedicine: NBM*, **2016**, *12(6)*, 1567-1579

PAINTING MATERIALS INVESTIGATION FROM DRAGU WOODEN CHURCH, SALAJ COUNTY

**VICTOR CONSTANTIN MARUTOIU[a], IOAN BRATU[b*],
OLIVIA FLORENA NEMES[a], CONSTANTIN MARUTOIU[a]**

ABSTRACT. The old wooden church from Dragu, Sălaj County, was built on the hill of Dragu village between 1806 and 1809, according to the inscription found inside. The investigations targeted the imperial gates (the main entry from the nave to the altar used by the priest during church service and adorned with painted icons and elaborated wood sculpture) and aimed to identify the materials used for their manufacture: the wood species, pigments, ground, binders. For the identification of materials two spectroscopic methods were employed: XRF (X-ray fluorescence) and FTIR (Fourier transform IR absorption). The employed materials are: linden wood for the imperial gates, gypsum for ground; lead white, Prussian blue, gold and silver leaf, iron red, lead red, cinnabar, realgar, orpiment, Scheele's green for pigments; egg yolk and bone glue as binders.

Keywords: XRF - non-destructive spectroscopy, FTIR absorption destructive spectroscopy, wooden church, imperial gates, painting materials, pigments

INTRODUCTION

The church, Fig 1, was built between 1806 and 1809, information available from the inscription found next to the church entry and is dedicated to St. Basil the Great. The structure has a rectangular shape with an attached altar apse, specific to the Transylvanian architecture and a covered porch on two sides. The high raising bell tower gives monumentality to the structure. The base of the tower is open with four arches on each side. It's four corners are decorated with small towers. On the interior, the narthex is covered with a level ceiling, the nave with a semi-cylindrical vault and the altar with an

[a] *Babeş-Bolyai University, Faculty of Orthodox Theology, F/N Episcop Nicolae Ivan St., 400117 Cluj-Napoca, Romania*
[b] *National Institute for R&D on Isotopic and Molecular Technologies, 67-103 Donath St., 400293, Cluj-Napoca, Romania*
* *Corresponding author: ibratu@gmail.com*

arching. The original painting can still be seen on the narthex walls (the nave painting was degraded by water ingress). The altarpiece was sculpted and painted in 1815 [1-6].

Figure 1. Old wooden church from Dragu village, Sălaj County
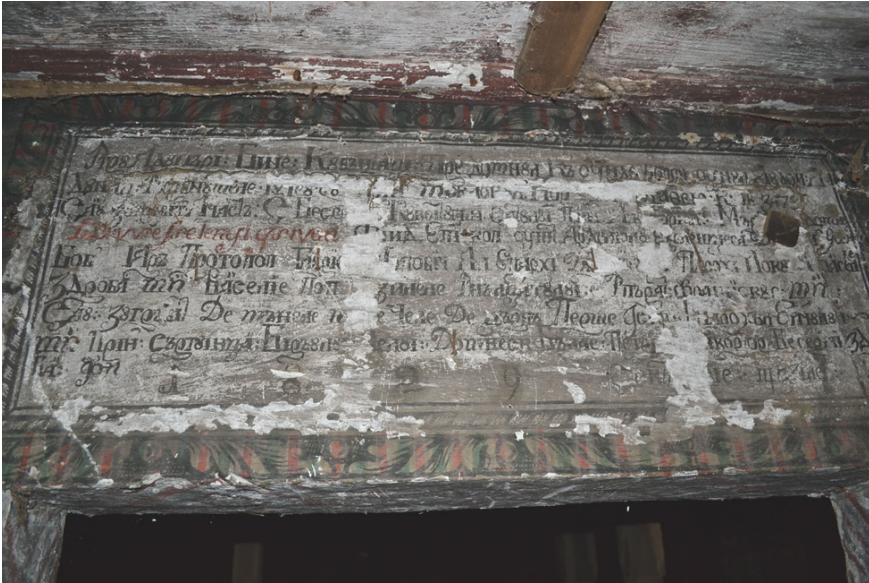and its location on the map.

Figure 2. Inscription above the nave entry

The inscription above the nave entry (Fig. 2) specifies the wall painting execution date and name of the painter (1829, Iosif Perșe), the funds being raised by the villagers. Names of priests, local personalities and emperor are also mentioned.

Figure 3. Imperial Gates (front and back)

The imperial gates, see Fig. 3, are made from a carved piece of wood with frames on the edges and the two icons inside each. The painter made only four icons representing the four evangelists, giving up the icon of the Annunciation probably due to lack of space or material.

According to the inscription on the back side, the imperial gates were made and painted in 1816.

This study aims to investigate the materials used by the painter for conservation and restoration purposes and to compare them with contemporary Transylvanian paintings. The pigment palette richness can also offer an insight to the economic situation of the local community, which provided the financial support for the execution.

RESULTS AND DISCUSSION

XRF- Spectroscopy

The non-destructive XRF spectroscopy investigations were performed in situ with a portable spectrometer and the analyzes targeted the primer layer and each color from the painting layer at different points.

The spectra and compositions of painting materials are presented in the Figs. 4 - 13.

Following the analysis of the primer layer (Fig. 4), the presence of large amounts of calcium was found. Fourier transform infrared spectroscopy (Fig. 14) confirmed the presence of gypsum (hydrated calcium sulfate).
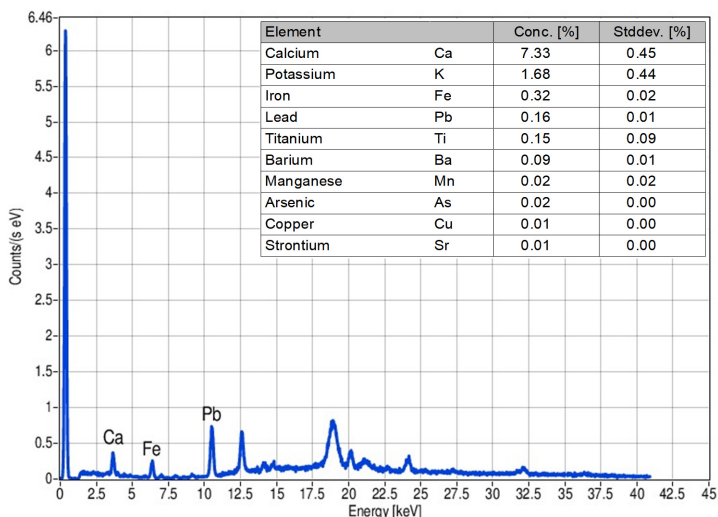

Element		Conc. [%]	Stddev. [%]
Calcium	Ca	7.33	0.45
Potassium	K	1.68	0.44
Iron	Fe	0.32	0.02
Lead	Pb	0.16	0.01
Titanium	Ti	0.15	0.09
Barium	Ba	0.09	0.01
Manganese	Mn	0.02	0.02
Arsenic	As	0.02	0.00
Copper	Cu	0.01	0.00
Strontium	Sr	0.01	0.00

Figure 4. XRF spectrum of ground – Calcium based – Gypsum
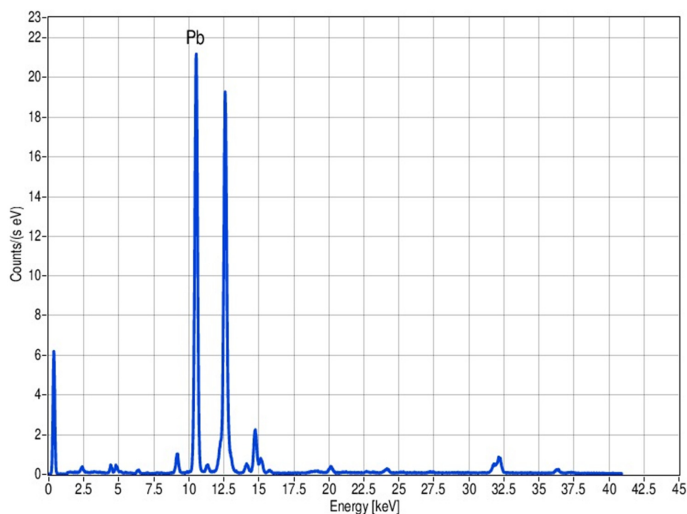(confirmed by FTIR spectrum)

Figure 5. XRF spectrum of white colour - lead white

As can be seen in the XRF spectrum shown in Fig. 5, the painter used lead hydroxycarbonate to render the white colour.
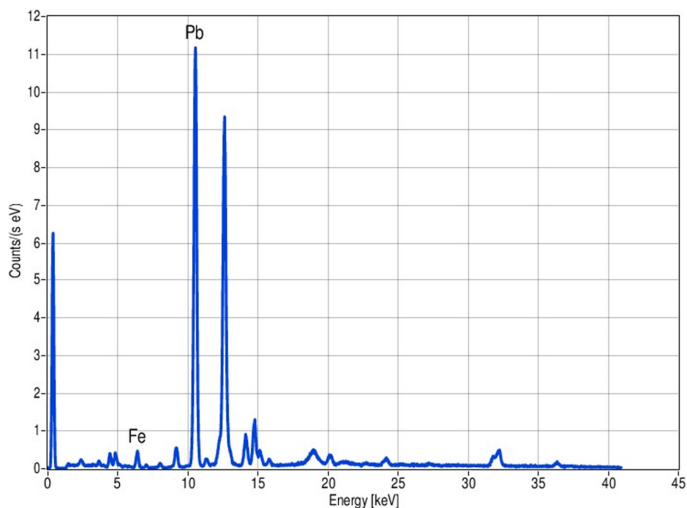

Figure 6. XRF spectrum of blue colour - Prussian blue mixed
with lead white (confirmed by FTIR spectrum)

The XRF spectrum for the blue colour shows the presence of iron, indicating that for this colour the author used Prussian blue, which is confirmed

by the FTIR analysis (Fig.16 and Fig. 17). Lead is also present (from lead white, used to decrease the intensity of blue).
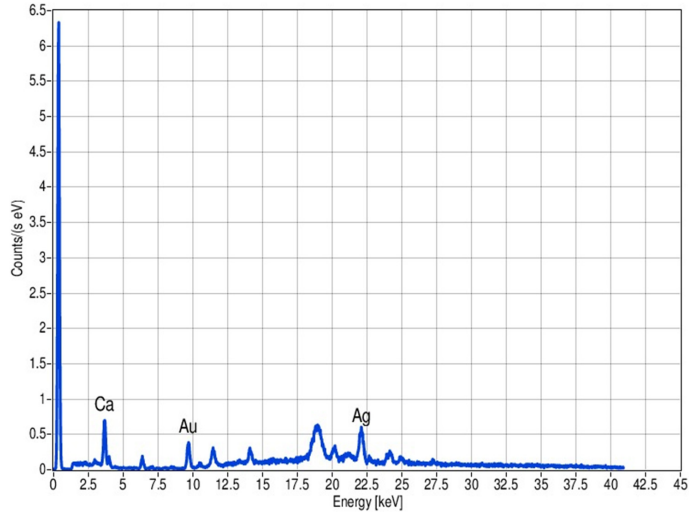
Figure 7. XRF spectrum of aura - gold and silver leaf

Gold and a silver leaf were used for the auras of the saints (Fig.7).
The use of gold and silver leaf is of note, a common and cheaper option to obtain the auras was the use of orpiment.
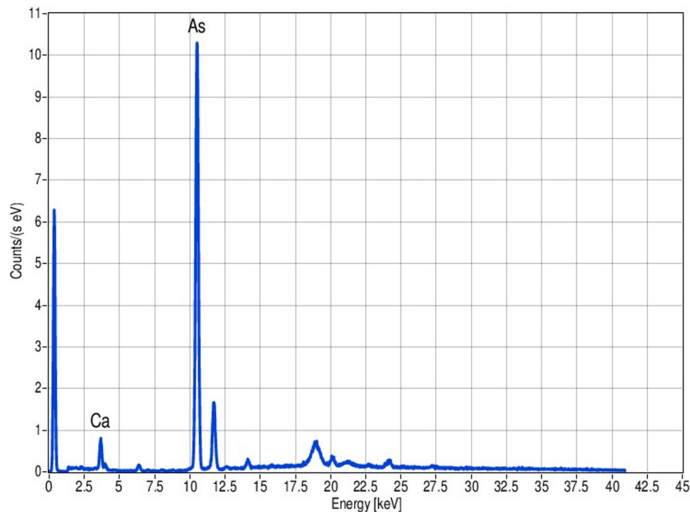

Figure 8. XRF spectrum of yellow pigment - orpiment

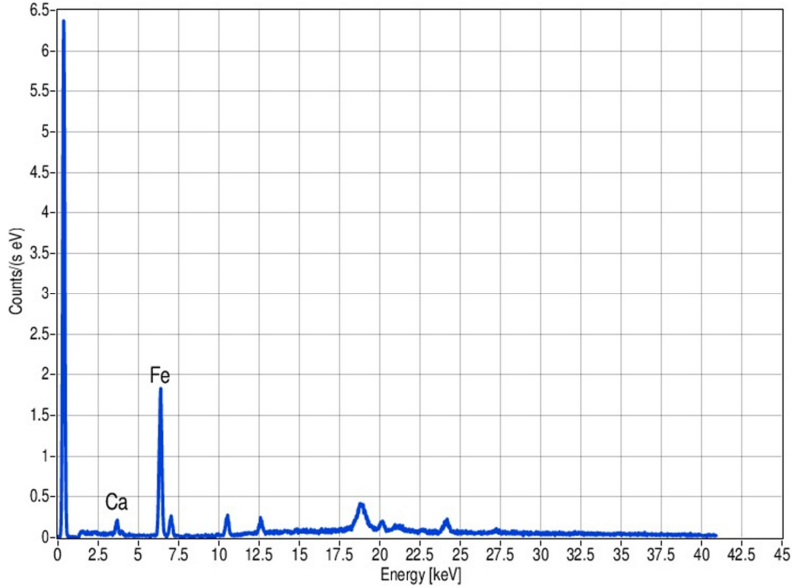The presence of arsenic in the XRF spectrum of the yellow colour shows the use of orpiment.

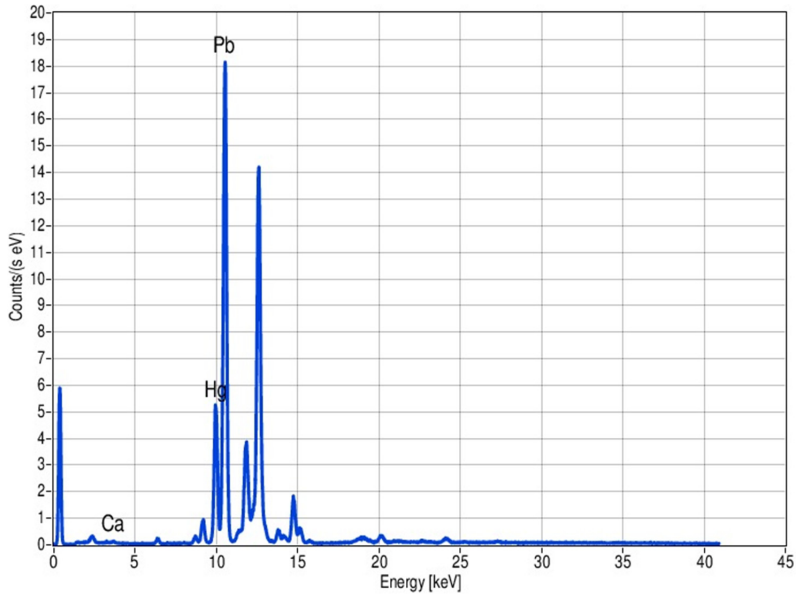**Figure 9.** XRF spectrum of red paint – iron red

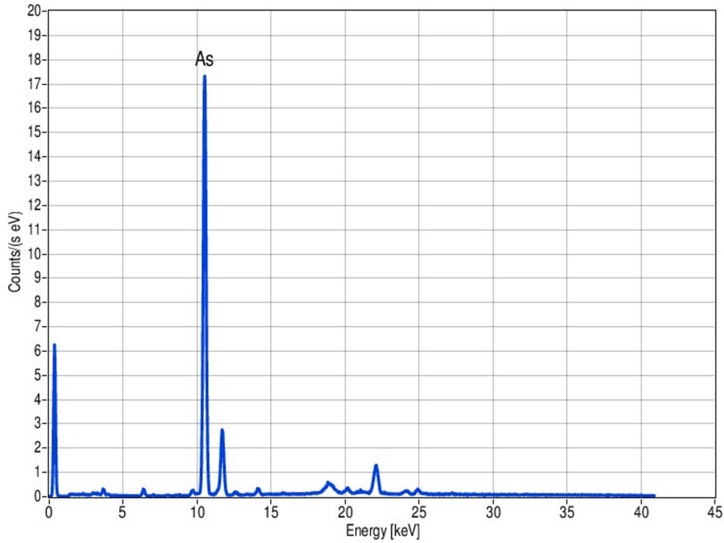**Figure 10**. XRF spectrum of red paint – lead read mixed with cinnabar

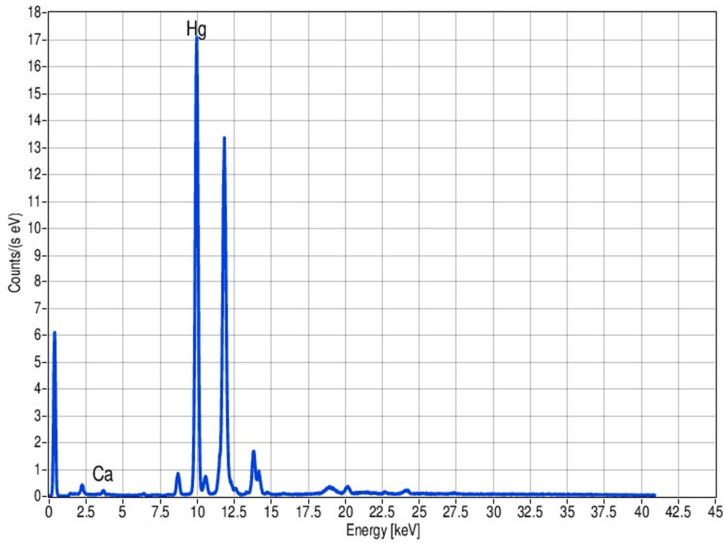**Figure 11**. XRF spectrum of red paint (Marc the Evangelist)– realgar

Figure 12. XRF spectrum of red paint from frame – cinnabar

To render the red colour, the author of the icons painted on the imperial gates used several pigments: iron red (Fig.9), lead red mixed with mercury red/cinnabar /(Fig.10) and realgar (Fig.11). The calcium identified in the spectra is from the primer composition.

The painter used an unusual number of red pigments, four being used individually or in combination to obtain various shades of red (Figs. 9-12). While the iron red and red led were commonly used in that period, the cinnabar (mercury sulfide) was used more scarcely, sometimes in just a few places (for the most important biblical figures) or smaller quantities (to give a slight red shade to the white carnation of depicted characters). The use of realgar, an arsenic sulfide mineral is of special note, not being previously detected by the current research team in other Transylvanian wooden church paintings and icons [7-12].
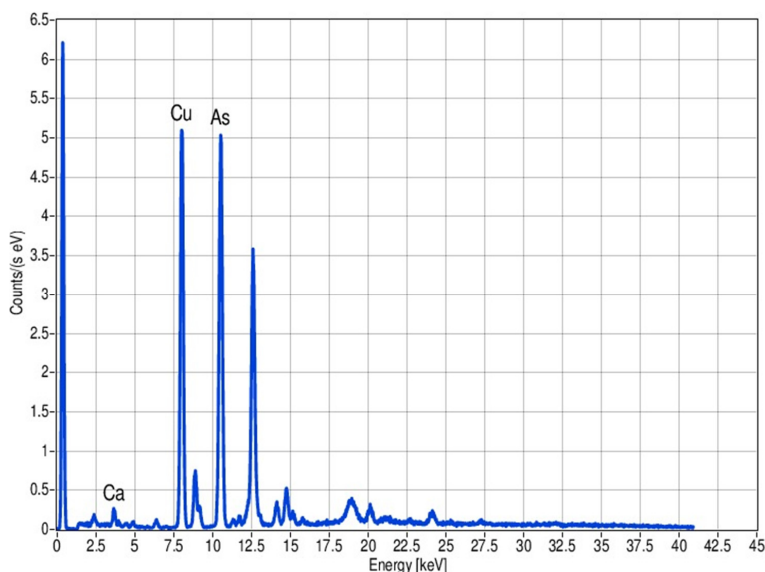

Figure 13. XRF spectrum of green paint – Scheele's green

The pigment used for the green colour was Scheele's green (shown by the presence of arsenic and copper in the Fig. 13 XRF spectrum).

The presence of the Scheele's green is of note, discovered in 1775 (the most commonly used green pigments in other contemporary wooden church paintings and icons being malachite, verdigris or green earth).

FTIR Spectroscopy

The identification of painting materials and of the wood are presented In the Figs 14 - 18.
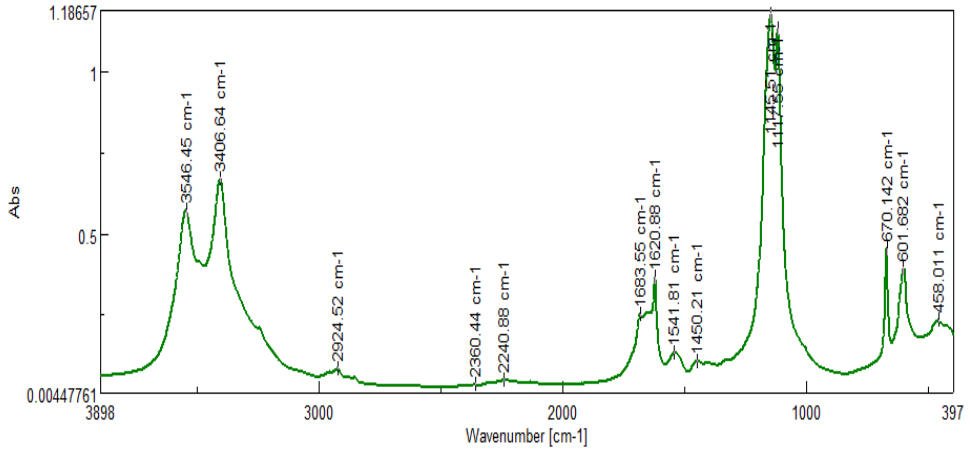
Figure 14. FTIR spectrum of gypsum ground
Gypsum: 3546, 2306, 1620, 1145, 1114 and 670 cm^{-1}
Proteins: 2924, 1645, 1541 cm^{-1}
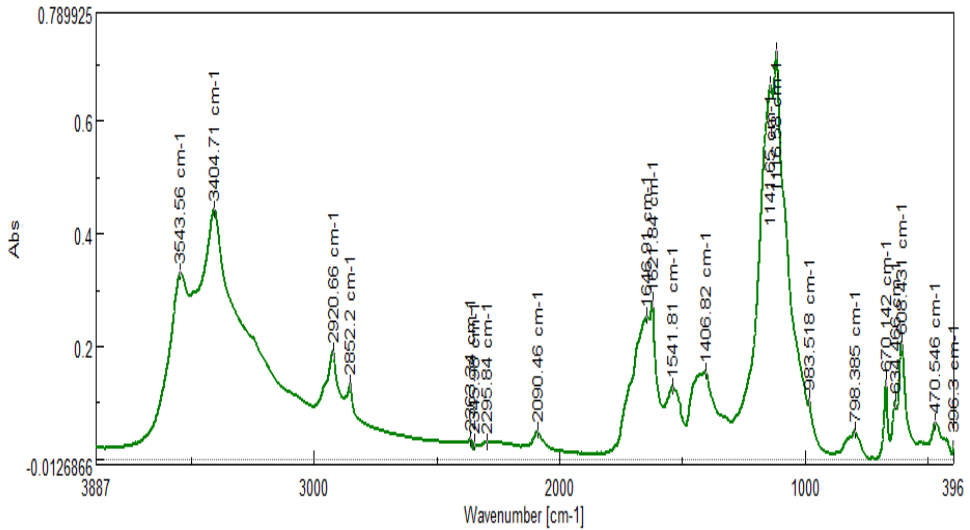
Figure 15. FTIR spectrum of yellow painting material.
Composition: gypsum (3546, 2306, 1620, 1145, 1114 and 670 cm^{-1}),
Proteins (2929, 2852, 1646, 1541, 793 cm^{-1}), orpiment (based only on XRF data)

Figure 16. FTIR spectra of the blue painting material- blue line
Prussian blue pigment; red line – red lead on frame (~530 and 475 cm^{-1});
violet line – red pigment (mercury red, based only on XRF data)

Figure 17. FTIR spectra of the blue painting material detailed - blue line
Prussian blue pigment (specific peak at 2091 cm^{-1}); red line – red frame;
violet line – red pigment

Figure 18. FTIR spectra of wooden samples: green line-Imperial Gate wood;
blue dash line – linden standard wood (based on absorptions
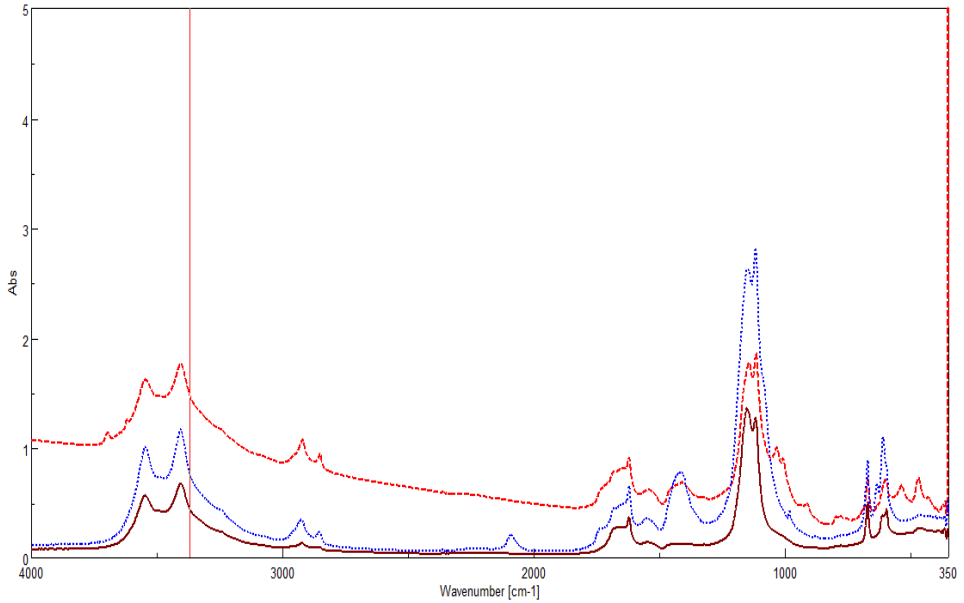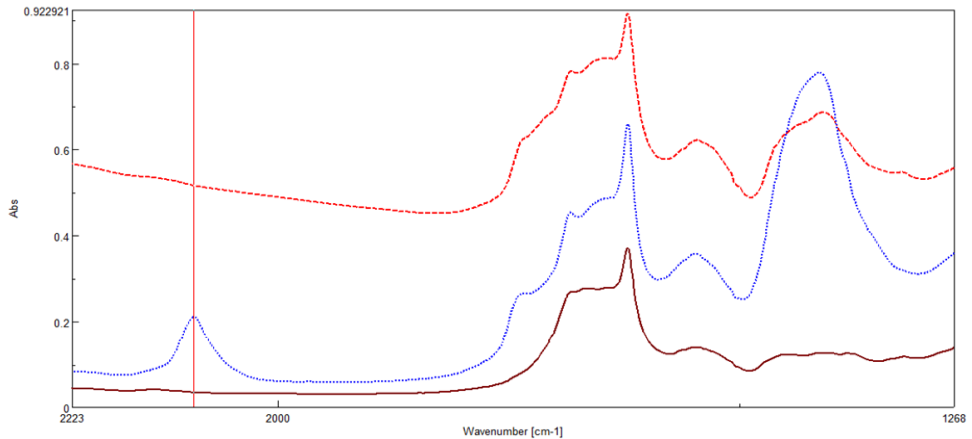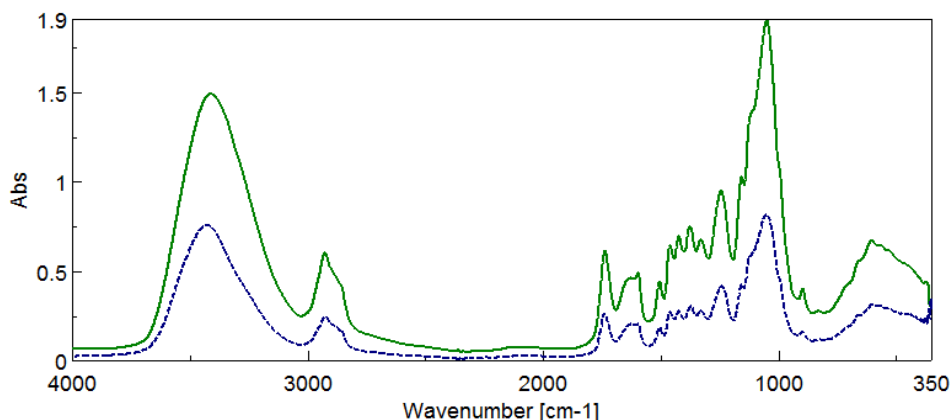located at~3400 and 1100-1000 cm^{-1})

The spectra comparison from Fig.18 is showing that the wood species used to manufacture the imperial gates is linden wood [13].

CONCLUSIONS

The imperial gates from the Dragu wooden Church are made from linden wood. The painting materials used by the painter are: gypsum for ground; lead white, Prussian blue, gold and silver leaf, iron red, lead red, cinnabar, realgar, orpiment, Scheele's green for pigments; egg yolk and bone glue as binders.

The rich palette of pigments is unusual compared to other sites, especially shown by the use of four different red pigments. This also suggests a better economic state of the community or possibly support received (the inscription above the nave entry mentioning help from a baron), many other communities from that time didn't afford such a vast palette of materials.

Many of the pigments used have various levels of toxicity (lead from red and white lead pigments, mercury from cinnabar, arsenic from realgar, orpiment and Scheele's green). While most of them were commonly used in the era, their very rich selection in only one site is of note.

EXPERIMENTAL SECTION

Non-destructive XRF spectroscopy

Non-destructive X-ray fluorescence elemental analysis (XRF) was performed with a handheld Bruker spectrometer, S1 TITAN series (EDXRF) configured with a Silicon diode PIN detector (SiPIN), Rh target X-ray tube with a maximum voltage of 50 kV.

FTIR absorption spectroscopy

Fourier-transform Infrared (FTIR) measurements were performed in the 4000 to 400 cm^{-1} spectral range with a Jasco 6100 spectrometer with a resolution of 4 cm^{-1} (256 scans) by employing 1 (< 1) mg of sample and about 200 mg of pure spectral KBr (KBr pellet technique was applied). The FTIR spectra were processed with the Spectral Analysis software.

DISCLOSURE

Victor Constantin Măruțoiu and **Olivia Florena Nemeș** are co-first authors.

REFERENCES

1. A. Bârcă, *Biserici de lemn din Sălaj*, Ed. Noi Media Print, București, **2011**.
2. I. Godea, Biserici de lemn din România (nord-vestul Transilvaniei), Ed. Meridiane, București, **1996**.
3. C. Brăcăcescu, *Lăcașuri din lemn: biserici de sat din Sălaj*, Ed. Igloo Media, București, **2015**.
4. I. Cristache-Panait, *Buletinul Monumentelor Istorice*, **1971**, *1*, 31-40.

5. I. Godea, I. Cristache-Panait, *Monumente istorice bisericești din Eparhia Ortodoxă Română a Oradiei. Biserici de lemn*, Ed. Episcopiei Ortodoxe Române a Oradiei, Oradea, **1978**.
6. C. Zebacinschi, I. Ciocian, *Acta Musei Porolissensis*,**1984**, *VIII*, 775-792.
7. O.F. Nemeș, I. Bratu, C. Măruțoiu, I. Kacso, M. Miclăus, D. Mihali, D. Nica Badea, *Rev.Chim. (Bucharest)*, **2018**, *69*, No. 1, 76-79.
8. I. Bratu, O.F. Nemeş, V.C. Măruţoiu, I. Kácso, D.Gh. Vlasin, ,*Anal. Lett.*, **2019**, *52*, 45-50.
9. I. Bratu, C. Măruțoiu, D. Nemeș, D. Toader, O.F. Nemeș, R.C. Suciu, *Anal. Lett*, **2020**, *53*, 204-211.
10. D. Nemeș, C. Măruțoiu, I. Bratu, C. Neamțu, I. Kacso, O.F. Nemeș, I. Udrea, Characterization of the Paint Used by Dumitru Ispas in the Wooden Straja Church, Cluj County, Romania, *Anal. Lett*, **2020**, *54*:1-2, 255-264.
11. C. Neamțu, V.C. Măruțoiu, I. Bratu, O.F. Măruțoiu, C. Măruțoiu, I. Chirilă, M. Dragomir, D. Popescu, *Sustainability* **2018**, *10*, 1503.
12. O.F. Măruțoiu, I. Bratu, C. Măruțoiu, D.L. Postolache, M. Dragomir, C. Tanaselia, S. Garabagiu, *X -Ray Spectrometry*, **2018**, *47*, 176–185.
13. M. Poletto, V. Pistor, A.J. Zattera, Structural characteristics and thermal properties of native cellulose. In *Cellulose – Fundamental Aspects*, Theo G.M. van de Ven Eds.; Intechopen, London, UK, **2013**.

THE FULL MAPPING OF LOW-LYING EXCITED STATE RELAXATION DYNAMIC PATHWAYS FOR ACETOPHENONE

ATTILA BENDE[a]

ABSTRACT. Several relaxation pathways of the low-lying electronic excited state dynamics for acetophenone including also the singlet-triplet intersystem crossings were studied. The multireference Hartree-Fock and second order perturbation theory methods together with def2-tzvp basis set were used to characterize the equilibrium geometries and the crossing points between different potential energy surfaces (PES) up to the third excited state level considering both the singlet and triplet spin states. The electronic deactivation pathways studies reveal that the acetophenone shows several possible deactivation channels but their occurring probability strongly depends on the local profile of the PES of the intermediate states.

Keywords: acetophenone, conical intersection, intersystem crossing, spin-orbit coupling, deactivation pathway

INTRODUCTION

Acetophenone (C6H5C(=O)CH3, APN) is an aromatic ketone molecule with interesting photochemical and spectroscopic properties. Due to the electronic excitation of the π electrons of the carbonyl group or the benzene ring, electron charges can easily migrate between the carbonyl fragment and the benzene ring and change the electronic structure of fragments. In general, this π electron conjugation between the aromatic and carbonyl groups could influence the ordering of the n → π* and π →π* states, their photochemical reactivities, and the photo-dissociation mechanisms [1-3].

It was experimentally shown, that the gas phase absorption spectrum for APN in the region of 210–380 nm exhibits three broad peaks centered at 325, 273 and 230 nm, which are assigned to the electronic transitions from the ground state to S1, S2 and S3 excited states, respectively [4]. On

---

[a] *Molecular and Biomolecular Physics Department, National Institute for Research and Development of Isotopic and Molecular Technologies, Str. Donat 67-103, C.P. 700, Cluj Napoca, RO-400293, Romania, attila.bende@itim-cj.ro*

the other hand, it is well known that APN shows both fluorescence [5] and phosphorescence [6] spectra; i.e., both the singlet and triplet states population can be experimentally achieved.

The first two singlet/triplet vertical and adiabatic excitation energies of the APN have already been studied [7-9] theoretically using complete active space self-consistent field (CASSCF) and second-order quasi-degenerate multi-reference perturbation theory (MR-PT2) methods. Theoretical studies on its non-radiative relaxation channel through the so-called conical intersections (CIs) [10] between different potential energy surfaces (PES) are rather limited, only Huix-Rotllant and co-workers [9] have studied in more details these crossing points. Most of the studies have been mainly focused on the mechanisms of photodissociation [11], especially, at S1/T2/T1 three-state intersection region [1,12] or on the elucidation of the population mechanism of the triplet manifold [9,13,14].

The aim of the present study is therefore to find, by means of minimum energy path and ISC point computations, alternative pathways for the acetophenone excited state relaxation mechanism. The paper is structured as follows: first, the computational details for the excited state characterization are discussed followed by a presentation and discussion of the conical intersection and intersystem crossing points as well as the spin-orbit couplings. Finally, conclusions about the excited state relaxation mechanism are given.

RESULTS AND DISCUSSION

Minima and crossing points. The ground state optimized geometry structure of APN was obtained using the SA-MCSCF method with the def2-TZVP basis set, considering the (10,9) complete active space configuration.
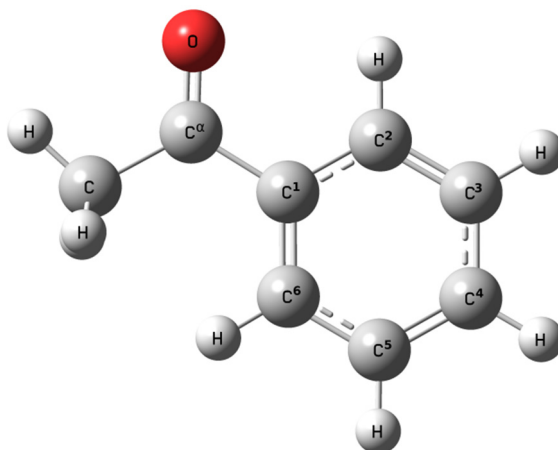

Figure 1. The equilibrium structure of the APN ground state geometry.

The geometry of the APN molecules is shown in Figure 1. Based on the NPA charge analysis, the carbonyl fragment shows negative charge (-0.024e), while the benzene fragment contains the same amount of charge but with opposite sign. Concerning the benzene ring geometry, the C–C

Table 1. Internal bond coordinates (in Å) of APN's optimized geometries at different equilibrium positions.[a]

Geom.	Carbonyl		Benzene						Energy (in eV)	
	C^α=O	C^α-C^1	C^1-C^2	C^2-C^3	C^3-C^4	C^4-C^5	C^5-C^6	C^6-C^1	SCF	PT2
$R_e(S_0)$	1.20	1.50	1.40	1.38	1.39	1.38	1.39	1.38	-	-
$R_e^C(S_1)$	1.39	1.41	1.41	1.37	1.39	1.39	1.37	1.42	3.34	3.77
$R_e^B(S_1)$	1.19	1.47	1.44	1.43	1.42	1.42	1.43	1.44	4.54	5.31
$R_{TS}(S_1)$	1.24	1.46	1.44	1.43	1.42	1.42	1.43	1.44	4.64	-
$R_e^C(S_2)$	1.44	1.35	1.47	1.40	1.36	1.45	1.33	1.45	6.05	6.45
$R_e^B(S_2)$	1.22	1.44	1.46	1.45	1.40	1.37	1.42	1.46	5.28	4.78
$R_e(S_3)$	1.36	1.39	1.51	1.43	1.34	1.45	1.41	1.40	6.30	
$R_e^C(T_0)$	1.35	1.41	1.41	1.39	1.39	1.40	1.37	1.42	3.04	3.73
$R_e^B(T_1)$	1.20	1.46	1.45	1.42	1.42	1.40	1.44	1.43	4.52	5.23
$R_e^B(T_2)$	1.19	1.48	1.43	1.44	1.42	1.41	1.43	1.43	4.60	5.30

[a]Bond lengths are given in Å and energies in eV. The labelling of atoms is given in Figure 1.

bonds vary between 1.38 and 1.40 Å, showing a slight deviation from its value in the perfect aromatic ring. The vertical excitation energies as well as the equilibrium geometries of the first and second excited states calculated at Hartree-Fock (HF) were already done in our previous work [8]. Accordingly, the vertical excitation energies are 4.52 eV for the S1 and 5.60 eV in case of S2 state, respectively. The corresponding values obtained at the XMS-CASPT2 level of theory are 4.54 and 4.85 eV, respectively. If one analyzes the charge redistribution for different excited states induced by the vertical excitation one can observe that the $S_0 \rightarrow S_1$ transition induces 0.095e fractional electronic charge migration from the carbonyl fragment to the benzene group, while the $S_0 \rightarrow S_2$ transition relocate -0.087e charges from the benzene group to the carbonyl fragment. Once the AP molecule is excited and gets into the corresponding excited electronic state, it tries to reach its global (or in some circumstances the local) energy minimum. Since, the structures of the optimized geometries for the first and second excited singlet states were already presented in our previous work [8]; we show their internal bond values only in tabular form (see Table 1) without discussing them again in more detail. Considering the two molecular fragments of the carbonyl group and the benzene ring, one global and one

local energy minimum were found for both S_1 and S_2 excited state cases. The only difference between the minima is the localization of the changes in the geometry of the fragments. For the simplicity, the geometries will be denoted by $R_e^X(Y_i)$, where X = B or C (B = benzene, C = carbonyl) is used to differentiate stationary points on carbonyl or benzene, Y=S or T is used to define the singlet or triplet spin state, i=0, 1 or 2 is used to show the order of the given excited state related to the energy quantum number, while e indicates the nature of the stationary point (equilibrium geometry, CI, ISC or TS). Accordingly, the global energy minimum of the S_1 state induces geo-metry changes on the carbonyl group ($R_e^C(S_1)$ with (n,π*) excitation character), while the S_2 state's global minimum shows enlarged benzene ring's periphery ($R_e^B(S_2)$ with (π,π*) excitation character). The opposite is true for the geometry changes for the local energy minima. Besides the analysis of the electronic configuration and geometry structure of the first two excited states, we have included in our present study the examination of the energy level of the S_3 third excited state. The vertical excitation energy of this electronic state is 6.98 eV (177 nm) obtained at SA-MCSCF/def2-TZVP levels of theory. The $S_0 \rightarrow S_3$ vertical transition induces 0.190e fractional electronic charge migration from the benzene group to the carbonyl fragment and shows a very large oscillator strength (f=0.0740).

Performing geometry optimization, we have observed important fragment deformations on both carbonyl and benzene parts (See Figure 2) where the C^α=O and the C^1-C^2 bonds significantly enlarge, while C^α-C^1 one becomes much shorter. Since we are also interested in the electronic relaxation process over the triplet states, we have performed further geometry optimizations for the ground and for the first two triplet states. In this case, only the global energy minima are presented.
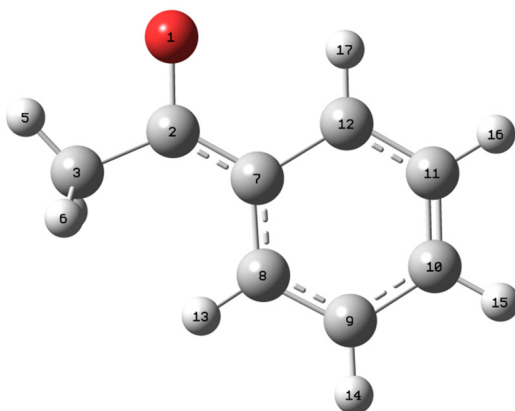

Figure 2. The equilibrium structure of the APN S_3 geometry.

By comparing the geometry configurations of the singlet ground state and the minima of the triplet states, one can observe that the ground triplet state $(R_e^C(T_0))$ geometry implies changes on the carbonyl group, while the first and second excited triplet states $(R_e^B(T_1)$ and $R_e^B(T_2))$ show changes mainly on the benzene ring (See Table 1). It can be also observed that $R_e^B(T_1)$ and $R_e^B(T_2)$ global energy minima are close to each other both from energetic and geometry parameter points of view. One should also mention that, all the obtained minimum-energy structures have planar geometry configuration allowing the maximum delocalization of the π* orbitals along the benzene ring and the C=O bond of the carbonyl fragment.

Table 2. Internal bond coordinates (in Å) of APN's geometries at different crossing points (conical intersection or intersystem crossing).[a]

Geom.	Carbonyl		Benzene						Energy (in eV)	
	C^α=O	C^α-C^1	C^1-C^2	C^2-C^3	C^3-C^4	C^4-C^5	C^5-C^6	C^6-C^1	SCF	PT2
$(S_1 \otimes S_2)^a$	1.16	1.50	1.49	1.50	1.42	1.36	1.44	1.49	5.58	5.54
$(T_0 \otimes T_1)$	1.29	1.39	1.47	1.37	1.41	1.45	1.33	1.46	3.40	3.79
$(T_1 \otimes T_2)$	1.19	1.49	1.44	1.44	1.46	1.39	1.43	1.41	4.63	5.15
$(T_2 \otimes T_3)$	1.21	1.45	1.44	1.42	1.39	1.38	1.43	1.45	4.87	4.70
$(S_1 \otimes T_1)$	1.20	1.46	1.45	1.42	1.41	1.41	1.44	1.43	4.53	5.14
$(S_1 \otimes T_2)$	1.22	1.45	1.44	1.37	1.41	1.44	1.46	1.45	5.13	5.27
$(S_2 \otimes T_3)$	1.22	1.45	1.45	1.45	1.44	1.41	1.37	1.44	5.30	4.89

[a]Bond lengths are given in Å and energies in eV. The labelling of atoms is given in Figure 1.

The existence of crossing points between different PESs in the configuration space is the key of the fast radiationless decay of the electronic excited state relaxation [10]. Accordingly, we have continued our investigation by searching for different CIs between electronic states with similar spin configuration as well as for ISCs between electronic states with singlet and triplet spin configurations (See Table 2). As a first step, let to consider the crossing between the ground and the first excited electronic singlet spin states. Here, we found three different geometry configurations (See Tables 2 and 3) with relatively close energy values: 5.17 eV, 5.26 eV and 5.15 eV, respectively. The first two CI structures show a broken benzene's ring planarity, close to the half-boat conformation found in the case of the isolated benzene molecule by Robb and co-workers [15,16], while the third one presents only carbonyl group distortion where the C=O bond enlarge over the single bond character (1.72 Å). No any structure with planar benzene ring was found for this $S_0 \otimes S_1$ crossing. Following the same

idea, we have investigated several possible CI configurations for the $S_1 \otimes S_2$ crossing. For this case, four different geometry structures were found having three different structural characteristics: planar benzene ring, half-boat benzene ring and carbonyl group deformations.

Among them the most relevant is that one which shows the planar ring deformation (See Figure 3 and for its geometrical parameter Table 2) because its energy (5.58 eV) lies very close to the S_2 vertical excitation energy value. The other three structures (See Table 4) show much higher energy values (7.12 eV, 7.91 eV and 8.61 eV, respectively) and they are
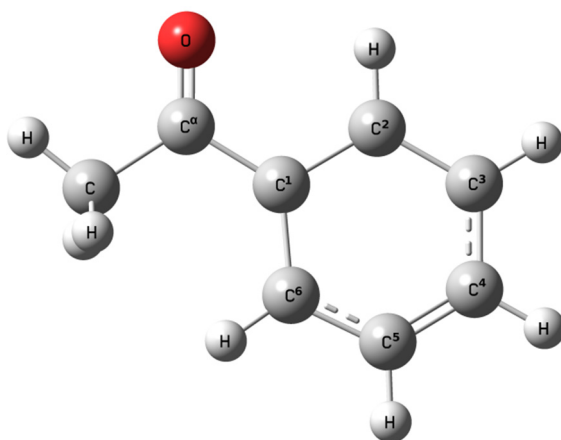
Figure 3. The equilibrium structure of the APN $(S_1 \otimes S_2)^a$ geometry.

Table 3. Geometries of three different conical intersection configurations between the first excited (S_1) and the ground (S_0) singlet spin states.
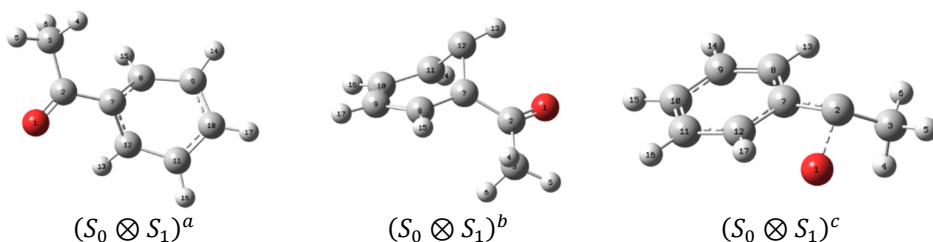
	O_1-C_2	C_2-C_3	C_2-C_7	C_7-C_8	C_8-C_9	C_9-C_{10}	C_{10}-C_{11}	C_{11}-C_{12}	C_{12}-C_7
$(S_0 \otimes S_1)^a$	1.193	1.510	1.464	1.443	1.461	1.389	1.389	1.460	1.436
$(S_0 \otimes S_1)^b$	1.190	1.511	1.488	1.470	1.385	1.391	1.455	1.448	1.459
$(S_0 \otimes S_1)^c$	1.720	1.483	1.418	1.419	1.353	1.416	1.357	1.405	1.392

Table 4. Geometries of three different conical intersection configurations between the second (S_2) and the first (S_1) excited singlet spin states.

$(S_1 \otimes S_2)^b$ $(S_1 \otimes S_2)^c$ $(S_1 \otimes S_2)^d$
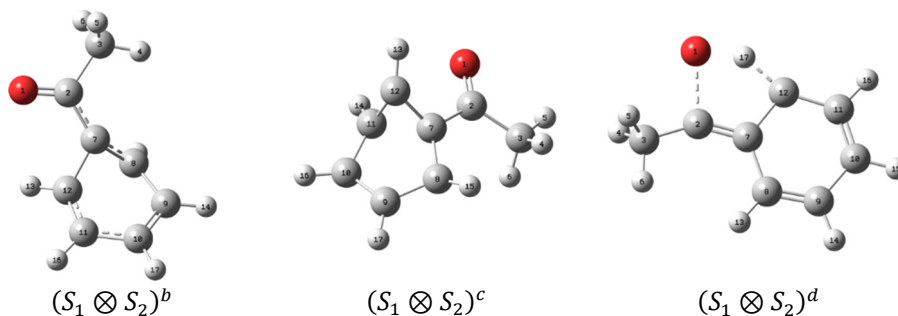
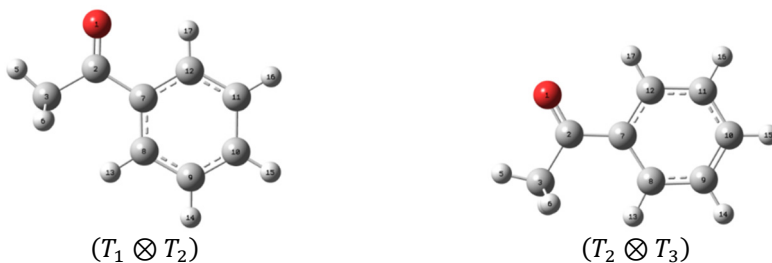|	O_1-C_2	C_2-C_3	C_2-C_7	C_7-C_8	C_8-C_9	C_9-C_{10}	C_{10}-C_{11}	C_{11}-C_{12}	C_{12}-C_7
$(S_1 \otimes S_2)^b$	1.205	1.517	1.416	1.425	1.454	1.382	1.426	1.388	1.551
$(S_1 \otimes S_2)^c$	1.189	1.507	1.499	1.489	1.467	1.469	1.485	1.465	1.484
$(S_1 \otimes S_2)^d$	1.886	1.455	1.302	1.479	1.337	1.475	1.330	1.458	1.508

slightly probable to be reached during the relaxation. From the phosphorescence point of view, the electronic relaxation over the triplet spin states also looks important. Starting from the T_0 ground triplet state its crossing with the T_1 first excited triplet state is reached at two different geometry configurations. The geometry with the lowest energy value (3.40 eV) shows a planar configuration with enlarged C=O bond (See Table 2 and Table 5), while the second one has a non-planar geometry (4.93 eV) with benzene ring in half-boat form (See Table 5). Continuing the present investigation by moving one step up to the crossing between T_1 and T_2 states, yet another CI point was found. This geometry also shows a planar configuration, with an enlarged benzene ring while the carbonyl group remains unchanged (See for its geometrical parameters Table 2 and Table 6). Moving even further, a new crossing point with similar geometry configuration was found between the T_2 and T_3 states. Its geometrical parameters are given in Table 2 and its molecular graphics is presented in Table 6. In this case we found also for the carbonyl group small changes in the C^α=O and C^α-C^1 bond distances.

To switch between different singlet and triplet states one need to locate the so-called intersystem crossing points and to compute the spin-orbit coupling to see how efficient could be the spin transition. Accordingly, we have searched for spin crossovers between $S_1 \otimes T_1$, $S_1 \otimes T_2$, $S_2 \otimes T_2$ and $S_2 \otimes T_3$ electronic spin states. Apart from the case of $S_2 \otimes T_2$, we have successfully located these

Table 5. Geometries of two different conical intersection configurations between the ground (T_0) and the first (T_1) excited triplet spin states.

$(T_0 \otimes T_1)^a$ $(T_0 \otimes T_1)^b$

	O_1-C_2	C_2-C_3	C_2-C_7	C_7-C_8	C_8-C_9	C_9-C_{10}	C_{10}-C_{11}	C_{11}-C_{12}	C_{12}-C_7
$(T_0 \otimes T_1)^a$	1.293	1.510	1.390	1.462	1.332	1.448	1.410	1.369	1.469
$(T_0 \otimes T_1)^b$	1.203	1.512	1.443	1.434	1.446	1.386	1.384	1.446	1.428
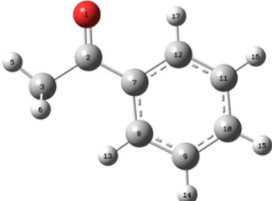
Table 6. Geometries of conical intersection configurations between different excited triplet spin states.

$(T_1 \otimes T_2)$ $(T_2 \otimes T_3)$

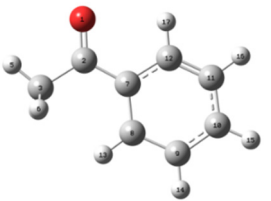|	O_1-C_2	C_2-C_3	C_2-C_7	C_7-C_8	C_8-C_9	C_9-C_{10}	C_{10}-C_{11}	C_{11}-C_{12}	C_{12}-C_7
$(T_1 \otimes T_2)$	1.190	1.511	1.492	1.414	1.426	1.390	1.461	1.438	1.439
$(T_2 \otimes T_3)$	1.213	1.516	1.448	1.449	1.428	1.384	1.388	1.424	1.443

crossing points between PESs. The first geometry we discuss is the $S_1 \otimes T_1$ crossing point. This geometry is characterized mainly by the benzene ring planar deformation, where C^1–C^2, C^5–C^6 and C^6–C^1 are slightly stretched, while the carbonyl fragment's geometry remains almost unchanged. Its geometrical parameters are given in Table 2 and its molecular graphics is presented in Table 7. Analyzing the strength of the spin-orbit coupling, we have observed that there is no any zero-field splitting, namely, the triplet spin state does not separate in three sublevels and the energies of the lowest 0th-order and of the lowest SO states derived from the Breit-Pauli Hamiltonian are identical. On the other hand, we found that the coupling between the singlet and triplet spin states is quite strong; the magnitude of

the spin-orbit coupling is 19.18 cm^{-1}. Continuing our investigation, we have found that the S_1 singlet state can cross not only the T_1 triplet state but also the T_2 one. The geometry of this ISC point only slightly differs from the previous case of the $S_1 \otimes T_1$ crossing. In this later case, the benzene ring planar deformations will be a bit larger (For the geometrical parameters see Table 2 and for its molecular graphics see Table 7) as well as we observe a small elongation of the C^{α}=O bond. Again, we have not found any zero-field splitting, and the magnitude of the spin-orbit coupling is only 1.15 cm^{-1}. As we already mention, we have been unable to find any crossing point between the S_2 singlet and T_2 triplet states, so we proceed to analyze the $S_2 \otimes T3$ crossing case. The geometry of this structure is almost identical with the previously obtained $S_1 \otimes T_2$ geometry, the only difference is the relative rotation with 180 degrees of the benzene ring with respect to the carbonyl group. The geometrical parameters of the $S_2 \otimes T_3$ ISC point are given in Table 2, while its molecular graphics is presented in Table 7.
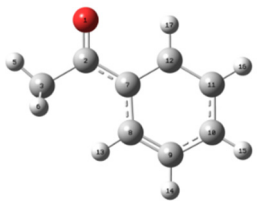
Table 7. Geometries of three different intersystem crossing configurations between the excited singlet and triplet spin states.

	O_1-C_2	C_2-C_3	C_2-C_7	C_7-C_8	C_8-C_9	C_9-C_{10}	C_{10}-C_{11}	C_{11}-C_{12}	C_{12}-C_7
$(S_1 \otimes T_1)$	1.197	1.514	1.464	1.432	1.436	1.405	1.414	1.422	1.446
$(S_1 \otimes T_2)$	1.216	1.513	1.452	1.450	1.457	1.437	1.407	1.367	1.437
$(S_2 \otimes T_3)$	1.216	1.515	1.446	1.441	1.366	1.409	1.437	1.454	1.453

The spin-orbit coupling is only 0.32 cm^{-1} which is even smaller than that of in the previous $S_1 \otimes T_2$ case and does not show any zero-field splitting.

Relaxation pathways. As we have already known [8,9] the oscillator strength of the $S_0 \rightarrow S_1$ electronic transition is very small. Therefore, one needs to excite the APN molecule to its higher electronic states in order to have efficient radiation absorption. Considering the next electronic transition of $S_0 \rightarrow S_2$ it looks that this is already sufficient to find our molecular system in an excited state (f = 0.0091). The nature of this electronic excitation is a

(π,π) → (π,π*) orbital transition. Once the molecule will reach its second excited state level, it begins its electronic excited state relaxation. It has two possibilities: either changing its electronic state to S_1 through the $S_1 \otimes S_2$ CI crossing or moving towards to its S_2 equilibrium conformation. From the optimized geometry position of the S_2 state one has again two further possibilities. First: to reach the previous CI crossing and move further the S_1 state and second: to change its spin configuration to the triplet one via the $S_2 \otimes T_3$ ISC point. Energetically, both alternatives are feasible, but considering the weak SO coupling (0.32 cm^{-1}) between the singlet and the triplet states, the first option looks more achievable than the second one. Hereupon the system can rapidly relax to its S_1 electronic state, since all these geometry changes involve benzene ring's planar deformation which doesn't mean significant energetic expense. As soon as, the molecule has changed its excited state, it reaches the local energy minimum on the $R_e^B(S_1)$ PES. Energetically, this geometry is a meta-stable conformation; since there is another minimum with lower energy ($R_e^C(S_1)$) showing geometrical changes at the carbonyl fragment. This $R_e^B(S_1)$ local minimum we consider to be the "cornerstone" of the further relaxation steps. From this point, the molecule can easily undergo to its $R_e^C(S_1)$ global minimum by passing a 0.1 eV higher $R_{TS}(S_1)$ saddle point (For geometrical parameters see Table 1, for its molecular graphics see Figure 4a and for its potential energy curve see Figure 4b). After reaching the global energy minimum of the S_1 state we have been unable to find any other critical point (CI or ISC) which would have moved the system to its singlet ground or a triplet state. The final step of the relaxation can be made only via the fluorescence deactivation [5]. Another very likely direction would be the crossing from the singlet spin state to the triplet one through the $S_1 \otimes T_1$ ISC point. This is close both energetically and geometrically to the local minimum geometry and the spin-orbit coupling is also strong enough to perform the spin transition. Once the molecule has changed its spin configuration the relaxation decay continues on the triplet deactivation path. Namely, from the $R_e^B(T_1)$ configuration the molecule comes rapidly down to its ground triplet state through the ($T_0 \otimes T_1$) a crossing. Finally, the molecule loses its triplet state and turn back to its ground singlet state by a long-life radiation (phosphorescence) deactivation. For the whole relaxation pathway along the triplet spin state see Figure 5. Besides of these two highly probable relaxation pathways which finally leads to different radiation emissions, APN can also show non-radiative deactivation. Indeed, close to the $R_e^B(S_1)$ local energy minimum there is a CI crossing ($S_0 \otimes S_1$) which could drive the molecule from the first excited to its ground state.

(a)

(b)
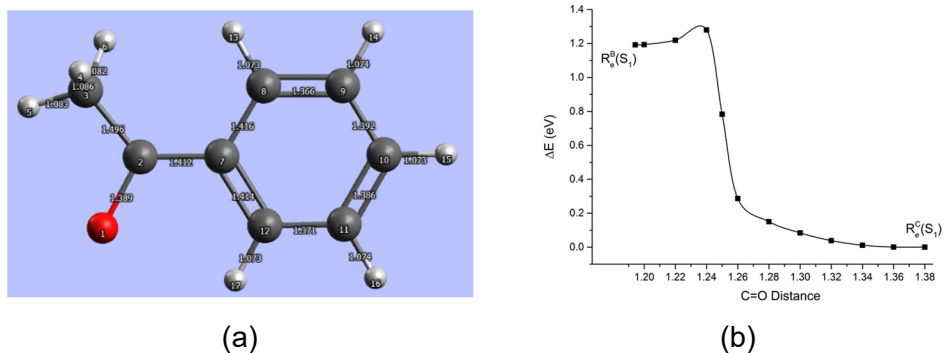
Figure 4. The geometry configuration of the global energy minimum of the APN's first excited state (a) and the PES of the transition state between the local minimum located at the benzene ring and the global equilibrium geometry of the APN's first excited state located at the carbonyl fragment (b).

Figure 5. Geometry configurations of the critical points ($S_2 \times T_3 \to T_3 \times T_2 \to T_2 \to T_2 \times T_1 \to T_1$) through the triplet relaxation pathway from the $S_2 \times T_3$ intersystem crossing to the T_1 equilibrium geometry of APN molecule.

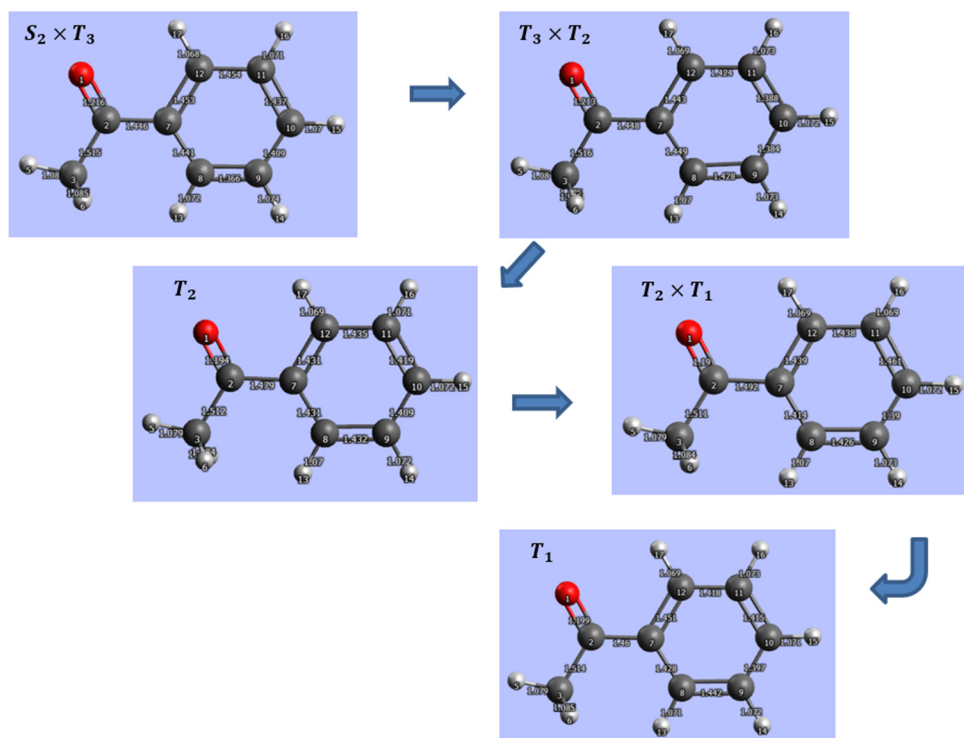In this case, the impediments could be the 0.63 eV energy barrier and the constraint of the benzene ring's non-planar deformation (See Table 3). Calculations show further two conceivable scenarios, but they might happen
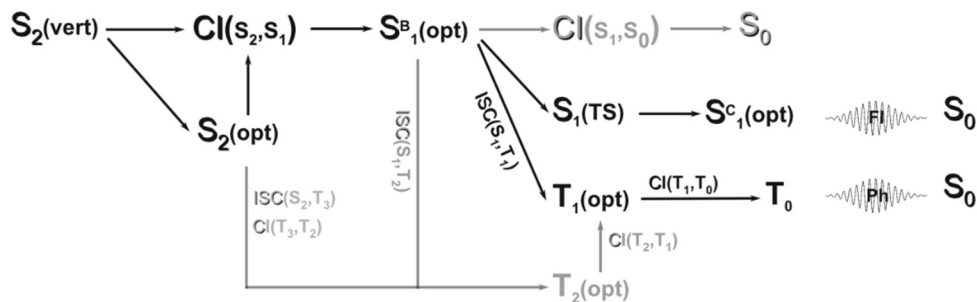

Figure 6. The possible relaxation pathways of the APN's low-lying electronic excited states.

with relatively small probabilities, due to the difficulty to achieve the different conditions necessary to reach the critical geometries. One of these deactivation schemes starts with the first step of the $S_2(vert) \rightarrow S_2(opt)$ relaxation, but from the optimized S_2 singlet state the system directly switches to the T_3 triplet one, via the $S_2 \otimes T_3$ ISC point. In this case the spin-orbit coupling is lower almost two orders of magnitude (0.32 cm^{-1}) than that for the $S_1 \otimes T_1$ crossing, but practically the geometry can be reached without crossing any energy gap or getting large geometry distortions. The second relaxation channel shows common pathway until the $R_e^B(S_1)$ local energy minimum is reached, but instead of the $S_1 \otimes T_1$ crossing it continues its relaxation passing the $S_1 \otimes T_2$ ISC point and follows its excited state decay along the triplet relaxation channel. For this case the spin-orbit coupling has a reasonable value of 1.15 cm^{-1}, but needs 0.6 eV excess of energy to reach the critical geometry of the $S_1 \otimes T_2$ ISC point. For the complete relaxation pathway see Figure 6.

COMPUTATIONAL DETAILS

The calculation of the equilibrium geometries as well as the localization of conical intersection (CI) and intersystem crossing (ISC) points between potential energy surfaces (PES) of the different electronic excited states of APN have been performed at the state-averaged CASSCF level of theory using the MOLPRO computational chemistry program package [17] In all cases the triple ζ quality def2-TZVP [18] basis set was

taken and no symmetry restrictions were considered for molecular geometries. Four π (one from C=O group of the carbonyl fragment and three from the benzene aromatic ring) and one n_O lone pair orbital of the oxygen atom were taken as occupied orbitals in the active space for the APN case, which was further completed with four virtual orbitals. One should mention that, using four virtual orbitals instead of three, further one-electron excitations are included in the excitation scheme and accordingly, better excitation energies can be obtained. In this way, the final electron-orbital configuration of the active space for the APN becomes (10,9), the nomenclature (*n,m*) denoting here an active space of *n* electrons and *m* orbitals. In order to take into account, the effect of electron correlations (static and dynamic) for different excitation energies evaluation, we have performed further calculations using the extended multistate CASPT2 [19] method which provides a better description of near degenerate situations and avoided crossings. For this case of XMS-CASPT2 calculations a level shift [20] parameter of 0.2 was considered. The computation of individual spin-orbit matrix elements for a given pair of states were obtained considering the Breit-Pauli operator as described in ref.-s [21,22] and implemented in MOLPRO the program package. The charge distribution analysis was performed by natural population analysis (NPA) [23,24] using the NBO module of the same MOLPRO package. The open source GABEDIT [25] molecular graphics program was used to visualize and analyze the molecular structures, and the molecular graphics (figures) were created using the GAUSSVIEW [26] molecule editor and visualizer software.

CONCLUSIONS

The full mapping of low-lying excited state relaxation dynamic pathways for acetophenone has been investigated considering the complete active space self-consistent field (CASSCF) and the extended multistate complete active space second-order perturbation theory (XMS-CASPT2) methods. All critical geometry configurations, whether equilibrium or surface crossing point geometries, have been located on the potential energy hyper-surface and the strength of the spin-orbit coupling at the crossing point geometries were characterized. Results reveal several excited state deactivation pathways including both the singlet and triplet spin states, which lead either to radiative or non-radiative relaxation. In the case of radiative relaxation both the fluorescence and phosphorescence phenomena could occur, depending on which type of intersection points (conical intersection or intersystem crossing) the system passes through in its higher electron states.

ACKNOWLEDGMENTS

REFERENCES

1. W. H. Fang; D. L. Phillips; *ChemPhysChem*, **2002**, *3*(10), 889-892.
2. J. Li; F. Zhang; W. H. Fang; *J. Phys. Chem. A*, **2005**, *109*(34), 7718-7724.
3. Q. Fang; Y. J. Liu; *J. Phys. Chem. A*, **2010**, *114*(1), 680-684.
4. M. Berger; C. Steel; *J. Am. Chem. Soc.*, **1975**, *97*(17), 4817-4821.
5. R. D. Vanselow; A. B. F. Duncan; *J. Am. Chem. Soc.*, **1953**, *75*(4), 829-832.
6. M. Koyanagi; R. J. Zwarich; L. J. Goodman; *Chem. Phys.*, **1972**, *56*(6), 3044-3060.
7. Y.-W. Wang; H.-Y. He; W.-H. Fang; *J. Mol. Struct. (THEOCHEM)*, **2003**, *634*(1-3), 281-287.
8. A. Bende; *AIP Conf. Proc.*, **2013**, *1565*, 24-28.
9. M. Huix-Rotllant; D. Siri; N. Ferré; *Phys. Chem. Chem. Phys.*, **2013**, *15*(44), 19293-19300.
10. M. Bear; Beyond Born--Oppenheimer: Electronic Nonadiabatic Coupling Terms and Conical Intersections, Wiley-Interscience, 2006.
11. H.-Y. Xiao; Y.-J. Liu; W.-H. Fang; *J. Mol. Struct. (THEOCHEM)*, **2007**, *802*(1-3), 99-103.
12. G. Cui; Y. Lu; W. Thiel; *Chem. Phys. Lett.*, **2012**, *537*, 21-26.
13. W.-H. Fang; *Acc. Chem. Res.*, **2008**, *41*(3), 452-457.
14. M. Huix-Rotllant; N. Ferré; *J. Chem. Phys.,* **2014**, *140*(13), 134305.
15. I. J. Palmer; I. N. Ragazos; F. Bernardi; M. Olivucci; M. A. Robb; *J. Am. Chem. Soc.*, **1993**, *115*, 673-682.
16. Q. Li, D. Mendive-Tapia; M. J. Paterson; A. Migani; M. J. Bearpark; M. A. Robb; L. Blancafort; *Chem. Phys.*, **2010**, *377*(1-3), 60-65.
17. MOLPRO version 2012.1 is a package of ab initio programs written by H.-J. Werner; P. J. Knowles; G. Knizia; F. R. Manby; M. Schütz; P. Celani; T. Korona; R. Lindh; A. Mitrushenkov; G. Rauhut; K. R. Shamasundar; T. B. Adler; R. D. Amos; A. Bernhardsson; A. Berning; D. L. Cooper; M. J. O. Deegan; A. J. Dobbyn; F. Eckert; E. Goll; C. Hampel; A. Hesselmann; G. Hetzer; T. Hrenar; G. Jansen; C. Köppl; Y. Liu; A. W. Lloyd; R. A. Mata; A. J. May; S. J.; McNicholas; W. Meyer; M. E. Mura; A. Nicklaβ; D. P. O'Neill; P. Palmieri; D. Peng; K. Pflüger; R. Pitzer; M. Reiher; T. Shiozaki; H. Stoll; A. J. Stone; R. Tarroni; T. Thorsteinsson; M. Wang; see http://www.molpro.net.
18. F. Weigend; R. Ahlrichs; *Phys. Chem. Chem. Phys.*, **2005**, *7*, 3297-3305.

19. T. Shiozaki; W. Györffy; P. Celani; H.-J. Werner; *J. Chem. Phys.*, **2014**, *135*(8), 081106.
20. J. Lorentzon; M. P. Fulscher; B. O. Roos; *J. Am. Chem. Soc.*, **1995**, *117*(36), 9265-9273.
21. A. Berning; M. Schweizer; H.-J. Werner; P. J. Knowles; P. Palmieri; *Mol. Phys.*, **2000**, *98*(21), 1823-1833.
22. A. O. Mitrushenkov; P. Palmieri; R. Tarroni; *Mol. Phys.*, **2003**, *101*(13), 2043-2046.
23. J. P. Foster; F. Weinhold; *J. Am. Chem. Soc.*, **1980**, *102*(24), 7211-7218.
24. A. E. Reed; R. B. Weinstock; F. Weinhold; *J. Chem. Phys.*, **1985**, *83*(2), 735-743.
25. A. R. Allouche; *J. Comput. Chem.*, **2011**, *32*, 174-182.
26. GaussView, Version 5.0.9, R. Dennington, T. Keith, J. Millam, Semichem Inc., Shawnee Mission, KS, 2009.

AMS RADIOCARBON DATING OF THE LARGE PEDUNCULATE OAK OF MERCHEAŞA, ROMANIA

ADRIAN PATRUT[a,b,*], LASZLO RAKOSY[c], ROXANA T. PATRUT[a], VICTOR BOCOS-BINTINTAN[d], ILEANA-ANDREEA RATIU[a,b], JENÖ BODIS[a,b], STEPHAN WOODBORNE[e]

ABSTRACT. The paper reports the AMS (accelerator mass spectrometry) radiocarbon dating results of the large pedunculate oak of Mercheaşa, Romania, which has a circumference of 10.16 m. Two wood samples were extracted from the trunk and from the largest horizontal branch. Five segments from these samples were analysed by AMS radiocarbon. The oldest dated sample segment originates from the largest horizontal branch, very close to its geometrical centre. It had a radiocarbon date of 386 ± 45 BP, which corresponds to a calibrated age of 540 ± 35 calendar years. This value indicates an age of 560 ± 35 years for the oak of Mercheaşa.

Keywords: *AMS radiocarbon dating, Quercus robur, dendrochronology, age determination, Romania.*

INTRODUCTION

The pedunculate oak (*Quercus robur* L.), which belongs to the family Fagaceae, is considered to be one of the most longevous native European trees. This columnar tree is typically 20-30 m tall, but can reach heights up to 40-50 m, and has a diameter of 3-4 m [1,2]. The largest specimens have died over the last two centuries or are very close to the end of their life cycle. The biggest known individual was the so-called Emperor's Oak (Kaisereiche),

---

[a] *Babeş-Bolyai University, Faculty of Chemstry and Chemical Engineering, 11 Arany Janos, RO-400028, Cluj-Napoca, Romania*

[b] *Babeş-Bolyai University, Raluca Ripan Institute for Research in Chemistry, 30 Fantanele, RO-400294 Cluj-Napoca, Romania*

[c] *Babeş-Bolyai University, Faculty of Biology and Geology, 44 Republicii, RO-400015, Cluj-Napoca, Romania*

[d] *Babeş-Bolyai University, Faculty of Envoronmental Science and Engineering, 30 Fantanele, RO-400294 Cluj-Napoca, Romania*

[e] *iThemba LABS, Private Bag 11, WITS 2050, South Africa*

* *Corresponding author: apatrut@gmail.com*

ADRIAN PATRUT, LASZLO RAKOSY, ROXANA T. PATRUT, VICTOR BOCOS-BINTINTAN,
ILEANA-ANDREEA RATIU, JENÖ BODIS, STEPHAN WOODBORNE

located in the village Randovici, close to Travnik in Bosnia. This giant oak toppled and died in 1998, during a storm. Its enormous hollow trunk, in which 66 infantrymen took shelter, had a circumference at breast height of almost 17 m. Recent research, based on ring counting and also on radiocarbon dating results of long cores, as well as on successive measurements of the circumference over longer periods of time, estimate the age limit of the largest oaks to 600-800 years, reaching up to 1,000 years only in exceptional cases, considerably less than previously considered [3].

In 2005, we initiated a research project for clarifying several controversial aspects regarding the architecture, growth and age of the African baobab and of other baobab species. The research based on our new approach is not limited to dead or fallen trees, but also enables to investigate and date standing live specimens. This approach consists of AMS radiocarbon dating of tiny wood samples collected from different areas of monumental baobabs [4-9]. We extended our research by investigating individuals which belong to other angiosperm species, including trees from Romania.

Romania hosts several monumental trees of large dimensions and old ages. We investigated and dated by radiocarbon some remains of the historic pedunculate oak of Ţebea [10], the large pedunculate oaks of Cajvana and Botoşana [11,12], the old black poplar of Mocod and the very big grey poplar of Rafaila [13], as well as the old ash of Aiton [14].

Here we present the investigation and AMS radiocarbon dating results of another very large Romanian tree, namely the pedunculate oak of Mercheaşa.

RESULTS AND DISCUSSION

The pedunculate oak of Mercheaşa and its area. The large tree can be found on a pasture with secular oaks, located on a hill at 1.7 km NE from the village Mercheaşa, commune Homorod, Braşov county, in the central part of Romania. The closest notable localities are Rupea (at 11 km), Sighişoara (55 km) and Braşov (65 km). Its GPS coordinates are 46º03.963' N, 025º21.730' E and the altitude is 528 m. The mean annual rainfall is around 627 mm (Sibiu station).

The oak of Mercheaşa has a height of 17.6 m, the circumference at breast height (cbh; at 1.30 m above mean ground level) is 10.16 m, while the circumference at ground level is 12.08 m. The overall wood volume is around 50 m^3, out of which 30 m^3 for the trunk and 20 m^3 for the crown (**Figure 1**).

Figure 1. General view of the pedunulate oak of Mercheaşa taken from the south-east.

The canopy is asymmetrical. While its eastern part is higher and narrower, the western part is shorter and wider. The horizontal dimensions of the canopy are 19.7 (NS) x 24.4 (WE) m (**Figure 2**).

In 2010, the very large oak was measured and identified by two young students from Rupea as the biggest tree of the pasture, which covers an area of 3 km². Certain forest engineers estimated the age of this oak to at least 900 years, according to a supposed relationship between the circumference of the trunk and the age of the tree. We want to emphasize that this relationship between circumference and age is based rather on guesstimates than on accepted scientific measurements [15].

In 2012, the oak of Mercheaşa was declared a Natural Monument in a protected area. The same year, a wooden fence was placed around it as a protection measure against animals. At the moment, the Carpaterra Association and ICAS Braşov manage its protection and promotion.

The claimed age value of at least 900 years has been intensely publicised and accepted without reservation. Dozens of visitors from all over the country come daily to the pasture of Mercheaşa to see "the oldest tree of Romania", which was also named "The Carpathian Elder" (Bătrânul Carpaţilor).

ADRIAN PATRUT, LASZLO RAKOSY, ROXANA T. PATRUT, VICTOR BOCOS-BINTINTAN, ILEANA-ANDREEA RATIU, JENÖ BODIS, STEPHAN WOODBORNE

Figure 2. The photograph shows the asymmetrical crown of the oak of Mercheaşa.

The oak of Mercheaşa is in an excellent state of vegetation, with few broken or dry branches and some traces of previous fire damage. The large trunk has no visible cavities. All these data suggest that the oak is considerably younger than currently believed. For these reasons we decided to determine the age of the oak by scientific methods.

Wood samples. Two wood samples, labelled M-1 and M-2, were extracted from the oak of Mercheaşa with an increment borer. The first wood sample M-1, with the length of 0.80 m, was collected from the big trunk, at a convenient height of 1.70 m above ground. The second sample M-2, with the length of 0.46 m, was collected close to the base of the largest horizontal branch, at a height of 2.10 m above ground (**Figure 3**).

Two pieces/segments, each of the length of 10^{-3} m (marked a and b), were extracted from determined positions of the sample M-1, while three segments of the same length (marked a, b and c), were extracted from sample M-2.

Figure 3. The image presents the two sampling positions.

AMS results and calibrated ages. Radiocarbon dates of the 5 sample segments are listed in Table 1. The radiocarbon dates are expressed in ^{14}C yr BP (radiocarbon years before present, i.e., before the reference year 1950). Radiocarbon dates and errors were rounded to the nearest year.

Calibrated (cal) ages, expressed in calendar years CE (CE, i.e., common era), are also displayed in Table 1. The 1σ probability distribution (68.3%) was selected to derive calibrated age ranges. For three segments (M-1a, M-2a, M-2c), the 1σ distribution is consistent with two ranges of calendar years, while for the other two sample segments (M-1b, M-2b) it corresponds to three ranges of calendar years. In all these cases, the confidence interval of one range is considerably greater than that of the other(s); therefore, it was selected as the cal CE range of the segment for the purpose of this discussion.

For obtaining single calendar age values of sample segments, we derived a mean calendar age of each sample segment from the selected range (marked in bold). Sample/segment ages represent the difference between the year 2021 CE and the mean value of the selected range, with

ADRIAN PATRUT, LASZLO RAKOSY, ROXANA T. PATRUT, VICTOR BOCOS-BINTINTAN,
ILEANA-ANDREEA RATIU, JENÖ BODIS, STEPHAN WOODBORNE

the corresponding error. Sample ages and errors were rounded to the nearest 5 yr. We used this approach for selecting calibrated age ranges and single values for sample ages in all our previous articles on AMS radiocarbon dating of large and old angiosperm trees [4-14,15-19].

Table 1. AMS Radiocarbon dating results and calibrated ages
of samples collected from the oak of Mercheaşa.

Sample code	Depth[1] [height[2]] (m)	Radiocarbon date [error] (^{14}C yr BP)	Cal CE range 1σ [confidence interval]	Assigned year [error] (cal CE)	Sample age [error] (cal CE)
M-1a	0.40 [1.70]	101 [± 44]	1694-1725 (16.4%) **1812-1916 (51.9%)**	1864 [± 52]	155 [± 50]
M-1b	0.80 [1.70]	235 [± 37]	**1636-1678 (36.8%)** 1741-1752 (4.5%) 1763-1800 (27.0%)	1657 [± 21]	365 [± 20]
M-2a	0.10 [2.10]	92 [± 43]	1694-1725 (17.3%) **1812-1916 (50.9%)**	1864 [± 52]	155 [± 50]
M-2b	0.30 [1.71]	212 [± 40]	1647-1682 (22.7%) **1735-1803 (38.0%)** 1930-... (8.8%)	1769 [± 34]	250 [± 35]
M-2c	0.47 [2.10]	386 [± 45]	**1450-1516 (48.3%)** 1590-1620 (20.0%)	1483 [± 33]	540 [±35]

[1] Depth in the wood from the sampling point.
[2] Height above ground level.

Dating results of samples (segments). The oldest dated segment, i.e., M-2c, represents the deepest end of sample M-2 which was collected from the largest horizontal branch, very close to its geometrical centre in the sampling direction. Its radiocarbon date of 386 ± 45 BP corresponds to a calibrated age of 540 ± 35 calendar yr. The lower ages of the other two segments, namely M-2a and M-2b, are in good agreement with their positions in the branch.

The oldest dated segment extracted from sample M-1, collected from the trunk, i.e., M-1b, represents its end and originates from a distance of 0.80 m from the sampling point. It had a radiocarbon date of 235 ± 37 BP, which corresponds to a calibrated age of 365 ± 40 calendar yr.

Ring counting. On the collected wood samples, the growth/annual rings are obvious in certain areas, while in other areas they are faint. The most interesting sample M-2 had a length of 0.47 m and was collected at a

height of 2.10 m, close to the base of the largest horizontal branch. At this point, the circumference of the branch is 3.03 m. This value corresponds to a radius of 0.48 m. The distance from the sample end to the centre of the branch, which theoretically corresponds to its maximum age, is of 0.01 m.

According to our counting, sample 2 contains around 520 growth rings. Taking into account the distance from the sample end to the centre of the branch and also the height of the branch above the ground, the ring counting suggests an age of 540 years for the pedunculate oak.

Age of the pedunculate oak of Mercheaşa. The age of the oak can be calculated by extrapolating the age of the oldest dated sample segment M-2c, namely 540 ± 35 years, which originates from the largest branch, to the centre of this branch and by considering also the height of the branch. By the already presented values, the radiocarbon dating results indicate an age of 560 ± 35 years for the oldest part of the pedunculate oak of Mercheaşa. This value is in good accordance with the age estimated from the ring counting.

CONCLUSIONS

Our research dicloses the AMS radiocarbon dating results of the large pedunculate oak of Mercheaşa. The aim of our investigation was to determine the age of tree. Two wood samples were collected from the trunk and from the largest horizontal branch, respectively. Five tiny segments were extracted from the samples, processed and dated by AMS radiocarbon.

The oldest dated segment had a radiocarbon date of 386 ± 45 BP, which corresponds to a calibrated age of 540 ± 35 calendar years. Its original position is very close to the geometrical centre of the largest horizontal branch. The dating value indicates an age of 560 ± 35 years for the oak of Mercheaşa. Therefore, one can state that the oak of Mercheaşa started growing around the year 1460 CE.

EXPERIMENTAL SECTION

Sample collection. The two investigated wood samples were collected with a Haglöf CH 800 increment borer (0.80 m long, 0.0108 m inner diametre). A number of five tiny pieces/segments, of the length of 10^{-3} m, were extracted from predetermined positions along the samples. The segments were processed and investigated by AMS radiocarbon dating.

Sample preparation. The α-cellulose pretreatment method was used for removing soluble and mobile organic components [20]. The resulting samples were combusted to CO_2, which was next reduced to graphite on iron catalyst [21,22]. The resulting graphite samples were analysed by AMS.

AMS measurements. The radiocarbon measurements were done at the AMS Facility of iThemba LABS, Johannesburg, Gauteng, South Africa, using the 6 MV Tandem AMS system [23]. The obtained fraction modern values were finally converted to a radiocarbon date. The radiocarbon dates and errors were rounded to the nearest year.

Calibration. Radiocarbon dates were calibrated and converted into calendar ages with the OxCal v4.4 for Windows [24], by using the IntCal20 atmospheric data set [25].

ACKNOWLEDGMENTS

REFERENCES

1. P.H. Raven, G.B. Johnson, J.B. Losos, S.R. Singer, "Biology: Seventh Edition", McGraw Hill, New York, **2005**.
2. A. le Hardÿ de Beaulieu, T. Lamant, "Le guide illustré des chênes", Vol. 1-2, Huitième, Paris, **2007**.
3. J. Pater, "Riesige Eichen: Baumpersönlichkeiten und ihre Geschichten", Franckh-Kosmos, Stuttgart, **2017**.
4. A. Patrut, K.F. von Reden, D.A. Lowy, A.H. Alberts, J.W. Pohlman, R. Wittmann, D. Gerlach, L. Xu, C. Mitchell, *Tree Phys.*, **2007**, *27*, 1569-1574.
5. A. Patrut, K.F. von Reden, R. Van Pelt, D.H. Mayne, D.A. Lowy, D. Margineanu, *Ann. Forest Sci.*, **2011**, *68*, 993-1003.
6. A. Patrut, S. Woodborne, K.F. von Reden, G. Hall, M. Hofmeyr, D. Lowy, R.T. Patrut, *PLoS ONE*, **2015**, *10(1)*, e0117193.
7. A. Patrut, L. Rakosy, R.T. Patrut, I.A. Ratiu, E. Forizs, D.A. Lowy, D. Margineanu, K.F. von Reden, *Studia UBB Chemia*, **2016**, *LXI*, *4*, 7-20.
8. A. Patrut, S. Woodborne, K.F. von Reden, G. Hall, R.T. Patrut, L. Rakosy, P. Danthu, J-M. Leong Pock-Tsy, D.A. Lowy, D. Margineanu, *Radiocarbon*, **2017**, 59(2), 435-448.
9. A. Patrut, S. Woodborne, R.T. Patrut, L. Rakosy, D.A. Lowy, G. Hall, K.F. von Reden, *Nat. Plants*, **2018**, *4*, 423-426.

10. A. Patrut, K.F. von Reden, D.A. Lowy, S. Pasca, L. Kekedy-Nagy, I. Sovago, *Studia UBB Chemia*, **2010**, *LV*, *1*, 113-120.
11. A. Patrut, K.F. von Reden, V. Savu, D.A. Lowy, R. Mitea, I. Barbul, *Studia UBB Chemia*, **2011**, *LVI*, *1*, 145-155.
12. A. Patrut, N. Robu, V. Savu, R.T. Patrut, L. Rakosy, I.A. Ratiu, D.A. Lowy, D. Margineanu, K.F. von Reden, *Studia UBB Chemia*, **2018**, *LXIII*, *4*, 7-13.
13. A. Patrut, K.F. von Reden, D.A. Lowy, R.T. Patrut, D.L. Vaida, D. Margineanu, *Nucl. Instrum. Methods Phys. Res. Sect. B.*, **2013**, *294*, 616-621.
14. A. Patrut, R.T. Patrut, L. Rakosy, I.A. Ratiu, D.A. Lowy, J. Bodis, K.F. von Reden, *Studia UBB Chemia*, **2018**, *LXIII*, *3*, 41-48.
15. Institutul de cercetări şi amenajări silvice Braşov, Asociaţia Geopark Perşani, "Stejarul secular din Mercheaşa - Bătrânul Carpaţilor (Studiu de fundamentare ştiinţifică pentru declararea Monumentului Naturii)", Braşov, **2011**.
16. A. Patrut, A. Garg, S. Woodborne, R.T. Patrut, L. Rakosy, I.A. Ratiu, *PLOS One*, **2020**, *15(1): e0227352.*
17. A. Patrut, K.F. von Reden, P. Danthu, J-M. Leong Pock-Tsy, L. Rakosy, R.T. Patrut, D.A. Lowy, D. Margineanu, *Nucl. Instrum. Methods Phys. Res. Sect. B,* **2015**, *361*, 591-598.
18. A. Patrut, R.T.Patrut, L. Rakosy, D.A. Lowy, D. Margineanu, K.F. von Reden, *Studia UBB Chemia*, **2019**, LXIV, 2 (II), 411-419.
19. A. Patrut, R.T. Patrut, P. Danthu, J-M. Leong Pock-Tsy, L. Rakosy, D.A. Lowy, K.F. von Reden, *PLOS One*, **2016**, *11(1): e0146977.*
20. N.J. Loader, I. Robertson, A.C. Barker, V.R. Switsur, J.S. Waterhouse, *Chem. Geol.*,**1997**, 136(3), 313–317.
21. Z. Sofer, *Anal. Chem.*, **1980**, *52(8)*, 1389-1391.
22. J.S. Vogel, J.R. Southon, D.E. Nelson, T.A. Brown, *Nucl. Instrum. Methods Phys. Res. Sect. B*, **1984**, *5*, 289-293.
23. V.L. Mbele, S.M. Mullins, S.R. Winkler, S. Woodborne, *Phys. Procedia*, **2017**, *90*, 10-16.
24. C. Bronk Ramsey, *Radiocarbon*, **2009**, *51*, 337-360.
25. P.J. Reimer, W.E. N. Austin, E. Bard, A. Bayliss, P.G. Blackwell, C. Bronk Ramsey, M. Butzin, H. Cheng, R. Lawrence Edwards, M. Friedrich, P.M. Grootes, T.P. Guilderson, I. Hajdas, T.J. Heaton, A. G. Hogg, K.A Hughen, B. Kromer, S.W. Manning, R. Muscheler, J.G. Palmer, C. Pearson, J. van der Plicht, R.W. Reimer, D.A. Richards, E.M. Scott, J.R. Southon, C.S.M. Turney, L. Wacker, F. Adolphi, U. Büntgen, M. Capano, S.M. Fahrni, A. Fogtmann-Schulz, R. Friedrich, P. Köhler, S. Kudsk, F. Miyake, J. Olsen, F. Reinig, M. Sakamoto, A. Sookdeo, S. Talamo, *Radiocarbon*, **2020**, *62(4)*, 727-757.